Long-Term Behaviour of GFRP Prestressed Concrete Beams

by

Mohamed Hamdy Mohamed Zawam

A thesis
presented to the University of Waterloo
in fulfillment of the
thesis requirement for the degree of
Doctor of Philosophy
in
Civil Engineering

Waterloo, Ontario, Canada, 2015

AUTHOR'S DECLARATION

I hereby declare that I am the sole author of this thesis. This is a true copy of the thesis, including any required final revisions, as accepted by my examiners.

I understand that my thesis may be made electronically available to the public.

Abstract

During the last two decades, fibre-reinforced polymer (FRP) composites have emerged as promising materials that can be used in lieu of steel for reinforcing concrete structures due to their corrosion-resistant properties, their high tensile strength, and their high stiffness to weight ratio. FRPs have lower moduli of elasticity compared to steel which may lead to increased deflections and deformations of FRP reinforced structures unless section sizes are increased. To overcome this serviceability concern, FRP bars can be prestressed. Previous research has focused on the use of carbon and aramid fibre reinforced polymers (CFRPs and AFRPs) in prestressed concrete while less attention was given to glass fibre reinforced polymers (GFRPs) because they have high relaxation and are susceptible to creep rupture. As well, only very limited data on the long-term behaviour of GFRP prestressed concrete members under sustained and fatigue loads is available. Also, no design guidelines are provided by CAN/CSA-S806-12 or ACI 440.4R-04 for using prestressed GFRP bars in concrete members.

This research study consisted of experimental and analytical phases, and was designed to assess the long-term properties of a concrete beams prestressed with a new generation of GFRP bars that are reported to have enhanced mechanical properties such that the bars are suitable for prestressed applications by overcoming the creep rupture and the relaxation problems (Weber and Baquero (2010), & Zawam and Soudki (2012)). This study investigated the transfer length of the prestressed GFRP bars of diameters 12 mm and 16 mm in concrete. Most of the available research studied the transfer length of CFRP and AFRP tendons, and both CAN/CSA-S6-06 and ACI 440.1R-06 give equations for predicting the transfer length for these bar types only. The GFRP bars were prestressed to 40% of their ultimate capacity, which is more than the 25% prestressing limit at transfer that is set by CAN/CSA-S6-06 to avoid creep rupture. The effects of the prestressing level, the GFRP bar diameter and the concrete strength on the long-term behaviour of GFRP prestressed concrete were investigated.

Twenty beams with dimensions of 150 x 255 x 3600 mm were cast and tested under different sustained load levels for 300 days. The long-term deflections, the concrete strains and the GFRP

strains were monitored throughout the testing period. The main parameters considered were the diameter of the GFRP prestressing bars (12 mm and 16 mm), the prestressing level (0%, 25% and 40% of the ultimate strength), and the sustained load level (35%, 60%, and 80% of the ultimate capacity of the beam). Following the sustained loading phase, all beams were tested to failure in four- point bending. The transfer length measurements were taken for the prestressed beams, and data on the early relaxation of the GFRP bars was recorded for 277 hours.

The experimental results showed that prestressing of GFRP bars significantly decreased the beams deflections, and the total and the concrete creep strains under service loading conditions. The results also showed that subjecting the beams to different levels of sustained loading for 300 days did not affect their ultimate capacity. It was concluded from the results that the increase in the GFRP strains in beams under sustained loading was mainly caused by the increase in the beam curvature due to creep and shrinkage of the concrete rather than the creep of the GFRP bars. The experimental measurements showed that the transfer length of 16 mm diameter GFRP bars in concrete with compressive strength of 30 MPa was about $17d_b$ (bar diameter), and $14d_b$ for prestressing levels of 40% and 25%, respectively.

The analytical phase in this study involved developing an analytical model based on layer-by-layer strain compatibility analysis that was used to predict the short-term load-deflection behaviour and the long-term deformations of GFRP prestressed concrete beams. A model based on layer-by-layer strain compatibility analysis was also proposed to predict the unloading behaviour of the GFRP reinforced/prestressed beams after being subjected to sustained loading. The predicted load-deflections curves from the model were in good agreement with the experimental curves except for a discrepancy appears between the experimental and the predicted curves where the predicted load-deflection curve tends to flatten at the low load levels, which is more obvious in the prestressed beam. The transfer length results were used to improve the transfer length estimates provided by the ACI 440.4 R-04 equation by calibrating the material coefficient factor (αt) used in the ACI equation. A value of 2.6 in N-mm units is proposed for that coefficient to predict transfer length values for the GFRP bars used in this study.

Acknowledgements

I will always be grateful to have had the honour of working with my late supervisor, Professor Khaled Soudki, whose support was phenomenal throughout the three years during which I worked under his supervision.

I am also thankful for Dr.Jeffrey West, who agreed to take over the responsibility after the passing away of Professor Khaled Soudki, and put exceptional time and effort to help me finish this study.

The effort of the laboratory technicians: Richard Morrison, Douglas Hirst, and Rob Sluban is greatly appreciated. The expertise and advice of Dr. Slamah Krem during the formative stages of this project is also gratefully acknowledged.

I would also like to express my gratitude to Schoeck-Canada Inc. and to the Natural Science and Engineering Research Council of Canada (NSERC) for their financial support.

I am particularly thankful for my colleagues who assisted me throughout various stages of this study. Special thanks to Olivier Daigle, Hesham Elhuni, Rizwan Azam, Martin Noel, Adham El Menoufy, Liam butler, Mohamed Yakhlaf, Abdulaziz Alaskar, Noran Abdel-Wahab, Amr Abdel-Havez, Rayed Alyousef, Hisham Alabduljabbar, and Taha Younes.

Lastly, I would like to express my deepest thanks to my family who have supported me during this important phase in my life. Special thanks to my parents who have always encouraged me and given me the confidence to reach my goals. Many thanks to my brothers; Hossam, Sherif, and Ahmed, for their continuous support. Thanks to my wife Heba whose support was phenomenal, and thanks to my daughter, Malak whose smile brings me my greatest joy.

Dedication

This thesis is dedicated to the memory of my late supervisor Professor Khaled Soudki, who passed away on September 17, 2013 after a long battle with cancer. He was a distinguished researcher in the field of using FRP in concrete structures, and an exceptional supervisor. He was a caring person who was willing to go the "extra mile" if one of his students needed assistance. He always paid attention to his students' personal issues and frustrations, and showed them that he really cared about them. He leaves behind a legacy of research all over the world, and will always be remembered for his contribution to the civil engineering field.

Table of Contents

List of Figures

List of Tables

Chapter 1
Introduction

1.1 General

Corrosion of steel reinforcement is the primary cause of premature deterioration of reinforced concrete structures in Canada and the USA, and affects their functionality and safety. Reinforced concrete bridges are the most widely affected type of concrete structure because of the use of road salts and chemicals for de-icing. More than 30,000 deteriorated bridges in Canada and 200,000 bridges in the USA need to be repaired (Mufti 2003). The rehabilitation of Canada‘s deteriorated infrastructure will cost about 49 billion dollars (Mufti 2003). This shows the significance of the corrosion problem and the importance of studying ways to overcome it.

During the last two decades, fibre-reinforced polymer (FRP) composites have emerged as promising materials that can be used for reinforcing concrete structures. The non-corroding properties of FRPs, their high tensile strength, and their high stiffness to weight ratio made them very attractive substitute to conventional reinforcing steel. Nowadays, FRPs have become common in many civil engineering applications including new construction, repair and rehabilitation, and architectural works. Three main types of fibres (Aramid, Carbon and Glass fibres) are used to produce FRP bars and strands for civil engineering applications.

Ongoing research is being conducted on the behaviour of concrete members reinforced or prestressed with FRP bars. The main difference between FRP and steel is that the FRP reinforcement has linear elastic behaviour up to failure and its modulus of elasticity is much lower than that of steel. An FRP reinforced beam will deform elastically until cracking, then continue to deform in an approximate linear manner under increasing load until the FRP bars rupture or the concrete crushes. The low modulus of elasticity of FRP results in larger deflections and deformations of FRP reinforced structures in comparison to steel structures. Using prestressed FRP bars is a suitable solution for the problem of excessive deflections at service loads.

1.2 Research Significance

Extensive research studies have been conducted since 1990 to investigate the short and long-term behaviour of FRP prestressed concrete elements. The main focus of the previous work was on CFRP and AFRP reinforcement, while less attention was given to GFRP reinforcement because prestressed glass tendons are used only very rarely (ISIS 2008). The use of GFRP bars in prestressed applications was limited due to their susceptibility to creep rupture and their high relaxation properties in comparison to CFRP and AFRP. Very limited data on the long-term behaviour of GFRP prestressed concrete members under sustained and fatigue loads is available. Also, no design guidelines are provided by CAN/CSA-S806-12 or ACI 440.4R-04 for using prestressed GFRP bars in concrete members.

A new generation of GFRP bars have been recently manufactured and are reported to have mechanical properties that make the bars suitable for prestressed applications (Weber and Baquero, 2010). The research presented in this thesis investigated the long-term flexural behaviour of concrete beams prestressed with these GFRP bars under sustained loads, and provided data about the transfer length of these bars.

1.3 Research Objectives

The general objective of this research was to investigate the long-term flexural behaviour of concrete beams prestressed with a new generation of GFRP bars that are reported to have low relaxation properties and are not affected by creep rupture at tensile stresses less than about 50% of their ultimate strength. The specific objectives were:

1. To add to the currently limited body of work on the structural behaviour of GFRP prestressed concrete beams.

2. Investigate the effect of bar diameter, prestressing level, concrete strength and sustained load level on the long-term flexural behaviour of GFRP prestressed concrete beams under sustained loads.

3. To investigate the effect of increasing the prestressing level of the GFRP bars beyond the 25% prestressing limit -set by CAN/CSA-S6-06 to avoid creep rupture- on the long-term behaviour of GFRP prestressed concrete.

4. To investigate the effect of creep of the GFRP bars on the overall long-term behaviour of GFRP prestressed concrete beams.

5. To investigate the transfer length of the prestressed GFRP bars of diameters 12 mm and 16 mm in concrete.

6. To improve the transfer length estimates provided by the ACI 440.4 R-04 equation by calibrating the material coefficient factor (α_t) used in the ACI equation.

7. To develop an analytical model to predict the long-term flexural behaviour of concrete beams prestressed with GFRP bars.

The parameters that were considered in this study are the prestressed GFRP bar diameter (12M and 16M), prestressing level (0%, 25% and 40% of the ultimate strength of the GFRP bars), sustained load level (35%, 60%, and 80% of the beam ultimate capacity), and concrete compressive strength (40 MPa and 80 MPa).

1.4 Thesis organization

This thesis consists of six chapters including this chapter. Chapter 2 provides a comprehensive background and a literature review. The experimental program is described in Chapter 3, and Chapter 4 includes the experimental results and discussion. The analytical work is given in Chapter 5, while Chapter 6 includes the conclusions and the recommendations for future work.

Chapter 2
Background and Literature Review

2.1 Fibre reinforced Polymers (FRPs)

2.1.1 Definition of FRP

FRP composites consist of continuous longitudinal high strength fibres impregnated in a polymer matrix with fibre content of about 40% to 70%. They were developed in the 1940s to be used in aerospace and naval industries, and later were introduced to the civil industry to benefit from their properties (Minosaku, 1992). FRP composites are known for their non-corroding properties, their high tensile strength, and their high stiffness to weight ratio which enabled them to provide sustainable solutions to civil engineers in both new construction and rehabilitation applications (ACI 440R- 07).

Three main types of fibre composites are being used in civil engineering applications, namely CFRP (Carbon Fibre Reinforced Polymer), GFRP (Glass Fibre Reinforced Polymer), and AFRP (Aramid Fibre Reinforced Polymer). These FRP types differ from each other and from steel in terms of their mechanical properties such as tensile strength and modulus of elasticity. CFRP has the highest tensile strength and modulus of elasticity while GFRP has the lowest strength and modulus of elasticity in FRPs. The tensile strength of FRPs is in general higher than that of reinforcing steel and is comparable to that of prestressing steel, but the modulus of elasticity of FRPs is less than that of steel. The modulus of elasticity of steel is about 1.4 to 1.7 times the modulus of elasticity of CFRP, about 2.5 times the modulus of elasticity of AFRP and about 4 times the modulus of elasticity of GFRP. Typical stress-strain relations for FRPs, reinforcing steel, and prestressing steel are shown in Figure 2.1 (ISIS Canada 2008).

The main drawback of FRP is the high material cost (ACI 440R- 07). CFRP is the most expensive, and it is used widely in prestressing because of its high strength and modulus of elasticity and because it is not susceptible to creep rupture or high relaxation. On the other hand, GFRP has lower cost but its susceptibility to creep rupture and its high relaxation has limited its use in prestressing applications.

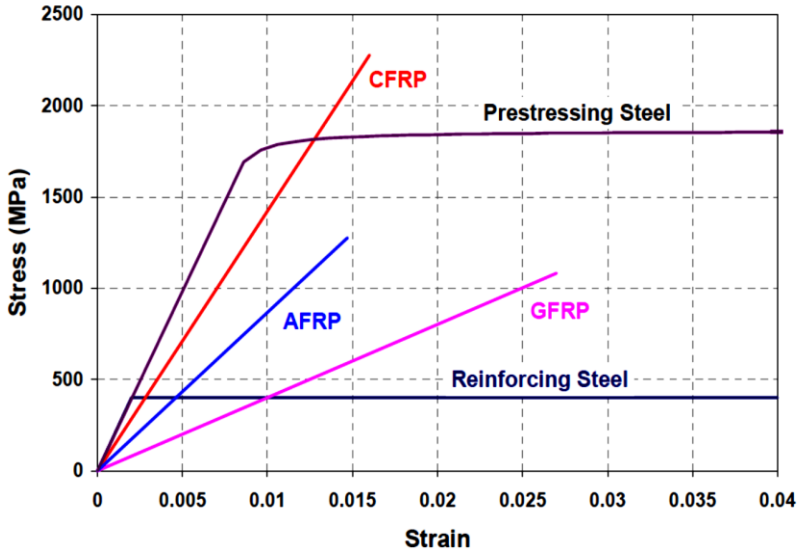

Figure 2.1: Stress-strain relation for FRP and reinforcing steel (ISIS Canada 2008)

With recent materials development, a new generation of GFRP bars was produced where the bars are reported to have high strength and stiffness and they can be loaded with sustained loads up to 50% of their ultimate strength without having creep rupture problems (Schoeck, 2009). The bars tensile strength range between 1100 MPa and 1500 MPa, and the modulus of elasticity is more than 60 GPa. The stress-strain behaviour of these bars is shown in Figure 2.2.

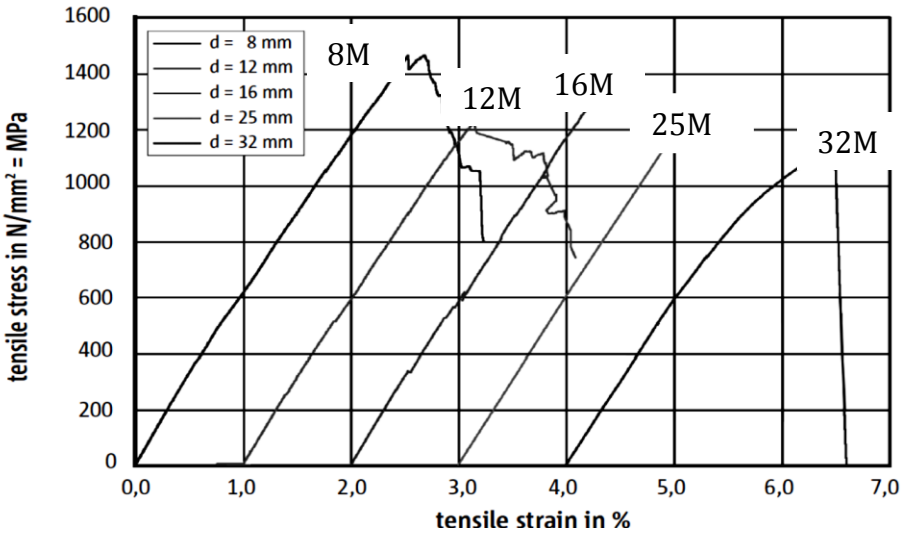

Figure 2.2 : Stress-strain relation for new generation of GFRP (Schoeck, 2009)

2.1.2 Long-term behaviour of GFRP bars

2.1.2.1 General

The most important long-term properties of FRPs are relaxation and creep rupture. Relaxation is defined as the reduction of stress in a material under constant strain (ACI 440.3R-04). Creep is the time dependent deformation under sustained load, while creep rupture is a material failure due to accumulated strain caused by creep (ACI 440.3R-04). ISIS Canada (2008) defines creep rupture as the failure of a material subjected to a sustained load level less than its short-term tensile capacity.

The glass fibers have excellent resistance to creep (fib 2006). Polymeric resins on the other hand are viscoelastic materials that are more susceptible to creep and relaxation (fib 2006). That is why the main factors that affect the creep of GFRP bars are the orientation of the fibres and the volume of fibres in the matrix. The straighter the fibres are within the matrix, the less creep the bar would have. Also, increasing the fiber percentage would result in decreasing the bar creep given that all the fibres are properly bonded within the matrix.

2.1.2.2 Previous work

Yamaguchi et al. (1997) conducted research on the creep rupture of CFRP, GFRP and AFRP rods. The results showed that the creep rupture capacity to the short-term capacity of the used FRP rods after 57 years were 0.93 for CFRP, 0.47 for AFRP and 0.29 for GFRP. These results were extrapolated from the linear relationship between creep rupture capacity and logarithmic time for test data collected within a period of 1000 hours. Similar values were found by Sheard et al. (1997) where the authors performed long-term durability tests on FRP bars under different stress levels and in various environments. They proposed service stress limits of about 25% for GFRP, 50% for AFRP, and 75% for CFRP for a 100-years structure's life (ACI 440R-07).

Almusallam et al. (2006) conducted residual tensile strength tests on GFRP bars embedded in concrete beams in different environmental conditions. A total of 36 beams of dimension 100 × 100 × 2000 mm with 1-10M GFRP bar in each beam were cast and placed in sustained loading frames under four-point bending. The sustained loads were designed to induce stresses to the

GFRP bars of about 20-25% of their ultimate strength. The GFRP bars had ultimate strength of 743 MPa, ultimate strain of 0.0187, and modulus of elasticity of 39 GPa. The surrounding environment was either tap water with continuous exposure at 40 ^{0}C, seawater with continuous exposure at 40 ^{0}C, or wet/dry cycles every two weeks in seawater exposure at 40 ^{0}C. Twelve beams were placed in each environment, where six of them were loaded with sustained loads and six of them were not loaded. The GFRP bars were extracted from the beams after periods of four, eight, and sixteen months and tested in axial tension. The results showed that sustained loading in the previously described conditions caused a reduction of 47% to 55% in the ultimate strength of the GFRP bars after 16 month (11,520 hours). Also, the ultimate strength of the GFRP bars decreased by about 16 to 22% in the same environments without any sustained loads.

Nkurunziza et al. (2005) conducted a research program to investigate the creep behaviour of GFRP bars under sustained loads in various environmental conditions. Twenty 9.5 mm GFRP bars having a guaranteed tensile strength of 628 MPa and a modulus of elasticity of 40 GPa were subjected to sustained loads of either 25% or 38% of the guaranteed tensile strength. The bars were loaded for 10,000 hours in either alkaline or de-ionized water mediums. The change in axial strain over time in the GFRP bars under different stress levels in both media is shown in Figure 2.3. The results showed that creep strain in the GFRP bars was about 5% and 3% of the initial strain value for the 38% and 25% stressing levels, respectively. The change of axial strain in alkaline solutions was less than 1.7%. As for the residual strength, the values were 97.1% and 100.8% of the guaranteed tensile strength for the specimens in de-ionized water for stress level 25% and 38% respectively. The residual strength of specimens in the alkaline solution dropped to 88.5% and 68.6% of the guaranteed strength for the 25% and 38% stressing levels, respectively.

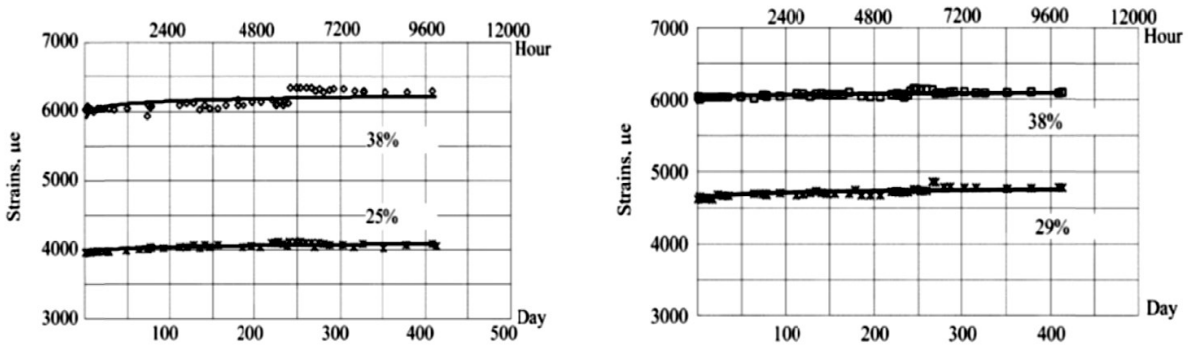

a) Alkaline solution **b) De-ionized water**

Figure 2.3: Change in axial strain in glass fiber-reinforced polymer bars with time under different stress levels in; a) alkaline solution and b) de-ionized water (Nkurunziza et al. 2005)

Debaiky et al. (2006) carried out tests to evaluate the residual tensile properties of GFRP bars under sustained load in various environmental conditions at elevated temperature. Three bar diameters were used in this study (9.5 mm, 12.7 mm, and 16 mm) and the test parameters were the sustained load, the surrounding environment and the temperature. The sustained stress ranged between 19% and 29% of the guaranteed tensile stress of the bar, the surrounding media was either alkaline solution or de-ionized water, and the temperature was either ambient temperature (20 ^{o}C) or elevated temperature which ranged between 43 and 73 ^{o}C. The test durations varied from one to four months. The results showed that the maximum reduction of strength was for the 9.5 mm bar stressed to 29% of its guaranteed strength in alkaline solution at 60 ^{o}C, and it was about 11%.

Fornůsek et al. (2009) conducted an experimental program including relaxation tests to examine the long-term behaviour of GFRP prestressing tendons. The used GFRP bars had an ultimate strength of 650 MPa and a modulus of elasticity of 40 GPa. For the relaxation test, a 5.4 m long GFRP tendon was stressed to 37% of its tensile strength, and the strain was fixed for 132 days. The stress degradation over time is shown in Figure 2.4. The relaxation results indicated that there was loss of tension of 3.3% after 24 hours, 7.3% after 28 days and 10.5% after 132 days.

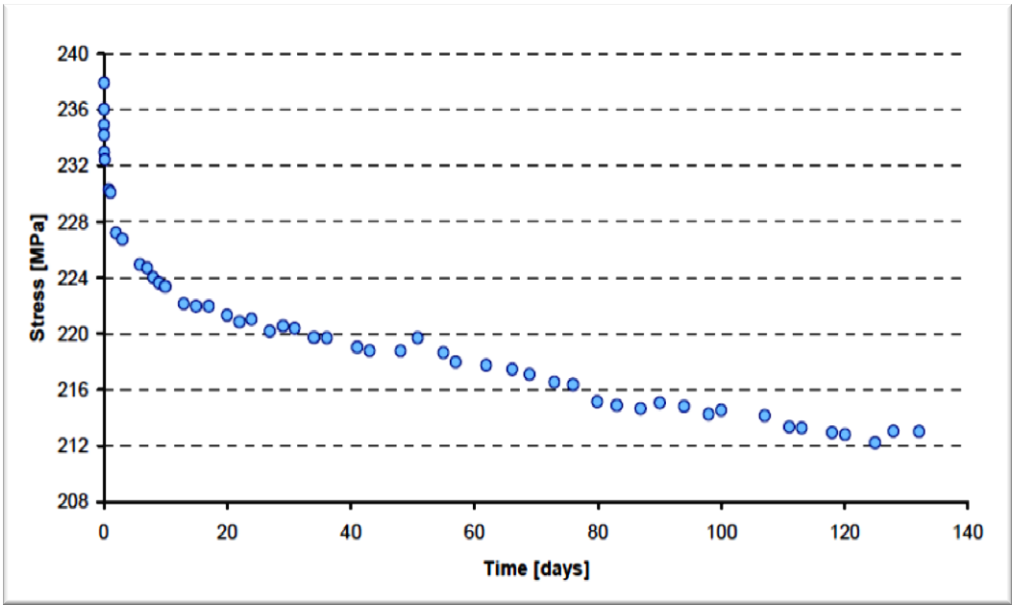

Figure 2.4: Decrease of stress over time for GFRP bar (Fornůsek et al, 2009)

Oskouei and Taleie (2010) studied the relaxation of FRP sheets. Four different tests were carried out in a controlled room with a constant temperature of 23±10 ^{o}C and a humidity of 50% and each test lasted for 1000 hours aiming to simulate the FRP prestressing conditions. The mechanical properties of GFRP fabrics were 1750 MPa for ultimate strength and 70 GPa for Young's modulus. The results showed that relaxation loss for GFRP after 48 h was 13.5% and after 1000 h was 15%. They concluded that unlike CFRP, GFRP and AFRP show significant decreases in tensile strength when they are subjected to constant load, and that the relaxation of AFRP is independent to the applied stress level.

Youssef and Benmokrane (2011) conducted a study to investigate the creep behaviour and tensile properties of GFRP bars under sustained service loads. 52 specimens of six commercial GFRP bars were tested. The tested parameters were the sustained load level, bar diameter and bar type. The sustained load levels used were 15% and 25-30% of the ultimate tensile strength of the bar, while the used bar diameters were 9.5 mm, 12.7 mm, 12.0 mm and 15.9 mm, and the bar types were obtained from three different manufacturers. Table 2.1 shows the mechanical properties of the tested bars. Tests were carried out at a temperature of 23 ± 3 ^{o}C and 50 ± 10% relative humidity. After loading for about 10,000 hours, all samples were tested in static tensile test to

measure their residual strength. It should be mentioned that the GFRP-4 bar is the same GFRP bar that will be used in the current study. The creep test results are shown in Figure 2.5. The maximum creep strain values for the for the 25-30% sustained load level specimens (GFRP 1 to 6) after 10000 hours were 3.8, 11.8, 12.0, 5.6, 8.6 and 11.8%. The results of the residual tensile strength test showed that the strength was not affected by the sustained loading in air as the reduction in strength ranged between 0% and 5.4% for all tested GFRP bars. They concluded from the results that there is no clear relationship between the applied load level and resulting creep strain after 10,000 hours and that the creep strain increases with increasing the bar diameter.

Table 2.1: Mechanical properties of tested GFRP bars (Youssef and Benmokrane, 2011)

	Nomenclature (ACI 440.1R-06)	GFRP-1 9.5 mm (0.374 in)	GFRP-2 9.5 mm (0.374 in)	GFRP-3 12.7 mm (0.5 in)	GFRP-4 12mm (0.472 in)	GFRP-5 15.9 mm (0.625 in)	GFRP-6 15.9 mm (0.625 in)
Average ultimate tensile stress MPa (ksi)	$f_{u,ave}$	854 ± 34 (124 ± 5)	828 ± 38 (120 ± 6)	774 ± 38 (112 ± 6)	1410 ± 23 (206 ± 3)	748 ± 35 (108 ± 5)	783 ± 20.5 (114 ± 3)
Guaranteed tensile stress MPa (ksi)	f^*_{fu} ($f^*_{fu} = f_{u,ave} - 3\sigma$)	752 (109)	714 (104)	660 (96)	1341 (194)	643 (93)	722 (105)
Design tensile stress MPa (ksi) (ACI 440.1R-06)	$f_{fu} = C_E \times f^*_{fu}$; $C_E = 0.8$	602 (87)	571 (83)	528 (77)	1073 (156)	514 (75)	578 (84)
Modulus of elasticity GPa (ksi)	E_f	46.9 ± 1.2 (6800 ± 174)	44.8 ± 1.4 (6500 ± 203)	49.9 ± 2.4 (7200 ± 248)	66.5 ± 6.2 (9600 ± 899)	42.5 ± 2.7 (6200 ± 392)	41 ± 0.3 (5900 ± 44)
Average ultimate strain (με)	$\varepsilon_{u,ave}$	18232 ± 767	18484 ± 868	15620 ± 956	21368 ± 1601	17712 ± 1082	19270 ± 541
Guaranteed strain (με)	$\varepsilon^*_{fu} = \varepsilon_{u,ave} - 3\sigma$	15931	15880	12752	16565	14467	17647
Design tensile strain (με) (ACI 440.1R-06)	$\varepsilon_{fu} = C_E \times \varepsilon^*_{fu}$	12745	12704	10202	13252	11574	14118
Allowable strain for sustained load (με) (ACI 440.1R-06)	$f_{f,s} = 0.2 \times \varepsilon_{fu}$	2549	2541	2040	2650	2315	2824

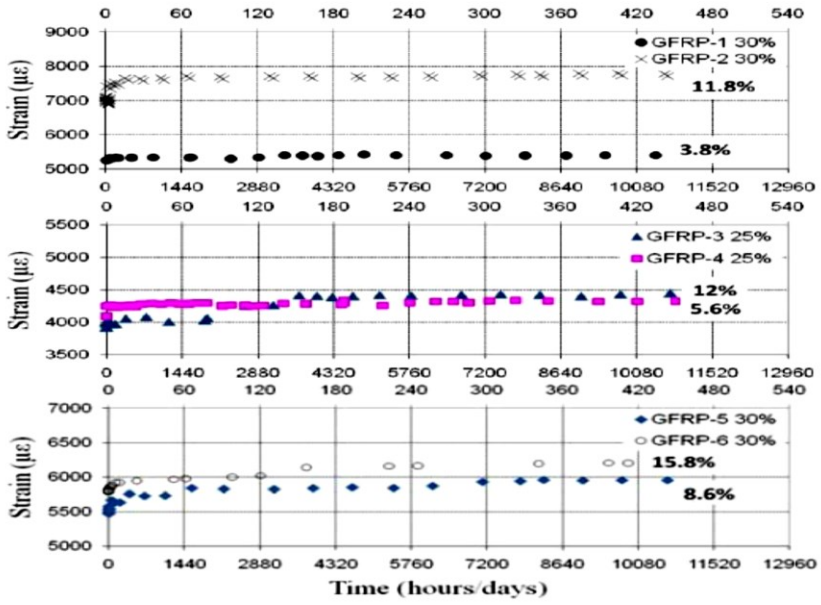

Figure 2.5: Creep strain evolution for samples at 25-30% sustained loading level (Youssef and Benmokrane, 2011)

The GFRP bars used in the current study were produced by Schöck Bauteile GmbH. Highly alkaline water-saturated concrete prisms with the GFRP bars inside them were loaded by tensile sustained loads at 23, 40, and 60°C (Weber and Baquero, 2010). The test setup followed the ACI 440.3R-04 test method B.8. The relationship between sustained stress and time to failure is shown in Figure 2.6. Using regression following the ACI 440.3R-04 guidelines, the creep-rupture curves showed that the bars can be stressed with a sustained stress of about 600 MPa (50% of the ultimate strength) at 40 ^{o}C and can have a service life of 100 years.

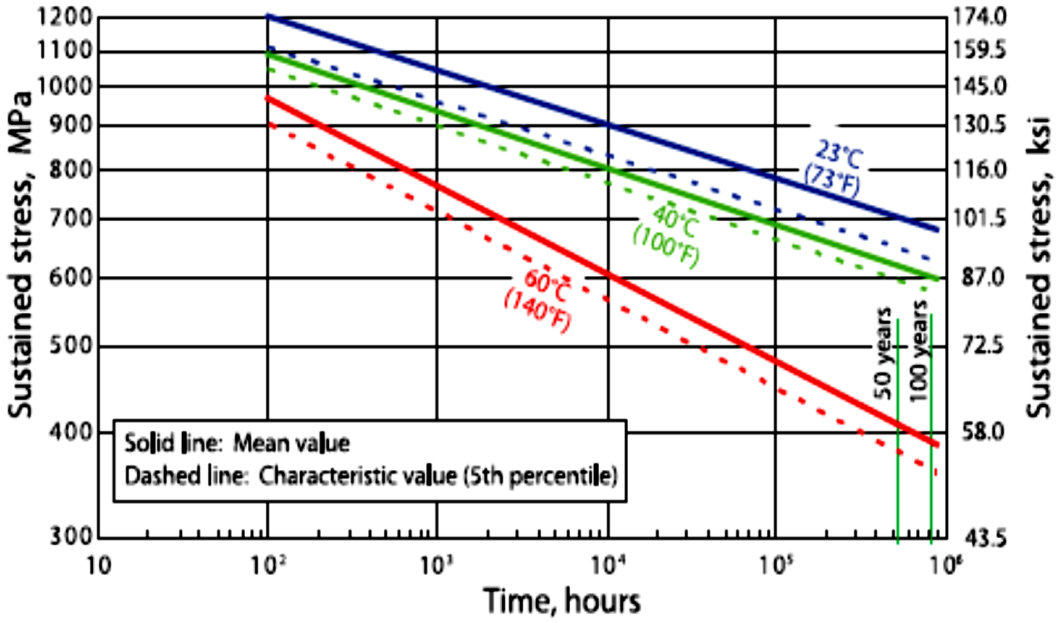

Figure 2.6: Time to failure lines of GFRP bars at different temperatures (Weber and Baquero, 2010)

2.1.2.3 Design codes and guidelines stress limits for FRP tendons

Design codes and guidelines impose sustained stress limits on FRPs in general to avoid failure of an FRP reinforced member due to creep rupture of the FRP. Limits on the initial prestressing level for GFRP are provided by CAN/CSA-S6-06. CAN/CSA-S806-12 and ACI 440.1R-06 only provide limits for tensile stress in GFRP reinforcement under sustained loads as they do not allow the use of GFRP in prestressed applications. These stress limits are shown below.

- CAN/CSA-S6-06:

For non-prestressed FRP reinforcement, the stresses in FRP under service loads must not exceed the ultimate strength of the FRP bar or grid (f_{FRPu}) multiplied by dimensionless factor (F_{SLS}) which equals 0.65 for CFRP, 0.35 for AFRP and 0.25 for GFRP. For prestressed FRP reinforcement, the maximum stresses at jacking and at transfer are shown in Table 2.2.

Table 2.2: Maximum permissible stresses in FRP tendons at jacking and transfer for concrete beams and slabs (CAN/CSA-S6-06)

Tendon	At jacking	At transfer
CFRP	$0.70\,f_{FRPu}$	$0.65\,f_{FRPu}$
AFRP	$0.40\,f_{FRPu}$	$0.35\,f_{FRPu}$
GFRP	$0.30\,f_{FRPu}$	$0.25\,f_{FRPu}$

- CAN/CSA-S806-12:

The maximum allowable tensile stress in GFRP reinforcement bars at serviceability limit state is 25% of the tensile strength of the bars.

- ACI 440.1R-06:

The creep rupture stress limits for CFRP, AFRP, and GFRP are respectively $0.55\,f_{fu}$, $0.30\,f_{fu,}$ and $0.2\,f_{fu}$, where f_{fu} is the guaranteed tensile strength.

2.2 Shrinkage and creep of concrete

2.2.1 General

Shrinkage and creep are very important time-dependent phenomena that occur in almost all cementitous products. Concrete has both instantaneous and long-term responses when loaded by sustained loads where an instantaneous strain takes place and increases with time. This increase is greatly influenced by creep and shrinkage properties of concrete.

2.2.2 Concrete shrinkage

Shrinkage is a volumetric contraction that is caused mainly by the loss of water due to evaporation and the cement hydration process. Shrinkage includes different forms as follows:

- Plastic Shrinkage: It takes place in the plastic stage of concrete due to the evaporation of bleeding water (Rao 2001).

- Autogenous Shrinkage: It is the change in volume produced by the continued hydration of cement, exclusive of the effects of applied loads and change in either thermal condition or moisture condition (Zhang et al 2003).
- Carbonation shrinkage : It takes place due to destroying the calcium hydroxide $Ca(OH)_2$, which is a source of alkalinity, by carbon dioxide CO2 (Rao 2001). The carbonation reaction is;

$$Ca(OH)_2 + CO_2 \longrightarrow CaCO_3 + H_2O$$

- Drying Shrinkage: It is the shrinkage of hardened concrete due to the evaporation of internal water (Zhang et al 2003).

Plastic shrinkage does not take place in the hardened stage of concrete. Autogenous shrinkage takes place in all types of concrete with any water/cement ratio but its value is negligible compared to drying shrinkage especially when concrete is cured in its early age. Autogenous shrinkage becomes critical (about 50% of the drying shrinkage) in high strength concrete with water/cement ratios around 0.3 (Aitcin 1999). The carbonation shrinkage takes place at the outer layers of concrete and the depth of carbonation depends on the concrete member size, the relative humidity and the moisture content in concrete (Neville 1995). Drying shrinkage is the main shrinkage mechanism that takes place in concrete. Because of its large value compared to autogenous shrinkage, it is not critical to distinguish them from each other and therefore, the shrinkage of a specimen under drying conditions without being subjected to applied load and temperature change includes both drying and autogenous shrinkage (Zhang et al 2003).

2.2.3 Creep of concrete

Creep is defined as the increase in strain under a sustained stress. When a specimen is loaded, the strain induced by the application of load is called instantaneous strain. Creep is the increase in strain above it. Creep of concrete can be divided into three phases. In the first phase, instantaneous strain takes place once the load is applied then the strain grows rapidly in a short time period, this phase is called the primary creep phase. After that, the slope of the time strain curve becomes constant over a long period of time, which is called the secondary creep phase. The third

phase occurs only when the sustained loads are at high levels and it is characterized by increasing strains at high rates strains until the material fails.

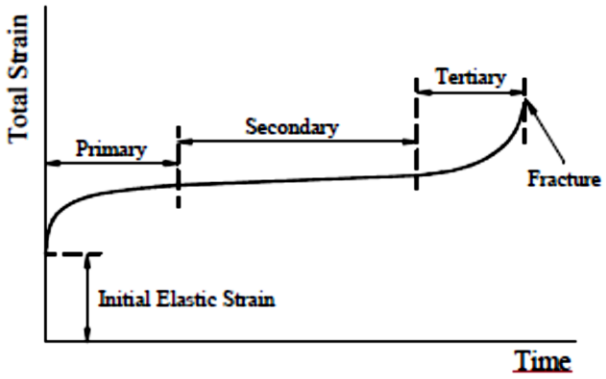

Figure 2.7: Typical strain history curve during creep deformation (Youssef 2010)

If concrete is subjected to drying conditions, shrinkage will take place simultaneously with creep and the strain measured in this case is considered as the summation of both. Therefore, creep in this case is considered as the deformation in excess of shrinkage (Neville 1995). Shrinkage and creep are not independent phenomena and there is an effect of shrinkage on creep, which is known to increase it. Therefore, scientists differentiate between two types of creep that take place in this case (Neville 1995):

- Basic creep: Creep of concrete under conditions of no moisture movement to or from the ambient medium.
- Drying creep: Additional creep caused by drying.

The total creep strain is the sum of the basic creep and drying creep. The change in the strain of a loaded and drying specimen is shown in Figure 2.8. The ratio of creep strain at age (t) to the instantaneous strain due to applied unit stress at age (t_0) is known as the creep coefficient Ø (t,t_0).

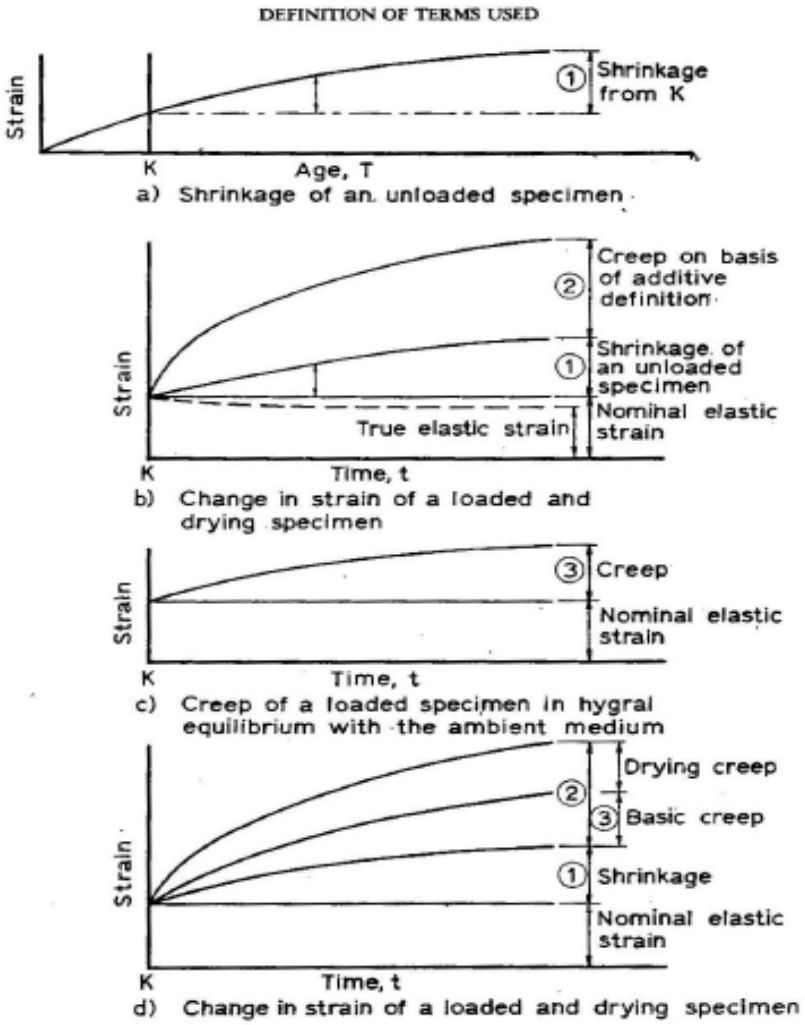

Figure 2.8: Change in strain of a loaded and drying specimen (Neville 1995).

Creep of concrete is the main factor affecting the long-term deflection of reinforced concrete structures. That is why many researchers have investigated the parameters influencing the creep of reinforced concrete. The main factors that affect the concrete creep are; the level of sustained load, concrete compressive strength, the age of concrete at the time of loading, member size, and magnitude of reinforcement.

Except for concrete specimens loaded at a very early age, there is a direct proportionality between creep and applied stress (Neville et al. 1983). This proportionality has an upper limit be-

yond which the creep increases with stress at an increasing rate. That increase in the creep is attributed to the severe internal micro-cracking that takes place in concrete at very high stress/concrete strength rates. This upper limit for proportionality is not constant and can vary between 0.3 and 0.75, with the latter value applying for high strength concrete (Neville 1995). At higher sustained stresses to strength ratios, creep can produces time failure as shown in Figure 2.9.

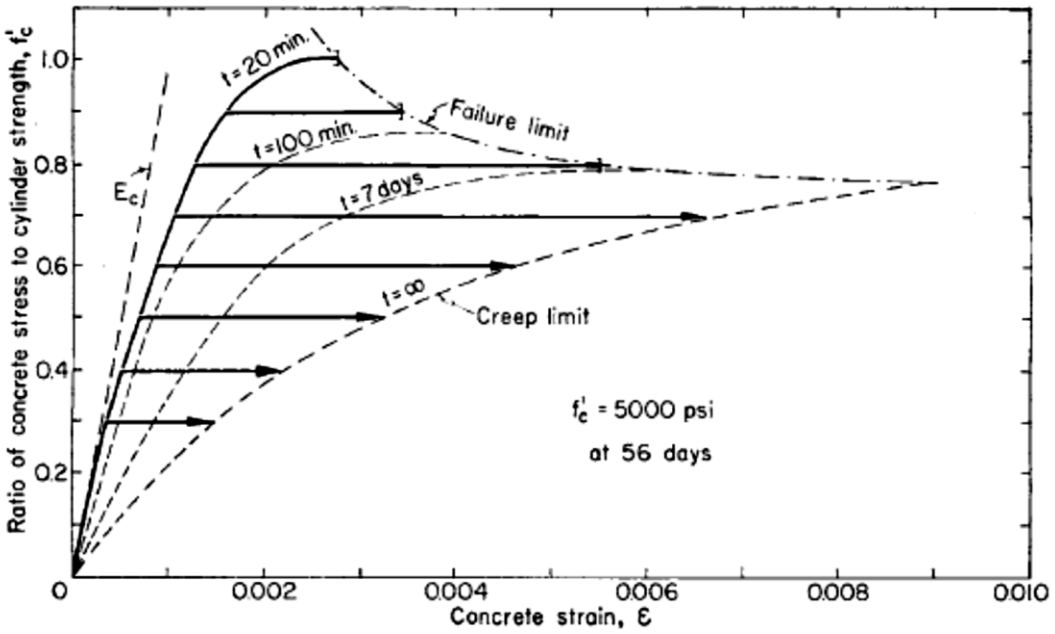

Figure 2.9: Stress-strain-time relationship for concrete (Rüsch, 1960)

The degree of cement hydration or the age of loading has a great influence on the creep of concrete. If the concrete member was loaded at an early age, concrete would exhibit much greater creep than concrete loaded at older age. This is due to the higher capillary porosity and lower degree of hydration at the early age of concrete, which results in higher creep (Neville 1995).

Concrete creep is also affected by the concrete member size. It is generally expressed by the volume/surface ratio of the concrete member. Creep for a larger specimen is known to be less than that for smaller specimen (Neville et al. 1983). This was attributed to the increase in the creep on the surface of the member compared to that within the core of the specimen (Bruegger 1974) due to the higher moisture content within the specimen core. The influence of the member size is

greatest during the initial period after the load application. After several weeks, the rate of creep becomes the same for all sizes under the same conditions (Neville et al. 1983).

Another main factor affecting concrete creep is the relative humidity. At lower relative humidity levels, creep increases for a given type of concrete as shown in Figure 2.10 (Neville 1995).

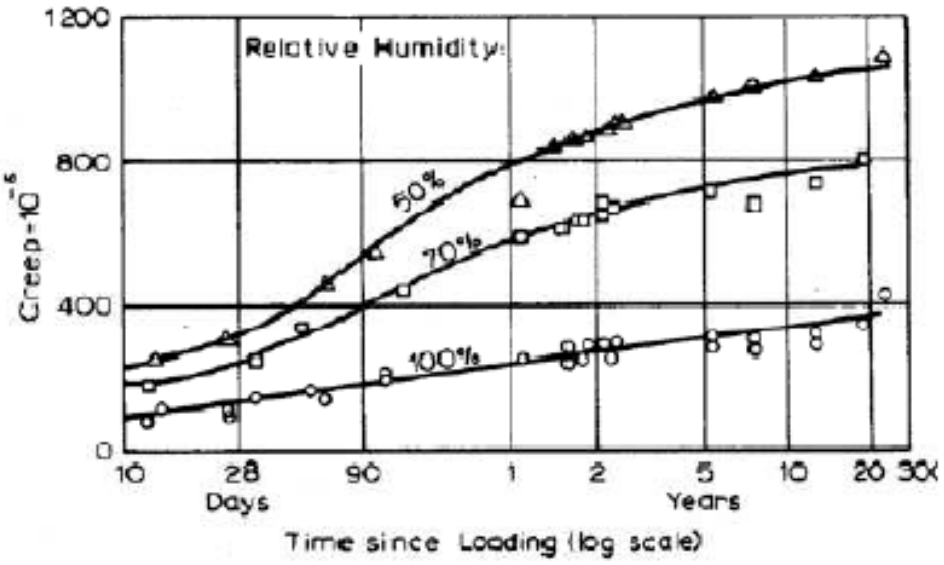

Figure 2.10: Creep of concrete cured in fog for 28 days, then loaded and stored at different relative-humidity levels (Neville (1995)

Other concrete properties that are known to affect the magnitude and rate of creep of concrete are the type of cement, mix proportions, and aggregate type. Increasing the cement content results in increasing creep if the water-cement ratio is kept constant (ACI 209R-92). Increasing the aggregate content decreases creep (Neville 1995).

2.3 Long-term behaviour of GFRP reinforced / prestressed concrete beams

2.3.1 Previous experimental work

Investigating the long-term behaviour of concrete structures prestressed with FRP bars is important since the reliability of any type of reinforcement in concrete will depend mainly on its performance under sustained loads (Braimah 2000). Most of the previous research reported in the

literature focused on the behaviour of CFRP prestressed members and GFRP reinforced members, while only limited research investigated the behaviour of GFRP prestressed members. The main studies available on the behaviour of GFRP reinforced or prestressed members are summarized in this subsection.

Singh and Svecova (2014) compared the time-dependent behaviour of GFRP prestressed, steel prestressed and GFRP reinforced concrete slabs with dimensions of 230 × 610 × 6600 mm subjected to sustained loads under natural environmental conditions. The prestressing levels used were 24% and 35% of the ultimate strength of the bars. The GFRP bars were 16 mm diameter with a tensile strength of 863 MPa and modulus of elasticity of 55 GPa, while the steel strands were low-relaxation 12.7 mm diameter with an ultimate strength of 1860 MPa. The results did not show any excessive loss in the prestressing force during the sustained load period of 10 months. The GFRP and steel prestressed concrete slabs both satisfied the maximum permissible deflection of 25.8 mm (span length/240) specified by CSA S806-12 (2012). However, the GFRP reinforced slabs exceeded the permissible deflection by 19.8% to 33.3%.

Youssef (2010) carried out a comprehensive experimental program to study the long-term behaviour of GFRP reinforced beams under sustained loads. The experimental program included 20 beams with dimensions 100 × 150 × 1800 mm reinforced with either GFRP, CFRP or steel bars. Each beam had two bars with 25 mm cover and no shear reinforcement. The beams were subjected to a sustained four- point loading representing 25% of the beam ultimate strength for a year. Six GFRP and two CFRP bar types were used in this study. It should be mentioned that the GFRP type-4 is the same type of GFRP bars the was used in the present study. The results showed that the ratio of the time dependent deflection after one year to the immediate deflection for the GFRP reinforced beams ranged between 30% and 59% and the ratio for GFRP-4 was about 30%. The results were compared with ACI 440.1R-06 and CAN/CSA S806-02 long-term predicted deflections, and it was concluded that ACI 440.1R-06 and CAN/CSA S806-02 over predict the long-term deflection values for FRP reinforced beams.

Sovják et al. (2009) studied the flexural behaviour of concrete slabs prestressed with GFRP bars. Three concrete slabs with dimensions of 600 × 200 x 4500 mm were used. Each slab had four GFRP bars of diameter 14 mm prestressed to 33% of their ultimate strength. The GFRP bars had

an ultimate strength of 650 MPa and a modulus of elasticity of 40 GPa. The slabs were loaded to 30% of their calculated capacity for ten cycles and then loaded to failure in four- point bending. The 30% represented the service limit state. The load deflection curve is shown in Figure 2.11. It was concluded that prestressing enhanced behaviour of concrete members with GFRP, and helped overcome the issue of bigger deflections and earlier crack due to the lower modulus of elasticity of GFRP compared to steel. It was recommended that future research should focus on the long-term behaviour of GFRP prestressed members under sustained loads and fatigue loads.

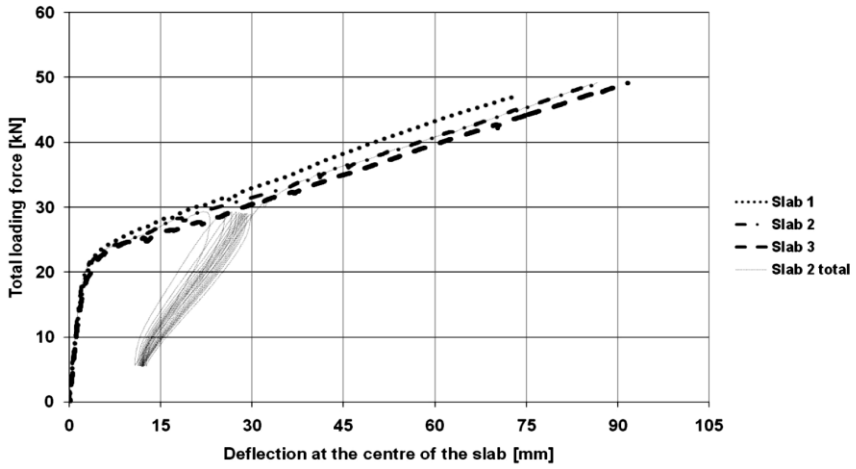

Figure 2.11: Load deflection behaviour of GFRP prestressed slabs (Sovják et al, 2009)

Al-Salloum and Almusallam (2007) studied the effect of different environmental conditions on the creep behaviour of concrete beams reinforced with GFRP bars under sustained loads. A total of eight beams were used with dimensions of 100 × 100 × 2000 mm, reinforced with 1-10M GFRP bar and had no stirrups. The GFRP bars had tensile strength of 730 MPa and modulus of elasticity of 39 GPa. The beams were divided into groups and subjected to sustained loads in different environments for 300 days. The sustained loads on the beams were the same for all beams and were designed to produce a strain of 23% of the ultimate strain of the GFRP. The environmental conditions were; controlled environment with temperature of 24 ± 3 ^{0}C (control group), tap water at a temperature of 40 ± 2 ^{0}C, sea water at a temperature of 40 ± 2 ^{0}C, and wet/dry cycles of sea water at a temperature of 40 ± 2 ^{0}C. The results showed that the increase in the mid span deflection for the control beams was 8% for the first 120 days, 11% for the second 120 days and 13% after 300 days. They concluded that the allowable strain in GFRP bars at service load

should not exceed 48% of the ultimate strain for elements at room temperature conditions, 32% for structures continuously exposed to non-saline water, 22% for structures exposed to sea water, and 13% for structures in splash zone near the coastal areas.

Hall and Ghali (2000) conducted an experimental investigation of the long-term deflection behaviour of concrete beams reinforced with either GFRP bars or steel bars. The beams were subjected to cyclic loading to produce cracking, and then they were subjected to sustained loading for 8 month under four- point bending. The sustained loads ranged between 1.5 to 3.0 times the cracking loads for the beams. The test parameters were the sustained load level and the reinforcement materials. The test results showed that under similar loading conditions and the same reinforcement ratio, the long-term deflections of GFRP-reinforced beams were 1.7 times those of the steel-reinforced beams. The long-term deflections were compared to the predicted results using CEB-FIP Model Code 1990, and the ACI 318-95. It was concluded that the ACI 318-95 code overestimates the deflections for the GFRP reinforced beams.

Joh et al. (1999) investigated the effect of different FRP materials on the long-term deflection of concrete beams. Seventeen (17) beams reinforced by nine types of FRP bars were tested and compared to a beam reinforced with a steel bar. All the beams were designed to have the same ultimate load capacity, and the sustained loads were designed to produce a stress on the reinforcing bars that was about one third of the bars tensile strength. The results showed that the long-term deflections of GFRP reinforced beams were the smallest among all of the tested beams.

2.3.2 Previous analytical work

2.3.2.1 Modeling creep in concrete

ACI 209R-92 gives formulas for predicting the creep coefficient and shrinkage strains of concrete. Equation 2.1 shows the creep coefficient formula.

$$\emptyset\,(t, t_0) = \frac{(t - t_0)^{0.6}}{10 + (t - t_0)^{0.6}}\,\emptyset_\infty \qquad \text{Equation 2.1}$$

where $\emptyset_\infty$ is the ultimate creep coefficient, and is given by Equation 2.2.

$$\emptyset_{\infty} = 2.35\, k_1 k_2 k_3 k_4 k_5 k_6 \qquad \text{Equation 2.2}$$

where k_1, k_2, k_3 , k_4, k_5, and k_6 are modification factors to account for curing conditions, relative humidity, member size, concrete composition, fine/coarse aggregate ratio, and air content ratio, respectively. The formulas for calculating these factors are given in Appendix B.

The shrinkage strain $\varepsilon_{sh(t,t0)}$ for moist cured concrete members at time (t) is calculated using Equation 2.3.

$$\varepsilon_{sh(t,t_0)} = \frac{t - t_0}{35 + t - t_0}\, \varepsilon_{sh\infty} \qquad \text{Equation 2.3}$$

where $\varepsilon_{sh\infty}$ is the ultimate shrinkage, and is given by Equation 2.4.

$$\varepsilon_{sh\infty} = 780 \times 10^{-6}\, k'_1 k'_2 k'_3 k'_4 k'_5 k'_6 k'_7 \qquad \text{Equation 2.4}$$

where k'_1, k'_2, k'_3 , k'_4, k'_5, k'_6 and k'_7 are modification factors to account for curing conditions, relative humidity, member size, concrete composition, fine / coarse aggregate ratio, cement content and air content ratio, respectively. The formulas for calculating these factors are given in Appendix B.

The two common methods for assessing creep effect in concrete structures are the effective modulus method and the age-adjusted effective modulus method.

In the effective modulus method, the total strain which is the summation of the elastic strain and the creep strain under sustained loads is calculated using an effective modulus of concrete. The effective concrete modulus is shown in Equation 2.5.

$$E_e(t, t_o) = \frac{E_c(t_o)}{1 + \emptyset\,(t, t_0)} \qquad \text{Equation 2.5}$$

where $E_c(t_o)$ is the modulus of elasticity of concrete at time t_0, and $\emptyset\,(t, t_0)$ is the creep coefficient at time t for concrete loaded at time t_0. This method gives accurate results for cases where the applied stress is constant (Sritharan and Fenwick 1995).

The creep strain of concrete is known to decrease as the age at the time of loading is increased. Therefore, in cases of variable applied stress, a modification is made to take into account the aging effect of concrete. The aging effect of concrete and the previous stress history are taken into account in the age-adjusted effective modulus method where the reduced creep coefficient $\chi(t, t_0)\emptyset(t, t_0)$ is used in calculating the effective concrete modulus. The term $\chi(t, t_0)$ is called the aging coefficient and its magnitude ranges between 0.6 and 0.9 (Ghali et al. 2002).

2.3.2.2 Modeling deflection behaviour in FRP reinforced/prestressed beams

Modeling the long-term deflection of FRP reinforced/prestressed beams is commonly carried out using the numerical approach by sectional analysis (Braimah (2000), Zou (2003)), or layered sectional analysis (Zamblauskaite et al. 2005). A set of equations modeling the change in strains and stresses in concrete and FRP with time are used to predict the behaviour of FRP reinforced/prestressed concrete beams.

Zou (2003) proposed a model to calculate the immediate and long-term deflections of CFRP prestressed concrete beams. A similar model was used by Braimah (2000) but the creep of the FRP was ignored. Figure 2.12 shows a schematic of a beam section with the stress and strain profiles across the section. The stress-strain relationship for the concrete was assumed to be linear.

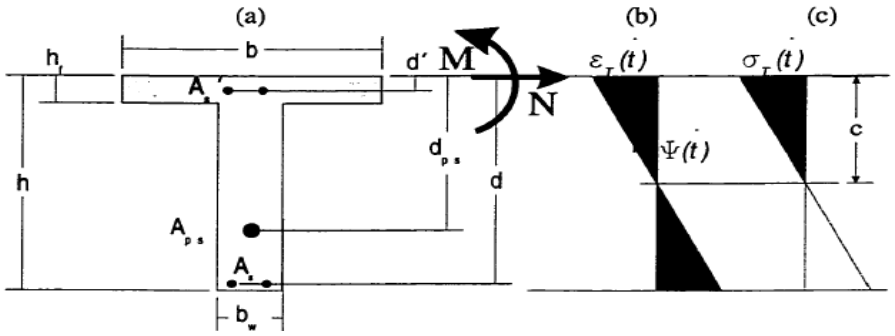

Figure 2.12: Cross-section and stress and strain distributions after applying load (Braimah 2000)

In this approach, the change in strain due to creep and shrinkage of concrete and creep of prestressed reinforcement is assumed to be restrained by a fictitious axial force and bending moment to keep the strain state unchanged. Afterwards, these restraining forces are removed by gradual

application of equal and opposite forces on the section, resulting in a change in the top fibre strain and the section curvature. The age-adjusted effective modulus method is used to model the effects of creep on concrete. The fictitious external force (ΔN) and bending moment (ΔM) are given by Equation 2.6 and Equation 2.7, respectively. The change in the top fibre strain and the curvature is calculated using Equation 2.8 and Equation 2.9, respectively. The change in the stress at any fibre is given by Equation 2.10.

$$\Delta N = E_{e(t,t_0)} \emptyset\,(t,t_0)\left[A_c \varepsilon_{top(t)} + S_c \Psi_{(t)}\right] - E_{e(t,t_0)} \varepsilon_{sh(t,t_0)} A_c + E_{frpe}\left[A_{frp} \varepsilon_{top(t)} + A_{frp} d_n \Psi_{(t)}\right] \quad \text{Equation 2.6}$$

$$\Delta M = E_{e(t,t_0)} \emptyset\,(t,t_0)\left[S_c \varepsilon_{top(t)} + I_c \Psi_{(t)}\right] - E_{e(t,t_0)} \varepsilon_{sh(t,t_0)} S_c + E_{frpe}\left[A_{frp} d_n \varepsilon_{top(t)} + A_{frp} d^2{}_n \Psi_{(t)}\right] \quad \text{Equation 2.7}$$

$$\Delta\varepsilon_{top(t)} = \frac{-S'(\Delta M) + I'(\Delta N)}{E_{e(t,t_0)}[S'^2 - A'I']} \quad \text{Equation 2.8}$$

$$\Delta\Psi_{(t)} = \frac{A'(\Delta M) - S'\Delta N}{E_{e(t,t_0)}[S'^2 - A'I']} \quad \text{Equation 2.9}$$

$$\Delta\sigma_{(t)} = E_{e(t,t_0)}\left[\Delta\varepsilon^{T}_{(t_0)} + \Delta\Psi_{(t_0)} y\right] \quad \text{Equation 2.10}$$

where A_c is the area of the concrete section, S_c, and I_c are its first moment of area and moment of inertia of concrete about the reference axis, A' is the area of age-adjusted transformed section, and S' and I' are the first moment of area and the moment of inertia of the age-adjusted transformed area of the cross-section about the reference axis, $E_{e(t,t0)}$ is the age-adjusted elastic modulus of concrete, $\emptyset\,(t, t_0)$ is the concrete creep coefficient, and E_{frpe} is the FRP effective modulus of elasticity.

Zamblauskaite et al. (2005) proposed a numerical technique based on layer-by-layer strain compatibility to predict the time-dependent behaviour of partially prestressed members (Figure 2.13). The stress-strain relationship for concrete in compression used in this approach is shown in Equation 2.11.

$$f_{c(t,t_0)} = f'_{c(t,t_0)} \left[2 \frac{\varepsilon_{c(t,t_0)}}{\varepsilon'_{c(t,t_0)}} - \left(\frac{\varepsilon_{c(t,t_0)}}{\varepsilon'_{c(t,t_0)}} \right)^2 \right] \qquad \text{Equation 2.11}$$

where $f_{c(t,t_0)}$ is the concrete compressive stress at strain $\varepsilon_{c(t,t_0)}$, $f'_{c(t,t_0)}$ is the concrete compressive strength,$\varepsilon'_{c(t,t_0)} = 2f'_{c(t,t_0)}/E_{e(t,t_0)}$, and $E_{e(t,t_0)}$ is the effective modulus of concrete for sustained loading between time t_0 and t.

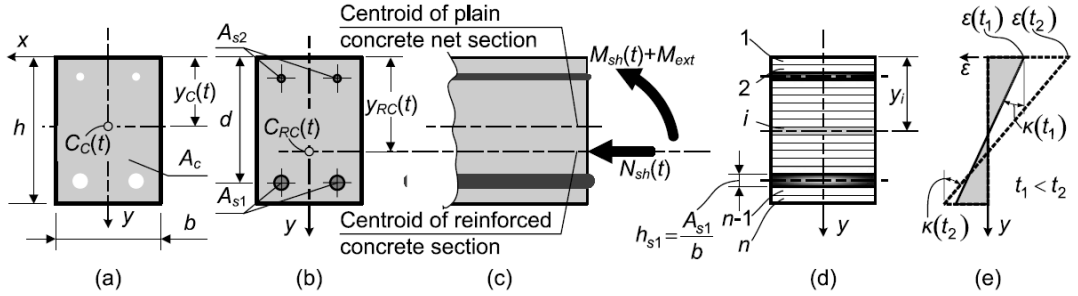

Figure 2.13: Modeling concrete section under sustained loads (Zamblauskaite et al., 2005)

The total sustained external force (N) and bending moment (M) are calculated using Equation 2.12 and Equation 2.13, respectively. The top fibre strain and the curvature are calculated using Equation 2.14 and Equation 2.15, respectively. The fictitious external force and bending moment due to shrinkage are calculated as shown in Equation 2.16 and Equation 2.17, respectively.

$$N = P + N_{sh(t,t_0)} \qquad \text{Equation 2.12}$$

$$M = M_{ext} - Pd_n + M_{sh(t,t_0)} \qquad \text{Equation 2.13}$$

$$\varepsilon_{top(t)} = \frac{-S_e(M) - I_e(N)}{E_{e(t,t_0)}\left[A_e I_e - {S_e}^2\right]} \qquad \text{Equation 2.14}$$

$$\Psi_{(t)} = \frac{A_e(M) + S_e(N)}{E_{e(t,t_0)}\left[A_e I_e - {S_e}^2\right]} \qquad \text{Equation 2.15}$$

$$N_{sh(t,t_0)} = -A_c E_{e(t,t_0)} \varepsilon_{sh(t,t_0)} \qquad \text{Equation 2.16}$$

$$M_{sh(t,t_0)} = S_c E_{e(t,t_0)} \varepsilon_{sh(t,t_0)}$$ Equation 2.17

where P is the prestressing force, d_n is the depth of the prestressing bar, A_e is the transformed section area, S_e is the first moment of area of the transformed area about the top fibre, and I_e is the moment of inertia of the transformed area about the top fibre. These section properties are calculated using Equation 2.18 to Equation 2.20. The terms A_c, S_c, and I_c are the same section properties for the concrete part only.

$$A_e = \sum b_i t_i \frac{E_i}{E_{e(t,t_0)}}$$ Equation 2.18

$$S_e = \sum b_i t_i y_i \frac{E_i}{E_{e(t,t_0)}}$$ Equation 2.19

$$I_e = \sum \left[\frac{b_i t_i^3}{12} + b_i t_i y_i^2\right] \frac{E_i}{E_{e(t,t_0)}}$$ Equation 2.20

where b_i, t_i, y_i and E_i are the width, the thickness, the depth measured from the top fibre of the section, and the secant deformation modulus of the layer (i), respectively.

2.3.3 Guidelines for long-term deflection prediction

Design codes provide some guidelines for predicting the long-term deflection of FRP prestressed beams. In both ISIS Canada (2008) and ACI 440.4 R-04, the empirical multiplier approach is used in which camber and deflection are separated into individual components, and adjusted by modifiers in order to compute the final deflection by superposition. The modifier values are provided only for AFRP and CFRP and no multiplier values are provided for GFRP prestressed members (see Table 2.3).

Table 2.3: Multipliers for FRP tendons (ISIS Canada and ACI 440.4 R-04)

		Without composite topping	
		Carbon	**Aramid**
At erection	Deflection due to self-weight	1.85	1.85
	Camber due to prestressing	1.80	2.00
Final	Deflection due to self-weight	2.70	2.70
	Camber due to prestressing	1.00	1.00
	Deflection due to applied	4.10	4.00

2.4 Transfer length of prestressed FRP bars

In prestressed prestensioned members, the length from the end of the member where the tendon stress is zero to the point along the tendon where the prestress is fully effective is called the transfer length (ISIS Canada 2008). ACI 440R-07 defines the transfer length as the length required to transfer the full prestressing force to the concrete. Accurate estimation of the transfer length is necessary for the stress calculations to check the limits at service limit state and for the shear design of prestressed members. Underestimation of the transfer length leads to unconservative shear calculations while overestimation leads to unconservative stress calculations at the service limit state (Barnes et al. 2003).

The transfer length of a prestressed FRP tendon is dependent on the surface condition of the FRP bar, the prestressing level, and the method used to transfer the FRP force to the concrete (ACI 440R-07). It was found that the transfer length increases with increasing bar diameter and prestressing force. Furthermore, the transfer length is slightly affected by the concrete strength, and changes slightly with time (Lu et al. 1999). The main factor that affects the transfer length is the "Hoyer effect" which is the increase in the normal stresses acting on the surface of the prestressed tendon upon release due to the radial expansion of the tendon because of Poisson's ratio (Mahmoud et al. 1999). Since the modulus of elasticity of FRPs in general is less than that of steel, the transfer length of most of the FRPs is less than that of steel (ACI 440R-07).

Most of the available research studied the transfer length of CFRP and AFRP tendons. CAN/CSA-S6-06 and ACI 440.1R-06 give equations for predicting the transfer length for these bar types only. Previous studies and code equations are discussed below.

2.4.1 Previous research

Iyer et al. (1991) studied the transfer length of prestressed fiberglass and graphite rods. The ultimate strength and the modulus of elasticity of the fiberglass rods and the graphite rods were 1860 MPa and 57 GPa, and 2240 MPa and 132 GPa, respectively. The bar diameter used was 9.5 mm and the concrete compressive strength at time of transfer was about 27.6 MPa. For the fiberglass rods, the effective prestressing stress was 882 MPa (47.4% of the ultimate strength of the rod), and for the graphite rods it was 992 MPa (44.3% of the ultimate strength of the rod). The measured transfer length values were 355 mm or 37 times the bar diameter (d_b) and 559 mm or 59 d_b, for the fiberglass and the graphite rods, respectively.

Issa et al. (1993) carried out an experimental study to determine the transfer length of prestressed fiberglass bars in concrete. 9.5 mm S-glass seven-wire strands with ultimate strength that ranged between 1736 and 2212 MPa, and modulus of elasticity that ranged between 65 and 78 GPa were used. The concrete compressive strength ranged between 38 MPa and 50 MPa at the time of transfer. The prestressing level of the strands was about 45% of their ultimate strength. The measured transfer length values ranged between 254 mm (about $20d_b$) and 279 mm (about $28d_b$).

Mahmoud et al. (1999) studied the transfer length of CFRP strands in concrete. The experimental program consisted of 52 prestressed specimens that were either prisms or beams to investigate the effect of the strand type (Leadline, CFCC and steel strands), strand diameter, concrete compressive strength, shear reinforcement, prestressing level, and shrinkage and creep of concrete on the transfer length measurements. The top reinforcement used was 2-10M steel bars while the shear reinforcement was 6M steel stirrups spaced at 80 mm. Strain gauges and DEMEC points were used to take readings for the transfer length at transfer, and after four weeks. The results showed that the transfer length of the Leadline increased by 22% after one year and no change was observed for the CFCC. From the results, they proposed an equation for the transfer length that was later adopted by ISIS Canada (2008) and ACI 440.4R-04, and will be given in Section 2.4.2.

Lu et al (2000) investigated the transfer length of three types of FRP tendons (Carbon Leadline, Aramid Technora and Carbon Strawman) in prestressed concrete beams. DEMEC gauge readings from 30 specimens prestressed with single FRP tendon and 12 specimens prestressed with steel tendons were used for the transfer length measurements. The test parameters were the prestressing force and the tendon type. It was concluded that both parameters had a negligible effect on the transfer length of the FRP tendons, and that the transfer length of steel tendons was longer than that for FRP.

Zou (2003) studied the short-term and long-term transfer length of FRP tendons. A total of 17 beams with cross-section of 150 × 300 and different lengths were used. The parameters studied were tendon type (CFRP, AFRP), concrete strength and prestressing force. DEMEC points were used to take readings for the transfer length at transfer. These readings were taken for 238 days for the AFRP tendon beams and for 390 days for the CFRP tendon beams in order to investigate the time effect on the transfer length. The results showed that the transfer length of CFRP was in the range of 300 mm to 800 mm depending on the concrete strength and prestressing level where the transfer length was found to decrease with the increase of the concrete strength. The effect of time on the transfer length of CFRP was negligible. Equation 2.21 was proposed for computing the transfer length of Leadline CFRP tendons:

$$L_t = 480\,\phi\,/\sqrt{f_{ci}} \qquad \text{Equation 2.21}$$

where ϕ is the tendon diameter. For the AFRP, the results showed that the transfer length ranged between 20 to 34 times the bar diameter (170-270 mm). The values were not significantly affected by the concrete strength, and they remained constant with time.

2.4.2 Code equations

Design codes and other guidelines provide equations and typical values for the transfer length of AFRP and CFRP tendons used in prestressed application, and no guidance is provided for the transfer length of GFRP tendons.

- ISIS Canada (2008) and ACI 440.4 R-04:

The equation proposed by Mahmoud et al (1999) is adopted by both of these documents where the transfer length can be computed as given in Equation 2.22.

$$L_t = \frac{f_{pi} \times d_p}{\alpha_t f_{ci}^{o.67}} \qquad \text{Equation 2.22}$$

where L_t is the transfer length in mm, f_{pi} is the initial prestressing level in MPa, d_p is the tendon diameter in mm, α_t is material dependent coefficient which equals 1.9 for Leadline bars and 4.8 for CFCC strands in N-mm units., f_{ci} is the concrete compressive strength at time of transfer.

- CAN/CSA-S806-12:

Typical values for predicting the transfer length of FRP prestressed tendons are given in Table 2.4.

Table 2.4: Typical values for transfer length for certain types of FRP (CAN/CSA-S806-12)

FRP type	Diameter (mm)	Transfer length
CFRP strand	N/A	26 d_t
CFRP rebar	N/A	60 d_t
AFRP	$8 \leq d_t < 12$	50 d_t
AFRP	$12 \leq d_t < 16$	40 d_t
AFRP	$16 \leq d_t$	35 d_t

2.5 Summary and Conclusions

The main information presented in this chapter can be summarized in the following points:

1. The use of GFRP in prestressed applications was limited due to their susceptibility to creep rupture and their high relaxation properties.
2. The use of GFRP in prestressed applications is not allowed by CAN/CSA-S806-12 and ACI 440.1R-06, while CAN/CSA-S6-06 allows prestressing of GFRP bars but it allows low initial prestressing levels (25% of the ultimate strength of the bar).
3. Very limited research has been done on the long-term behaviour of GFRP prestressed beams.
4. Very limited research has been done on the transfer length of GFRP prestressed bars.

5. No design guidelines are available to predict the long-term deflection of GFRP prestressed beams.
6. No equations or guidelines are available to compute the transfer length of prestressed GFRP bars.

This literature has revealed a lack of information regarding the use of GFRP in prestressed applications, primarily due to concerns for relaxation and creep rupture pf the GFRP bars. Recent developments in the manufacturing of GFRP bars have led to improved mechanical properties including resistance to relaxation and creep rupture. Therefore, it is important to study the long-term flexural behaviour of GFRP prestressed beams and the transfer length of GFRP prestressed bars if these bars are to be used in practice.

Chapter 3
Experimental Program

3.1 General

This chapter provides a description of the experimental program undertaken to determine the transfer length of a new generation of GFRP prestressed bars and to investigate the long-term flexural behaviour of GFRP prestressed beams. Several ancillary tests were conducted to evaluate the material properties of the GFRP bars. The following sections give details of the experimental program.

3.2 GFRP bar specimens

3.2.1 GFRP bar/anchor assembly test

Eight GFRP bars (four 12M and four 16M diameter) with bar length of 1200 mm were tested in axial tension in order to verify the ability of the UW anchor - developed at the University of Waterloo for CFRP bars (Al-Mayah et al. 2006) - to grip the GFRP bars under the prestressing loads.

The ribs on the GFRP bar ends were machined to leave a smooth bar end for ease of gripping using the UW anchor. The machined bar end is shown in Figure 3.1.

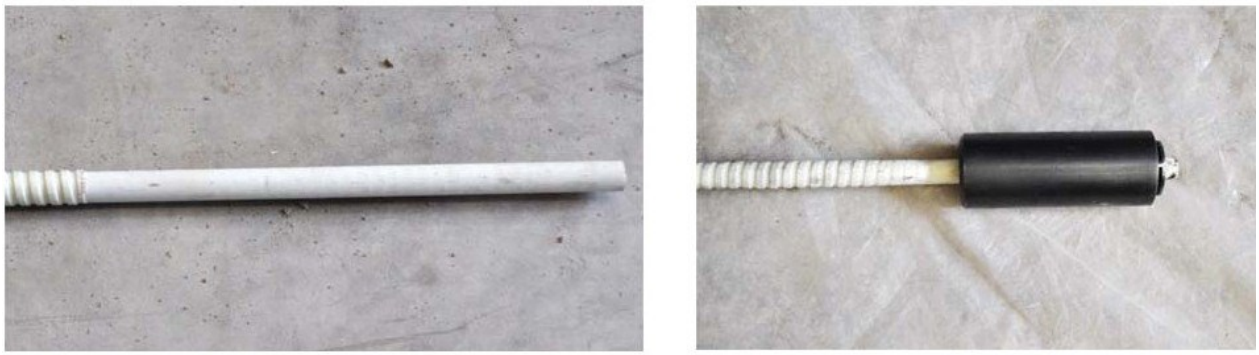

Figure 3.1: Ribs machined off at bar ends

Strain gauges (5 mm long) were mounted on the GFRP bars to measure the strains during the tensile loading. A National Instrumentation Data Acquisition System was used to record both the load and strain. First, the anchors on both bar ends were seated and the bar was inserted in the testing setup shown in Figure 3.2. Tensile load was applied at a rate of 40 kN/min, which produced failure within about 5 minutes. The recommended tensile loading rate for testing FRP bars by the ASTM D7205/D7205M (2006) is the rate that produces failure within 1 to 10 minutes.

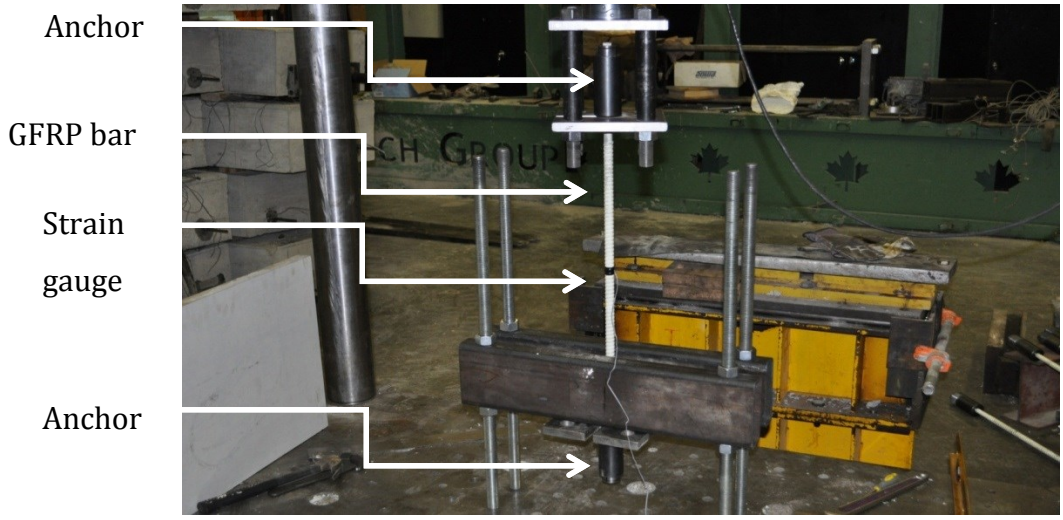

Figure 3.2: Anchors test setup

3.2.2 GFRP bar sustained load test

Two GFRP bars with 16M diameter were subjected to sustained loading for 110 days to monitor the creep behaviour of the bars in air. One bar was subjected to a sustained load of 145 kN, which produced a stress of 722 MPa, or about 60% of the bar ultimate tensile strength. The second bar was subjected to a load of 109 kN which produced a stress of 542 MPa, or about 45% of the bar ultimate tensile strength.

Strain gauges (5 mm long) were mounted on the GFRP bars to measure the strains during the sustained loading. A National Instrumentation Data Acquisition System was used to record both the load and strain.

The goal of this test was to investigate the creep behaviour of the GFRP bar at higher sustained load levels than the ones reported in the literature by Youssef and Benmokrane (2011).

3.3 Beam Specimens

3.3.1 Specimens details

A total of 20 specimens were fabricated (Table 3.1), and divided into 5 groups of 4 specimens; one specimen was tested to failure under static loading, and the three other specimens were subjected to different levels of sustained loading for 300 days, followed by testing to failure under static loading to determine the residual strength. The test parameters in this study were; the sustained load level (35%, 60%, and 80% of the ultimate capacity of the beam), the prestressing levels of the GFRP bars (40% of the ultimate strength (500 MPa) and 25% of the ultimate strength (300 MPa)), the GFRP bar diameter (12M and 16M), and concrete strength (40 MPa and 80 MPa). The 25% prestressing level is the maximum prestressing level allowed by CAN/CSA-S6-06 at transfer for prestressed GFRP bars, and the 40% prestressing level is a proposed prestressing level that the GFRP bars in this study can be prestressed to without failure due to creep rupture (Schoeck, 2009). The stresses on all of the prestressed beams at transfer were less than the limits set by A23.3-04. Also, the stresses due to the 35% sustained loading on the beams that had 40% prestressing level were less than the stress limits due to sustained loads set by A23.3-04, while the 25% prestressed beam exceeded the tensile stress limit. Detailed calculations are shown in Appendix D.

All specimens are large-scale beams with dimensions of 150 mm wide × 255 mm depth × 3600 mm long, reinforced with one prestressed or one non-prestressed GFRP bar (12M or 16M) placed in the tension zone with a concrete cover of at least three times the bar diameter to avoid splitting failure. Each beam was reinforced with 2-12M GFRP bars as top reinforcement. 10M closed steel stirrups spaced at 100 mm spacing along the length of the beam were used as shear reinforcement. The beam reinforcement ratios were selected so that the beams will be either tension-controlled or compression-controlled, and the compression-controlled beams had reinforcement ratios that were slightly above the balanced reinforcement ratio. The length of the beam was chosen to provide a sufficient development length for the prestressed bars, and the stirrups were provided to ensure flexural failure of the beams. The cross-section details of the beams are shown in Figure 3.3.

Table 3.1: Beam test specimen parameters

Beam	Prestressing level	Prestressed bar diameter	Concrete compressive strength	Sustained load level
N40-16-0	40%	16M	40 MPa	Static
N40-16-35				0.35 M_u
N40-16-60				0.60 M_u
N40-16-80				0.80 M_u
N25-16-0	25%			Static
N25-16-35				0.35 M_u
N25-16-60				0.60 M_u
N25-16-80				0.80 M_u
N0-16-0	0%			Static
N0-16-35				0.35 M_u
N0-16-60				0.60 M_u
N0-16-80				0.80 M_u
H40-16-0	40%		80 MPa	Static
H40-16-35				0.35 M_u
H40-16-60				0.60 M_u
H40-16-80				0.80 M_u
N40-12-0	40%	12M	40MPa	Static
N40-12-35				0.35 M_u
N40-12-60				0.60 M_u
N40-12-80				0.80 M_u

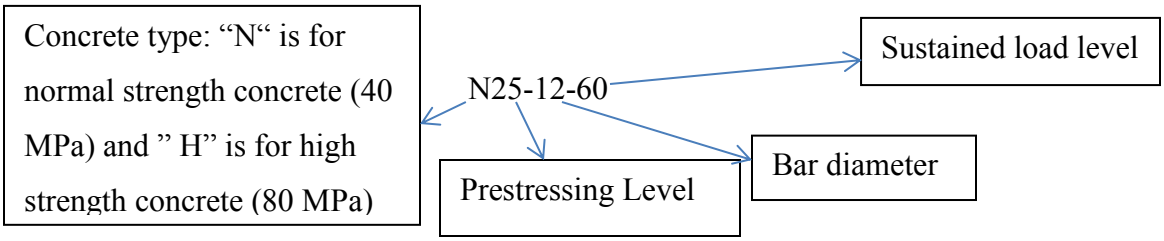

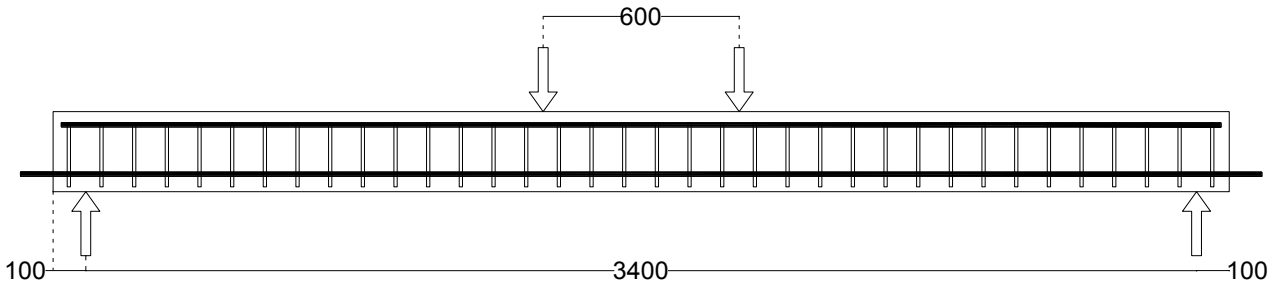

Beam specimen elevation

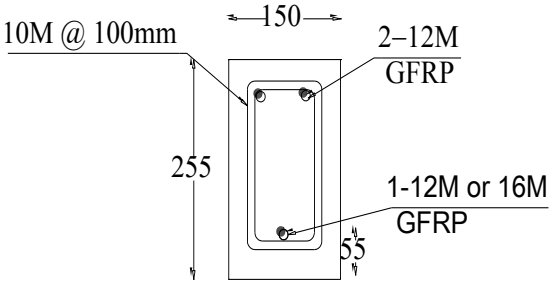

Figure 3.3: Beam specimen details

3.3.2 Prestress losses

The short-term prestress losses due to the elastic shortening were calculated according to CPCI (2007) guidelines, and were taken into account in order to achieve prestressing levels of 25% or 40% of the bar ultimate strength at transfer. The calculations are shown in Appendix C.

The long-term losses due to creep and shrinkage of concrete for the period prior to the initiation of the sustained loads were also calculated according to CPCI (2007) guidelines and are shown in Appendix C. These losses were used when calculating the shrinkage strains, creep coefficient, and the effective prestressing level, to be input in the long-term flexural behaviour model given in Section 5.3.

3.4 Prestressing setup

Three wedge type anchors that were developed at the University of Waterloo for CFRP bars (Al-Mayah et al. 2006) were used to grip the GFRP bars during the prestressing process. This anchoring system consists of an exterior barrel, three-piece wedges and a copper sleeve as shown in Figure 3.4.

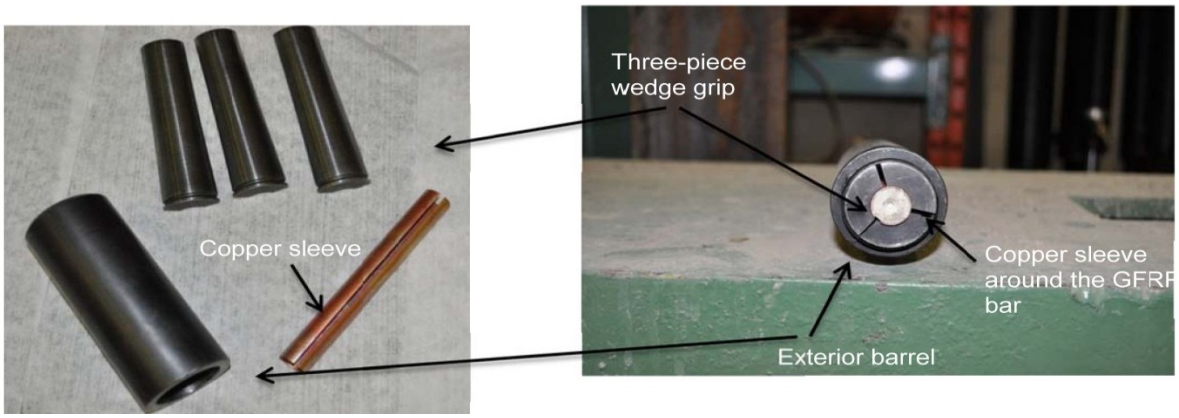

Figure 3.4: Anchoring system

The prestressing force for the pretensioned beams was applied using a self-reacting frame that was developed and fabricated at the University of Waterloo to be used as a prestressing bed (Krem and Soudki, 2012). It consisted of two C-channels (C12 × 20.7) at each end and two (W10 × 39) side beams. The frame can accommodate prestressing four beams at a time. The GFRP bars used were 4500 mm long. The GFRP bar was passed through a 37.5 mm gap in the 2 C12 × 20.7 and the two ends of the bar were seated. One end of the bar was a dead end and the other end was the live end that was attached to a steel coupler arrangement which was set on a wood plate that allowed its movement. A 25 mm threaded bar was bolted onto the steel coupler arrangement, while the other end of the threaded bar was attached to a 30 ton hollow jack that was used to apply the prestressing force to the GFRP bar. The prestressing force was locked mechanically by a nut on the threaded rod which allowed for fine adjustment and gradual release of the prestressing force. Photos of the prestressing system are shown in Figure 3.5, and a sketch is shown in Figure 3.6. The prestressing procedure can be summarized in the following steps:

- The ribs on the GFRP bars were machined off at both ends for a length of 200 mm long.
- The GFRP bars were passed through the 37.5 mm gap in the 2 C12 × 20.7, and placed in the center of the formwork for each beam.
- The dead and live ends of the bars were pre-seated using the UW anchors.
- The live end anchor for each GFRP bar was attached to the steel coupler arrangement.
- The hollow jack was installed on the 25mm threaded bar and bolted using a nut.

- Load was applied gradually at a rate of about 1 kN/second.
- The load was locked using a nut on the 25 mm threaded rod.
- Concrete was placed in the formwork.
- When concrete strength reaches the desired strength, the inner sides of the two formworks of the middle beams were removed to allow gluing the DEMEC points on the concrete surface for transfer length measurements (the process is described in details in section 3.6.2).
- The prestressing force was released for these two beams, and then they were removed from the frame to give access to the other two beams to remove the sides of their formworks and do the transfer length measurements using the DEMEC points.

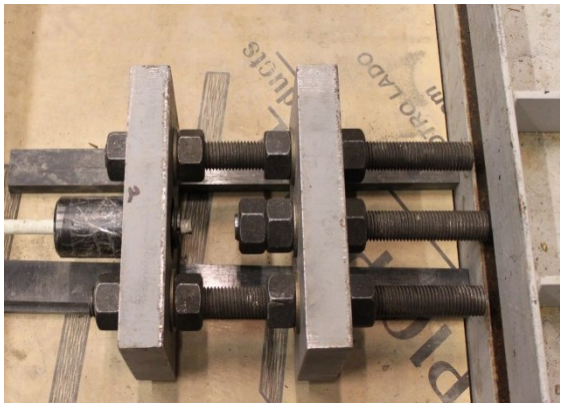

Steel coupler arrangement

Jack installed on the threaded rod

Frame dead end

Frame live end

Figure 3.5: Prestressing bed photos

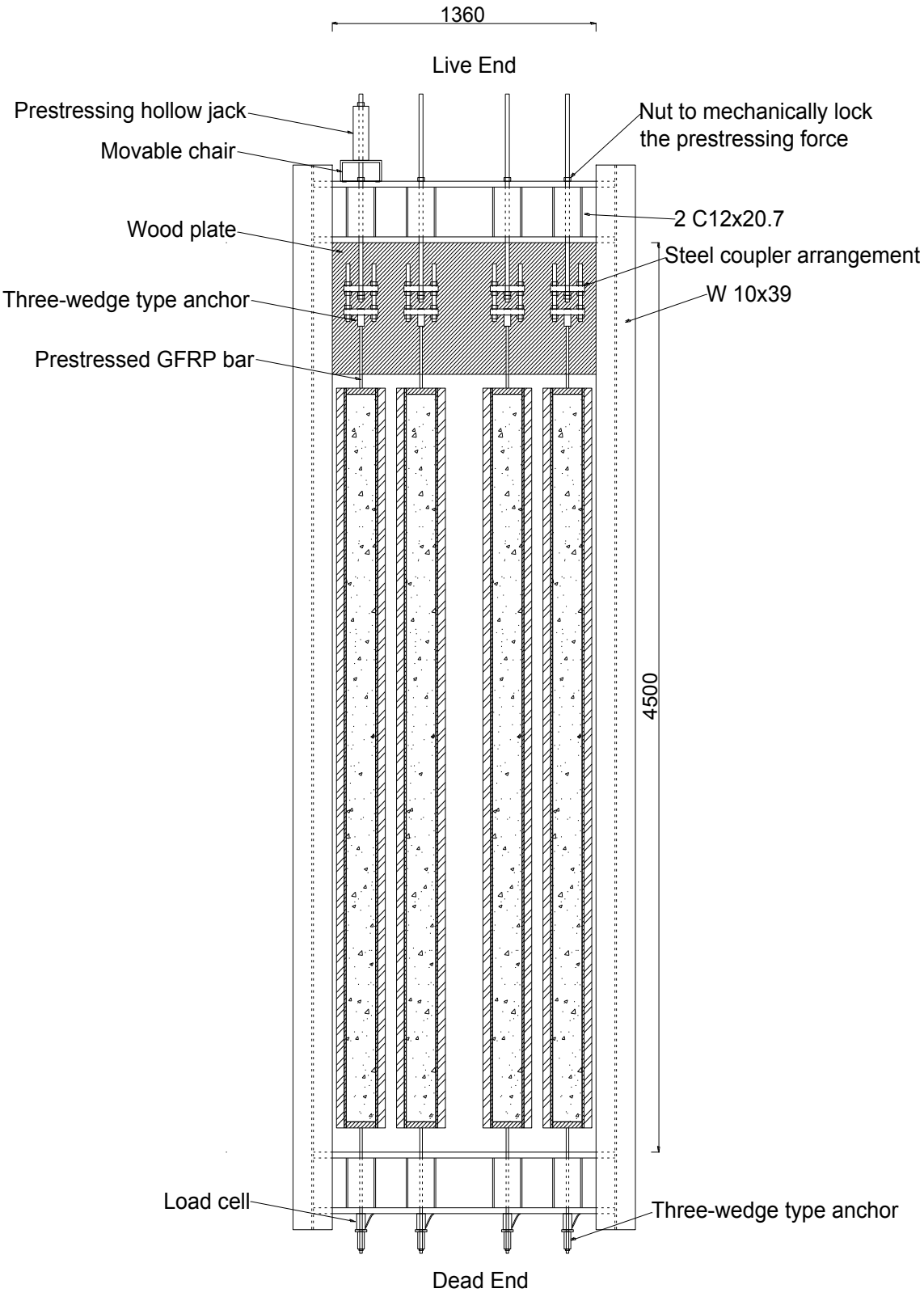

Figure 3.6: A sketch of the prestressing bed (plan view)

3.5 Material properties

3.5.1 Concrete

The concrete used for the beams was provided by Hogg Ready Mix. The concrete was designed to have a 28 day compressive strength of either 40 MP for the normal strength concrete or 80 MPa for the High strength concrete. The concrete mix designs are presented in Table 3.2, and Table 3.3. The concrete had a slump of 200 mm. The choice of using concrete with high slump was made because of safety concerns about vibrating the concrete near the prestressed GFRP bar.

Table 3.2 : Normal strength concrete mix design

Material	Quantity
Coarse aggregate	1110 kg
Sand	247 kg
Cement	347 kg
Water reducing agent	200 mm/ 100 kg
Plasticizer	350 ml/kg
Water	150 L/m^3

Table 3.3 : High strength concrete mix design

Material	Quantity
Coarse aggregate	1120 kg
Sand	680 kg
Cement	510 kg
Water reducing agent	150 mm/ 100 kg
Plasticizer	400 ml/kg
Water	155 L/m^3

3.5.2 GFRP bars

The GFRP bars are produced by Schöck Bauteile GmbH. The bars consist of continuous longitudinal fibres of about 20 μm, bundled and impregnated in Vinyl-Ester resin. Ribs are cut along the length of the bars to provide better bond with concrete (Schoeck, 2009). The mechanical properties of the 12M and 16M bars are shown in Table 3.4.

Table 3.4: Mechanical properties of GFRP bars (Schoeck, 2009)

Bar diameter	12 mm	16 mm
Ultimate tensile strength	1350 MPa	1200 MPa
Modulus of elasticity	60 GPa	60 GPa
Cross sectional area	113 mm^2	201 mm^2

3.5.3 Steel stirrups

Deformed 10M steel stirrups are used as shear reinforcement for all beams. The stirrups have a nominal yield stress of 400 MPa and a modulus of elasticity of 200 GPa.

3.6 Transfer length

The transfer length of the GFRP bars in concrete was measured using two different methods; strain gauges mounted on the GFRP bars to measure strains directly and DEMEC points glued on the concrete surface at the level of the prestressed GFRP bar to measure the concrete surface strains using a DEMEC gauge. The two methods are described below.

3.6.1 Strain gauge measurements

Five strain gauges (5 mm long) were mounted on the GFRP bars at different locations to capture the change in strains along the bar during transfer as shown Figure 3.7. The strain gauge locations were different in each beam type because the transfer length is dependent on concrete strength, bar diameter and prestressing level. The gauge locations for each group are given in Table 3.5.

Table 3.5: strain gauge location on the prestressed GFRP bars

Group	Strain gauge location measured from beam ends (mm)				
	1	2	3	4	5
N40-16	150	300	250	350	1800
H40-16	80	180	130	230	1800
N25-16	60	160	110	210	1800
N40-12	150	250	200	300	1800

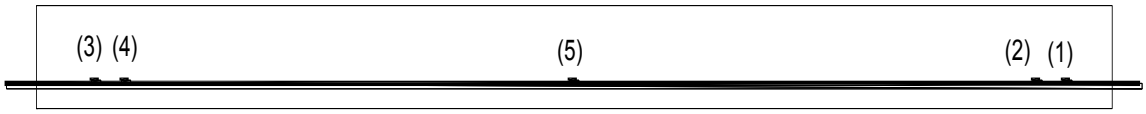

Figure 3.7: Strain gauges locations on the GFRP bars

3.6.2 Concrete surface strain measurements

DEMEC points were glued to the surface of the concrete at the level of the prestressed GFRP bar as shown in Figure 3.8. The DEMEC points are stainless steel circular discs with 1mm pin hole in the centre to provide precise measurements. A DEMEC gauge with accuracy of 0.001 mm was used to measure the distance between the points before and after release (Figure 3.9), from which the concrete surface strain at the bar location is calculated. The transfer length was measured as the distance from the beam end to the distance where concrete strain reaches 95% of its maximum strain due to prestressing (Russell and Burns, 1993).

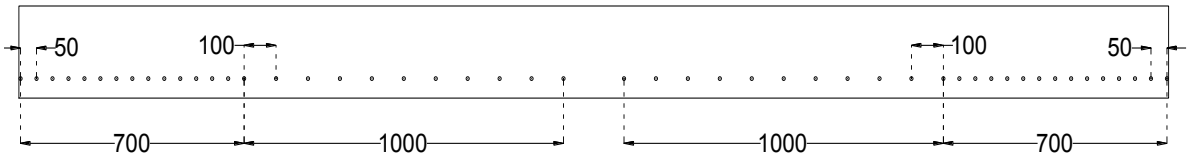

Figure 3.8: DEMEC points locations on the concrete surface

Figure 3.9: Concrete surface strains readings using the DEMEC gauge

3.7 Static loading test

The beams were tested to failure in a four-point bending test setup with a total span of 3400 mm and shear span of 1400 mm. The test setup is shown in Figure 3.10. The beam was supported on a roller at one end and a hinge on the other end and load was applied with a ramp generator at a rate of 1.5 mm/min. The actuator capacity was 280 kN. Strains in the GFRP bar and the concrete at mid-span were measured using 5 mm long strain gauges on the GFRP bars and 60 mm long gauges on the concrete compression face. One LVDT of ±25mm range and accuracy of 0.01 mm was used to measure the mid-span deflection of each beam up to failure. Data was recorded using a National Instrumentation Data Acquisition System.

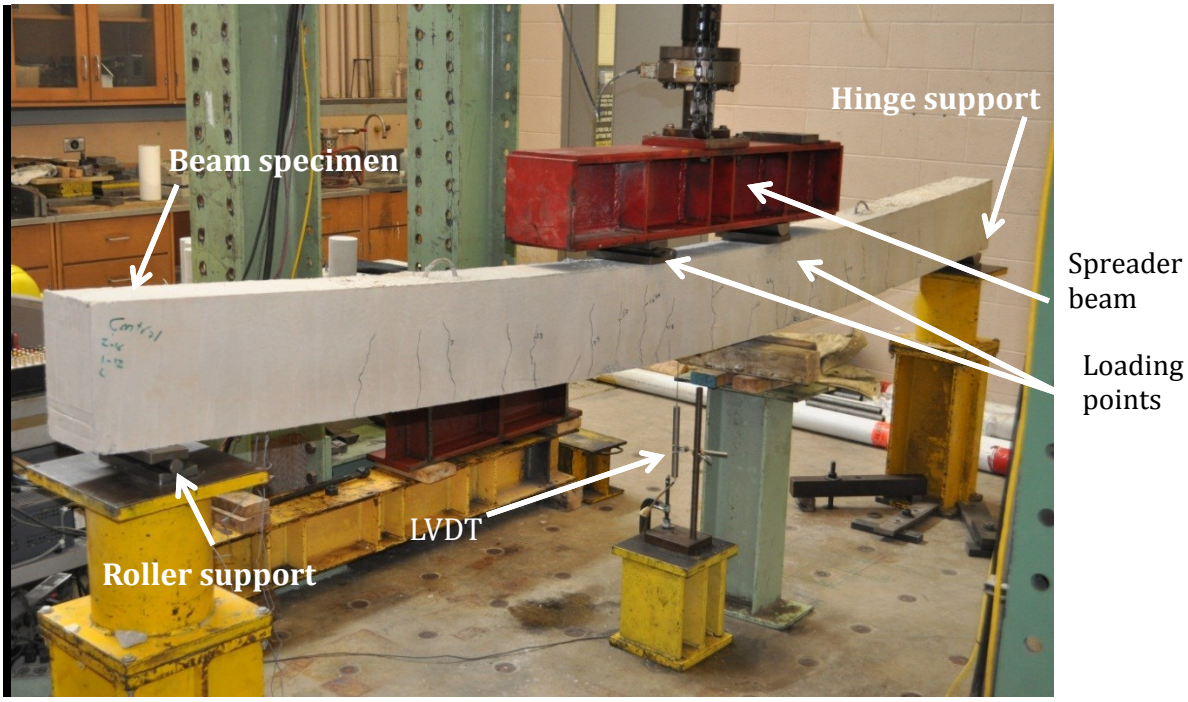

Figure 3.10: Test setup for static loading beams test

3.8 Sustained loading Test

The sustained loading tests were initiated between three and six month after casting. Four steel mechanical loading frames designed and constructed at the University of Waterloo were used to apply the sustained loads on the beams as shown in the photograph in Figure 3.11 and schematically in Figure 3.12.

Two beams were placed horizontally back-to-back in each frame: the top beam oriented with the tension side down while the bottom beam oriented with the tension side up. The base of the frame is a 3500 mm long steel beam (HSS 178 x 127 x 8), on which the supports that load the bottom beam are placed. This steel beam sits on two hollow steel sections (HSS 100 x 100 x 10 mm with a length of 500 mm each) that rest on the rigid floor of the laboratory. The load was applied using two lever arms made of hollow steel sections of HSS 102 x 51 x 6.4 mm with a total length of 1080 mm for the lower arm, and HSS 178 x 127 x 8 mm with a total length of 2430 mm for the upper arm. One end of the lower lever arm was clamped to the steel beam at the base using a turnbuckle. The dimensions of turnbuckle are 10 mm diameter and 500 mm length. The turnbuckle has two steel plates of 630 x 60 x 6 mm. The upper lever arm has one end

clamped to the base steel beam using two steel plates, 1650 x 152 x 12 mm, while the other end is clamped to the lower lever arm using two steel plates, 300 x 100 x 19 mm. A pin is placed under the upper lever arm at 2200 mm from the clamped end to the lower lever arm and is used to apply the load onto the specimen through a spreader beam. Weights are hung to the lower lever arm at 800mm away from the clamped end. The mechanical composition of the frames allows the magnification of the hung weight to be 48 times plus 7 kN (the own weight of the steel sections) at the mid-span of the spreader beam (ElMaaddawy 2004).

Five (5) mm long strain gauge mounted on the GFRP bar and 60 mm long gauges mounted on the concrete compression face at mid span were used to measure the strains in GFRP bar and concrete under sustained loads, respectively.

Figure 3.11 : Mechanical frames used for the beam sustained loading test.

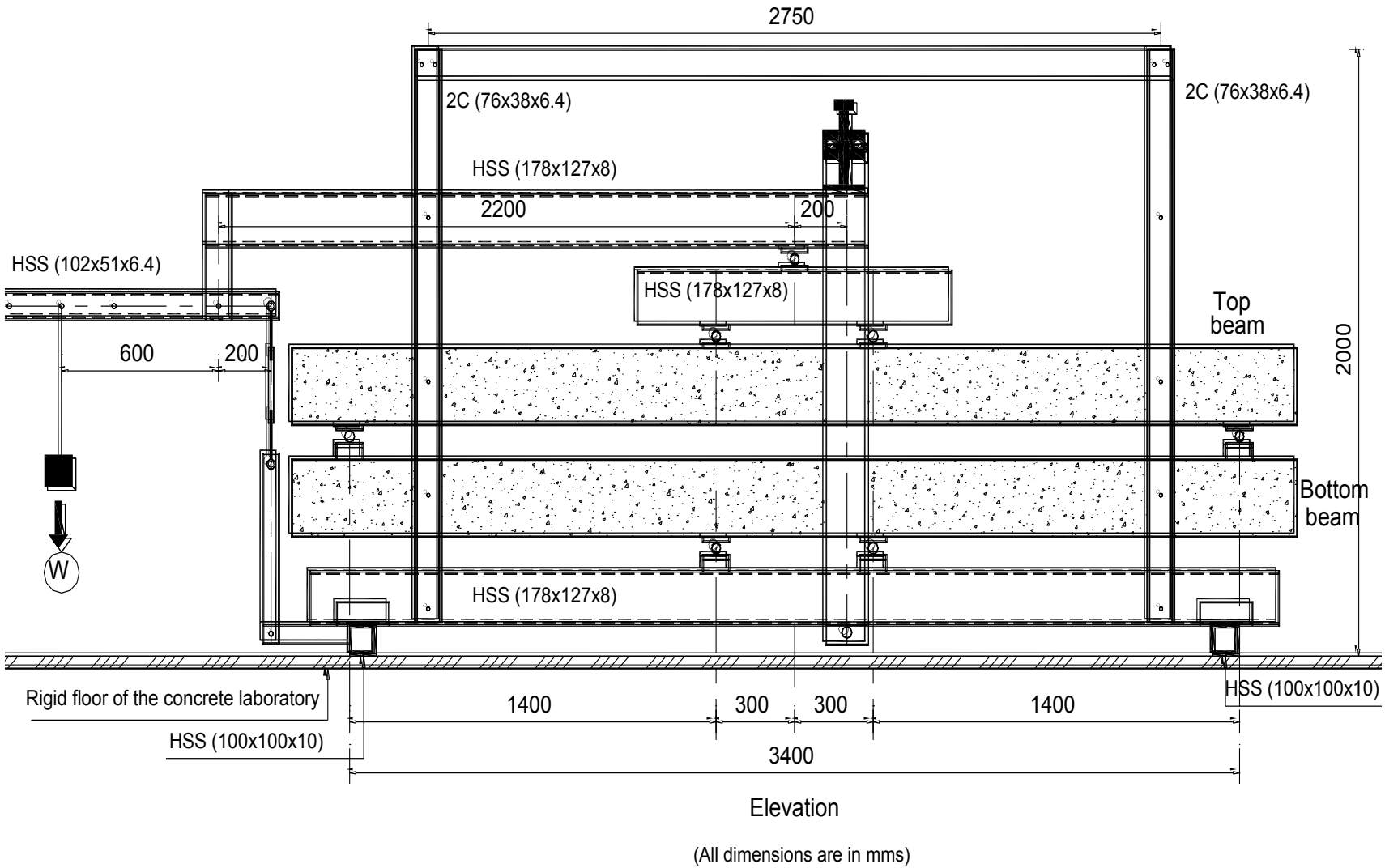

Figure 3.12: Sketch of the sustained loading frame (ElMaaddawy 2004)

Three LVDTs of ±25mm range were used with each frame to measure the mid-span deflection of the two beams under sustained loads. All of the LVDTs were fixed on the ground; two of them (LVDT1 and LVDT 2) were used to measure the deflection of the mid-span points of the top and bottom beams, respectively, and the third one was used to measure the deflection at one of the supports at end of the beams (LVDT 3). The mid-span deflections were calculated as follows:

Top beam mid-span deflection = LDVT 1 – LVDT 3

Bottom beam mid-span deflection = LVDT 2 + LVDT 3

Following the long-term exposure, all beams were tested to failure in four-point bending using the same setup described in Section 3.7.

Chapter 4
Experimental Results

4.1 General

This chapter presents the results of the experimental program conducted on GFRP bars and the GFRP prestressed/reinforced concrete beams. Eight GFRP bar/anchor assembly specimens were tested to failure in an axial tension test, and two specimens were subjected to different levels of sustained loading for 110 days. Five beams were tested to failure under four-point bending. Fifteen beams were subjected to sustained loading, where the mid-span deflection, the GFRP tension strains and the concrete compressive strains were recorded for 300 days. At the end of the 300 days, the beams were unloaded and then tested to failure under four-point bending. Transfer length measurements were taken and the early relaxation of the prestressed GFRP bars was recorded for all the prestressed beams.

4.2 GFRP bar/anchor assembly test results

Table 4.1 shows the results of the tension tests that were carried out on four 12M and four 16M GFRP bars gripped with the UW anchors. The failure mode was brittle with fibers shattering everywhere at onset of failure. In some cases failure was initiated inside the anchor. The failure mode is shown in Figure 4.1. The stress-strain curves for the 16M and 12M bars were linear elastic to failure as shown in Figure 4.2 and Figure 4.3, respectively. The strain gauges stopped working at a strain value around 10000 μs and the curve was extrapolated up to the measured failure stress. In this manner, the estimated strain at failure for all the specimens ranged between 17000 μs to 21300 μs. The modulus of elasticity ranged from 57 GPa to 60.5 GPa, while the manufacturer's reported modulus is 60 GPa.

Table 4.1: Results of GFRP bar/ anchor assembly test

	12M GFRP bars		16M GFRP bars	
	Rupture stress (MPa)	**% measured/ guaranteed**	**Rupture stress (MPa)**	**% measured/ guaranteed**
Specimen (1)	1055*	78.1%	942 *	78.5%
Specimen (2)	1150 *	85.2%	1064 *	88.7%
Specimen (3)	1230	91.1%	1088	90.7%
Specimen (4)	1309	97.0%	1122	93.5%
Average rupture stress	1186 *	87.9%	1054 *	87.8%
Standard deviation	94	7.0%	68	5.7%

*Failure initiated inside the anchor

The maximum prestressing stress in this study is taken as 500 MPa (40% of the guaranteed strength of the GFRP bars). The results of the axial tension test on the GFRP bar/anchor assembly showed that the average rupture stress was 1186 MPa (87.9% of the bar guaranteed strength) with a standard deviation of 94 MPa (7.0% of the bar guaranteed strength) for the 12M diameter GFRP bars, and 1054 (87.8% of the bar guaranteed strength) with a standard deviation of 68 MPa (5.7% of the bar guaranteed strength) for the 16M diameter GFRP bars. These test results confirmed that the anchor system originally developed for CFRP bars can be used safely to prestress the GFRP bars.

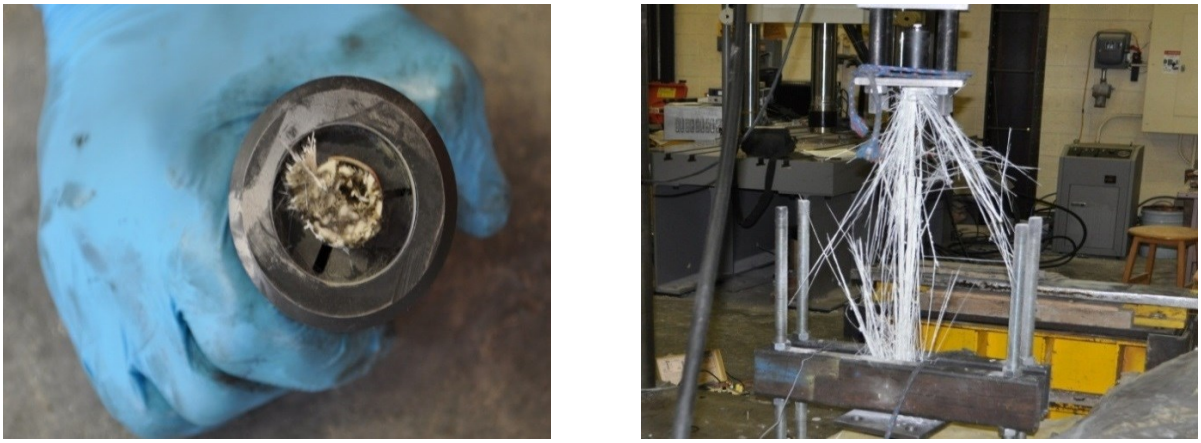

Figure 4.1: Failure mode of gripped GFRP bars in axial tension test

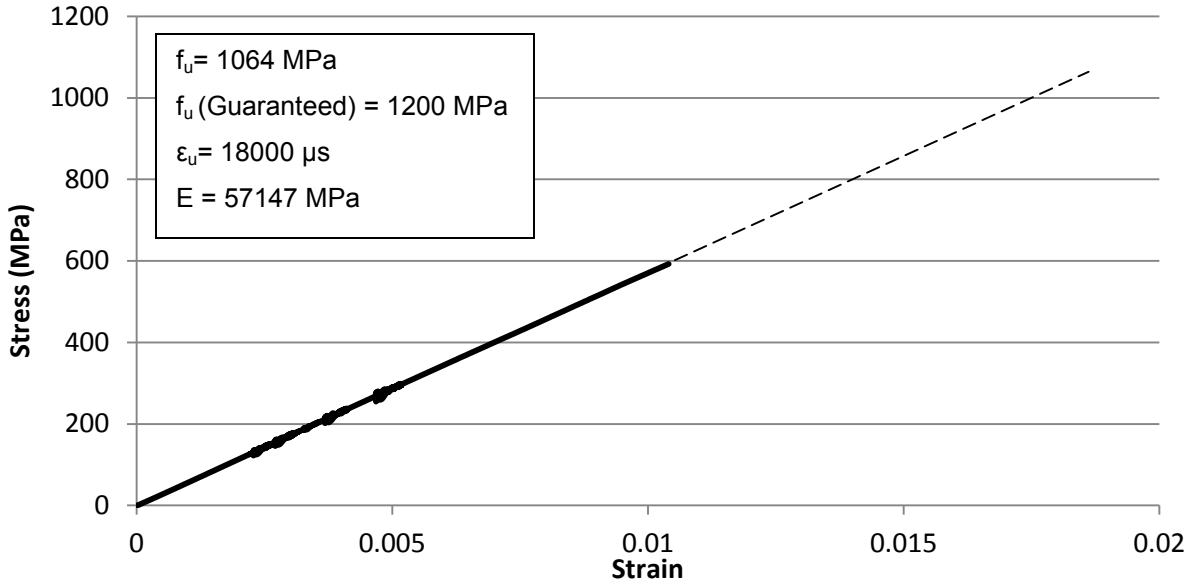

Figure 4.2: Stress –Strain curve for 16M bar under axial tension using the UW anchor

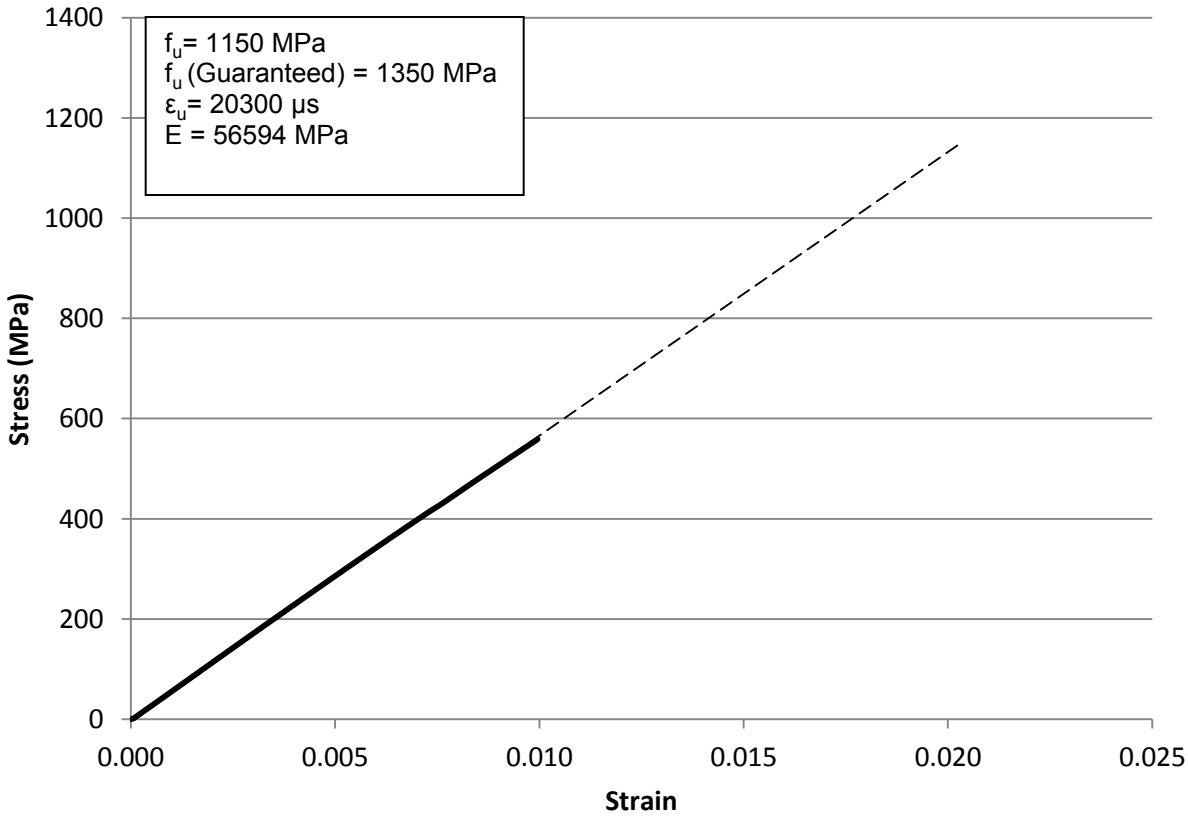

Figure 4.3: Stress –Strain curve for 12M bar under axial tension using the UW anchor

4.3 GFRP bar sustained load test

The creep properties of the GFRP bars were assessed by monitoring the change in the axial strain with time under constant applied stress. Two stress levels were used; 45% (545 MPa) and 60% (725 MPa). Only one bar was tested for each level. The change in the bar strains with time for the 45% bar (16M-45) and the 60% bar (16M-60) are shown in Figure 4.4 and Figure 4.5, respectively. It was observed that for both sustained load levels while under standard laboratory conditions, there was no sign of creep failure. The initial strains for the 16M-45 and the 16M-60 specimens were 9190 μs and 11911 μs, respectively. After 110 days of sustained loading, the total strains were 9794 μs and 12895 μs. This means that the creep strain was about 6.5% of the initial strain for the 16M-45 specimen and 8.3% of the initial strain for the 16M-60 specimens. The creep strain/initial strain for the same type of bars was reported by Youssef and Benmokrane (2011) to be 4.1% and 5.6% for loading levels of 15% and 30%, respectively. The equation for the total strain of the material can be written as (fib 2006):

$$\varepsilon_{frp}(t) = \beta \log t + \varepsilon_{frp,0}$$

where $\varepsilon_{frp}(t)$ is the total strain in the material after a time period t (in hours), $\varepsilon_{frp,0}$ is the initial (elastic) strain value and β is the creep rate parameter. Using the strains values from the experimental results for the bars 16M-45 and 16M-60, the β value was found to be 176.5 and 287.6, respectively. Youssef and Benmokrane (2011) used linear regression to obtain the values for β for 15% and 30% sustained loading levels, and they were found to be 38.5 and 98.9, respectively.

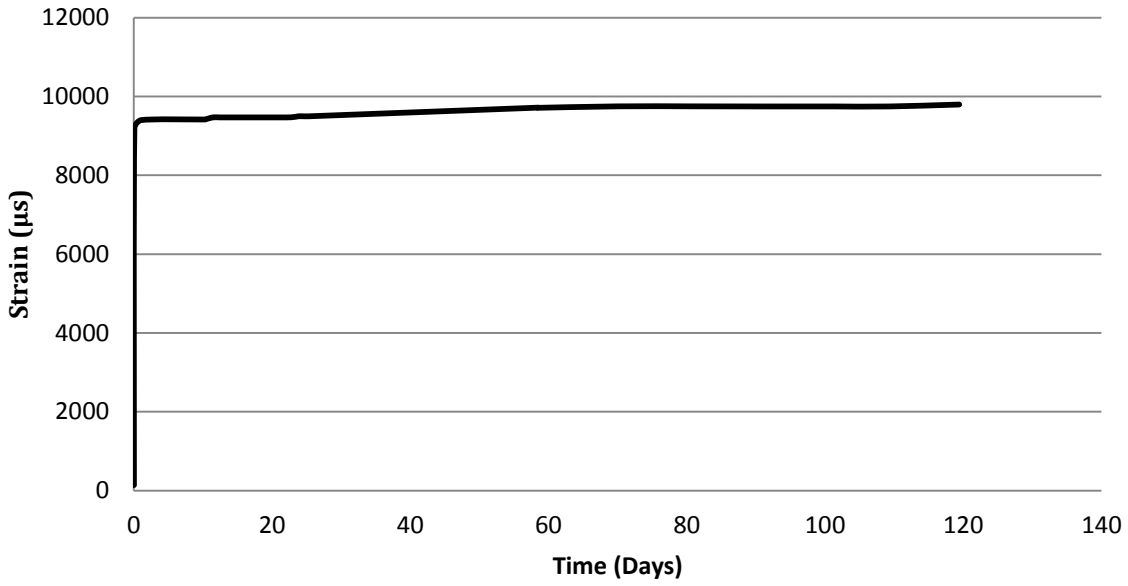

Figure 4.4: Strain vs time for GFRP bar specimen 16M-45

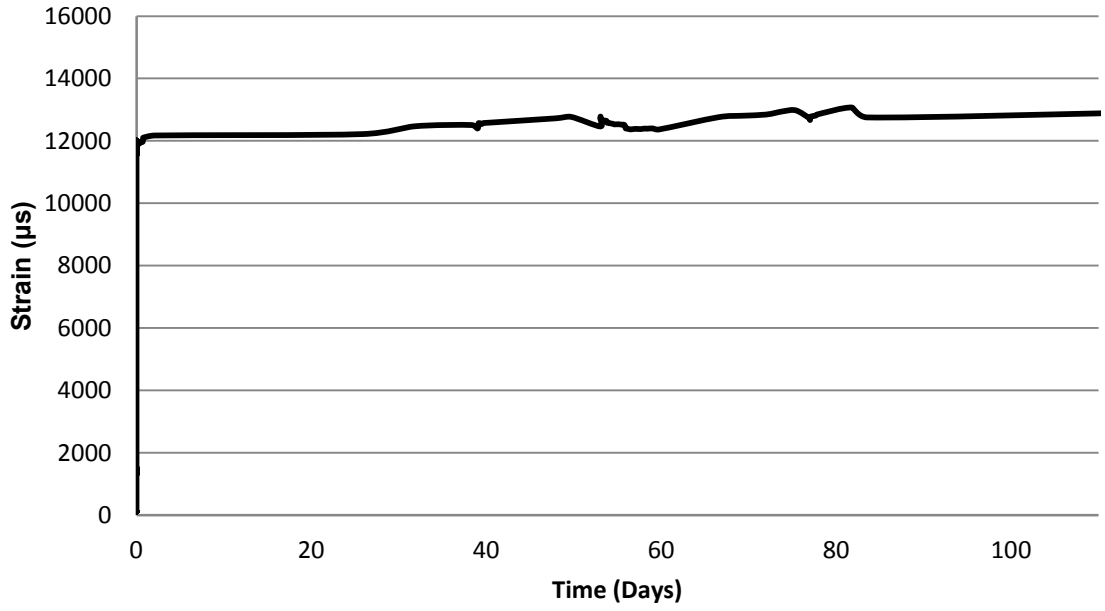

Figure 4.5: Strain vs time for GFRP bar specimen 16M-60

4.4 Early relaxation of prestressed GFRP bars

The early-age variation of the prestressing force in the GFRP bar prior to transfer for the 16 pre-stressed beams was monitored using load cells. The 4500 mm long 12M bars were prestressed to a stress level of 500 MPa, and the 16M GFRP bars were prestressed to either 300 MPa or 500 MPa. The 500 MPa stress corresponds to a prestressing force of about 100 kN for the 16M bars and 56 kN for the 12M bars, while the 300 MPa corresponds to a prestressing force of about 60 kN. Relaxation readings were taken after two hours of prestressing. This was done to ensure that each bar maintained the prestress force after anchorage seating losses took place. Readings were continuously recorded until transfer of the prestressing force to the beams. The load versus time curves for 12M and 16M bars for 277 hours are shown in Figure 4.6.

It can be concluded from the figure that the GFRP bars had no measurable relaxation over time up to 277 hours. These results are better than those reported by Fornůsek et al (2009) where the relaxation for other GFRP bars was 3.3% after 24 hours, and 7.3% after 28 days.

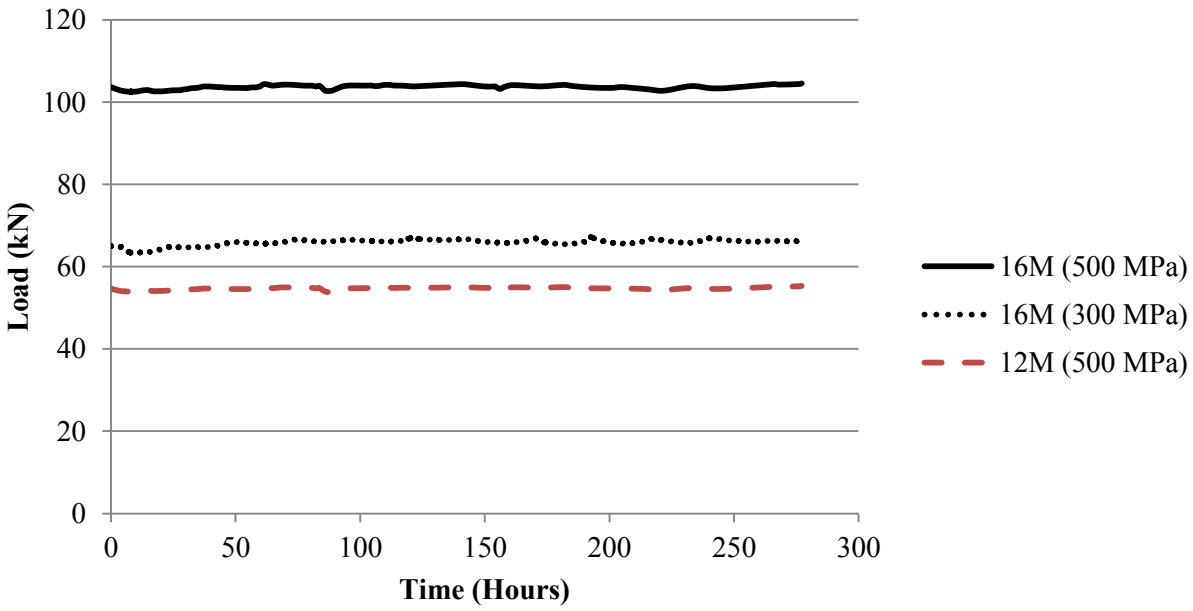

Figure 4.6: Variation of GFRP bar force over time prior to transfer

4.5 Transfer length

The transfer of the prestressing force in the GFRP prestressed beams took place when the concrete strength reached an average of 30 MPa for the normal concrete specimens and 70 MPa for the high strength specimens. Four beams were cast at a time. The strains in the GFRP bars were measured using strain gauges mounted on the bars. The concrete surface strains were measured as follows: First, the inner-side forms of the two middle beams were removed, DEMEC points were glued on the concrete surface at the prestressed bar level along the length of the beam, initial DEMEC gauge readings were taken, then the prestressing force was released, and another set of DEMEC gauge readings was taken. The same procedure was followed for the other two beams after removing the first two beams from the prestressing frame. No splitting cracks were observed in the beams after the transfer of the prestressing force.

To reduce noise in the concrete strain data measurement, the data was smoothed by averaging the strain at a point over three points along the length of the beam as follows (Kose and Burkett 2005):

$$\varepsilon_{i,smoothed} = \frac{\varepsilon_{i-1} + \varepsilon_i + \varepsilon_{i+1}}{3} \qquad \text{Equation 4.1}$$

where $\varepsilon_{i,smoothed}$ is the smoothed or averaged strain at point "i", ε_i is the original strain at point "i", and ε_{i-1} and ε_{i+1} are the original strains at the points before "i" and after "i", respectively. Figure 4.7 and Figure 4.8 show the GFRP bar strains for beams N40-16-35 and N25-16-60, respectively. Figure 4.9 and Figure 4.10 show the concrete surface strain profile after transfer for these two beams. The GFRP bar strains and surface strains profile curves for the other beams are shown in Appendix A.

The strain is zero at the beam end, and it gradually increases with distance towards the middle portion of the beam length to reach the maximum effective prestressing strain over a certain distance beyond which the strain becomes almost uniform. The shape of the curve is similar for the two bar diameters investigated in this study.

The transfer length was measured as the distance from the beam end to the distance where concrete strain reaches 95% of its effective prestressing strain (Russel and Burns 1993). In this

method, the average maximum strain (AMS) is determined by computing the numerical average of all of the compressive strains contained within the plateau region of the strain profile of the fully effective prestress force.

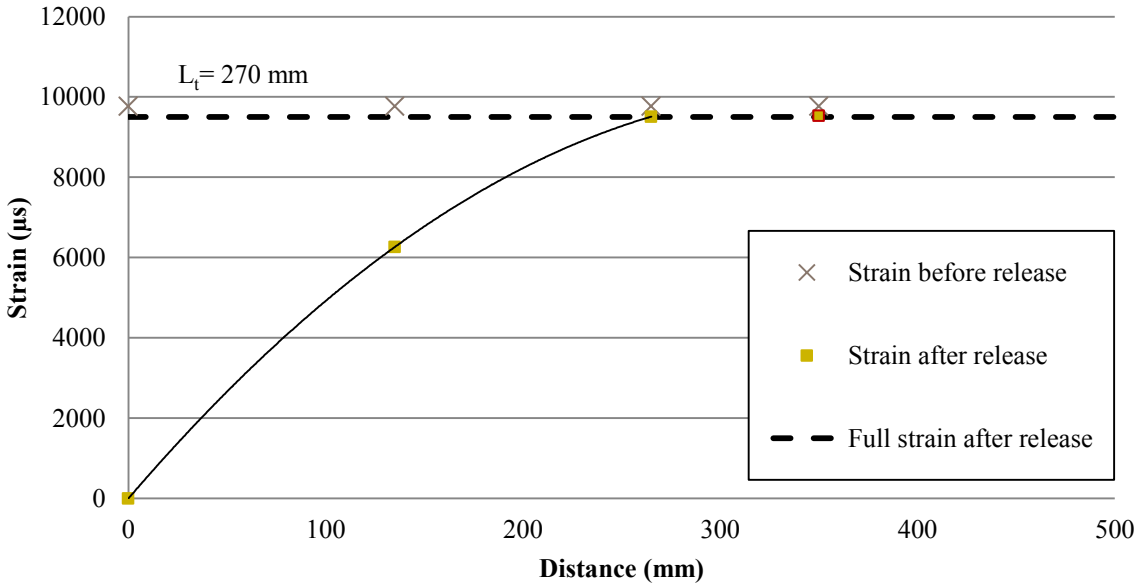

Figure 4.7: GFRP bar strains after transfer for beams N40-16-35

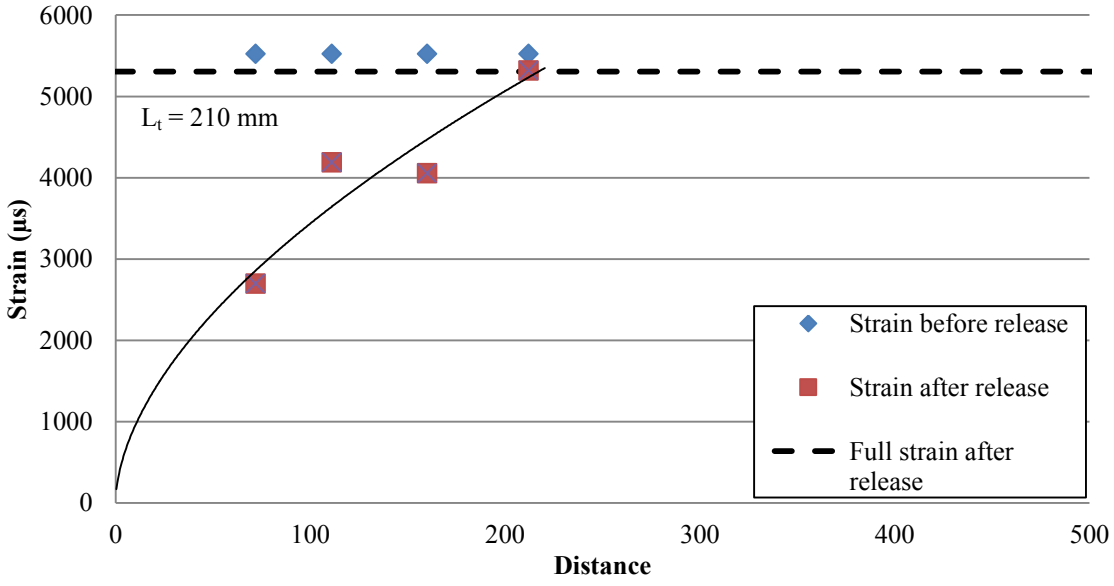

Figure 4.8: GFRP bar strains after transfer for N25-16-60

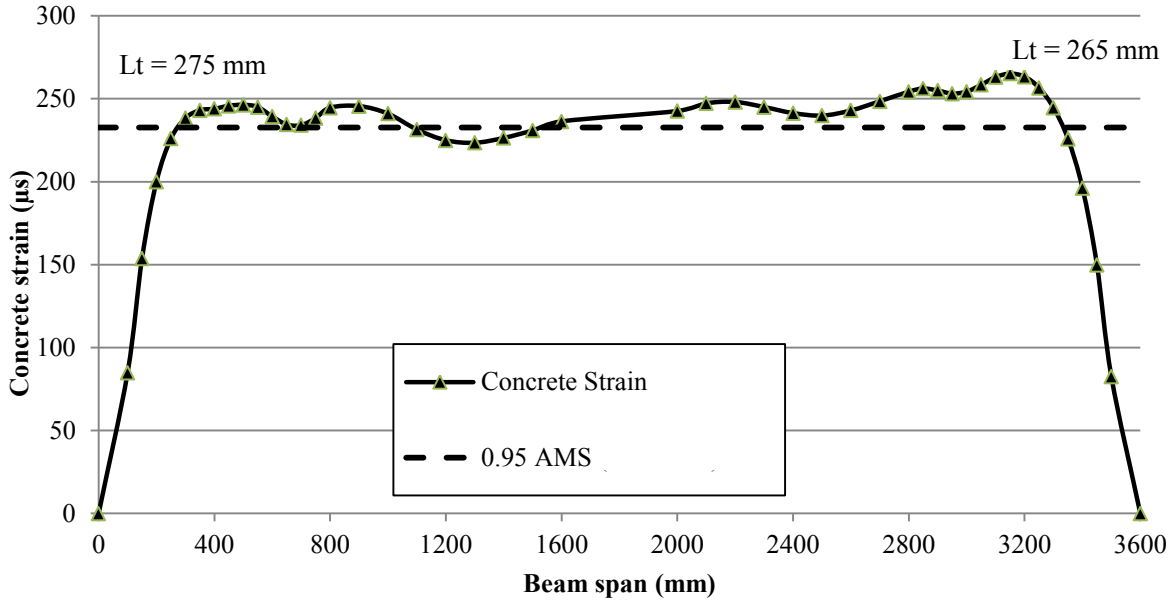

Figure 4.9: Concrete surface strain profile after transfer for beam N40-16-35

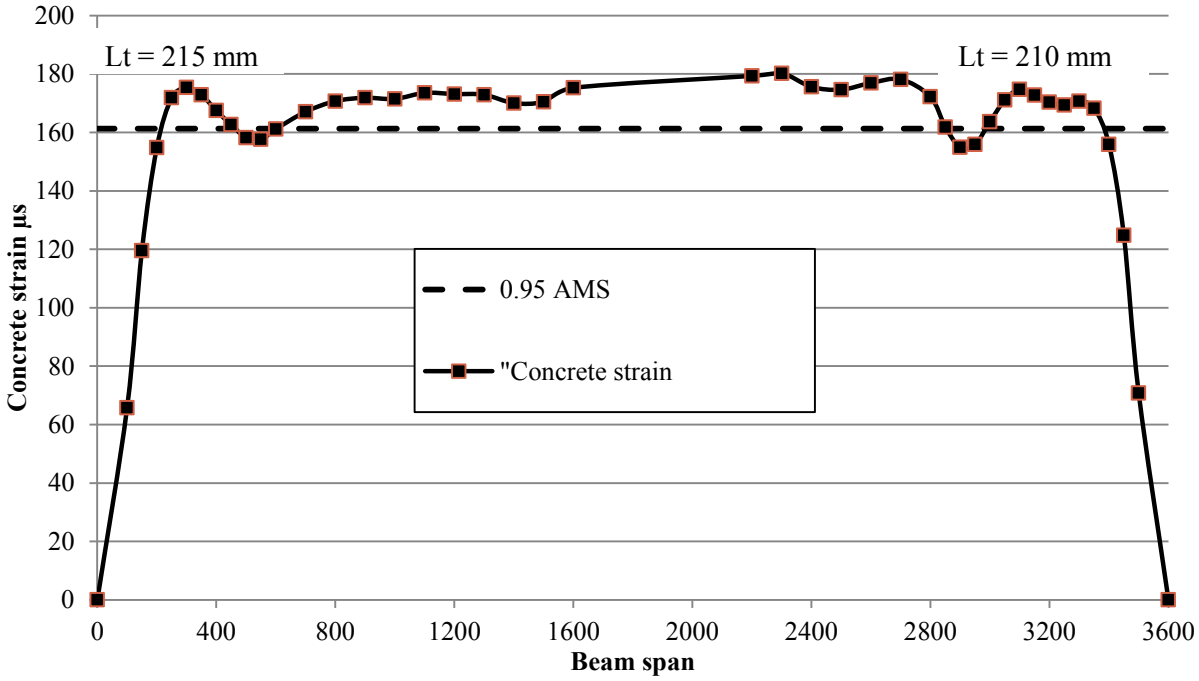

Figure 4.10: Concrete surface strain profile after transfer for beams N25-16-60

Table 4.2: Transfer length results

Beam	Prestress-ing level (MPa)	Concrete Compres-sive strength (MPa)	Transfer length mm			Average (mm)	Standard deviation (mm)
			Concrete sur-face strain		Strain gauges on bar		
			Live end	Dead end			
N40-16-0	490	31	275	300	-	276	14
N40-16-35	490	31	295	275	-		
N40-16-60	490	31	275	265	265		
N40-16-80	490	31	280	260	270		
N40-12-0	490	31	230	220	-	224	13
N40-12-35	490	31	240	200	-		
N40-12-60	490	31	210	210	245		
N40-12-80	490	31	230	225	225		
H40-16-0	500	71	170	185	185	188	13
H40-16-35	500	71	190	210	180		
H40-16-60	500	71	190	185	190		
H40-16-80	500	71	200	175	190		
N25-16-0	313	29	220	210	230	214	10
N25-16-35	313	29	225	190	210		
N25-16-60	313	29	215	210	210		
N25-16-80	313	29	210	210	230		

Transfer length results from this research program showed no clear difference or correlations between live-end and dead-end transfer lengths for any of the beams tested. This is attributed to the gradual release of the prestressing force (Staton et al. 2009). Therefore, the average transfer length for a beam series is calculated using all of the measurements from both ends of the beam.

For the beams series N40-16 and N40-12, both series had the same concrete compressive strength and prestressing stress with different bar diameters. The average transfer length for the N40-16 series was 276 mm (about $17.3d_b$) with a standard deviation of 14 mm, while the average transfer length for the N40-12 series was 224 mm (about $18.6d_b$) with a standard deviation of 13 mm. This shows that the value of the transfer length decreased by about 19% when the bar diameter decreased from 16mm to 12mm. This agrees reasonably with the literature where it is reported that the transfer length is directly proportional to the diameter of the prestressed bar.

Comparing the results of the beams series N40-16 and H40-16 shows the effect of concrete compressive strength on the transfer length of prestressed GFRP bars. The concrete compressive strength in the N40-16 series at the time of release was about 31 MPa while the H40-16 had a concrete compressive strength of about 71 MPa at the time of release. The average transfer length was found to be about 188 mm (about $11.8d_b$) with a standard deviation of 13 mm for the H40-16 series compared to the 276 mm transfer length for the N40-16 series. This indicates that the transfer length of prestressed GFRP bars decreased by about 32% when the concrete compressive strength at the time of release increased by 56%. The concrete strength is reported in the literature to decrease the transfer length of CFRP bars when it increases. For AFRP, it was reported by several researchers (Nanni et al. (1992), Zou (2003)) that concrete strength had a minimal effect on the transfer length of AFRP bars. This can be attributed to the short transfer length values measured for the AFRP bars. Although, the modulus of elasticity of AFRP is similar to that of GFRP, the diameter of the AFRP bars used in the literature (normally <=8mm) was smaller than the diameters of GFRP bars used in this study. The larger diameter of GFRP bars resulted in longer measured transfer lengths which allowed the effect of concrete strength on the transfer length to be more obviously observed.

The effect of prestressing level on the transfer length of prestressed GFRP bars is evident when comparing the results of the N40-16 series and the N25-16 series. The only difference between

the two series was the prestressing level of the GFRP bar where in the first series it was about 500 MPa and in the second series, it was about 300 MPa. The average transfer length for the N25-16 series was about 214 mm (about $13.4d_b$) with a standard deviation of 10 mm. Decreasing the prestressing level from 500 MPa to 300 MPa decreased the transfer length by about 21%.

In general, the transfer length values in terms of bar diameter for the GFRP bars used in this study were found to be less than the values for CFRP and AFRP given in the CAN/CSA-S806-12 and the values found in the literature. This can be attributed to two reasons: the lower modulus of elasticity of GFRP compared to CFRP, and the ribbed surface of the GFRP bars used in this study. The lower modulus of elasticity results in an increase in the normal stresses acting on the surface of the prestressed bar upon release, due to the radial expansion of the bar because of Poisson's ratio (Mahmoud et al. 1999). The ribbed surface of the GFRP bars provides a mechanical interlock with concrete, which decreases slip of the bar in concrete resulting in shorter transfer length when compared to AFRP tendons with almost a similar modulus of elasticity.

4.6 Beam static loading test

Five beams (one of each group) were tested to failure in static four-point bending. The applied load, mid-span deflection, concrete compression strains and the GFRP bar tension strains were monitored during the test. Table 4.3 gives a summary of the test results for all the beams including the cracking load, the ultimate load, and the deflection at ultimate. The load-deflection behaviour of all the beams is shown in Figure 4.11.

Table 4.3: Static loading test results

Beam	Cracking Load (kN)	Deflection at cracking (mm)	Ultimate Load (kN)	Deflection at failure (mm)
N 40-16-0	21	3.7	59	125
N 40-12-0	16	3.2	41	91
H 40-16-0	27	4.5	68	89
N 25-16-0	17	3.5	55	142
N 0-16-0	6	2.3	54	198

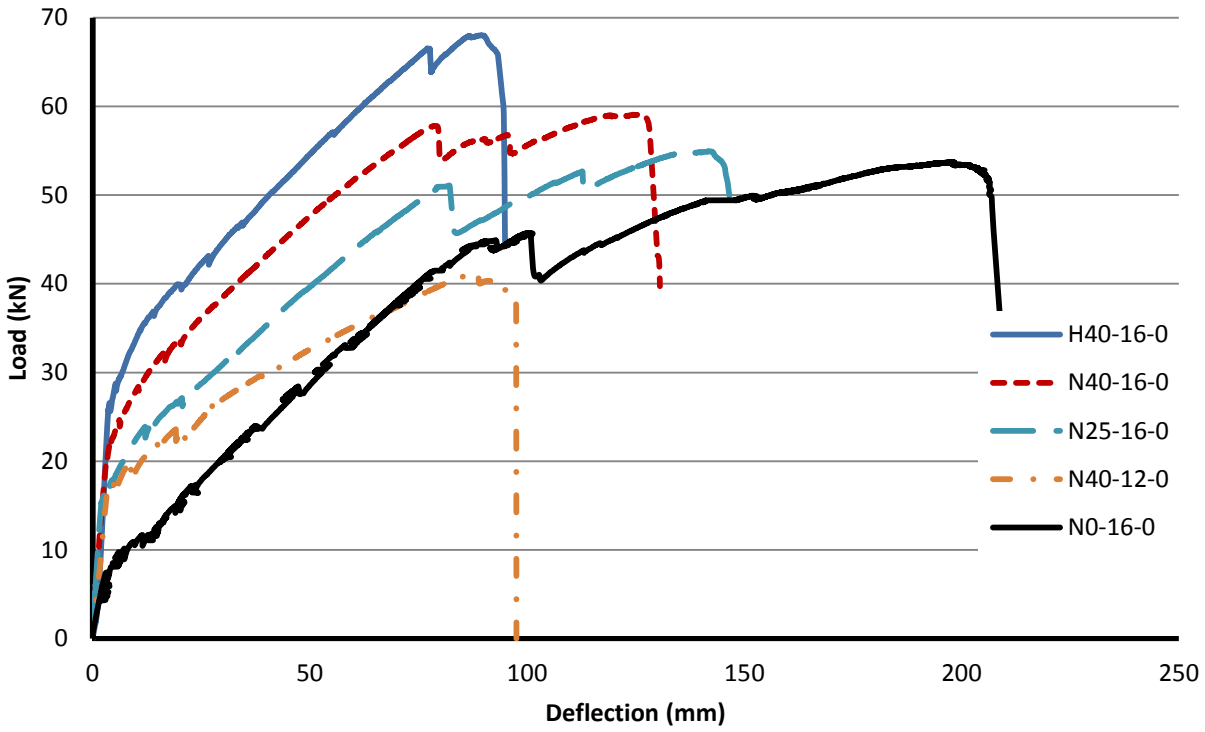

Figure 4.11:Load- Deflection curves for all beam types

In general, the behaviour of the GFRP reinforced/prestressed concrete beams was bilinear. It consisted of two phases; the first phase was before concrete cracking and was characterized by a stiff response with small deflections. The second phase was after concrete cracking where most of the tensile stresses were carried by the GFRP bars, and since the bars have linear behaviour, this phase was also linear but with a lower stiffness.

It can be observed that the stiffness of all the beams before cracking was almost similar regardless the concrete strength, the bar diameter or the prestressing level. The prestressing level does not affect the stiffness of the beam. The decrease in the bar diameter would have a negligible effect on the stiffness of the beam since it slightly decreases the gross moment of inertia of the section. The effect of increasing the concrete strength appears only in increasing the concrete modulus of elasticity, and that increase is also negligible compared to the effect of the moment of inertia of the section on flexural stiffness.

The cracking load depends on the prestressing level and the concrete strength. For the non-prestressed beam N0-16-0, the cracking load was about 6 kN, whereas the cracking load was 21 kN and 17 kN for N40-16-0 and N25-16-0, respectively. This difference in the cracking load was because of the prestressing force which was higher for the N40-16-0 beam. For beam H40-16-0, the higher concrete strength resulted in a higher cracking load (27 kN) compared to the normal strength concrete specimen with the same prestressing level. Typically the first crack occurred in the constant moment region. At this stage, the tensile stresses transferred from the concrete to the GFRP bar on the tension side. The influence of the cracks appeared as an increase in the rate of deflection per unit load after cracking, which is an indication of reduction in the beam stiffness.

The beam stiffness after cracking depends on the reinforcement ratio and the modular ratio. That is why the stiffness of the beams N40-16-0, N25-16-0, and N0-16-0 after cracking is almost the same. The beam H40-16-0 has a slightly higher stiffness because of the higher modulus of elasticity of concrete. The beam N40-12-0 had a lower stiffness after cracking due to its lower reinforcement ratio compared to the other specimens.

Beam N40-12-0 and beam H40-16-0 failed by rupture of the GFRP bar followed by concrete crushing in the compression zone. This is termed as tension-controlled failure.

Beams N40-16-0, N25-16-0, and N0-16-0 failed by concrete crushing in the compression zone followed by rupture of the GFRP bar in the tension zone. This is termed a compression controlled failure. The transition from the uncracked state to the cracked state for the three beams was smooth. The beams continued to carry loads after cracking until the concrete at the top fibre within the constant moment region reached its ultimate strain value initiating crushing. The concrete crushing load was 57 kN, 51 kN and 45 kN for N40-16-0, N25-16-0, and N0-16-0, respectively. It can be seen that the concrete crushing load increased with the increase of the prestressing force. The prestressing force results in lowering of the neutral axis of the section, leading to decreased concrete strains compared to the non-prestressed section at the same load levels. Concrete crushing resulted in a sudden drop in the load as shown on the load- deflection curve. Consequently, the section depth was reduced to about 210 mm with the GFRP bars in the tension zone remaining in the elastic range. The new reduced section started to carry additional loads with a reduced stiffness until the rupture of the GFRP bar.

The effect of prestressing on serviceability can be seen when comparing the load-deflection behaviour of the beams N40-16-0 and N0-16-0. At a load of 30% of the ultimate strength of each beam, which can be considered as a service load level, it is found that prestressing reduced the deflection from 21 mm to 3 mm (85.7% deflection reduction).

Figure 4.12: Failure mode for N0-16-0 beam

Figure 4.13: Failure mode for H40-16-0 beam

4.7 Sustained loading test

4.7.1 General behaviour

15 beams were subjected to different levels of sustained loading for 300 days. The beams were divided into five groups as shown before in Table 3.1. Within each group, one beam was subjected to a sustained load level that was 35%, 60% or 80% of the ultimate load capacity of the beam. Figure 4.15 to Figure 4.18 present the time-dependent mid-span deflection of the 15 tested beams. It should be noted that the jumps that appear on some of the curves are due to modifying the loads on the mechanical loading frames. Table 4.4 shows the detailed results for all of the tested beams. The total deflection includes the immediate deflection after loading and the long-term deflection due to creep and shrinkage. The curves for all of the beams have similar shapes. The general trend is a high rate of increase of deflection for the early period after loading followed by a more gradual rate of increase of deflection. This behaviour was exhibited by all beams, irrespective of the level of prestressing, the bar diameter or the concrete strength. The total deflection after 20 days was 70% of the total deflection after 300 days for all of the beams, and the total deflection after 100 days was more than 90% of the total deflection after 300 days. The behaviour of each group is described below:

N40-16:

The prestressed beam N40-16-35 was subjected to a load of 22.5 kN which produced a moment of 15.8 kNm at the mid-span. This was less than the cracking moment of the beam. The immediate deflection, top concrete strains and the GFRP tension strains were 4.5 mm, -520 μs, and 7775 μs, respectively. The GFRP strain is the summation of the effective prestressing strain which was about 7400 μs, and the load dependent strain which was about 375 μs. After being loaded for 300 days, the deflection increased to 9.1 mm, and the concrete and the GFRP strains were -703.5 μs and 8036 μs, respectively. The final deflection increased by 4.6 mm to be about 2.02 times the initial deflection or 1/373 of the beam span.

Prestressed beam N40-16-60 was subjected to a load of 38 kN which produced a 26.6 kNm bending moment at the mid-span, exceeding the cracking moment of the beam. This load led to a 28.5 mm immediate mid-span deflection, -1744 μs concrete compression strain and 13267 μs

GFRP tension strain (7400 μs from prestressing and 5867 μs due to loading). After the 300 days of loading, the final mid-span deflection, concrete strain and GFRP strains were 36.7 mm, -2315 μs and 12758 μs, respectively. The final deflection increased by 8.2 mm to be 1.29 times the initial deflection or 1/92.6 of the beam span.

The last prestressed beam in this set, N40-16-80, was subjected to a load of 48 kN which produced a 33.6 kNm bending moment at the mid-span (exceeds cracking moment). The initial deflection, concrete strain and GFRP strain at the mid-span were 51.8 mm, -2220 μs and 16600 μs (7400μs from prestressing and 9200 μs due to loading), respectively. The final readings were 72.1 mm and -3800 μs for the deflection and the concrete strain. The GFRP strain gauge stopped reading shortly after the initial loading, so the final GFRP reading was unavailable. The final deflection increased by 20.3 mm to be about 1.39 times the initial deflection or 1/47.2 of the beam span.

N0-16:

The sustained loads for the group of the non-prestressed beams all exceeded the cracking moment of the beams. The beam N0-16-35 was subjected to a load of 18.5 kN that produced a bending moment of 13.2 kNm at the mid-span. The initial deflection, concrete strain and GFRP strain at the mid-span were 29 mm, -760 μs and 4860 μs, respectively. The final readings were 45.8 mm for the deflection, -1790 μs for the concrete and 5924 μs for the GFRP. The deflection increased by 16.8 mm to be 1.58 times the initial deflection or 1/74 of the beam span.

Beam N0-16-60 was subjected to a load of 29.5 kN that produced a bending moment of 20.4 kNm at the mid-span. The initial deflection, concrete strain and GFRP strain at the mid-span were 54.4 mm, -2380 μs and 10100 μs, respectively. The final readings for deflection, concrete strain and GFRP strain were 69.5 mm, -3213 μs and 11373 μs, respectively. The increase in the deflection was 15.1, and the total deflection was 1.28 times the initial deflection or about 1/48.9 of the beam span.

The last beam in the non-prestressed group was N0-16-80. It was subjected to a sustained load of 39 kN that produced a bending moment of 27.3 kNm. The initial deflection, concrete strain and GFRP strain at the mid-span were 73.5 mm, -2980 μs and 10922 μs, respectively. The final read-

ings for deflection, concrete strain and GFRP strain were 91.7 mm, -4356 μs and 12657 μs, respectively. The deflection increase under the sustained load was 18.2 mm, and the total deflection was 1.25 times the initial deflection or 1/37 of the beam span.

N25-16:

The beam N25-16-35 was subjected to a sustained load of 19 kN which produced a bending moment of 13.5 kNm, which was less than the cracking moment of the beam. The initial deflection, concrete strain and GFRP strain at the mid-span were 5.6 mm, -390 μs and 4810 μs (4600μs from prestressing and 210 μs due to loading), respectively. The final readings for deflection, concrete strain and GFRP strain were 9.3 mm, -788 μs and 5260 μs, respectively. The deflection increase under the sustained load was 3.7 mm, and the total deflection was 1.67 times the initial deflection or 1/365 of the beam span.

Beam N25-16-60 was subjected to a load of 34.5 kN which produced 24.2 kNm bending moment at the mid-span. This load caused a 38.7 mm immediate mid-span deflection, -2100 μs concrete compression strain and 10770 μs GFRP tension strain (4600 μs from prestressing and 6170 μs due to loading). After the 300 days of loading, the final mid-span deflection, and concrete strains were 53.5 mm, and -3387 μs, respectively. The final deflection increased by 14.8 mm to be 1.38 times the initial deflection or 1/63.6 of the beam span.

The last beam in this group, N25-16-80, was subjected to a load of 44 kN which produced 30.8 kNm bending moment at the mid-span. The initial deflection, concrete strain and GFRP strain at the mid-span were 48.8 mm, -2140 μs and 13000 μs (4600μs from prestressing and 8400 μs due to loading), respectively. The final readings were 66.2 mm for the deflection and -4640 μs for the concrete strain. The GFRP strain gauge stopped reading shortly after the initial loading, so the final GFRP reading is unavailable. The final deflection increased by 17.4 mm to be about 1.36 times the initial deflection or 1/51.4 of the beam span.

H40-16:

The first beam in this group is H40-16-35. The value of the sustained load was 24.5 kN (17.2 kNm) which was less than the cracking moment. This caused an immediate mid-span deflection

of 3.5 mm, concrete strain of -312 μs and GFRP strain of 7595 μs (7400μs from prestressing and 195 μs due to loading). The load was sustained on the beam for only 190 days due to laboratory technical problems. The mid-span deflection increased by 2.25 mm, the concrete strain increased by 377 μs and the GFRP strain increased by 455 μs. The total final deflection was 1/590 of the beam span.

Beam H40-16-60 was subjected to a load of 39.5 kN that produced a bending moment of 27.7 kNm at the mid-span. The initial deflection, concrete strain and GFRP strain at the mid-span were 24.0 mm, -1280 μs and 12553 μs (7400μs from prestressing and 5153 μs due to loading), respectively. The final readings for deflection, and concrete strain were 38.5 mm, and -2210 μs, respectively. The GFRP strain gauge stopped working few days after the initial loading of the beam. The increase in the deflection was 14.5, and the total deflection was 1.6 times the initial deflection or 1/88 of the beam span.

Beam H40-16-80 was subjected to a load of 52 kN which produced 36.4 kNm bending moment at the mid-span. This load led to 47.5 mm immediate mid-span deflection, -2550 μs concrete compression strain and 13500 μs GFRP tension strain (7400 μs from prestressing and 5867 μs due to loading). This beam was only loaded for only 200 days due to time constraints. The final mid-span deflection, and the concrete strains were 58.0 mm, and -3374 μs, respectively. The final deflection increased by 10.5 mm to be 1.22 times the initial deflection or 1/58.6 of the beam span.

N40-12:

In the N40-12 group, the beam N40-12-35 was subjected to a load of 14 kN which produced a moment of 9.8 kNm at the mid-span. That applied moment was less than the predicted cracking moment of the beam which was 13 kNm. The immediate deflection, top concrete strain and the GFRP tension strain were 4.7 mm, -202 μs, and 8000 μs (7850 μs from prestressing and 150 μs due to loading), respectively. At the end of the sustained loading period (300 days), the total deflection became 8.8 mm, and the concrete and the GFRP strains were -395 μs and 8210 μs, respectively. The final deflection increased by 4.1 mm to be about 1.87 times the initial deflection or 1/386 of the beam span.

Beam N40-12-60 was subjected to a load of 24 kN that produced a bending moment of 27.7 kNm at the mid-span. This applied bending moment exceeded the cracking moment of the beam. The initial deflection, concrete strain and GFRP strain at the mid-span caused by the applied load were 22.5 mm, -1240 μs and 15950 μs (7850 μs from prestressing and 8100 μs due to loading), respectively. The final readings after 300 days for the deflection, the concrete strain and the GFRP strain were 31.2 mm, -1945 μs, and 16890 μs, respectively. The total final deflection was 1.39 times the initial deflection or about 1/109 of the beam span.

The last beam in this group is N40-12-80 which was subjected to a load of 32 kN which produced 22.4 kNm bending moment at the mid-span. The initial deflection, concrete strain and GFRP strain at the mid-span were 60.0 mm, -2096 μs and 17912 μs (7850 μs from prestressing and 10062 μs due to loading), respectively. After 300 days, the final readings were 80.8 mm for the deflection and -2906 μs for the concrete strain. The GFRP strain gauge stopped reading shortly after the initial loading, so the final GFRP reading is unavailable. The final deflection increased by 20.8 mm to be about 1.35 times the initial deflection or 1/42 of the beam span.

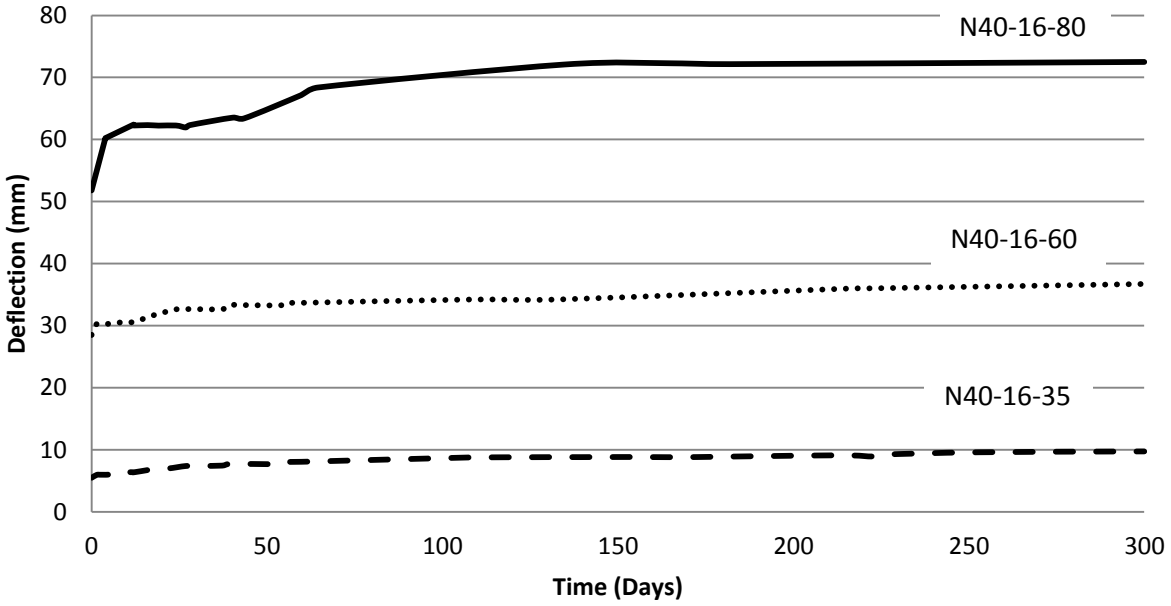

Figure 4.14: Time-dependent mid-span deflection for N40-16 beams

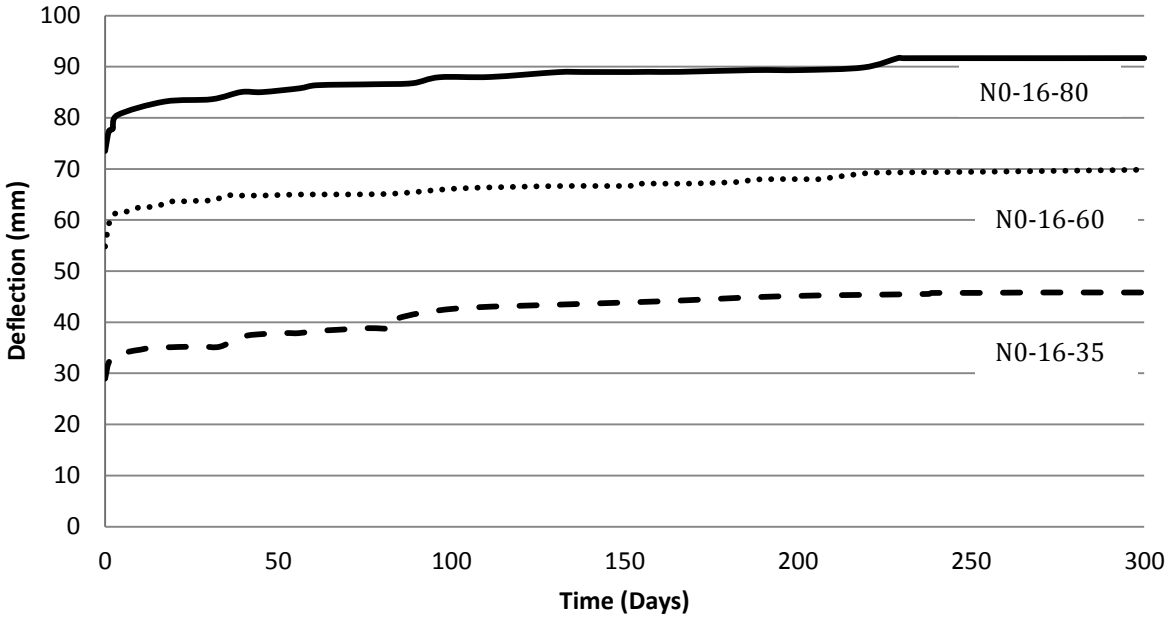

Figure 4.15: Time-dependent mid-span deflection for N0-16 beams

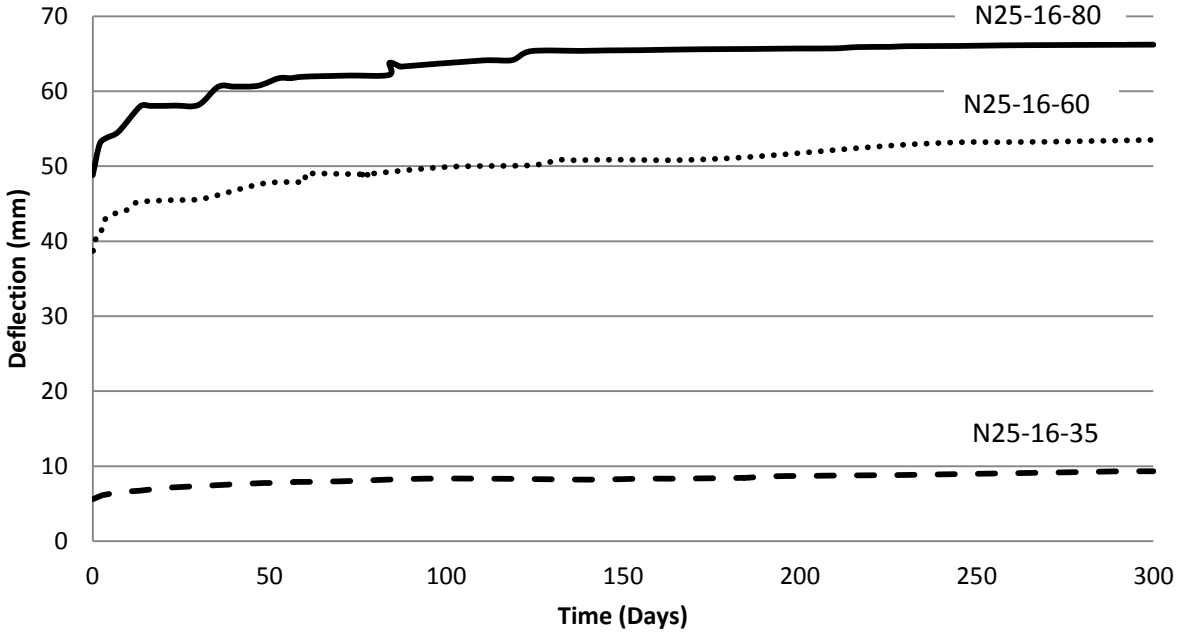

Figure 4.16: Time-dependent mid-span deflection for N25-16 beams

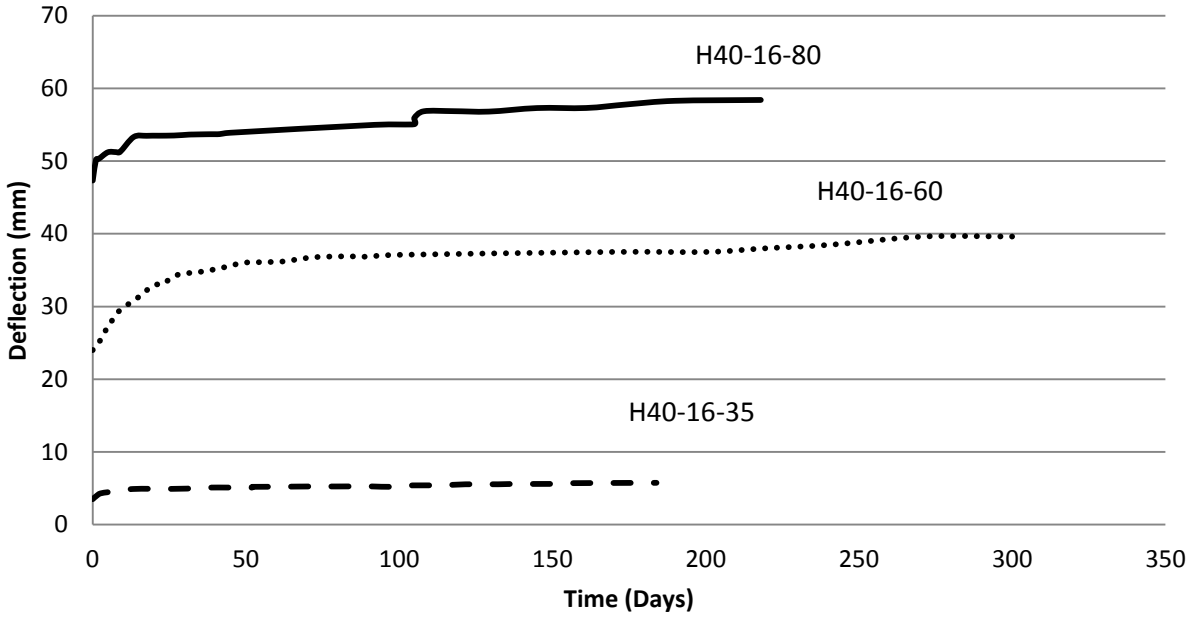

Figure 4.17: Time-dependent mid-span deflection for H40-16 beams

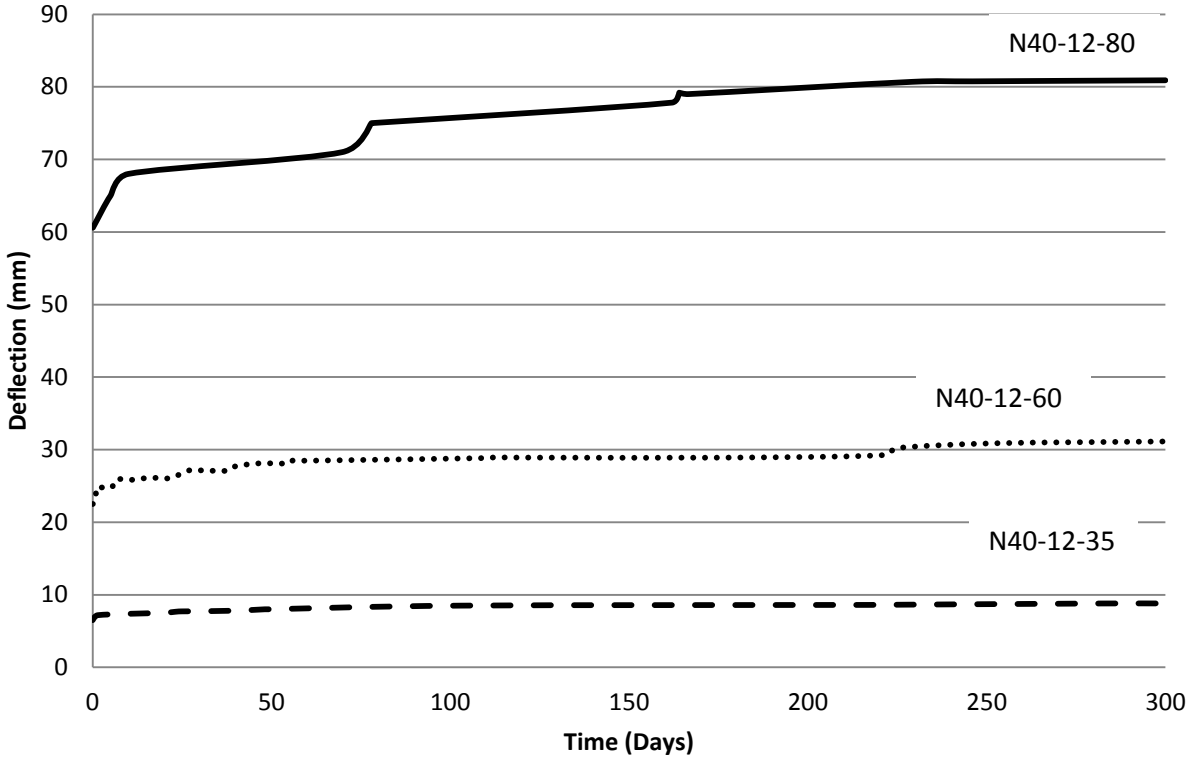

Figure 4.18: Time-dependent mid-span deflection for N40-12 beams

Table 4.4: Initial and final readings for deflection, concrete strains and GFRP strains for all sustained load beams

Beam	Days	Initial reading			Final reading		
		Deflection (mm)	Concrete strain (μs)	GFRP strain (μs)	Deflection (mm)	Concrete strain (μs)	GFRP strain (μs)
N0-16-35	300	29.0	-760	4860	45.8	-1792	5924
N0-16-60	300	54.5	-2380	10100	69.8	-3213	11373
N0-16-80	300	73.5	-2980	10922	91.7	-4356	12657
N25-16-35	300	5.6	-390	4810	9.3	-788	5260
N25-16-60	300	37.0	-2100	10770	53.6	-3387	N/A
N25-16-80	300	48.0	-2140	13000	66.2	-4640	N/A
H40-16-35	183	3.5	-312	7595	5.8	-690	8050
H40-16-60	300	24.0	-1280	12553	38.5	-2210	N/A
H40-16-80	230	47.5	-2550	13500	58.6	-3288	N/A
N40-12-35	300	4.7	-202	8000	8.8	-395	8210
N40-12-60	300	22.5	-1242	15950	31.2	-1945	16890
N40-12-80	300	60.0	-2096	17912	80.8	-2906	N/A
N40-16-35	300	4.5	-528	7775	9.1	-800	8036
N40-16-60	300	28.5	-1744	14161	36.7	-2315	14521
N40-16-80	300	51.8	-2221	16600	72.1	-3800	N/A

4.7.2 Effect of prestressing

Comparisons between the prestressed beams (25% and 40%) and the non-prestressed beams are made to examine the effect of prestressing on the long-term behaviour of the beams. The results showed that the prestressing had a noticeable effect on the long-term deflections, the concrete strains, and the GFRP strains, particularly at the lower sustained loading levels.

The total deflection for the prestressed beams was always less than that of the non-prestressed beams, and it decreased as the prestressing level increased. The ratio of the total deflection for the non-prestressed beam N0-16-35 to the total deflection of the prestressed beams N40-16-35 and N25-16-35 was 5.0 and 4.9, respectively. The ratios decreased to 1.9 and 1.3 at the 60% loading levels, and 1.3 and 1.4 at the 80% loading levels.

On the other hand, the ratio of the long-term deflection (the difference between the initial and the final deflections) for the non-prestressed to that of the 25% and 40% prestressed beams was 4.5 and 3.7 at the 35% loading level, and 0.9 and 1.9 at the 60% loading levels, respectively. The long-term deflections were almost the same at the 80% load level for all of the beams.

The decrease in the total deflection for the prestressed beams compared to the non-prestressed beams is mainly due to the increase in the cracking moment of the prestressed beams, while the decrease in the long-term deflection is attributed to the decrease in the concrete compressive stresses due to the prestressing forces.

At the 80% loading, the prestressing had no significant effect on the long-term deflection of the beams. This was attributed to the fact that severe internal micro-cracking takes place in the concrete at sustained stress levels that are more than 60% of the concrete stress (Neville et al. 1983). Once the cracking has accelerated, the creep of the concrete increases leading to increasing the deflection of the beam.

The concrete total strains of the 40% prestressed beams were always less than those of the non-prestressed beams. For the 25% prestressed beams, the total concrete strain values were less than half those of the non-prestressed beams at the 35% loading level, and they were almost the same

at the higher load levels. Figure 4.19 and Figure 4.20 show the change of concrete strain with time for the beams of groups N40-16 and N0-16, and N25-16 and N0-16, respectively.

The total GFRP bar strains of the prestressed beams were higher than or equal to those of the non-prestressed beams. However, the creep GFRP strains (increase in GFRP strains with time) were always less than those of the non- prestressed beams, and they decreased as the prestressing level increased. The increase in the GFRP strains is mainly derived by the increase in the beam curvature rather than the creep of the GFRP bars (Youssef, 2010), and since the increase in the curvature under sustained loading for the prestressed beams is less than that for the non-prestressed beams, the increase in the GFRP strains was less for the prestressed beams. The creep effect of the GFRP bar on the long-term behaviour of the beams will be discussed in more details in Chapter 5.

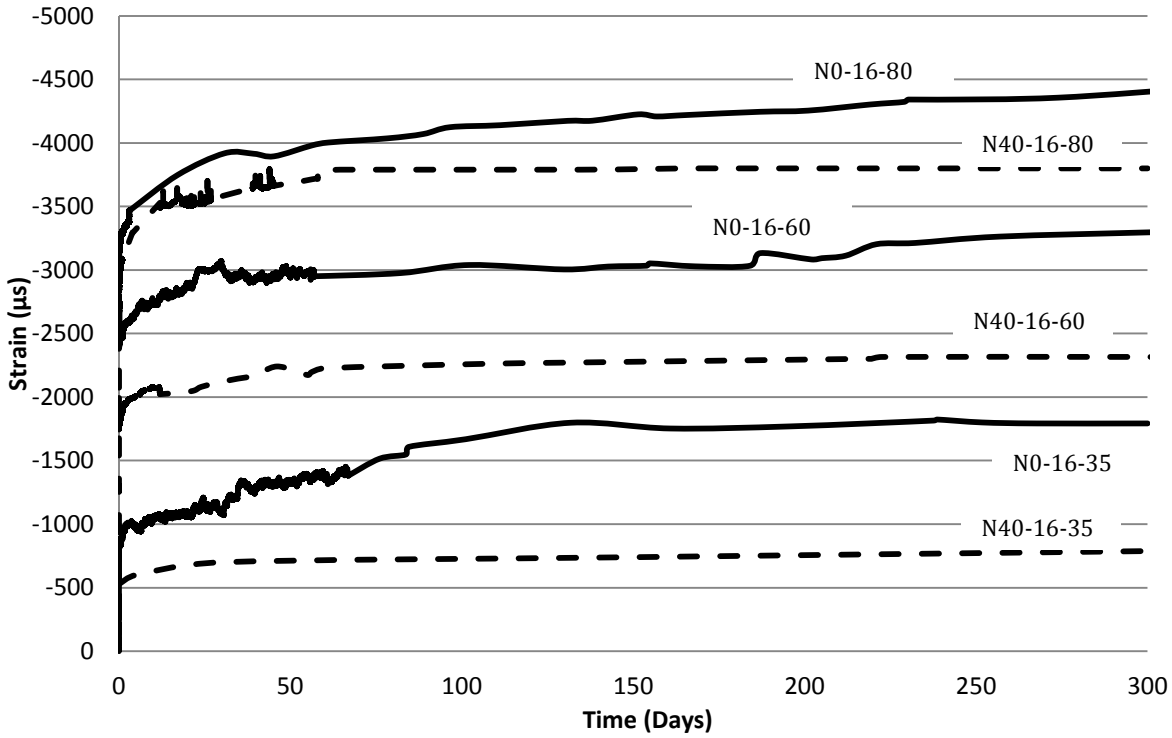

Figure 4.19: Concrete strain with time for the N0-16 and N40-16 beams

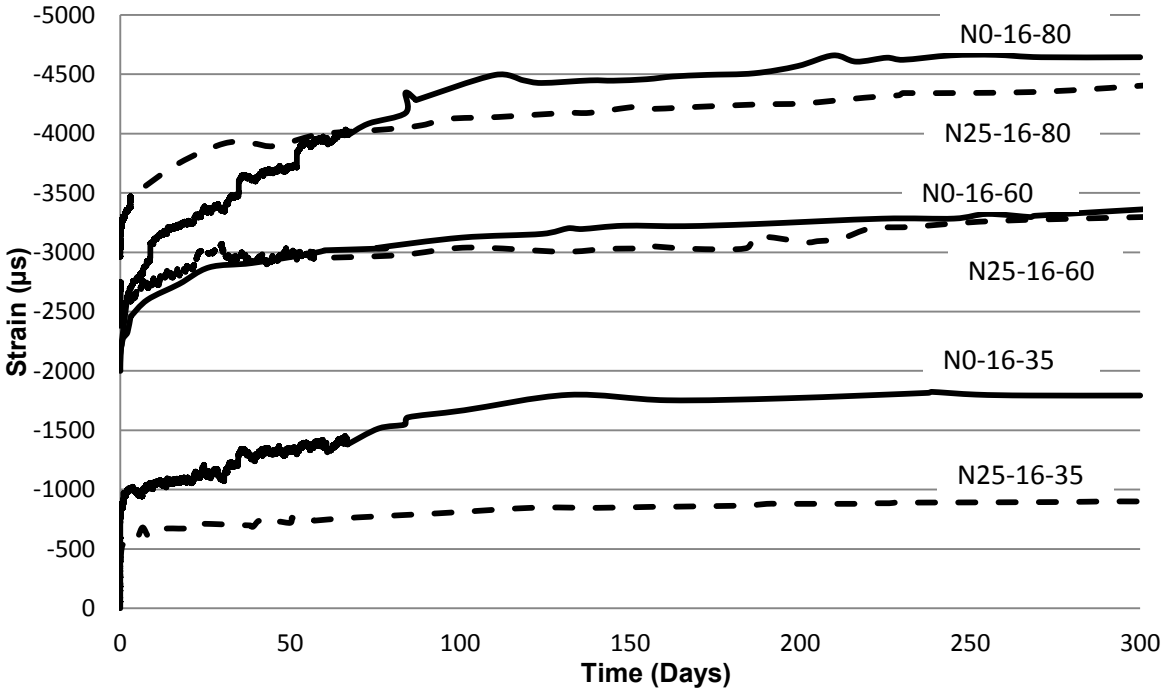

Figure 4.20: Concrete strain with time for the N0-16 and N25-16 beams

4.7.3 Effect of concrete strength

The effect of the concrete strength on the long-term behaviour of GFRP prestressed concrete beams can be seen by comparing the results of the beams in the N40-16 group and H40-16 group.

At the 35% and the 60% sustained load levels, there was no clear difference or correlation between the results of the beams from both groups. Therefore, there was no significant effect of the concrete strength on the long-term results.

Figure 4.21 shows the change of the concrete strain with time for the beams in H40-16 and N40-16 groups. The effect of the concrete strength is evident at the 80% load level, where the normal strength beam had higher values for the total deflection, the total concrete strain, the long-term deflection and the creep concrete strain when compared to the high strength beam. This can be explained as follows; the ratio between the applied stress and the concrete strength for the nor-

mal strength beam was about 80%, which led to the initiation of severe internal micro-cracking in the concrete that resulted in increased creep (Neville et al. 1983). The stress /strength ratio for the high strength beam on the other hand was about 50%. Therefore, the severe micro-cracking didn't take place, which resulted in less creep for the high strength beam.

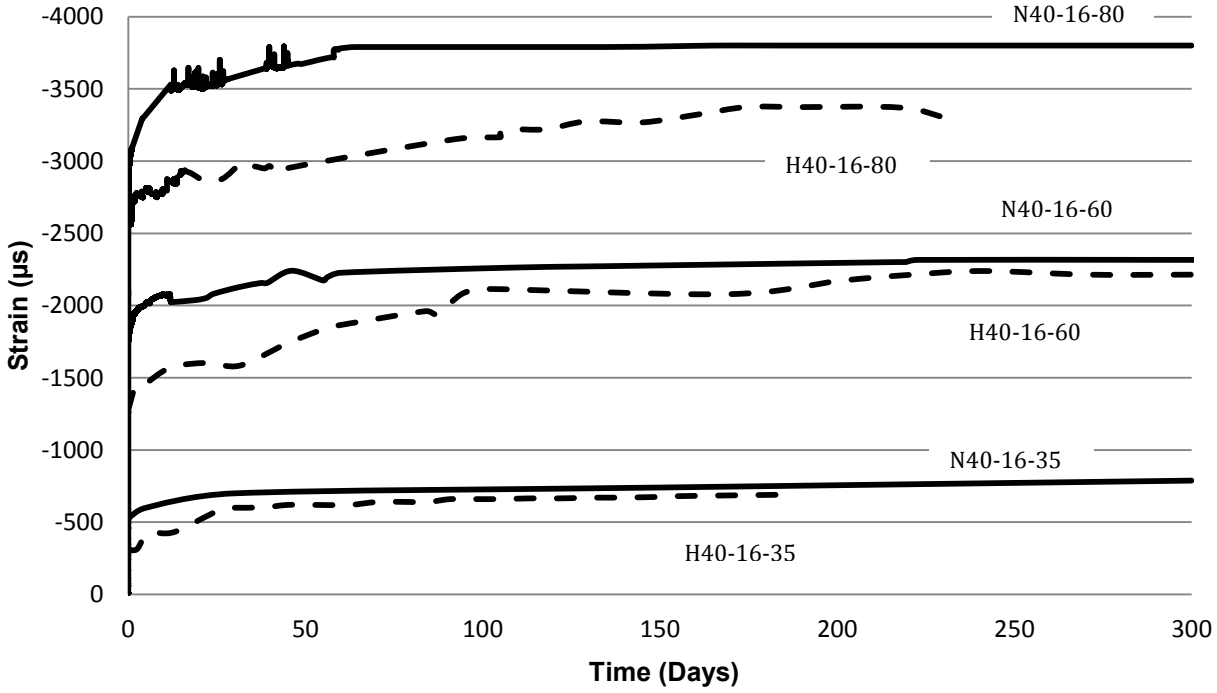

Figure 4.21:Concrete strain with time for the H40-16 and N40-16 beams

4.7.4 Effect of GFRP bar diameter

Comparing the results of the N40-16 beams and the N40-12 beams showed no direct relation between the long-term deflection behaviour of the beam and the prestressed GFRP bar diameter. The difference in the initial and the total deflection for the beams at the same sustained loading level in both groups is less than 10%. This is due to the fact that the beams were loaded to the same percentage of load, not the same absolute load. At the same value of the applied load, the N40-16 beams had a smaller deflection than the N40-12 beams due to the higher stiffness caused by the larger reinforcement area of the N40-16 beams.

Figure 4.22 and Figure 4.23 show the change in the GFRP strains and the concrete strains for the beams in both groups, respectively. It can be seen that the N40-12 beams had a higher GFRP initial and the total strains and lower concrete initial and the total strains than the N40-16 beams. This is due to the difference in the reinforcement ratio and mode of failure between the control beams in each group. The N40-12-0 failed by the rupture of the GFRP bar while the N40-16-0 failed by the crushing of the concrete prior to the rupture of the GFRP bar. Therefore, when the other beams in each group were loaded to a specific percentage of the ultimate load of their control beam, the concrete strain was higher in the compression-controlled group (N40-16) than that in the tension-controlled group (N40-12), while the GFRP strains were higher in the N40-12 group than that in the N40-16 group.

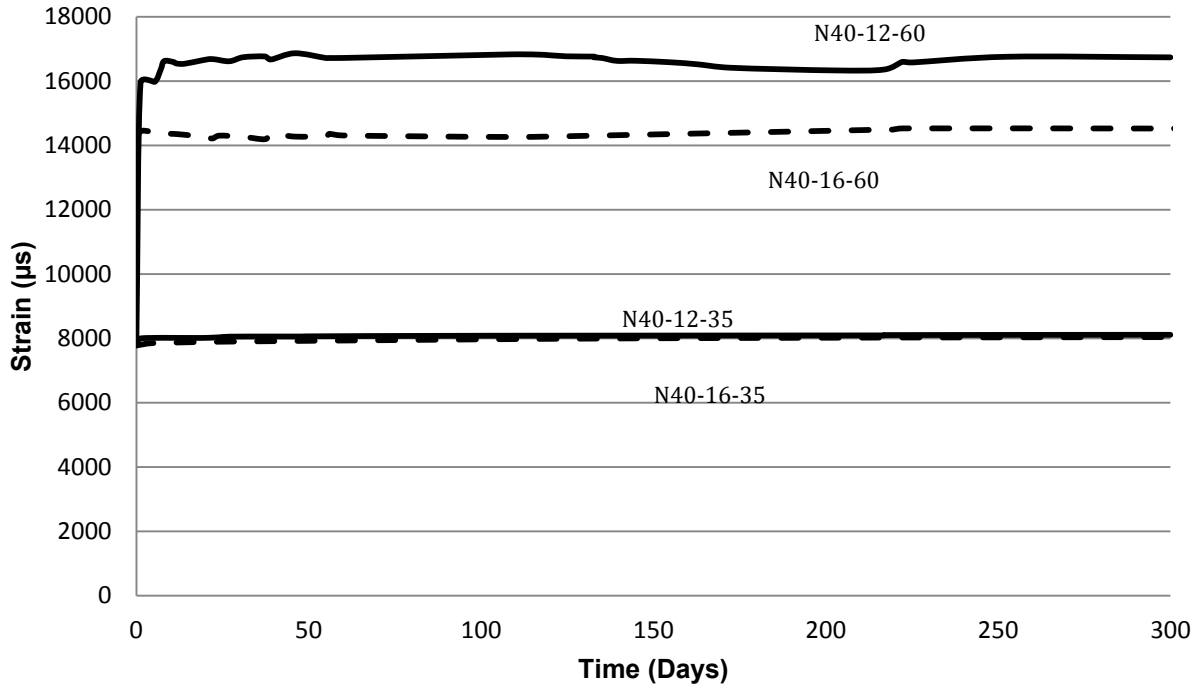

Figure 4.22: GFRP strain with time for the N40-16 and N40-12

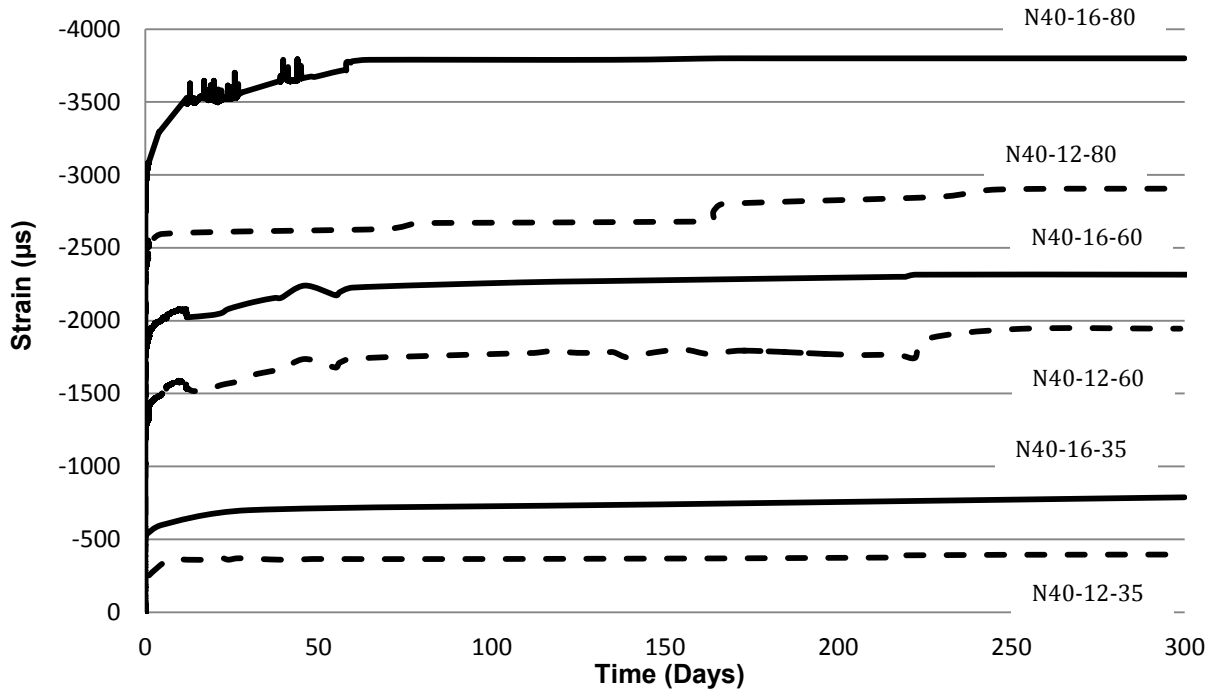

Figure 4.23: Concrete strain with time for the N40-16 and N40-12

4.8 Unloading behaviour

4.8.1 Concrete behaviour during unloading

The stress-strain response of concrete is non-linear. The non-linearity is primarily a function of the development and growth of micro-cracks around the coarse aggregate and in the mortar. When concrete is subjected to compression stresses, the total strain resulting from this loading is actually the summation of two components; an elastic strain component and a plastic strain component. When this load is removed, the elastic strain will be recovered but the plastic strain will act as a strain offset similar to the elastic offsets resulting from thermal expansion or other pre-strain effects (Vecchio, 1999). This would cause a shift in the tensile stress-strain curve from the point of zero strain to the point of the compressive plastic offset strain. Therefore, the concrete can change the sense of the stress from compression to tension only after recovering the elastic part of the strain and not the total strain as shown in Figure 4.24, where ε_{el} is the elastic strain and ε_{pl} is the plastic strain.

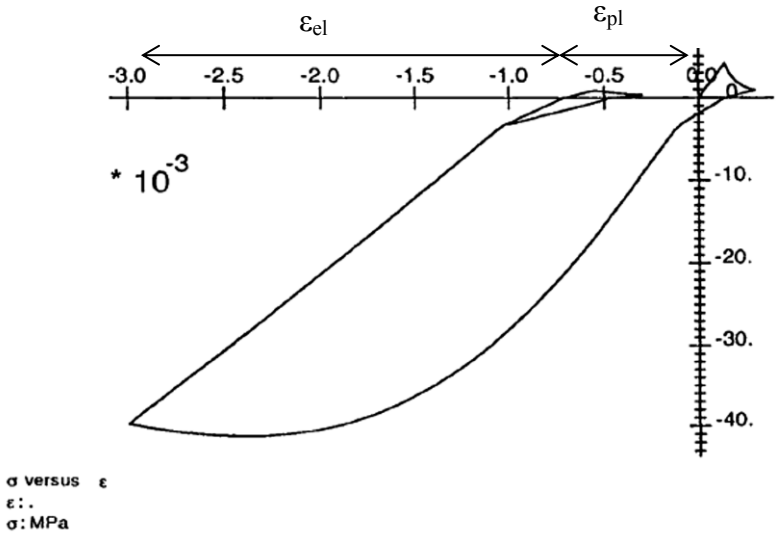

Figure 4.24: Simulated uniaxial behaviour of concrete under cyclic loading (La Borderie et al. 1992)

For the concrete that is being loaded in tension and then unloaded, the strain also can be divided into elastic and plastic components. The plastic strain represents the strain value at which the two surfaces of the cracked concrete come together. Similar to the compression loading case, the compressive stresses do not remain at zero until the cracks completely close. But in fact, the compressive stresses occur in the tensile strain region and begin at the tensile plastic strain (re-contact strain). The stiffness of the concrete during closing of cracks, after the two cracked surfaces have come into contact and before the cracks completely close, is smaller than that of crack-free concrete. Once the cracks completely close, the stiffness increases to the same value as the initial stiffness value. The literature has shown that the cracks close when the compression stress on the concrete is about 1/10 of the concrete compressive strength (Sima et al. 2008). The crack closing model proposed by Palermo and Vecchio (2003) is shown in Figure 4.25, where ε_{lc} is the unloading strain in tension, and ε_c^p is the plastic strain in tension.

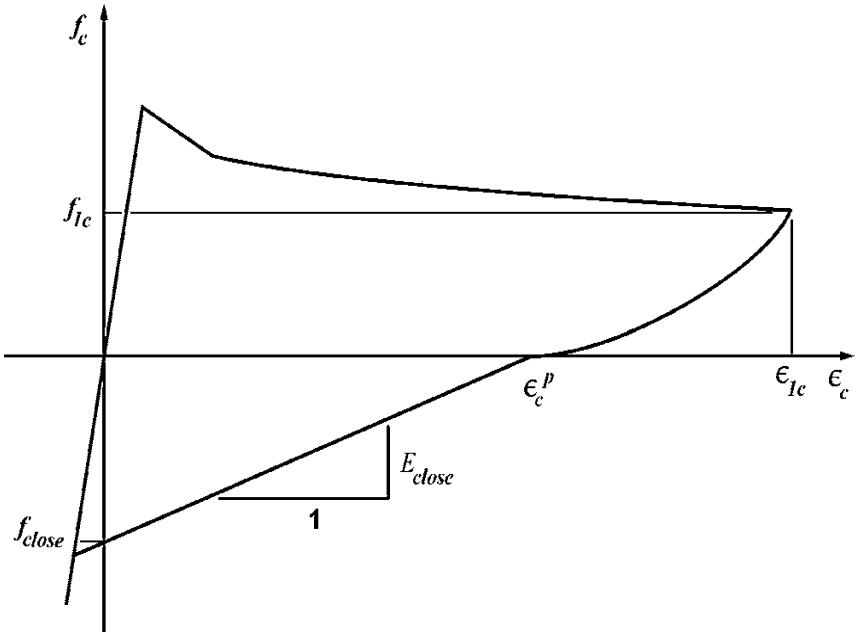

Figure 4.25: Crack closing model (Palermo and Vecchio 2003)

4.8.2 Beam behaviour during unloading

After being subjected to sustained loading for 300 days, the load was removed gradually while the deflections and the strains were being recorded for the beams. The behaviour of the beams was different depending on whether they were prestressed or non-prestressed.

Figure 4.26, Figure 4.27, and Figure 4.28 show the load-deflection behaviour of the beams N40-16-80, N25-16-60, and H40-16-80, respectively. It can be seen from the figures that the behaviour of the beams is bilinear.

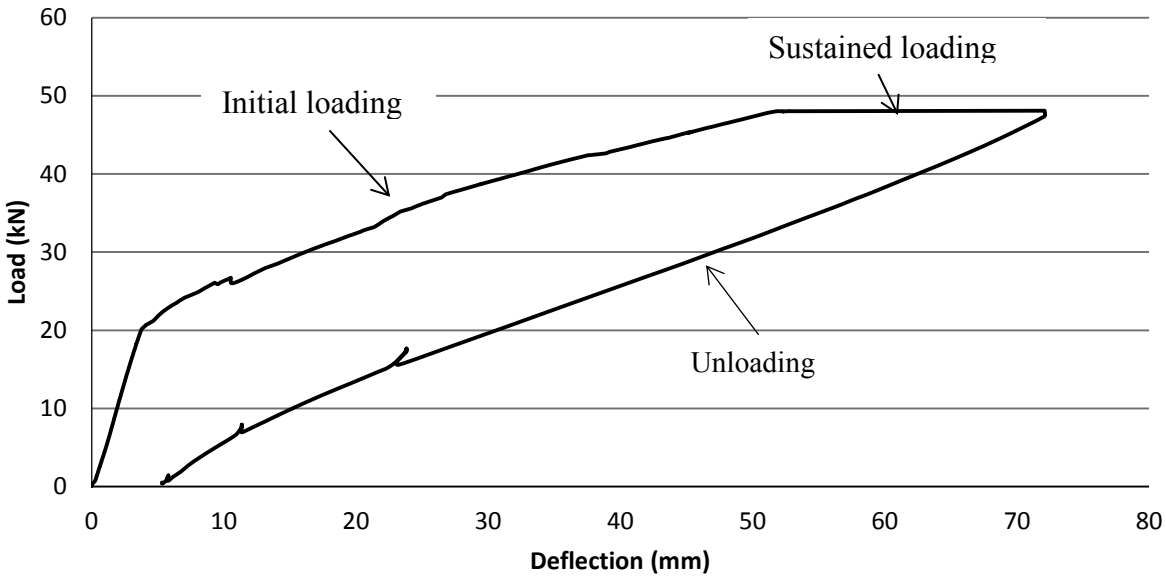

Figure 4.26: Load deflection behaviour of beam N40-16-80 under initial loading, sustained loading, and unloading

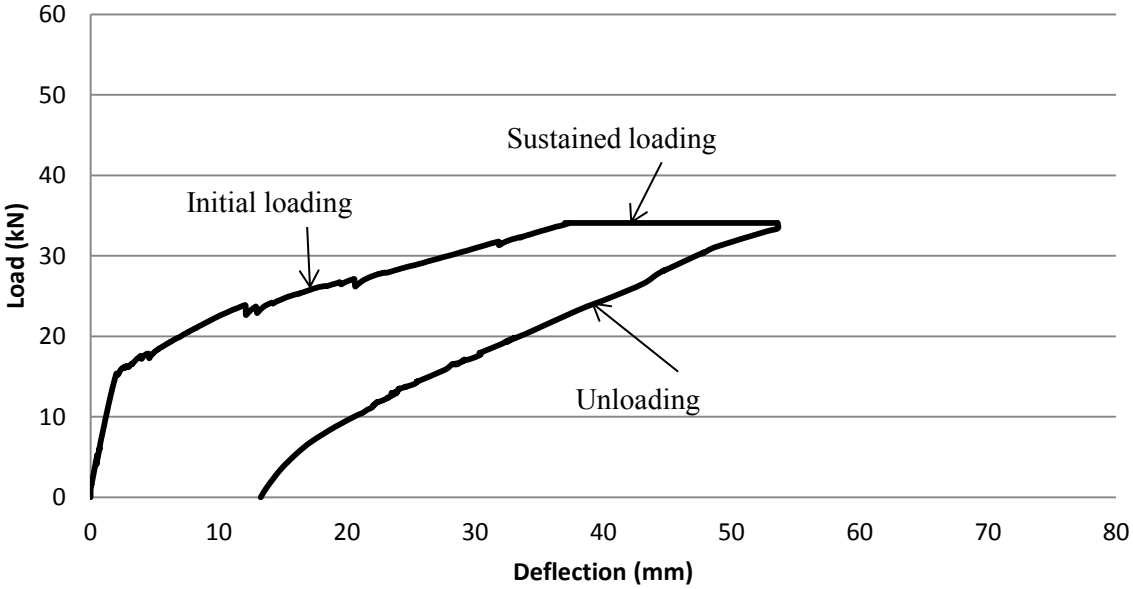

Figure 4.27: Load deflection behaviour of beam N25-16-60 under initial loading, sustained loading, and unloading

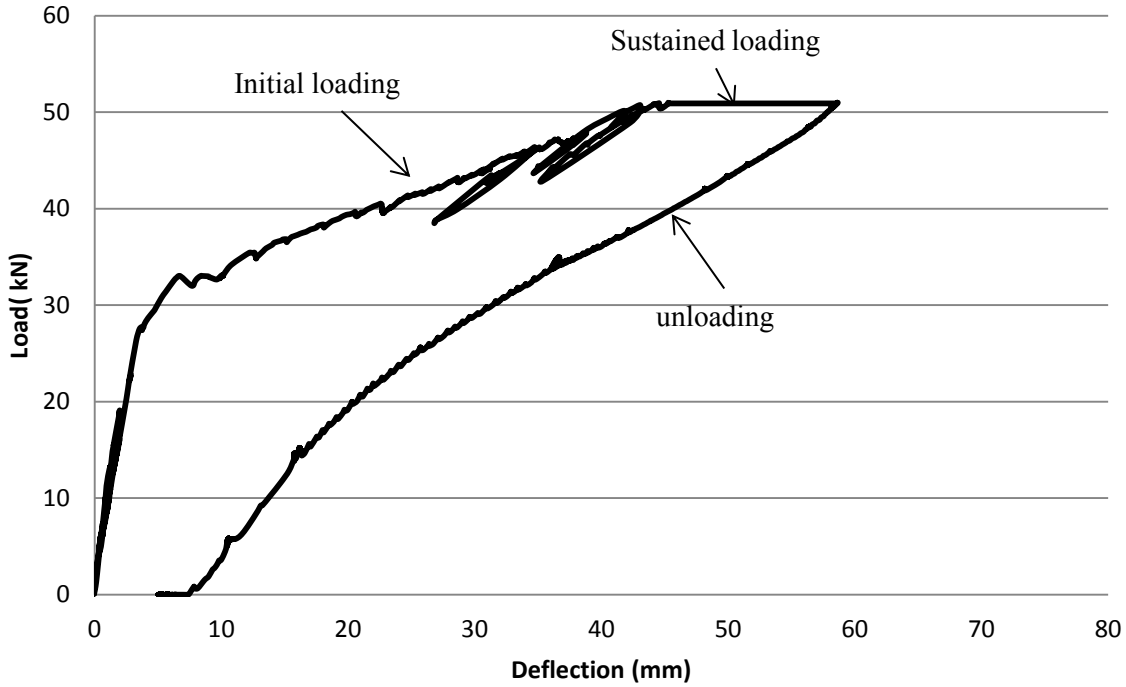

Figure 4.28: Load deflection behaviour of beam H40-16-80 under initial loading, sustained loading, and unloading

When the unloading started, the beams had stiffness almost the same as the cracked section stiffness until the load reached a value of about 10 kN, 8 kN , and 18 kN for beams N40-16-80, N25-16-60, and H40-16-80, respectively. When the load decreased below these values, the stiffness of the beams increased. This can be explained as follows: the effect of the prestressing force that tends to apply compression on the bottom side of the section overcame the applied loads tensile effects. This caused the cracks in the tension zone to partially close which gave the beams a stiffness that was between the gross section stiffness and the cracked section stiffness. This partial crack closure was captured experimentally for the H40-16-80 beam. The crack widths at the bottom of the mid-span section and at 75 mm from the bottom were found to decrease from 2.3 mm and 1.8 mm, to 0.3 mm and 0.1 mm, respectively.

The effect of the prestressing force did not exist in the case of unloading the non-prestressed beams. Therefore, the beams had a linear behaviour during the whole unloading process as shown in Figure 4.29.

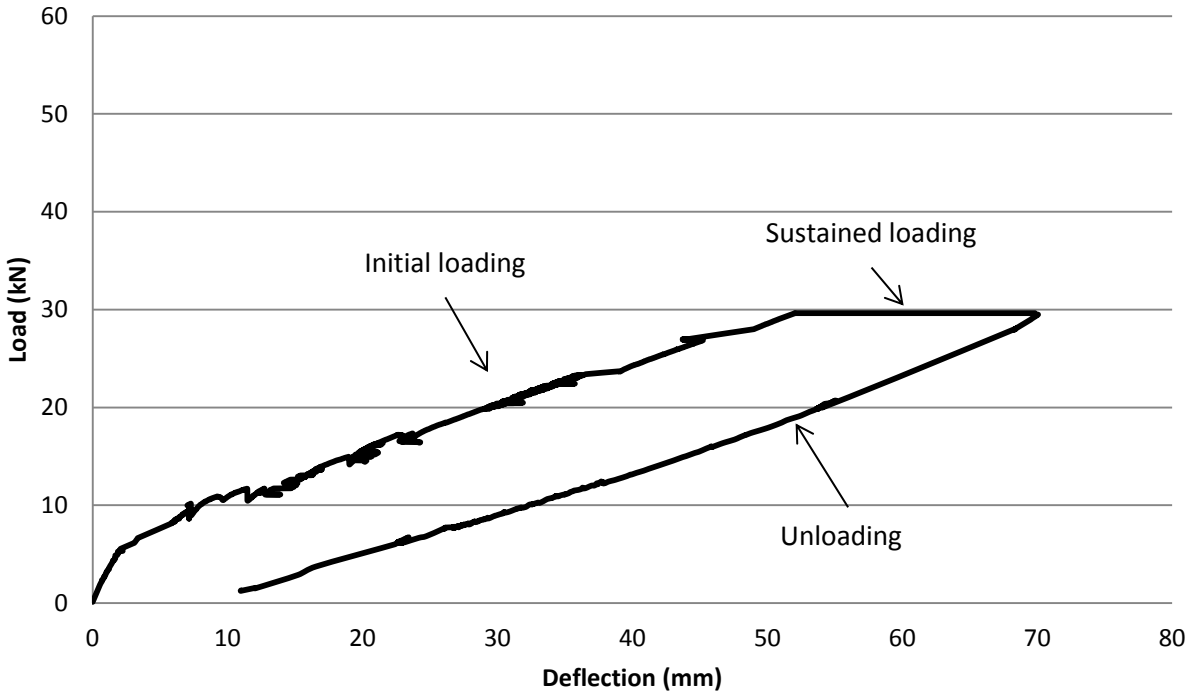

Figure 4.29: Load deflection behaviour of beam N0-16-60 under initial loading, sustained loading, and unloading

As the applied load was decreased, the stresses on the top fibres of the concrete section changed from compression to tension stresses for both the prestressed and the non-prestressed beams resulting in crack formation on the top surface of the beams as shown in Figure 4.30.

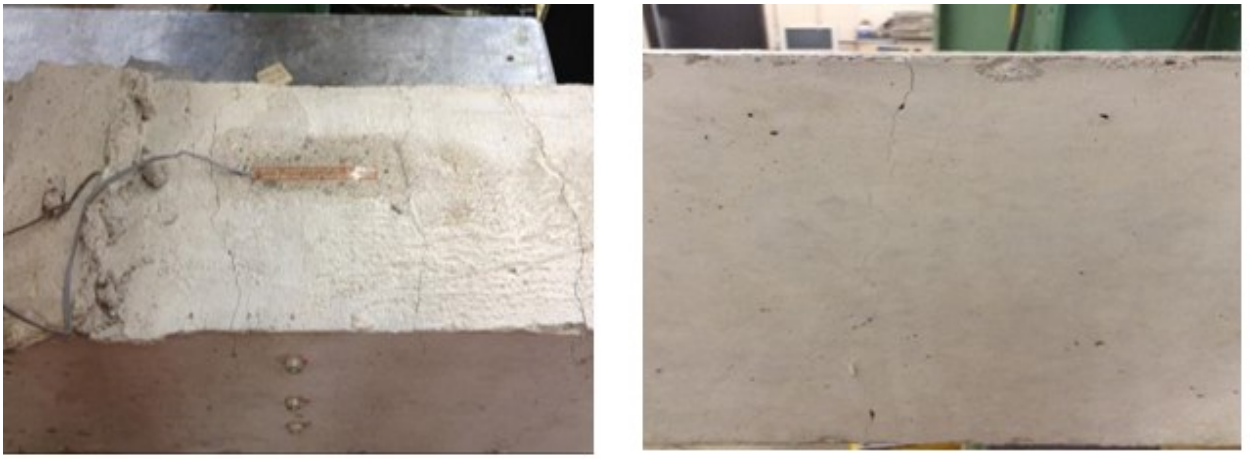

Figure 4.30: Cracks on the top fibre of the concrete sections during unloading.

The formation of the top fibre cracks can also be observed from the top concrete strain vs. load curve, as shown in Figure 4.31 to Figure 4.34 for beams N40-16-80, N25-16-60, H40-16-80, and N0-16-60, respectively. When the cracks started to form, the concrete strains measurements became inaccurate because the strain gauges were either located between two cracks as in the case of beam N40-16-80 where the change in the strain readings become very small, or a crack was initiated underneath the gauge as in the case of beams N25-16-60 and H40-16-80 where the gauges reads large values for the tension strains.

The formation of the cracks can be explained as follows: when the load was removed, the deflected beam tried to deform back to its original position, and as discussed in Section 4.8.1, the concrete will be under tension stresses only after recovering the elastic portion of the strain. Therefore, the concrete at the top of the beam will crack if the stresses exceed the cracking stress as shown before in Figure 4.24. That behaviour is independent of the prestressing level and the concrete strength.

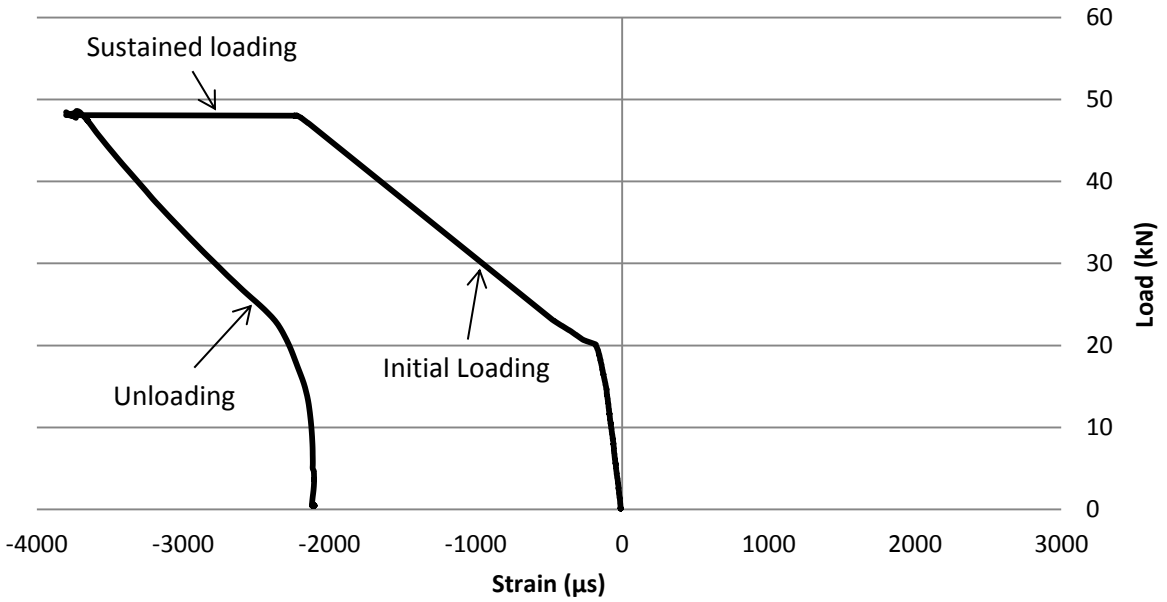

Figure 4.31: Concrete top strains due to initial loading, sustained loading, and unloading for beam N40-16-80

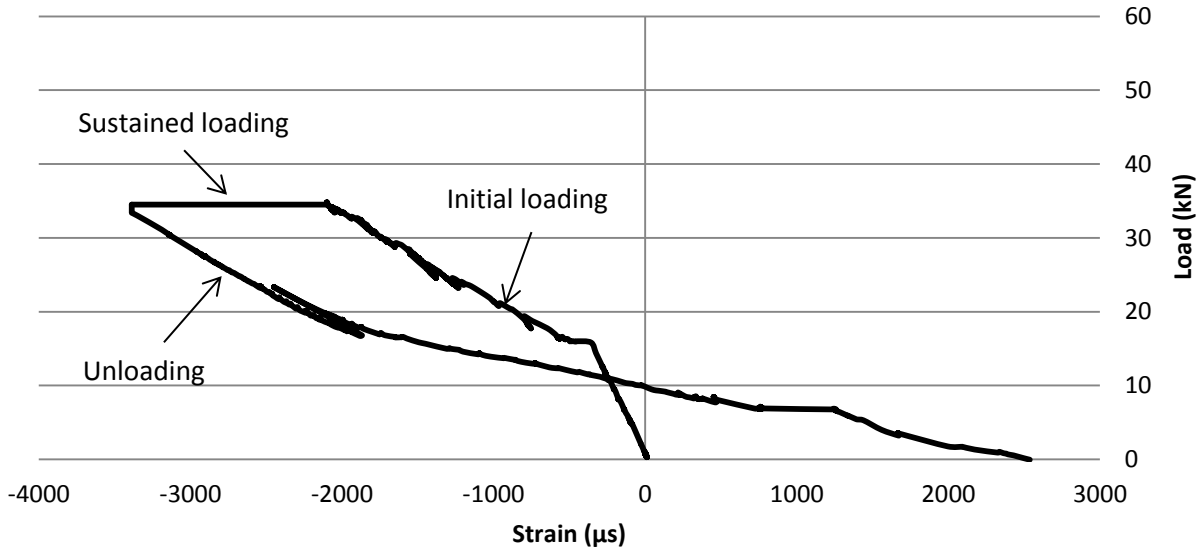

Figure 4.32: Concrete top strains due to initial loading, sustained loading, and unloading for beam N25-16-60

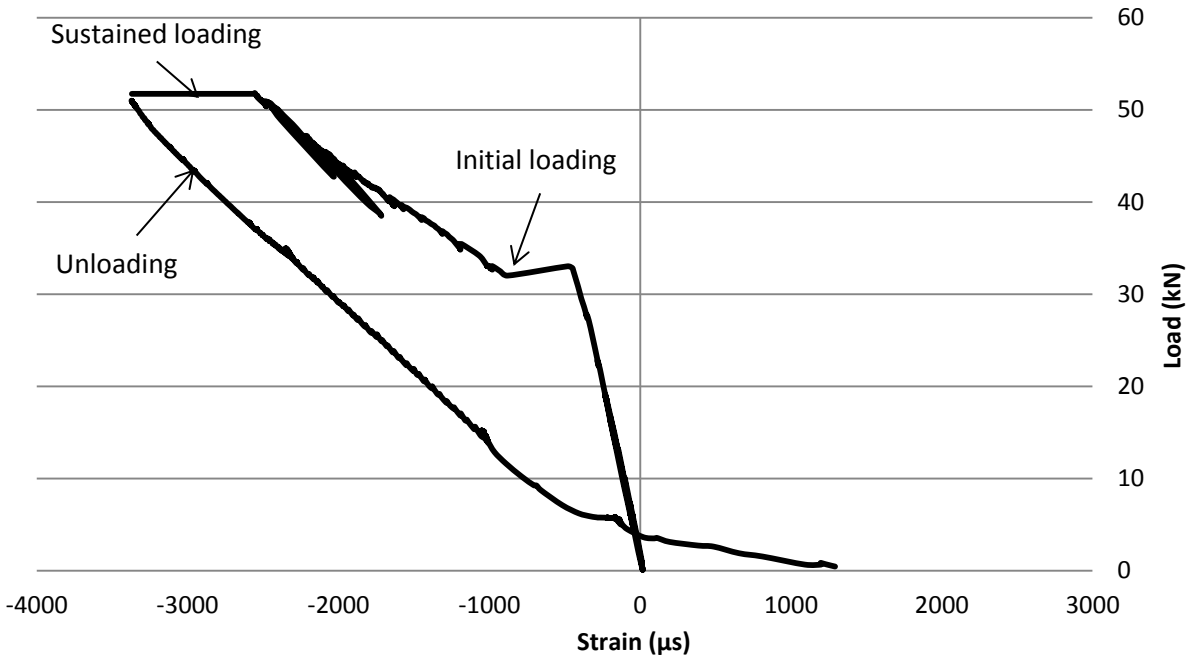

Figure 4.33: Concrete top strains due to initial loading, sustained loading, and unloading for beam H40-16-80

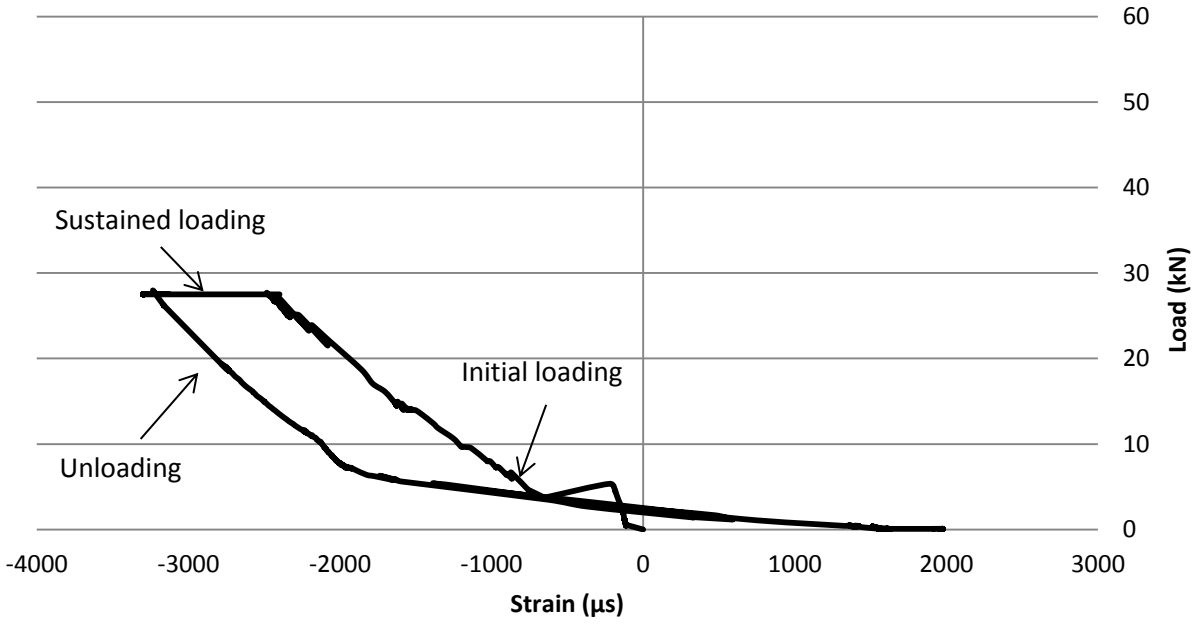

Figure 4.34: Concrete top strains due to initial loading, sustained loading, and unloading for beam N0-16-60

4.9 Static residual strength test (reloading behaviour)

After the sustained loading test, all the beams were unloaded followed by reloading to failure in a four-point bending test to investigate their residual strength. Figure 4.35 to Figure 4.39 show the load-deflection behaviour for the reloaded beams.

Within each of the prestressed beams groups, the beam that was under the 35% sustained load was not cracked, and its load-deflection behaviour was similar to the control beam that was tested directly in the static loading test. Both beams had essentially the same gross section stiffness before the cracking load and the same cracked section stiffness after the cracking load. The two other beams that were subjected to the 60% and the 80% sustained load were cracked and they both had bilinear load-deflection responses during unloading. This can be explained as follows: when the sustained load was removed from the beam, the prestressing force caused the cracks in the tension zone to partially close which gave the beam a stiffness that was between the gross and cracked section stiffness. During reloading, when the load exceeded the decompression load, the stiffness of the beams decreased. As for the beams in the N0-16 group, they all had the same linear behaviour up to failure as they were all cracked in the sustained loading test. The stiffness of all the beams was essentially the fully cracked section stiffness.

It can be noticed that the stiffness of the beams that were cracked under the sustained loads had a slightly higher stiffness than their control beams. This increase in the stiffness is mainly due to "*a form of solid body compaction produced by the creep of the concrete and the autogenous healing of the internal cracks*" caused by the sustained loading (Cook and Chindaprasirt, 1980). The ratio of the stiffness increase was found by Cook and Chindaprasirt (1980) to range between 3.8% and 10.5% for concrete cylinders subjected to sustained loading for 30 days. The sustained loads ranged between 0.3 and 0.6 of the ultimate load capacity of the cylinders.

The residual strength test results show that there was no reduction in the ultimate strength of any of the beams due to the sustained loading. The failure of the all the beams including the control one occurred when the GFRP bar in the tension zone ruptured. This provides additional support for the conclusion that the creep of the GFRP bars was minimal and that the overall creep of the beams was primarily due to the creep of the concrete rather than the creep of the GFRP bars.

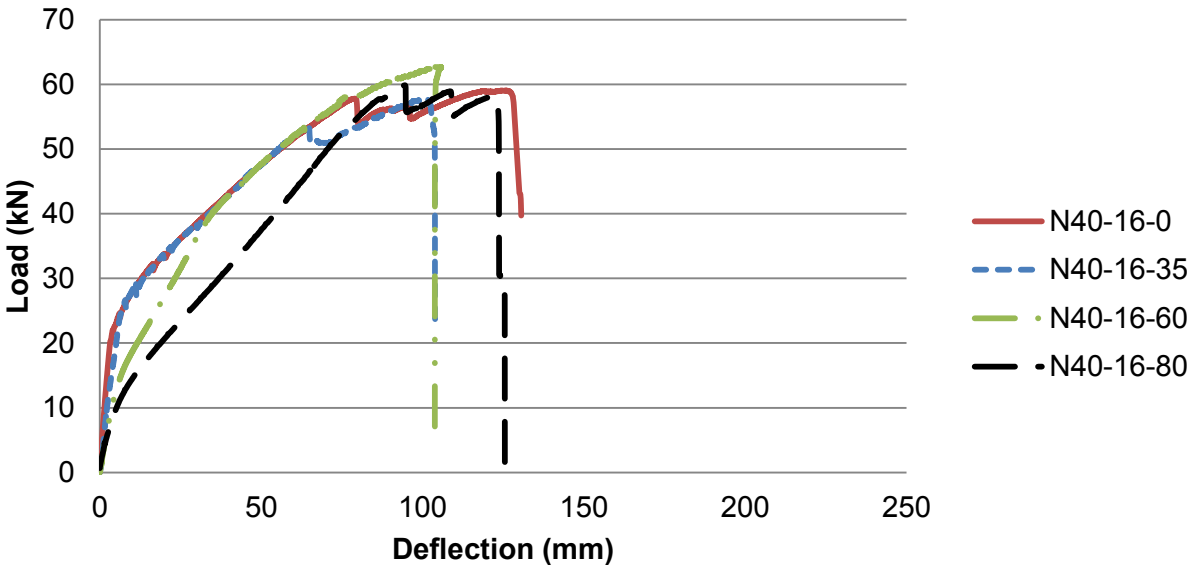

Figure 4.35: Load-deflection curves for N40-16 beams-reloading after sustained load test

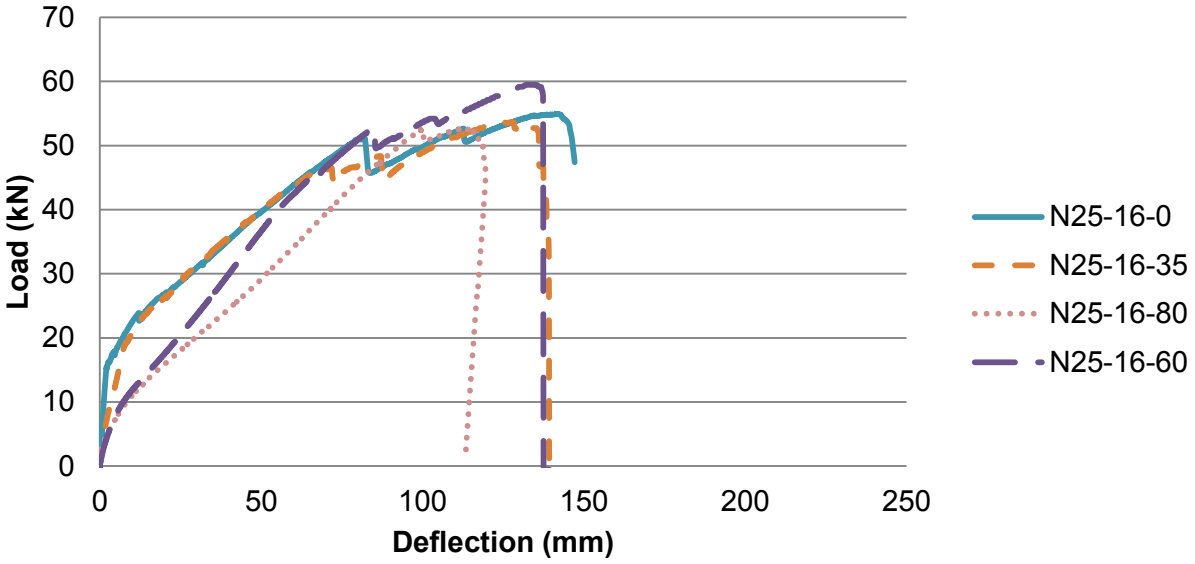

Figure 4.36: Load-deflection curves for N25-16 beams-reloading after sustained load test

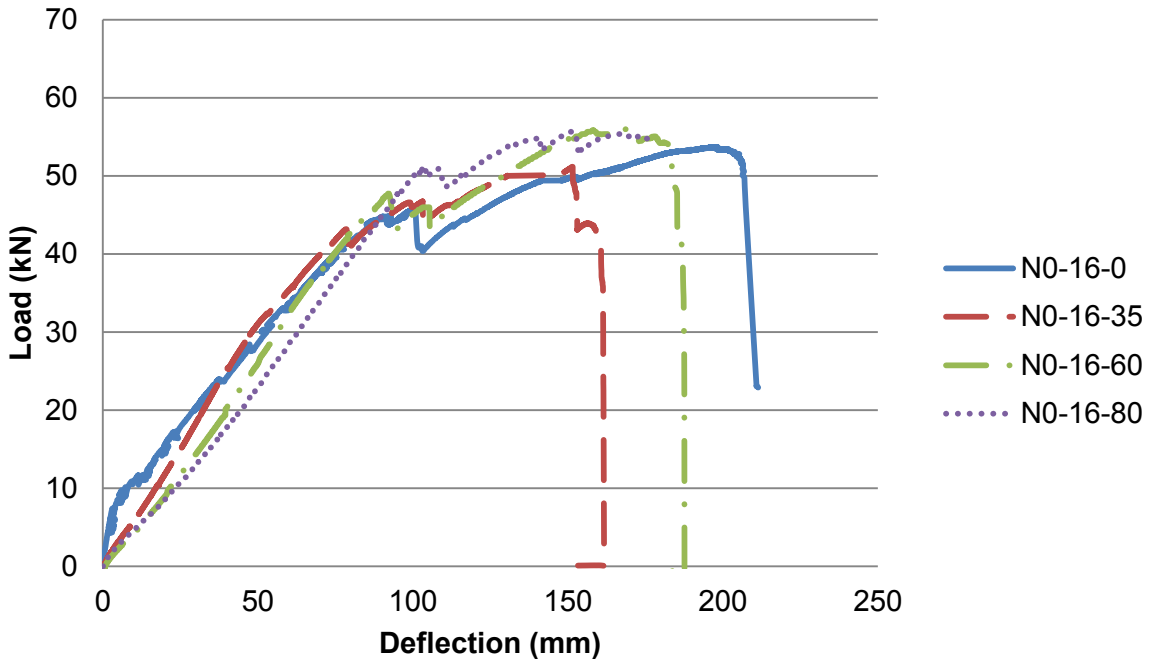

Figure 4.37: Load-deflection curves for N0-16 beams-reloading after sustained load test

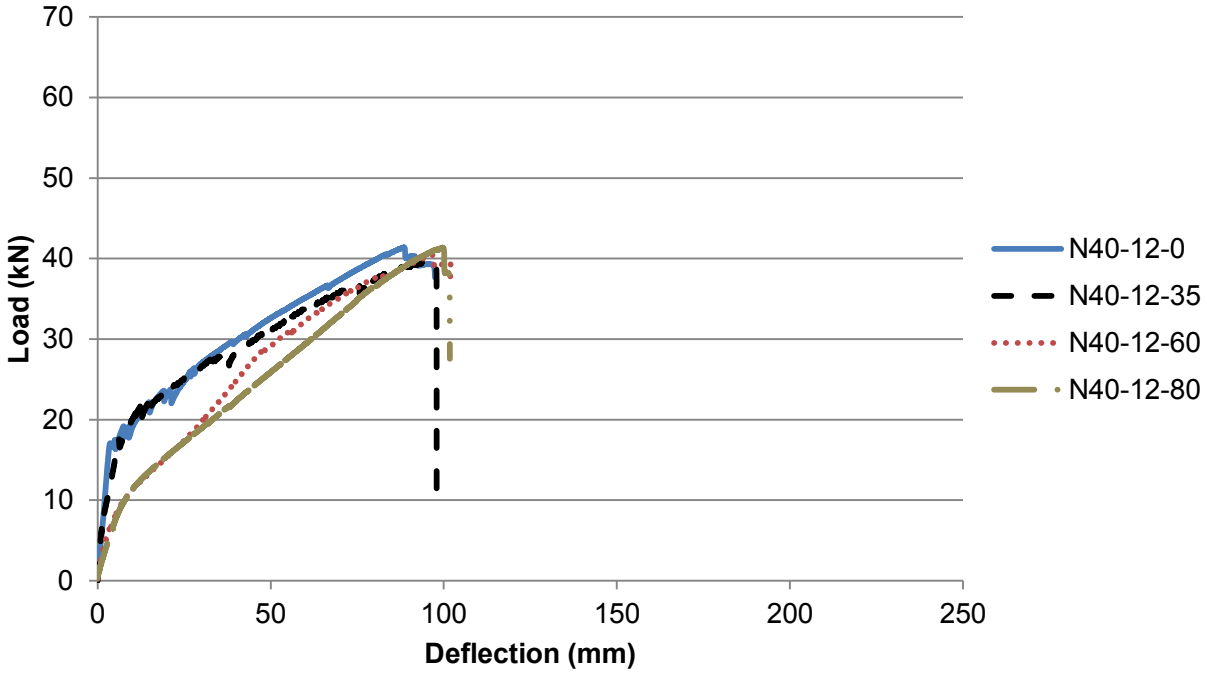

Figure 4.38: Load-deflection curves for N40-12 beams-reloading after sustained load test

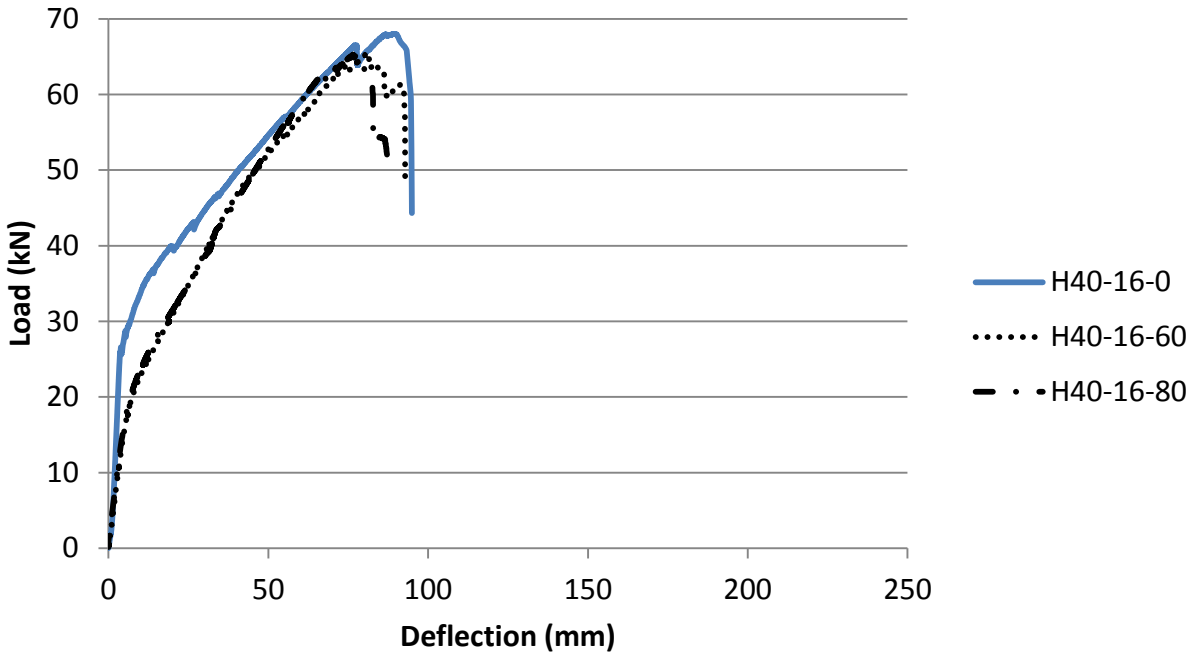

Figure 4.39: Load-deflection curves for H40-16 beams-reloading after sustained load test

Chapter 5
Analytical Models

5.1 General

This chapter presents the analytical approaches that were used to predict the short-term behaviour, long-term behaviour, unloading behaviour and the static residual strength behaviour of GFRP prestressed beams. In addition, the measured transfer length values were used to improve the transfer length estimates provided by the ACI 440.4 R-04 equation by calibrating the material coefficient factor (α_t) used in the ACI equation.

5.2 Model for short-term flexural behaviour

5.2.1 General

The flexural behaviour of reinforced/prestressed concrete members is well understood. Typical sectional analysis based on force equilibrium and strain compatibility gives reasonably accurate predictions for the flexural capacity of concrete beams reinforced or prestressed with GFRP reinforcement. Concrete in compression can be modeled using the equivalent stress block approach or the layer-by-layer strain compatibility analysis.

For the equivalent-stress-block approach, the non-linear concrete stress-strain curve is transformed to an equivalent stress block using α_1 and β_1 factors given by codes. In the layer-by-layer strain compatibility analysis, the cross-section is divided into horizontal layers where the strains in each layer are calculated using strain compatibility and the stresses are calculated using material stress-strain relationships (Kaklauskas, 2004). The moment resistance is calculated by taking the summation of the moments of the forces at each layer about the neutral axis. Schematics of the equivalent stress block approach and the layered approach are shown in Figure 5.1 and Figure 5.2, respectively.

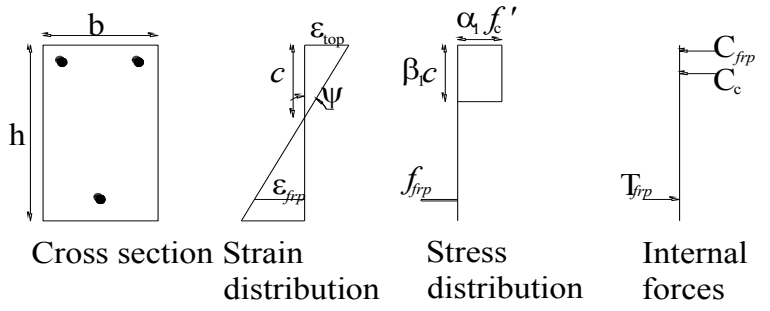

Figure 5.1: Schematic of the equivalent stress block approach

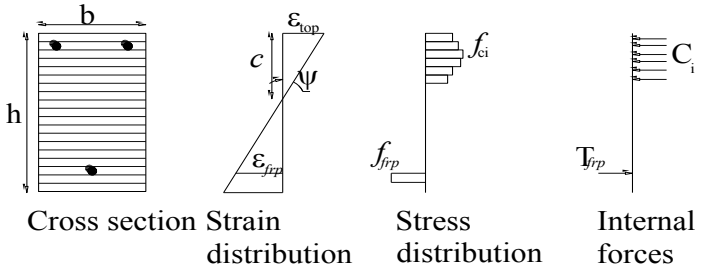

Figure 5.2: Schematic of the layered approach

5.2.2 Cracking

The behaviour of GFRP reinforced or prestressed beams is similar; linear up to the cracking moment, and then approximately linear with a reduced stiffness up to failure. Therefore, calculating the cracking moment and the cracked moment of inertia is important to model the behaviour of such beams.

The cracking moment of reinforced concrete sections is given by Equation 5.1, with the modulus of rupture given by Equation 5.2. For prestressed members, the cracking moment is given by Equation 5.3.

$$M_{cr} = \frac{f_r \times I_t}{y_t} \qquad \text{Equation 5.1}$$

$$f_r = 0.6 \times \sqrt{f_c'} \qquad \text{Equation 5.2}$$

$$M_{cr} = \frac{f_r \times I_g}{y_t} + \frac{P \times I_g}{A \times y_t} + P \times e \qquad \text{Equation 5.3}$$

where M_{cr} is the cracking moment, f_r is the modulus of rupture of the concrete, I_t is the transformed moment of inertia of the section, y_t is the depth to the centroid of the section, P is the effective prestressing force, A is the area of the concrete section, e is the eccentricity of the prestressing tendons with respect to the centroid of the section, f_c' is the concrete compressive strength.

The determination of the cracked moment of inertia for prestressed concrete sections is not as simple as for reinforced sections. The main reason is that unlike the case of reinforced concrete sections, the neutral axis for prestressed concrete sections does not coincide with the centroid of the cracked transformed section. Figure 5.3 shows a schematic for a typical stress diagram of a cracked prestressed concrete section under service loads ignoring the concrete in tension.

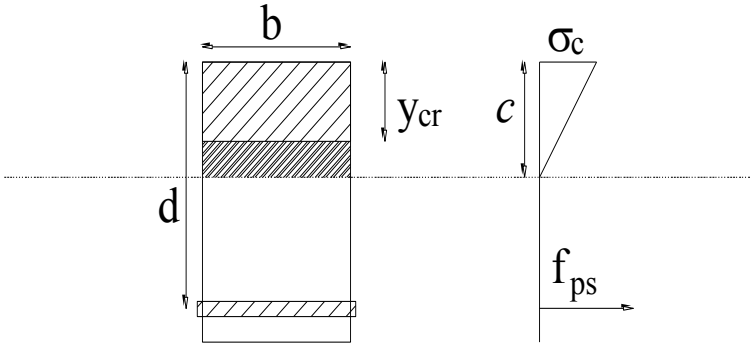

Figure 5.3: Schematic of typical stress diagram for a cracked prestressed concrete section

Therefore, the cracked moment of inertia for prestressed sections should be calculated with respect to the cracked centroid of the section which is at a distance y_{cr} from the extreme compression fibre of the concrete, as given in Equation 5.4 and Equation 5.5.

$$y_{cr} = \frac{\frac{b \times c^2}{2} + A'_s \times (n-1) \times d'^2 + A_s \times n \times d^2}{A_t} \qquad \text{Equation 5.4}$$

$$I_{cr} = \frac{b \times y_{cr}^3}{3} + \frac{b \times (\mathrm{c} - y_{cr})^3}{3} + A'_s \times (n-1) \times (d' - y_{cr})^2 + A_s \times n \times (d - y_{cr})^2 \quad \text{Equation 5.5}$$

where I_{cr} is the moment of inertia of the cracked transformed section, y_{cr} is the centroid of the cracked transformed section, b is the section width, c is the depth of the neutral axis, A'_s is the compression reinforcement, d' is the depth of the compression reinforcement, A_s is the tension reinforcement, d is the depth of the tension reinforcement, and n is the modular ratio.

The value of the prestressed cracked section moment of inertia should be between the gross moment of inertia and the cracked moment of inertia for the same section without prestressing (Naaman, 2004). The value of the cracked moment of inertia is almost constant due to the fact that, in a prestressed concrete section, the neutral axis remains essentially constant after cracking, while the concrete stress-strain response is approximately linear.

5.2.3 Load-deflection response

Modeling the load-deflection response of FRP reinforced/prestressed concrete beams is commonly done using one of two approaches: effective moment of inertia approach, and the curvature approach. In the effective moment of inertia approach, a uniform moment of inertia for the total length of the beam is calculated and is used instead of the gross moment of inertia to calculate the deflection. Several models exist to calculate the effective moment of inertia of a section. The CAN/CSA S6-06 uses Branson (1977) model to calculate the effective moment of inertia as shown in Equation 5.6:

$$I_e = I_{cr} + \left[(I_g - I_{cr}) \left(\frac{M_{cr}}{M_a} \right)^{\mathrm{m}} \right] \leq I_g \quad \text{Equation 5.6}$$

where M_{cr} is the cracking moment of the member, M_a is the maximum moment at the load stage at which deflection is being calculated, I_g is the moment of inertia of gross concrete section about the centroid axis, I_{cr} is the moment of inertia of the cracked transformed section, and m is an empirical factor that equals 3. The same equation was used by Abdelrahman (1995) to calculate the effective moment of inertia for CFRP prestressed concrete beams and used a value for m of 2.5.

The layer-by-layer strain compatibility analysis can also be used to calculate the effective moment of inertia using a reduced cross-section depth based on the depth of the neutral axis c. This moment of inertia can be computed from the moment–curvature relationship given in Equation 5.7. The curvature of the section is calculated from Equation 5.8.

$$I_e = \frac{M}{E_c \Psi} \leq I_g \qquad \text{Equation 5.7}$$

$$\Psi = \frac{\varepsilon_{top}}{c} \qquad \text{Equation 5.8}$$

where M is the external applied moment, Ψ is the section curvature, ε_{top} is the top fibre strain, and E_c is the modulus of elasticity of concrete.

In the curvature approach, the deflection is calculated by the integration of curvature along the beam length. The moment-curvature relationship is assumed to be tri-linear as shown in Figure 5.4 (CAN/CSA S806-12). For each load increment, the curvature at different sections along the entire length of the beam is determined using Equation 5.8, establishing a beam curvature diagram for a given load level.

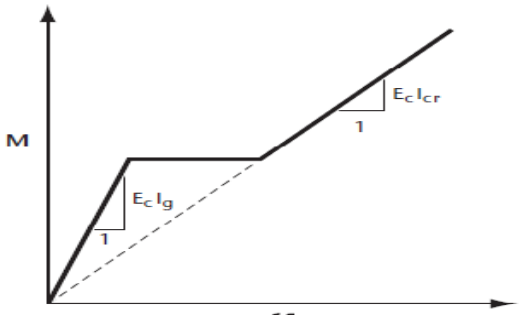

Figure 5.4: Moment-curvature (M-Ψ) relation for FRP reinforced concrete (CAN/CSA S806-12)

The deflection at mid-span is obtained by integrating the beam curvature diagram twice as shown in Equation 5.9. The integration can be done using the numerical form shown in Equation 5.10 (Zou 2007).

$$\Delta_{mid-span} = \iint \Psi_{(t)} dx\, dx \qquad \text{Equation 5.9}$$

$$\Delta_{mid-span} = \sum \frac{\Psi_j x_j + \Psi_{j+1} x_{j+1}}{2} \left(x_{j+1} - x_j\right) \qquad \text{Equation 5.10}$$

where j is the number of a given section along the beam length and x_{j+1} is the distance between the support and the section j.

The analytical results of four methods were compared with the load-deflection behaviour of the GFRP prestressed beams tested in this study to determine the best approach: 1) the effective moment of inertia obtained from the layer-by-layer strain compatibility approach, 2) the effective moment of inertia obtained using the CAN/CSA S6-06 equation (m=3) 3) the effective moment of inertia obtained using Abdelrahman (1995) equation (m=2.5), and 4) the integration of curvature approach. The results showed that the effective moment of inertia obtained from the layer-by-layer strain compatibility approach gives better agreement with the experimental results as shown in Figure 5.5.

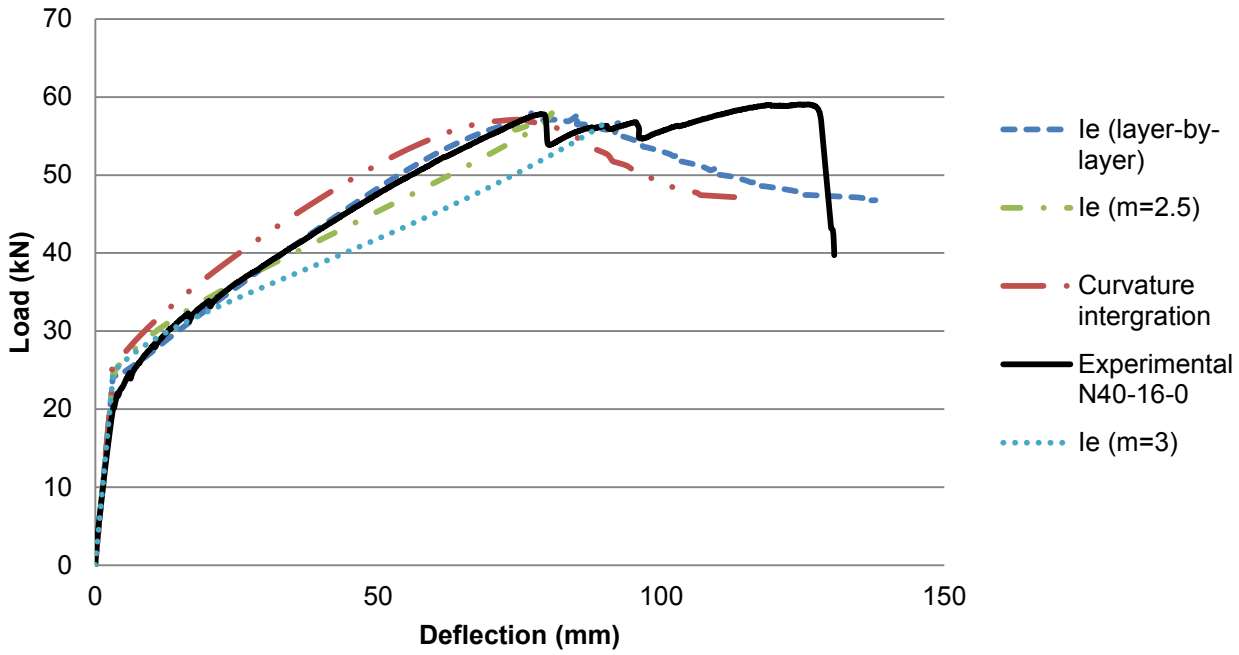

Figure 5.5: Load-deflection curve for beam N40-16-0 using different analytical approaches

The details of the layer-by-layer strain compatibility analysis are described below. Equation 5.11 shows the material model used for the stress-strain behaviour of concrete in compression (Thorenfeldt et al. 1987). The concrete was ignored in tension after cracking. The concrete strain at any layer was calculated based on strain compatibility as given in Equation 5.12 and the strain in the prestressed GFRP bar was calculated using Equation 5.13. The stresses in the GFRP bars were calculated by multiplying the strains in the GFRP bars by the modulus of elasticity as shown in Equation 5.14. The internal forces in the concrete layers were calculated by multiplying the stress in the layer by the area of the layer (thickness by width), as given in Equation 5.15. The force in the GFRP was calculated by multiplying the stress in the GFRP by the area of the GFRP bar (Equation 5.16). The resultant moment on the section was calculated by taking the summation of the moments of the internal force in each layer about the neutral axis. A single value for the effective moment of inertia calculated from Equation 5.8 was assumed along the beam length, and was used to calculate the mid-span deflection using Equation 5.17.

$$f_{ci} = \left(n \times f_c' \times \frac{\varepsilon_{ci}}{\varepsilon_c'}\right) \Big/ \left((n-1) + \left(\frac{\varepsilon_{ci}}{\varepsilon_c'}\right)^{nk}\right) \qquad \text{Equation 5.11}$$

where

$$\varepsilon_c' = nf_c'/(n-1)E_c$$

$$n = 0.8 + f_c'/17$$

$$k = 0.67 + f_c'/62 \text{ for } \varepsilon_{ci}/\varepsilon_c' > 1 \text{ and } k = 1 \text{ otherwise}$$

$$\varepsilon_{ci} = \varepsilon_{top} \times \left(\frac{y_i}{c}\right) \qquad \text{Equation 5.12}$$

$$\varepsilon_{frp} = \varepsilon_{top} \times \left(\frac{d}{c}\right) + \varepsilon_{pe} - \varepsilon_{top} \qquad \text{Equation 5.13}$$

$$f_{frp} = E_{frp} \times \varepsilon_{frp} \qquad \text{Equation 5.14}$$

$$C_i = f_{ci} \times t_i \times b_i \qquad \text{Equation 5.15}$$

$$T_{frp} = f_{frp} \times A_{frp} \qquad \text{Equation 5.16}$$

$$\Delta_{mid-span} = \frac{P\,a}{24\,E_c I_e}\,[\,3L^2\, - 4a^2] \qquad \text{Equation 5.17}$$

where f_c is the concrete compressive stress at strain ε_{ci} located at y_i from the top fibre of the section, f_c' is the concrete compressive strength, ε_{top} is the section top fibre strain, ε_{pe} is the effective strain in FRP due to prestressing, t_i is the concrete layer thickness, b_i is the concrete layer width, P is the value of the point load, a is the of shear span, and L is the total beam span. The procedure for predicting the ultimate capacity and the load-deflection of GFRP prestressed/reinforced concrete beams using the layered approach is shown in Figure 5.6.

As previously described in Section 4.6, the failure of beams N40-16-0, N25-16-0, and N0-16-0 was a compression-controlled failure, where the concrete crushed in the compression zone followed by rupture of the GFRP bar in the tension zone. The concrete crushing in the top layers resulted in section depth reduction to about 210 mm with the GFRP bars in the tension zone remaining in the elastic range. The formation of the new reduced section resulted in dramatic increases in the deflections with only small increases in the load, which appears in the nearly plateaued load-deflection part of the curves. The equation used to model the stress-strain behaviour of concrete allows the concrete strain to exceed concrete crushing strain value (3500 μs) where the concrete stress decreases and approaches zero, which would represent the crushing of the top concrete layers. Thus, the failure was controlled by the rupture of the GFRP bar in the tension zone and the failure strain was set to 20,000 μs.

Figure 5.7 to Figure 5.11 show a comparison of the analytical vs. experimental load-deflection curves for the static loaded beams of each group. It is evident that the layer-by-layer strain compatibility approach gives predicted results that are in a good correlation with the experimental response.

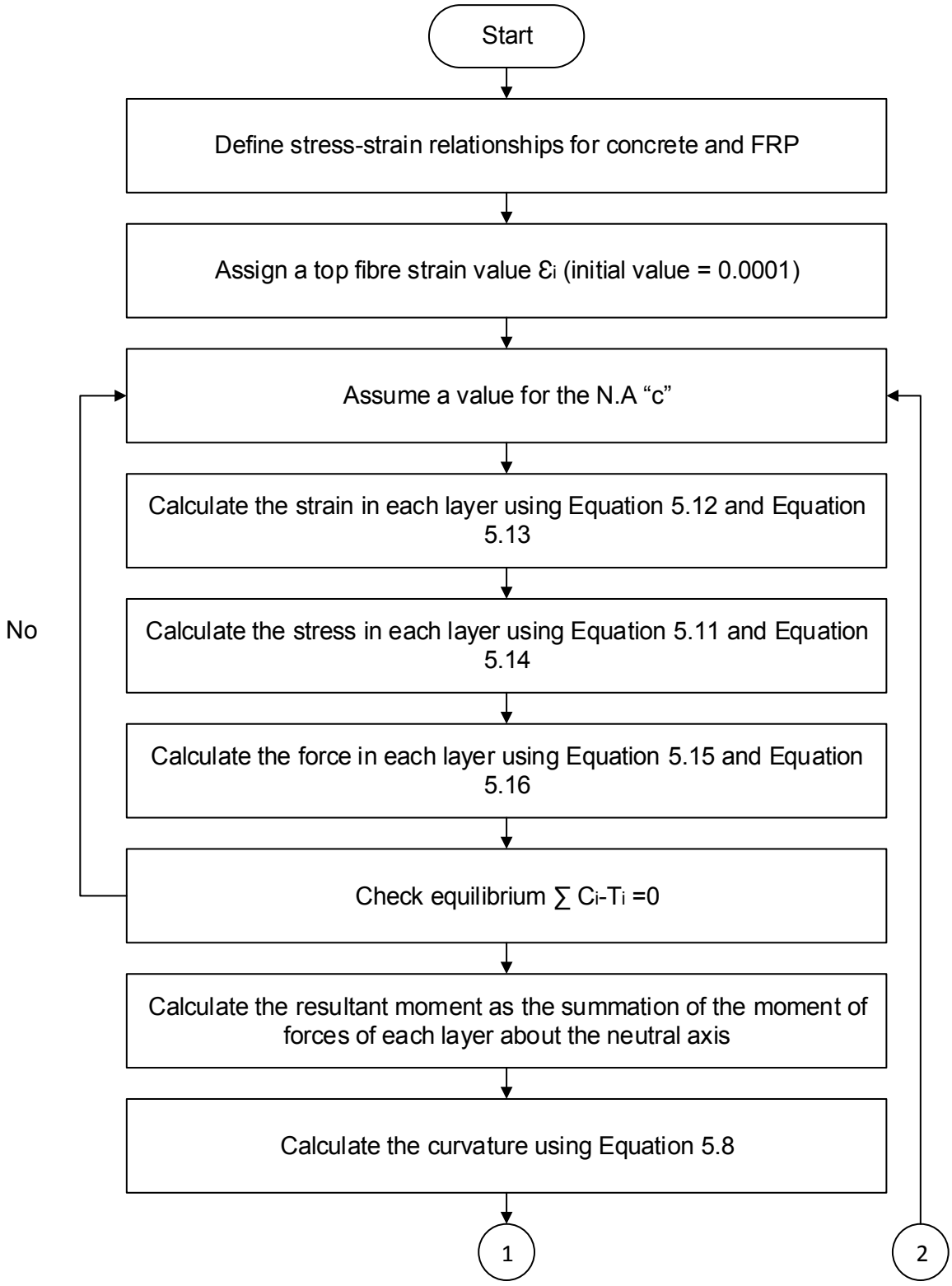
Start
Define stress-strain relationships for concrete and FRP
Assign a top fibre strain value εi (initial value = 0.0001)
Assume a value for the N.A "c"
Calculate the strain in each layer using Equation 5.12 and Equation 5.13
No
Calculate the stress in each layer using Equation 5.11 and Equation 5.14
Calculate the force in each layer using Equation 5.15 and Equation 5.16
Check equilibrium ∑ Ci-Ti =0
Calculate the resultant moment as the summation of the moment of forces of each layer about the neutral axis
Calculate the curvature using Equation 5.8
1
2

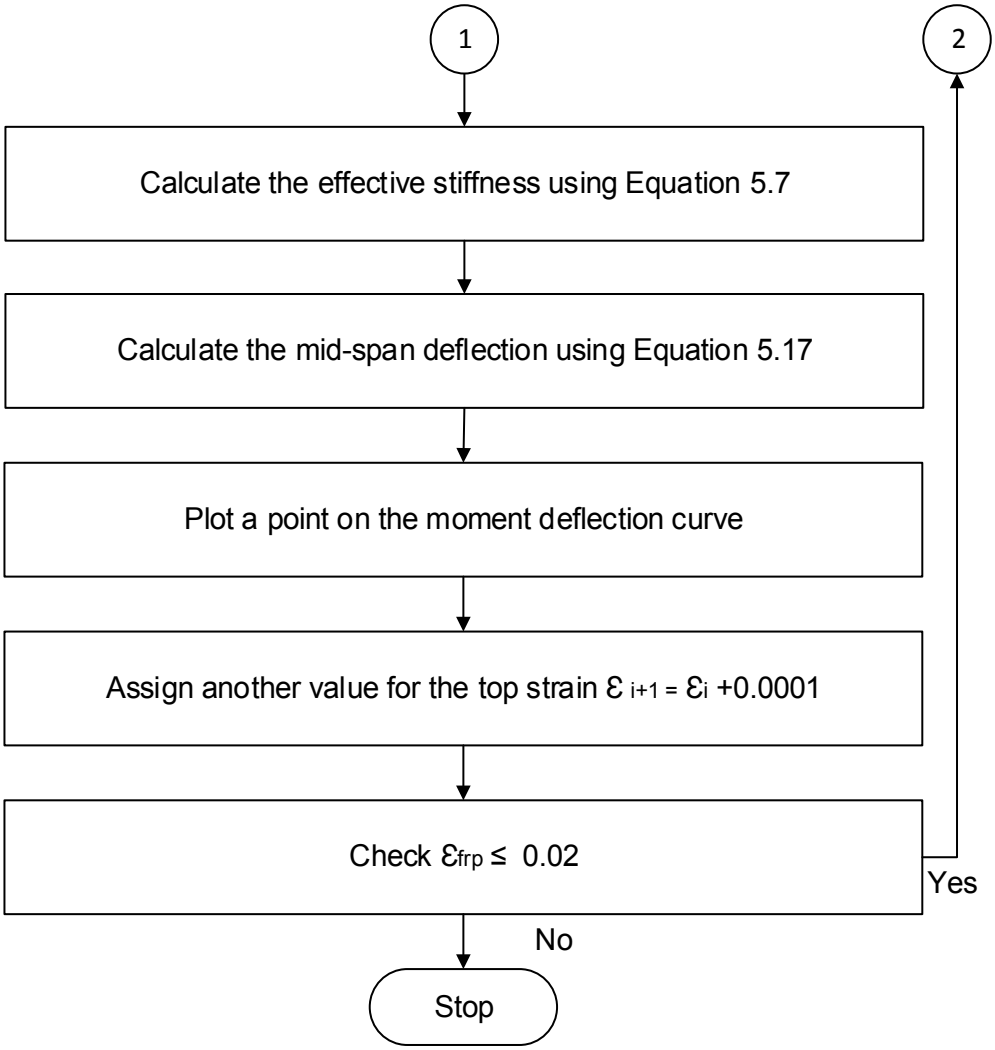

Figure 5.6: Flow chart for using the layered approach for ultimate moment capacity and load-deflection calculations

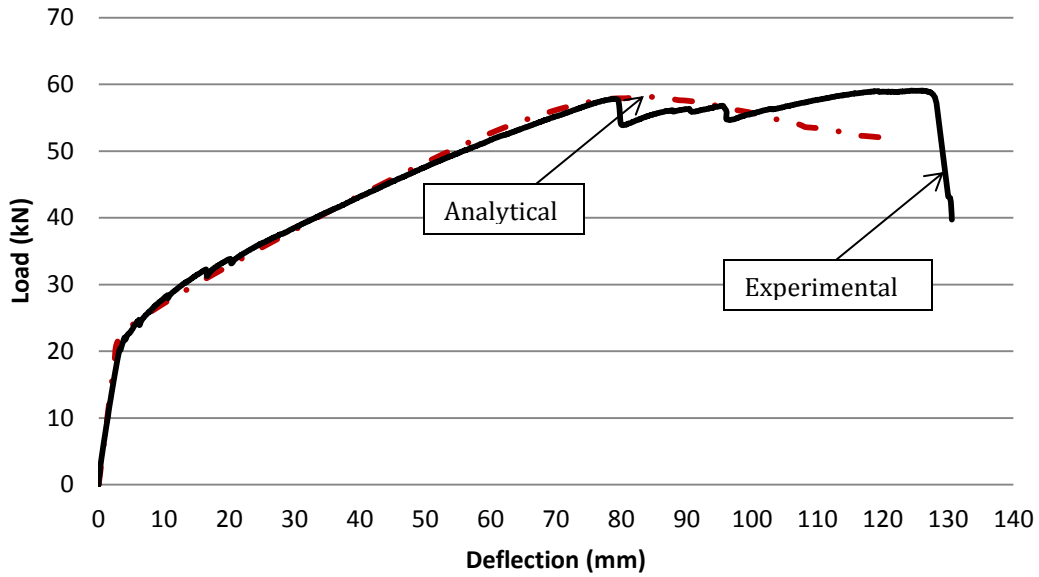

Figure 5.7: Analytical and experimental load-deflection curves for N40-16-0

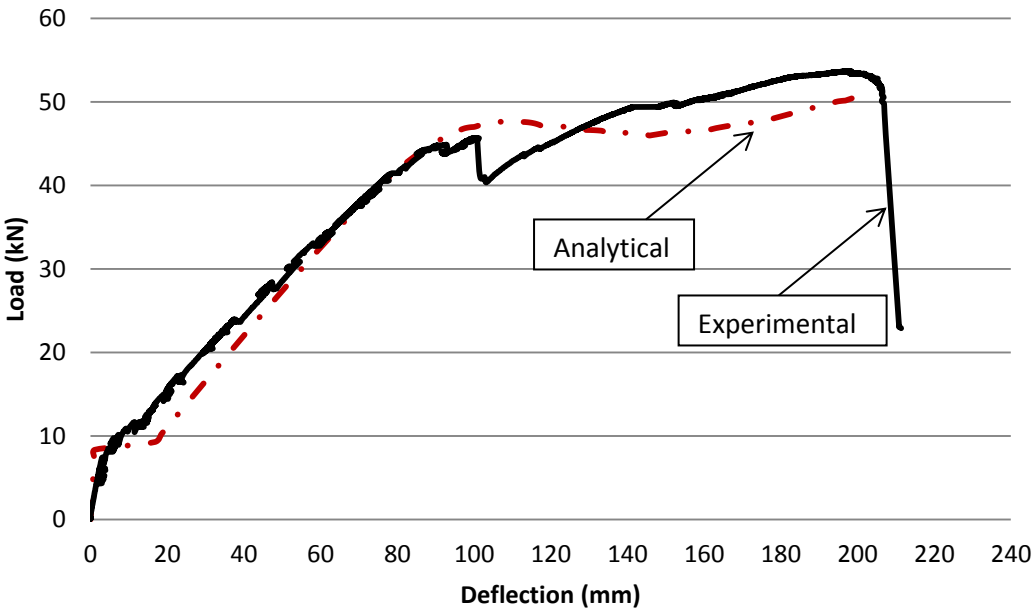

Figure 5.8: Analytical and experimental load-deflection curves for N0-16-0

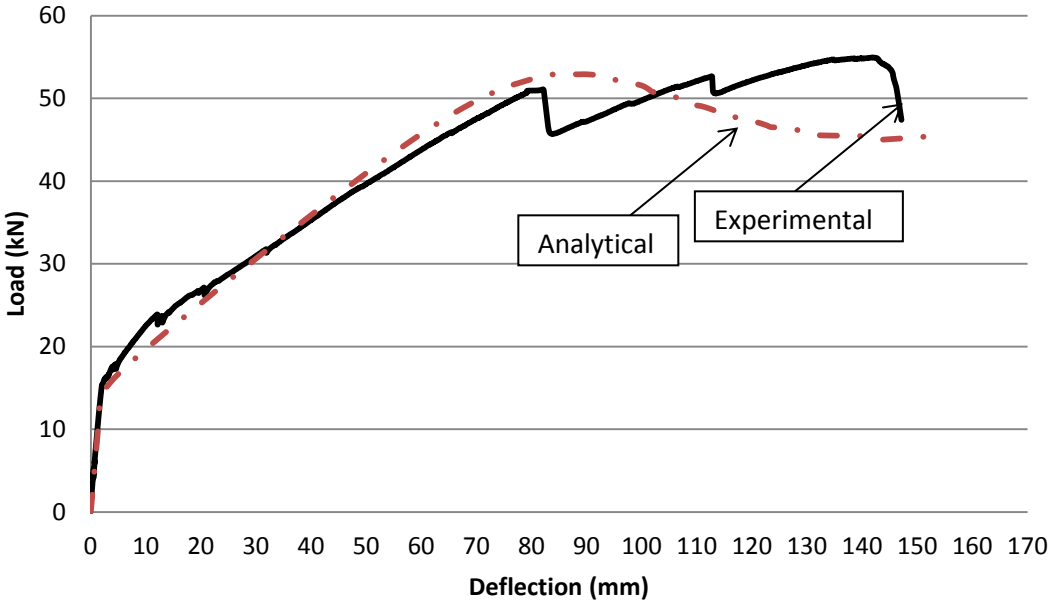

Figure 5.9: Analytical and experimental load-deflection curves for N25-16-0

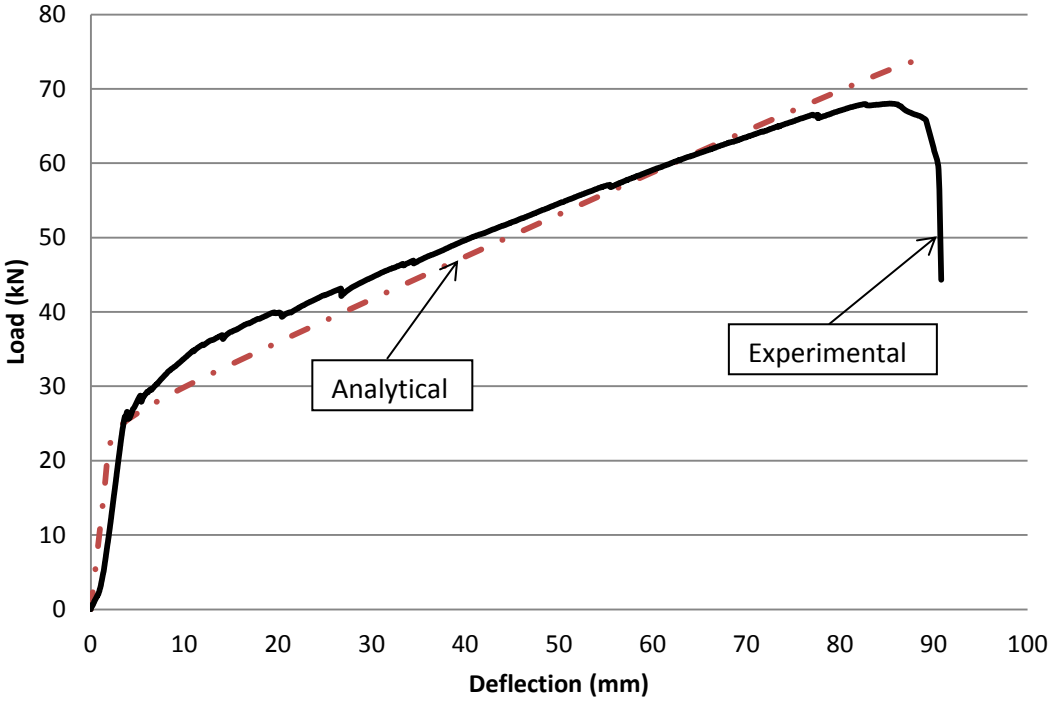

Figure 5.10: Analytical and experimental load-deflection curves for H40-16-0

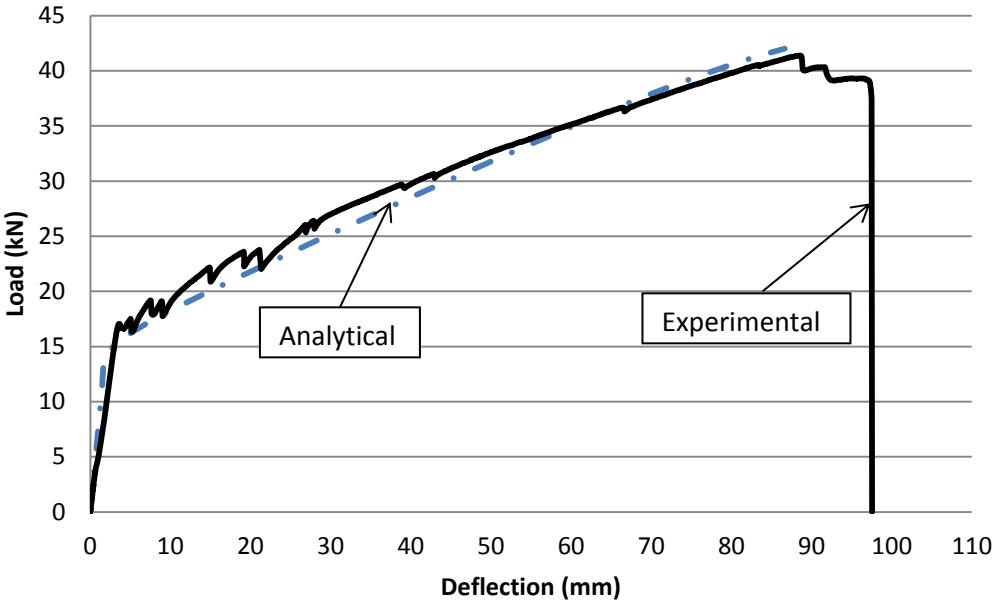

Figure 5.11: Analytical and experimental load-deflection curves for N40-12-0

5.3 Model for long-term flexural behaviour

The layer-by-layer strain compatibility approach was used in this study to model the long-term behaviour of GFRP prestressed/reinforced concrete beams under sustained loads. The model accounts for the long-term effects due to the concrete creep and shrinkage. Modeling the creep of the GFRP bars is discussed in Section 5.4. The main assumptions in this approach are the following:

- Concrete in tension is ignored after cracking.
- Linear strain distribution along the section depth.
- Uniform concrete shrinkage strain over the depth of the section.
- The effective modulus of elasticity of concrete is used to model the creep effect.
- The superposition principle for strains of concrete due to different effects is applied.

If the concrete was subjected to sustained loads, the resulting concrete strains can be divided into the following components based on the superposition assumption: instantaneous strains, creep strains, and shrinkage strains, as given in Equation 5.20. The instantaneous strains and the creep strains are dependent on the value of the applied load, while the shrinkage strains are independ-

ent of the applied load. Therefore, the stress-dependent strain component for the concrete is the summation of the instantaneous and the creep strains as shown in Equation 5.21 (Gilbert and Ranzi, 2011). The creep of the GFRP bars was ignored at this stage and its effect is discussed later in Section 5.4. Thus, the change in the stresses and strains of the GFRP bars is the result of stress redistribution within the section due to creep and shrinkage of the concrete.

Based on the strain compatibility concept, the strain at any layer is calculated as given in Equation 5.18. The curvature is calculated as given in Equation 5.19. The stress-strain relationship for concrete in compression is given in Equation 5.22, and the time-dependent stress in the pre-stressed GFRP bars is given in Equation 5.23. The internal forces in the concrete layers are calculated by multiplying the stress in the layer by area of the layer (thickness by width) as given in Equation 5.24, and the force in the GFRP is calculated by multiplying the stress in the GFRP by the area of the GFRP bar as given in Equation 5.25.

$$\varepsilon_i = \varepsilon_{top(t)} + \Psi_{(t)} y_i \qquad \text{Equation 5.18}$$

$$\Psi_{(t)} = \frac{\varepsilon_{top(t)}}{c} \qquad \text{Equation 5.19}$$

$$\varepsilon_i = \varepsilon_{(t_0)i} + \varepsilon_{cr(t,t_0)i} + \varepsilon_{sh(t,t_0)} = \varepsilon_{c(t,t_0)i} + \varepsilon_{sh(t,t_0)} \qquad \text{Equation 5.20}$$

$$\varepsilon_{c(t,t_0)i} = \varepsilon_i - \varepsilon_{sh(t,t_0)} \qquad \text{Equation 5.21}$$

$$f_{c(t,t_0)i} = \left(n \times f_c' \times \frac{\varepsilon_{c(t,t_0)i}}{\varepsilon'_{c(t,t_0)}}\right) \Big/ \left((n-1) + \left(\frac{\varepsilon_{c(t,t_0)i}}{\varepsilon'_{c(t,t_0)}}\right)^{nk}\right) \qquad \text{Equation 5.22}$$

where

$$\varepsilon'_{c(t,t_0)} = \mathrm{n} f_c' / (n-1) \mathrm{E}_{\mathrm{e}(t,t_o)}$$

$$E_{e(t,t_o)} = E_c(t_o) / \left(1 + \emptyset\,(t,t_0)\right)$$

$$\mathrm{n} = 0.8 + f_c'/17$$

$$\mathrm{k} = 0.67 + f_c'/62 \text{ for } \varepsilon_\mathrm{i}/\varepsilon'_{c(t,t_0)} > 1 \text{ and } \mathrm{k} = 1 \text{ otherwise}$$

$$f_{frpe} = E_{frp}\left[\varepsilon_{top(t)} + \Psi_{(t)} d_n + \varepsilon_{pei}\right] \quad \text{Equation 5.23}$$

$$C_i = f_{c(t,t_0)i} \times t_i \times b_i \quad \text{Equation 5.24}$$

$$T_{frp} = f_{frpe} \times A_{frp} \quad \text{Equation 5.25}$$

where $\varepsilon_{top(t)}$ is the concrete top strain at time (t), c is the neutral axis depth , y_i is the depth of the layer (i) measured from the section top fibre, $\varepsilon_{(t_0)i}$ is the elastic strain at layer (i), $\varepsilon_{cr(t,t_0)}$ is the creep strain in layer (i) at time (t), $\varepsilon_{sh(t,t_0)}$ is the shrinkage strain as given previously in Section 2.2, f'_c is the concrete compressive strength, ε_{pei} is the effective GFRP strain due to prestressing at the time of applying the sustained loads, d_n is the depth of the GFRP bar, and $\emptyset\,(t, t_0)$ is the concrete creep coefficient as given before in Section 2.3.2.1.

The analysis is done for a cross-section with a known initial stress and strain state. For a given loading period (t-t_0) and sustained moment, the creep coefficient and the shrinkage strain are computed first calculated based on the guidelines given by ACI 209-92. Iterative calculations are then carried out to compute the value of the neutral axis depth (c) which satisfies equilibrium of forces and strain compatibility over the section, using the long-term constitutive relationships for concrete and GFRP bars (if included). The iterations start by assuming an initial value for the top fibre strain; then, a value for the neutral axis depth (c) is calculated iteratively to satisfy equilibrium. The resultant moment is then calculated and compared to the applied moment. If the two moment values are not equal, other values for the top fibre strain are assumed and the whole procedure is repeated until the resultant moment equals the applied moment. The obtained values for the top strain and the neutral axis are used to compute the effective stiffness as given previously in Equation 5.7 and Equation 5.8, which is then used to calculate the long-term deflection using Equation 5.17.

Figure 5.12 shows the procedure coded in Microsoft Excel to predict the long-term behaviour of GFRP prestressed/reinforced concrete beams. These predictions were compared with the experimental results of the sustained loading test.

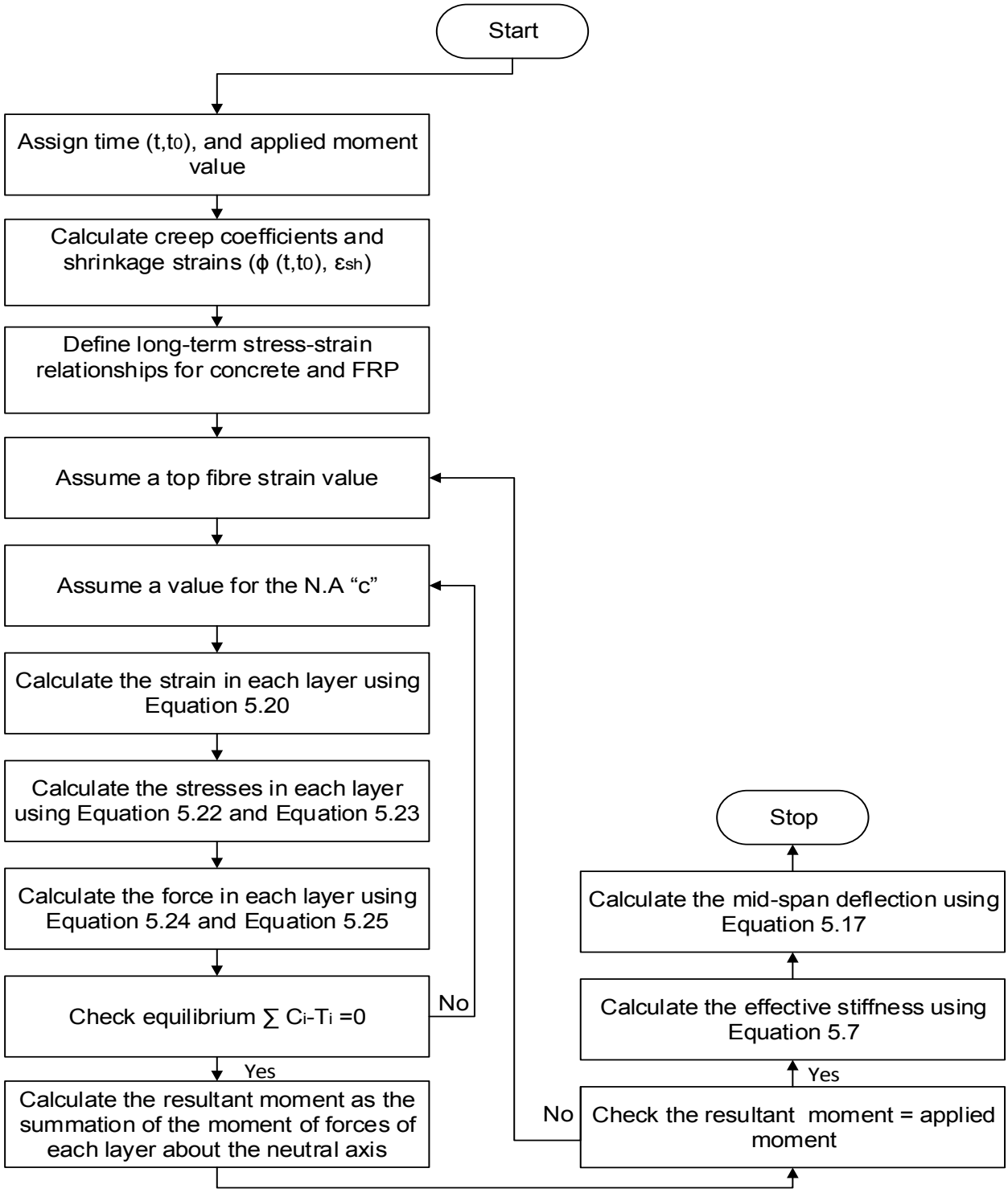

Figure 5.12: Flow chart for using the layered approach for long-term deflection prediction of GFRP prestressed concrete beams

A difference between the analytical model presented here and some of the models reported in the literature is that this model captures the redistribution of stresses between concrete and the bonded GFRP bars, and the neutral axis movement caused by the creep and shrinkage of concrete as shown in Figure 5.13 and Figure 5.14 for beam N40-16-60 as an example. In general, after applying the initial load, creep and shrinkage took place in the concrete. This caused a change in position of the neutral axis, pushing it downwards, and hence, increasing the area of concrete in compression. To maintain equilibrium and compatibility, the stresses and strains in the GFRP bars on the tension side of the section increased. This gradual development of creep strains caused an increase of curvature, and a consequent increase in the beam deflection. The neutral axis movement was ignored by other models reported in the literature for simplicity (Ghali et al., (2002), Gilbert and Ranzi (2011)).

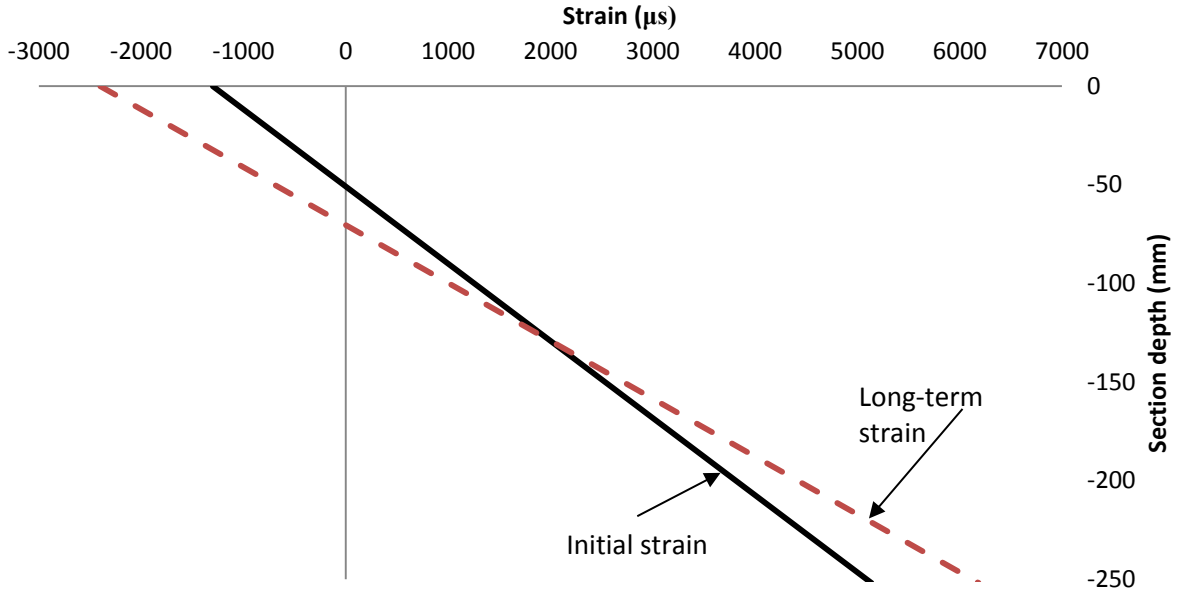

Figure 5.13: Strain profiles due to initial and long-term loading for beam N40-16-60

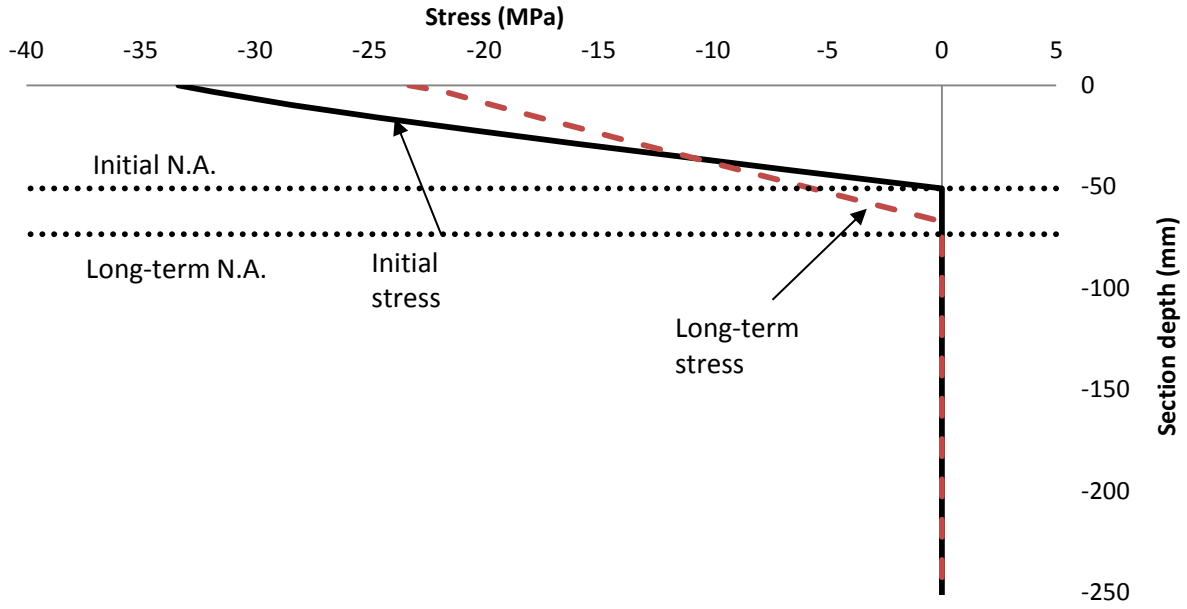

Figure 5.14: Stress profiles due to initial and long-term loading for beam N40-16-60

Table 5.1 to Table 5.5 give the initial and the long-term experimental and analytical mid-span deflections, concrete strains and GFRP strains for all of the beams that were under sustained loading, along with the analytical results of the concrete stresses, the GFRP stresses, and the neutral axis locations.

The creep coefficients and the shrinkage strains for the concrete beams were calculated based on the ACI 209-92, and the effective prestressing stresses were calculated by subtracting the long-term prestress losses given in Appendix C from the prestress values at transfer. For the normal strength concrete beams, the calculated creep coefficient was 1.8 for the sustained loading period of 300 days. Using this coefficient, the analytical model had good correlation with the measured values for the lower sustained load levels (35% and 60%). For the 80% loading level, the analytical model underestimated the deflection and the strain values for all of the beams. This can be explained as follows: the relationship between creep and the applied stress is linear up to a certain limit of applied stress to strength ratio that ranges between 0.4 and 0.8, depending on the concrete properties and the age of loading. When concrete is subjected to a stress higher than that linearity limit, severe internal micro-cracking takes place resulting in increased creep (Neville et

al. 1983). Thus, to account for the increase in concrete creep at high stress levels, a higher value for the creep coefficient should be used.

Neville et al. (1983) provide scale factors for the creep coefficient values for different stress/strength ratios. Using these values, the creep coefficient was multiplied by a factor of 1.56, and this modified value was used to predict the long-term behaviour of the normal strength beams at the 80% sustained loading level. The analytical model results obtained with the modified creep coefficient gave good correlation with the measured values as shown in Table 5.1 to Table 5.4 in the "Analytical(m)" column.

Such modification was not required for the high strength concrete because of two main factors: 1) the lower stress/strength ratio, and 2) the higher concrete strength led to a higher limit for the proportionality between creep and stress/strength ratio (Neville et al. 1983).

Table 5.1: Experimental and analytical results of N40-16 group

		N40-16-35		N40-16-60		N40-16-80		
		Experimental	Analytical	Experimental	Analytical	Experimental	Analytical	Analytical(m)
Initial loading	ε_{ci} (με)	-528	-400	-1744	-1300	-2221	-2100	
	ε_{GFRPi} (με)	7775	7787	14161	10975	16600	14616	
	Δ_i (mm)	4.5	4.2	28.5	29.2	51.8	50.1	
	N.A.		105		50		46	
	σ_{ci} (MPa)		-11.4		-33.4		-39.3	
	σ_{frp} (MPa)		467		685		876	
Sustained loading	ε_{ct} (με)	-800	-950	-2315	-2400	-3800	-3550	4150
	ε_{GFRPt} (με)	8036	8014	14521	12090	N/A	15288	15728
	Δ_t (mm)	9.1	8.4	36.7	38.3	72.1	61.5	67.1
	N.A.		126		70		64	69
	σ_{ct} (MPa)		-8.5		-23.3		-35	-30.3
	σ_{frpt} (MPa)		480		725		917	943

Table 5.2: Experimental and analytical results of N25-16 group

		N25-16-35		N25-16-60		N25-16-80		
		Exper-imental	Analytical	Experi-mental	Analytical	Experi-mental	Analyt-ical	Analyt-ical(m)
Initial loading	ε_{ci} (με)	-390	-450	-2100	-1500	-2140	-1980	
	ε_{GFRPi} (με)	4810	5872	10770	10435	13000	12377	
	Δ_i (mm)	5.6	7.0	37.0	37.9	48.0	51.0	
	N.A.		71		44		43	
	σ_{ci} (MPa)		-12.75		-34.5		38.0	
	σ_{frp} (MPa)		352		626		742	
Sustained loading	ε_{ct} (με)	-790	-995	-3387	-2800	-4640	-3450	-4000
	ε_{GFRPt} (με)	5260	6090	N/A	11166	N/A	13196	13407
	Δ_t (mm)	9.3	12.1	53.6	50.0	66.2	63.0	67.1
	N.A.		91.0		62.6		61	66
	σ_{ct} (MPa)		-9.0		-26.7		-33.0	-27.3
	σ_{frpt} (MPa)		365		670		792	804

Table 5.3: Experimental and analytical results of N0-16 group

		N0-16-35		N0-16-60		N0-16-80		
		Exper-imental	Analyti-cal	Experi-mental	Analytical	Experi-mental	Analyt-ical	Analyt-ical(m)
Initial loading	ε_{ci} (με)	-760	-1000	-2380	1650	-2980	-2200	
	ε_{GFRPi} (με)	4860	4711	10100	8333	10922	10587	
	Δ_i (mm)	29	33.1	54.5	53.1	73.5	68.1	
	N.A.		34		36		36	
	σ_{ci} (MPa)		-24.7		-38		-38.8	
	σ_{frp} (MPa)		313		499		635	
Sustained loading	ε_{ct} (με)	-1792	-1930	-3213	-3000	-4356	-3650	-4400
	ε_{GFRPt} (με)	5924	5647	11373	8870	12567	10777	11618
	Δ_t (mm)	45.8	40.5	69.8	63.2	91.7	76.8	85
	N.A.		54		54		53	57.7
	σ_{ct} (MPa)		-18.5		-29.4		-36	-32
	σ_{frpt} (MPa)		338		532		647	697

Table 5.4: Experimental and analytical results of N40-12 group

		N40-12-35		N40-12-60		N40-12-80		
		Experi-mental	Analyti-cal	Experi-mental	Analytical	Experi-mental	Analyt-ical	Analyt-ical(m)
Initial loading	ε_{ci} (με)	-202	-300	-1242	-900	-2096	-1750	
	ε_{GFRPi} (με)	8000	8317	15950	11600	17912	16700	
	Δ_i (mm)	4.7	3.9	22.5	24.7	60	57	
	N.A.		85		41		34	
	σ_{ci} (MPa)		-8.5		-26.5		-43	
	σ_{frp} (MPa)		499		697		1000	
Sustained loading	ε_{ct} (με)	-395	-750	-1945	-1700	-2906	-3200	-3750
	ε_{GFRPt} (με)	8210	8664	16890	12030	N/A	17120	18000
	Δ_t (mm)	8.8	8.2	31.2	31.2	80.8	66.9	74.5
	N.A.		102		61		53	56
	σ_{ct} (MPa)		-6.5		-17.2		-31.5	-29
	σ_{frpt} (MPa)		519		722		1027	1080

Table 5.5: Experimental and analytical results of H40-16 group

		H40-16-35		H40-16-60		H40-16-80	
		Experi-mental	Analytical	Experi-mental	Analytical	Experi-mental	Analytical
Initial loading	ε_{ci} (με)	-312	-350	-1280	-1100	-2550	-1700
	ε_{GFRPi} (με)	7595	7884	12553	11659	13500	15195
	Δ_i (mm)	3.5	4.5	24	28.5	47.5	50.5
	N.A.		87		43		37
	σ_{ci} (MPa)		-14		-44.1		-66.4
	σ_{frp} (MPa)		473		700		911
Sustained loading	ε_{ct} (με)	-690	-800	-2210	-2150	-3288	-3100
	ε_{GFRPt} (με)	8050	8113	N/A	12332	N/A	15846
	Δ_t (mm)	5.8	8	38.5	37.7	58.6	61.4
	N.A.		109		63		56
	σ_{ct} (MPa)		-10.8		-29.5		-45.5
	σ_{frpt} (MPa)		486		-740		950

5.4 Effect of GFRP bar creep

The creep in the GFRP bars is modeled using a creep coefficient which is defined as the ratio between the creep strain and the elastic strain under sustained constant load. The equation for the total strain of the material can be written as (fib 2006):

$$\varepsilon_{frp}\,(t) = \beta \log t + \varepsilon_{frp(t_o)} \qquad \text{Equation 5.26}$$

where $\varepsilon_{frp}(t)$ is the total GFRP strain after a time period (t), $\varepsilon_{frp(t_o)}$ is the elastic strain value and β is the creep rate parameter.

As mentioned before in Section 4.3, the values of the creep parameter β were found to be 38.5 98.9, 176.5 and 287.6 for the sustained load levels of 15%, 30%, 45% and 60%, respectively. Using the previous equation, the creep coefficient can be computed as given in Equation 5.27.

$$\emptyset_p = \frac{\varepsilon_{frp(cr)}}{\varepsilon_{frp(t_o)}} = \frac{\beta \log t}{\varepsilon_{frp(t_o)}} \qquad \text{Equation 5.27}$$

where $\varepsilon_{frp}(t)$ is the total strain in the material after a time period t (in hours), $\varepsilon_{frp,0}$ is the initial (elastic) strain value, $\varepsilon_{frp(cr)}$ is the creep strain in the material after a time period t, and β is the creep rate parameter.

Figure 5.15 shows the relationship between the creep strain obtained using βLog(t) for t = 7200 hours (300 days) values and the initial GFRP bar strain $\varepsilon_{frp(t0)}$ obtained from Youssef and Benmokrane (2011) and from this study. The relationship is close to linear, and the slope of the line gives the value for the creep coefficient for the GFRP bars.

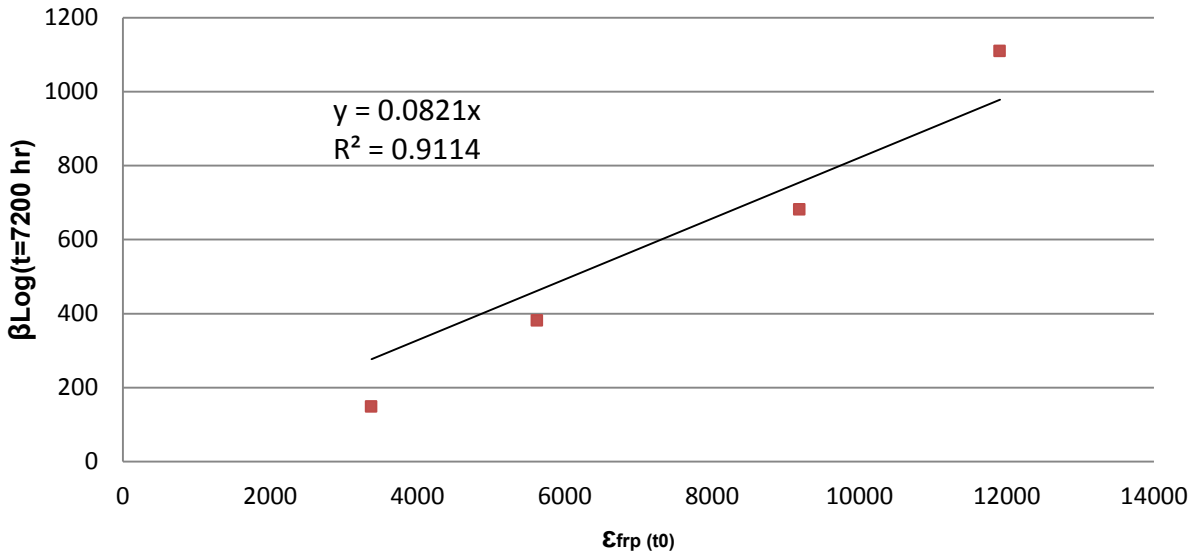

Figure 5.15: βLog(t) versus the initial GFRP bar strain $\varepsilon_{frp(t0)}$

The effective modulus of elasticity of the GFRP can be computed using Equation 5.28.

$$E_{frpe} = \frac{E_{frp}}{1 + \emptyset_p} \qquad \text{Equation 5.28}$$

where E_{frpe} is the effective modulus of elasticity of the GFRP bars, E_{frp} is the original modulus of elasticity and $\emptyset_p$ is the creep coefficient. Using a value of 0.0821 for the creep coefficient at 300 days, the effective modulus of elasticity was found to be about 55.4 GPa.

The GFRP bar creep was implemented into the analytical model to investigate its effect on the overall long-term behaviour of the beams. The results are shown in Table 5.6 to Table 5.10. In general, the GFRP creep resulted in stress redistribution between the concrete and the GFRP where the stress increased in the concrete and decreased in the GFRP bars. The neutral axis moved upwards and both the concrete and the GFRP strains increased.

It can be seen from these results that the effect of the GFRP creep on the beam total deflection was almost negligible for the 35% sustained load level beams, and it resulted in about 5% increase in the total deflection of the 60% and 80% sustained load level beams.

It should be noted that the long-term GFRP effective modulus of elasticity was about 92% of the short-term GFRP modulus of elasticity, while the long-term concrete effective modulus of elasticity was about 38% of the short-term concrete modulus of elasticity. Thus, the effect of GFRP creep on the overall behaviour of the beams was negligible compared to the effect of the concrete creep.

This finding confirms what was concluded by Youssef (2010) that the creep of the GFRP has a minimal effect on the long-term behaviour of the beams. Furthermore, the results suggest that the increase in the GFRP bar strains observed in the beam experiments and predicted by the analytical model are primarily due to the increase in the beam curvature caused by concrete creep and shrinkage rather than the creep of the GFRP bars.

Table 5.6: Effect of GFRP creep on the analytical results of N40-16 group

		N40-16-35			**N40-16-60**			**N40-16-80**		
		EXP	No GFRP creep	GFRP creep	EXP	No GFRP creep	GFRP creep	EXP	No GFRP creep	GFRP creep
Sustained loading	ε_{ct} (μs)	-800	-950	-960	-2315	-2400	-2430	-3800	4150	-4350
	ε_{GFRPt} (μs)	8036	8014	8720	14521	12090	12854	N/A	15728	17106
	Δ_t (mm)	9.1	8.4	8.6	36.7	38.3	38.7	72.1	67.1	71.9
	N.A.		126	124		70	70		69	67.7
	σ_{ct} (MPa)		-8.5	-8.6		-23.3	-23.6		-30.3	-31.7
	σ_{frpt} (MPa)		480	479		725	707		943	940

Table 5.7: Effect of GFRP creep on the analytical results of N25-16 group

		N25-16-35			N25-16-60			N25-16-80		
		EXP	No GFRP creep	GFRP creep	EXP	No GFRP creep	GFRP creep	EXP	No GFRP creep	GFRP creep
Sustained loading	ε_{ct} (μs)	-790	-995	-1010	-3387	-2800	-2900	-4640	-3450	-4020
	ε_{GFRPt} (μs)	5260	6090	6496	N/A	11166	12078	N/A	13196	14160
	Δ_t (mm)	9.3	12.1	12.6	53.6	50.0	53.1	66.2	63.0	68.9
	N.A.		91.0	89.7		62.6	61.0		61	65.2
	σ_{ct} (MPa)		-9.0	-9.1		-26.7	-27.6		-33.0	-27.4
	σ_{frpt} (MPa)		365	363		670	665		792	778

Table 5.8: Effect of GFRP creep on the analytical results of N0-16 group

		N0-16-35			N0-16-60			N0-16-80		
		EXP	No GFRP creep	GFRP creep	EXP	No GFRP creep	GFRP creep	EXP	No GFRP creep	GFRP creep
Sustained loading	ε_{ct} (μs)	-1792	-1930	-1990	-3213	-3000	-3130	-4356	-4400	-4600
	ε_{GFRPt} (μs)	5924	5647	5973	11373	8870	9544	12567	11618	12518
	Δ_t (mm)	45.8	40.5	42.4	69.8	63.2	67.5	91.7	85	91.2
	N.A.		54	52.5		54	51.8		57.7	56.4
	σ_{ct} (MPa)		-18.5	-19.0		-29.4	-30.7		-32	-33.6
	σ_{frpt} (MPa)		338	334		532	525		697	688

Table 5.9: Effect of GFRP creep on the analytical results of N40-12 group

		N40-12-35			N40-12-60			N40-12-80		
		EXP	No GFRP creep	GFRP creep	EXP	No GFRP creep	GFRP creep	EXP	No GFRP creep	GFRP creep
Sustained loading	ε_{ct} (μs)	-395	-750	-760	-1945	-1700	-1750	-2906	-3750	-3900
	ε_{GFRPt} (μs)	8210	8664	9264	16890	12030	13007	N/A	18000	19135
	Δ_t (mm)	8.8	8.2	8.5	31.2	31.2	32.8	80.8	74.5	77.7
	N.A.		102	100		61	59		56	56.2
	σ_{ct} (MPa)		-6.5	-6.6		-17.2	-17.7		-29	-28.4
	σ_{frpt} (MPa)		519	518		722	715		1080	1052

Table 5.10: Effect of GFRP creep on the analytical results of N40-16 group

		H40-16-35			H40-16-60			H40-16-80		
		EXP	No GFRP creep	GFRP creep	EXP	No GFRP creep	GFRP creep	EXP	No GFRP creep	GFRP creep
Sustained loading	ε_{ct} (μs)	-690	-800	-800	-2210	-2150	-2220	-3288	-3100	-3210
	ε_{GFRPt} (μs)	8050	8113	8796	N/A	12332	13377	N/A	15846	17146
	Δ_t (mm)	5.8	8	8	38.5	37.7	40.1	58.6	61.4	65.4
	N.A.		109	109		63	62		56	55
	σ_{ct} (MPa)		-10.8	-10.8		-29.5	-30.5		-45.5	-47.5
	σ_{frpt} (MPa)		486	483		-740	735		950	943

5.5 Modeling beam unloading

A number of diverse approaches have been used for material modeling of concrete under cyclic loading. In general, the experimental work in the literature provided the following concepts regarding the behaviour of concrete during unloading and reloading cycles (Sinha et al. (1964), Vecchio (1999), Palermo and Vecchio (2003)):

- The unloading and the reloading curves of concrete have pronounced hysteresis.
- The unloading curves are slightly nonlinear with a marked increase in curvature near the residual strain.
- Reloading curves are nearly linear up to the intersection with the unloading curve, after which the behaviour follows the stress-strain curve for concrete under static loading.
- The plastic strains are dependent on the strain at unloading.
- The plastic strain acts as a strain offset similar to the elastic offsets resulting from thermal expansion or other pre-strain effects.
- A continuous degradation of the concrete is reflected in the decrease of the slopes of the reloading curves.
- The stress-strain curve for concrete under static loading is considered as an envelope curve that the stress-strain curves under cyclic loading do not exceed.
- The point at which the reloading curve crosses the unloading curve represents the point beyond which stresses cause additional strains.

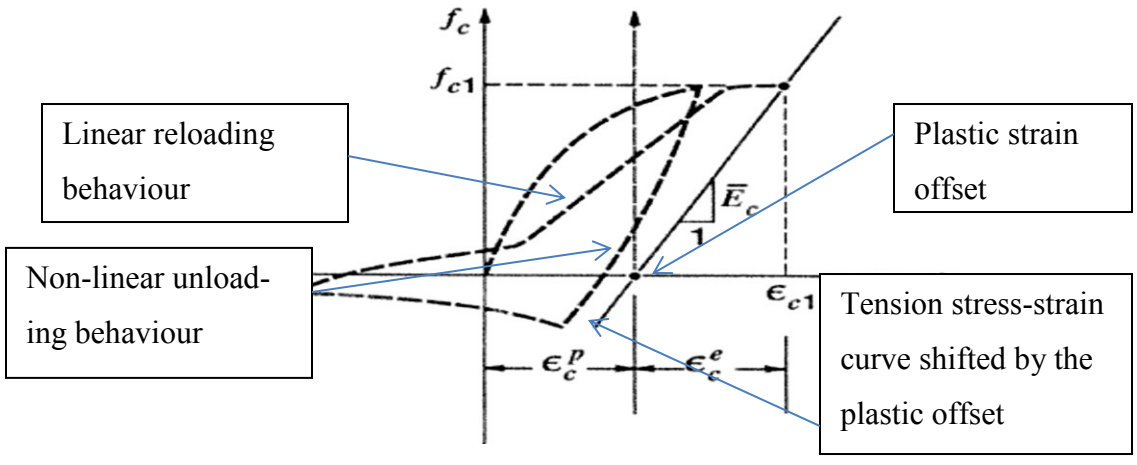

Figure 5.16: Stress-strain behaviour of concrete under cyclic loading (Vecchio (1999)

Many constitutive models in the literature described the behaviour of concrete under cyclic loading for a simple uniaxial case. These models were only describing the behaviour of concrete under short-term loading and unloading, and typically have been developed for implementation into nonlinear finite element programs. The literature does not provide guidance on the cyclic behaviour of concrete after being subjected to sustained loading. The following sections discuss the proposed models for the behaviour of concrete including unloading curves, plastic offsets, and crack closing curves.

5.5.1 Estimating the plastic offset

The loading of the concrete leads to internal cracking, and compression of internal voids. This leads to non-recoverable damage in the concrete. This damage is represented by the plastic offset strains. The plastic offset is the parameter that defines the unloading path and determines the shift in the tension model from the origin as shown in Figure 5.16. For the concrete in tension, the plastic strain offset is also dependent on the strain at unloading and it occurs when the cracked surfaces come into contact during unloading and do not realign.

Various plastic offset models for concrete have been proposed in the literature. The model proposed by Aslani and Jowkarmeimandi (2012) was adopted in this study to model the behaviour of concrete under cyclic loading without the effect of sustained loading. The plastic strain in compression was calculated based on a damaged modulus of elasticity that depends on the initial loading stress and strain as shown in Equation 5.29 and Equation 5.30, while the plastic strain in tension was computed as shown in Equation 5.31.

$$E_r = E_c \left({(\sigma_{un}/E_c\varepsilon_c' + 0.57)}\Big/{(\varepsilon_{un}/\varepsilon_c' + 0.57)} \right) \qquad \text{Equation 5.29}$$

$$\varepsilon_{pl} = \varepsilon_{un} - \frac{\sigma_{un}}{E_r} \qquad \text{Equation 5.30}$$

$$\varepsilon_{plt} = 0.725\, \varepsilon_{unt} \qquad \text{Equation 5.31}$$

where E_r is the damaged modulus of elasticity of concrete in compression, σ_{un} is the unloading stress in compression, E_c is the modulus of elasticity o concrete, ε_c' is the compression strain corresponding to the maximum compression stress, ε_{un} is the unloading strain in compression, ε_{pl} is the plastic compression strain, ε_{plt} is the plastic tension strain, and ε_{unt} is the unloading tension strain.

The different effects of the sustained loading are implemented in this model as follows:

1. If the initial strain was compression strain and the final long-term strain was also compression (like the case for the top layers of the beam), then the total plastic strain is considered as the summation of the creep strain of the concrete due to the sustained loading and the initial plastic strain calculated by Equation 5.30.
2. If the initial strain was tension strain or small compression strain and the final long-term strain was compression associated with higher compression stress (the case for concrete layers in the vicinity of the neutral axis), then the total plastic strain is calculated by offsetting the normal stress-strain curve for concrete in compression to the point of the long-term stress and strain. Therefore, the total plastic strain can be calculated using tion 5.32 as follows:

$$\varepsilon_{pl} = \varepsilon_{un} - \frac{\sigma_{un}}{E_c} \qquad \text{Equation 5.32}$$

3. If the initial strain was tension, and the final long-term strain was also tension (the case for the bottom layers of the beam), then the final plastic strain is calculated using Equation 5.31, with the unload strain in tension being the long-term strain.

5.5.2 Modeling crack closing upon unloading

If concrete was initially loaded in tension beyond the cracking load and then unloaded, the compressive stresses do not remain at zero until the cracks completely close. Compressive stresses begin when the tensile strains reach the tension plastic strain (Sima et al. 2008). The crack closure mechanism is governed by the crack closure stress which is the stress required to close the

crack. The literature proposed that the crack closure stress can be taken as 1/10 of the concrete compressive strength. Figure 5.17 shows a schematic of the proposed crack-closing model.

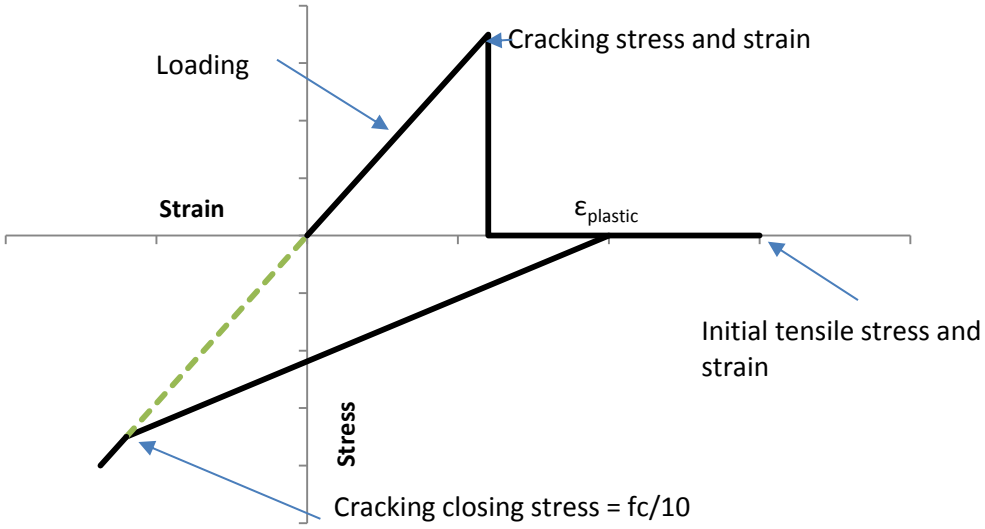

Figure 5.17: Concrete stress-strain behaviour during crack closing

5.5.3 Concrete stress-strain curves for unloading

For the concrete loaded in compression, the unloading response of concrete, in its simplest form, can be represented by a linear expression from the unloading strain to the plastic strain (Vecchio, 1999). Therefore, the short-term loading and unloading curves for concrete are assumed to be as shown in Figure 5.18 and Figure 5.19, where E_r is the damaged modulus of elasticity as previously shown in Equation 5.29.

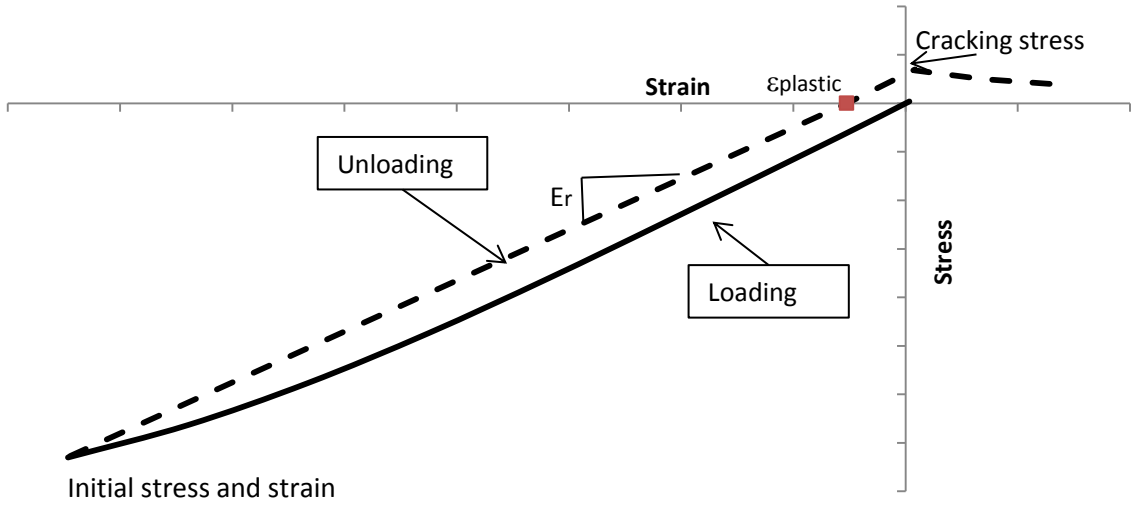

Figure 5.18: Short-term stress-strain unloading model for concrete loaded in compression

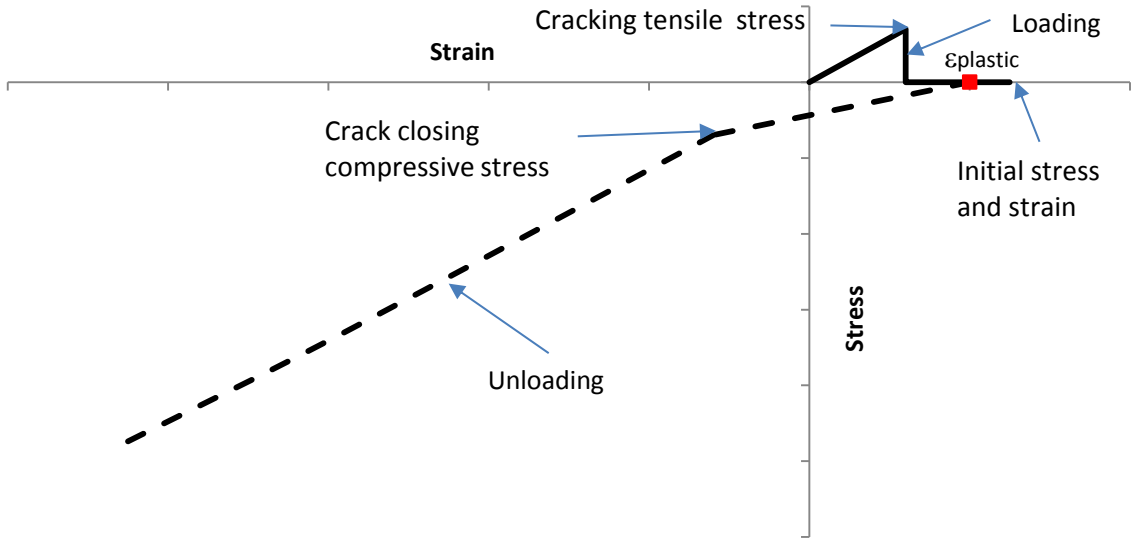

Figure 5.19: Short-term stress-strain unloading model for concrete loaded in tension

For concrete that was subjected to sustained loading, the short-term model was modified for different unloading cases as follows:

1. If the initial strain was compression strain and the final long-term strain was also compression (like the case for the top layers of the beam), then the unloading response of the concrete will be linear from the unloading strain to the plastic strain. The plastic strain is calculated as previously described in Section 5.5.1. The stress will change from compression to tension when the strain exceeds the plastic strain until the concrete reaches its cracking stress, then tension stress will follow the tension stiffening smeared crack model given by Equation 5.35 (Collins & Mitchell 1991).

$$f_t = \alpha_1 \alpha_2 f_r / (1 + \sqrt{500 \varepsilon_r}) \qquad \text{Equation 5.33}$$

   where f_t is the average tensile stress in the concrete, α_1 and α_2 are coefficients accounting for the bond characteristics of the reinforcement and the loading conditions, respectively, f_r is the modulus of rupture of the concrete and ε_r is the average tensile strain in the concrete.

   The tension stiffening was considered in this case due to the existence of the two compression bars, and to account for the fact that these cracks have smaller crack widths and wider crack spacing compared to the conventional tension cracks.
2. If the initial strain was a tension strain less than the cracking strain or a small compression strain, and the final long-term strain was compression associated with higher compression stress (the case for concrete layers in the vicinity of the neutral axis), then the unloading response of the concrete will follow the static stress-strain response of concrete shifted by the plastic strain offset.
3. If the initial strain was tension strain that exceeded the cracking strain and the final long-term strain was also tension (the case for the bottom layers of the beam), then the concrete unloading response will follow the crack-closing model until the strain reaches the crack closing strain, then it will follow the static stress-strain response of the concrete in compression.

The schematics of the proposed model are shown in Figure 5.20 to Figure 5.22, and a flowchart that describes the steps of plotting the unloading load-deflection curves is shown in Figure 5.23.

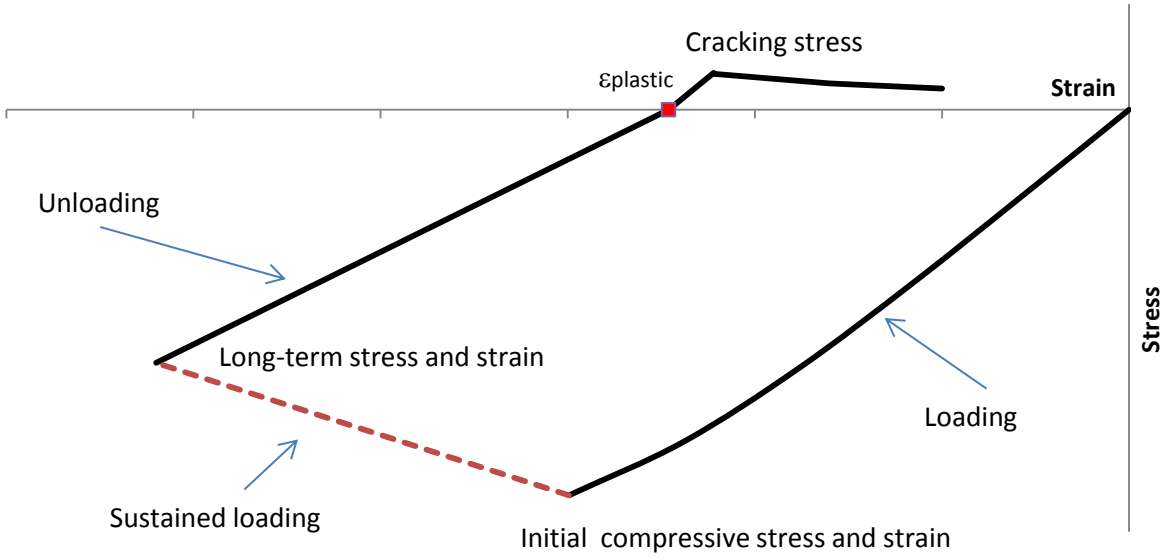

Figure 5.20: Schematic for Unloading case (1)

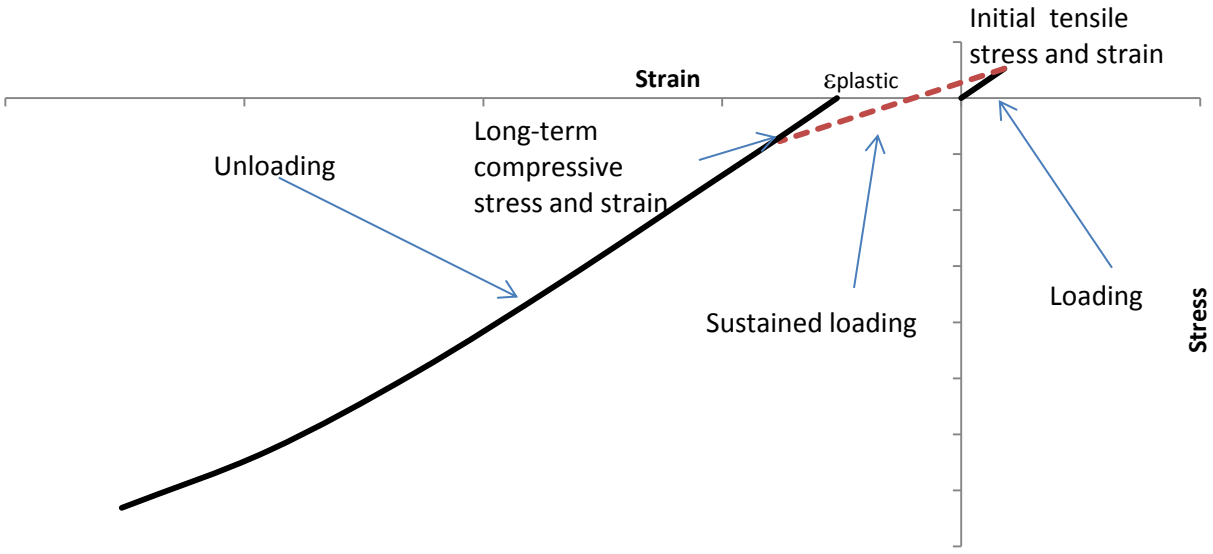

Figure 5.21: Schematic for Unloading case (2)

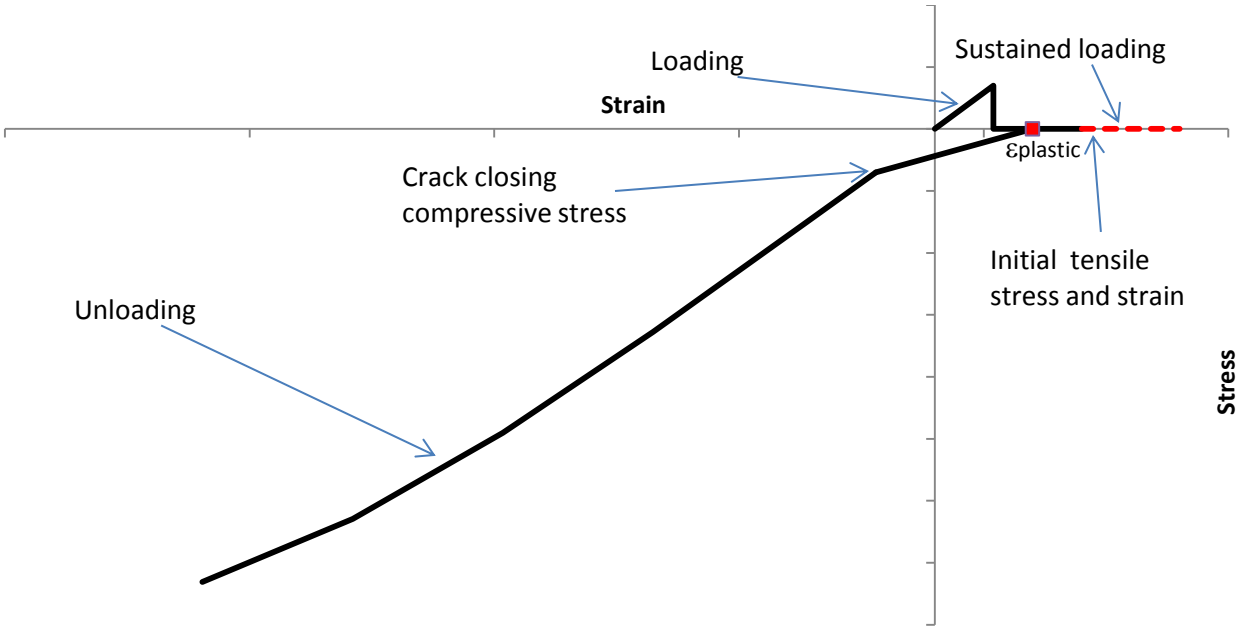

Figure 5.22: Schematic for Unloading case (3)

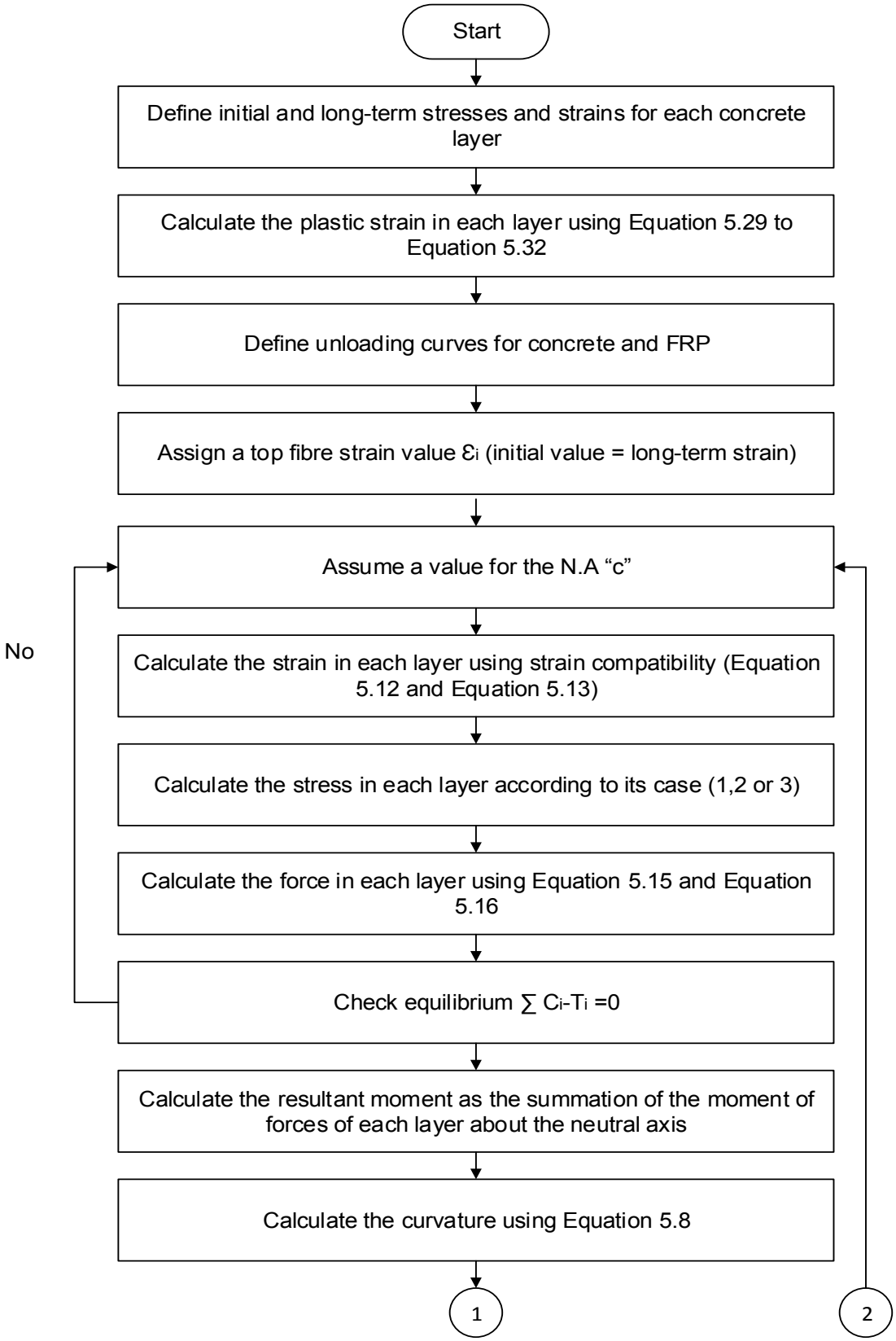
Start
Define initial and long-term stresses and strains for each concrete layer
Calculate the plastic strain in each layer using Equation 5.29 to Equation 5.32
Define unloading curves for concrete and FRP
Assign a top fibre strain value εi (initial value = long-term strain)
Assume a value for the N.A "c"
No
Calculate the strain in each layer using strain compatibility (Equation 5.12 and Equation 5.13)
Calculate the stress in each layer according to its case (1,2 or 3)
Calculate the force in each layer using Equation 5.15 and Equation 5.16
Check equilibrium ∑ Ci-Ti =0
Calculate the resultant moment as the summation of the moment of forces of each layer about the neutral axis
Calculate the curvature using Equation 5.8
1
2

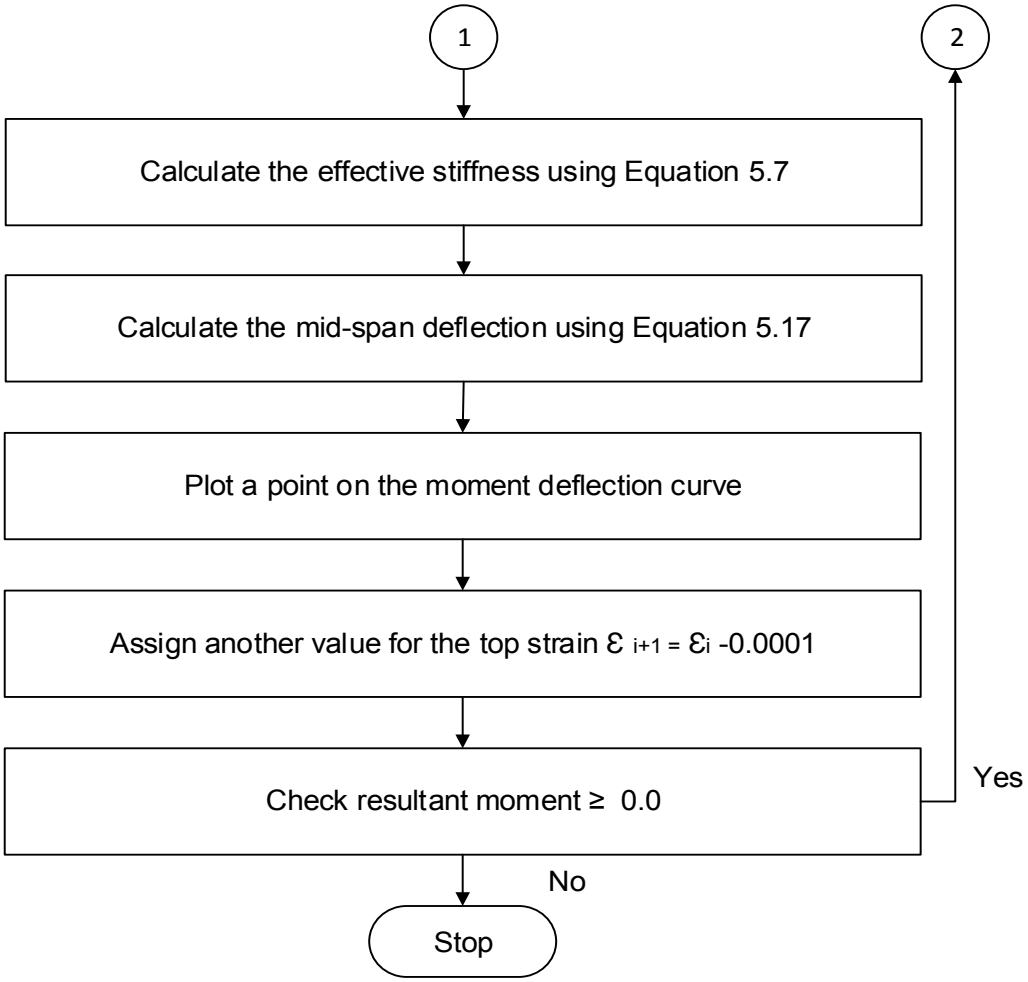

Figure 5.23: Flow chart for the unloading model

5.5.4 Unloading model results

The models described in the previous section were coded into Microsoft Excel similar to the short-term and the long-term models. The main assumptions were as follows:

- Linear strain distribution over the cross-section depth.
- The equilibrium of internal forces is satisfied.

- The stress-strain behaviour of concrete will follow the assumptions made in sections 5.5.1 to 5.5.3.
- The behaviour of GFRP bars is linear (creep of GFRP bars is ignored).

5.5.4.1 Short-term unloading model

Since there is no experimental data for the case of short-term loading and unloading available in this study, the predicted results from the model were compared to the predicted results from the empirical model proposed by Abdel-Rahman (1995).

The Abdel-Rahman (1995) model is shown in Figure 5.24, where the main features of the model are as follows:

1) The load-deflection behaviour is linear up to the cracking load (point A), and then it continues with a linear behaviour but with a lower stiffness until it reaches the desired load (point B)
2) The permanent deflection after unloading (point D) is calculated using a repeated loading moment of inertia (I_{rep}) given in Equation 5.34

$$I_{rep} = I_{cr} + \left(\frac{M_{cr} - M_{dc}}{M_a - M_{dc}}\right)^{2.5}\left(I_g - I_{cr}\right) \leq I_g \qquad \text{Equation 5.34}$$

where, M_{cr} is the cracking moment, M_{dc} is the decompression moment, M_a is the applied moment, I_{cr} is the cracked moment of inertia, and I_g is the gross moment of inertia.

3) The deflection up to the decompression load (point C) during reloading is calculated using the gross moment of inertia of the section.
4) The deflection at any point between the points "C" and "B" during reloading is calculated using linear interpolation between the deflections at the two points.

The comparison between the proposed model and Abdel-Rahman (1995) empirical model is shown in Figure 5.25 and Figure 5.26 for the prestressed beams N40-16-60 and N25-16-60, respectively.

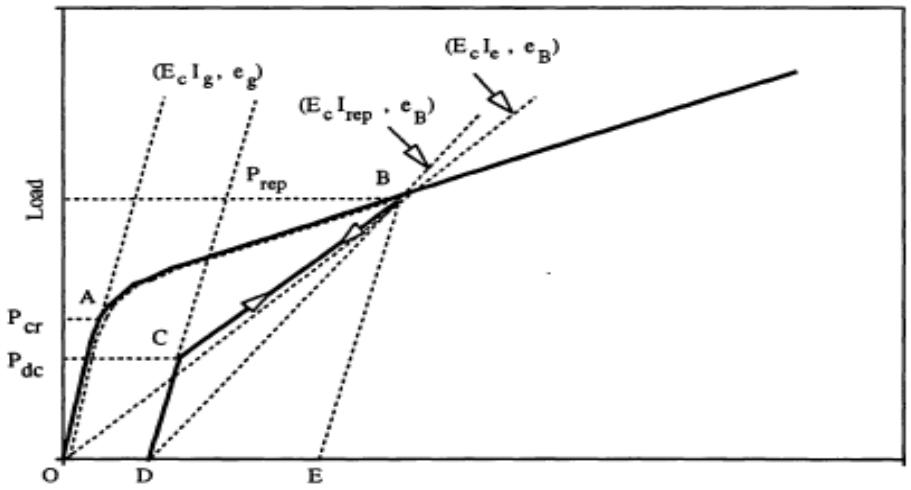

Figure 5.24: Abdel-Rahman (1995) empirical model

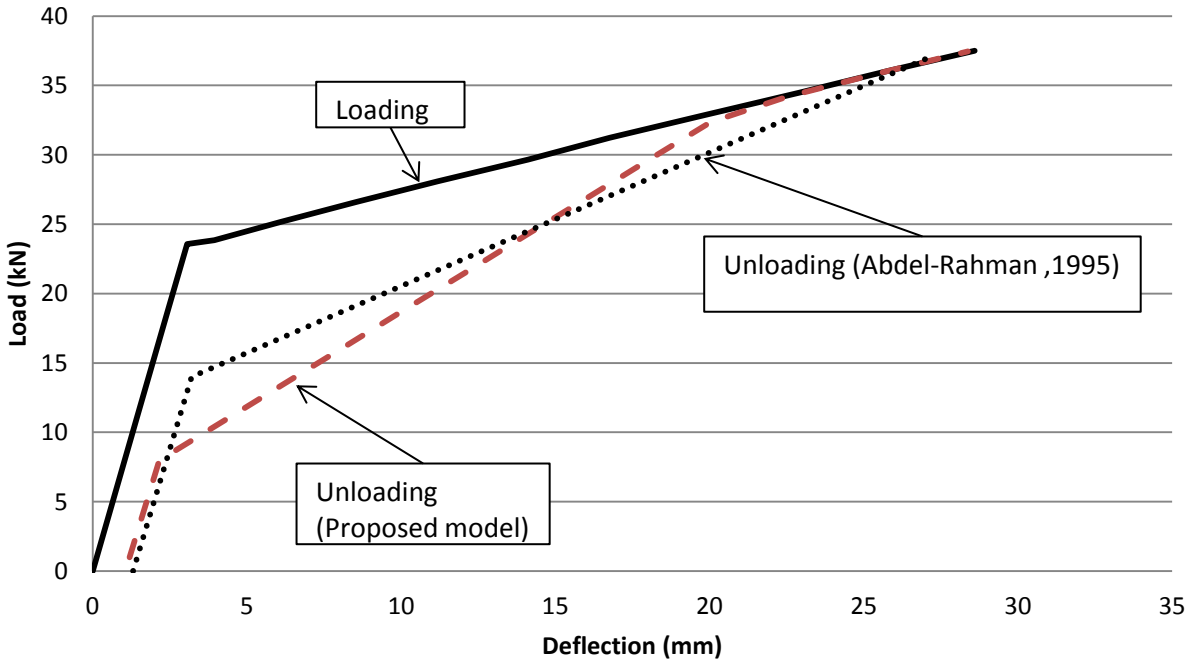

Figure 5.25: Analytical short-term loading/unloading behaviour for N40-16-60

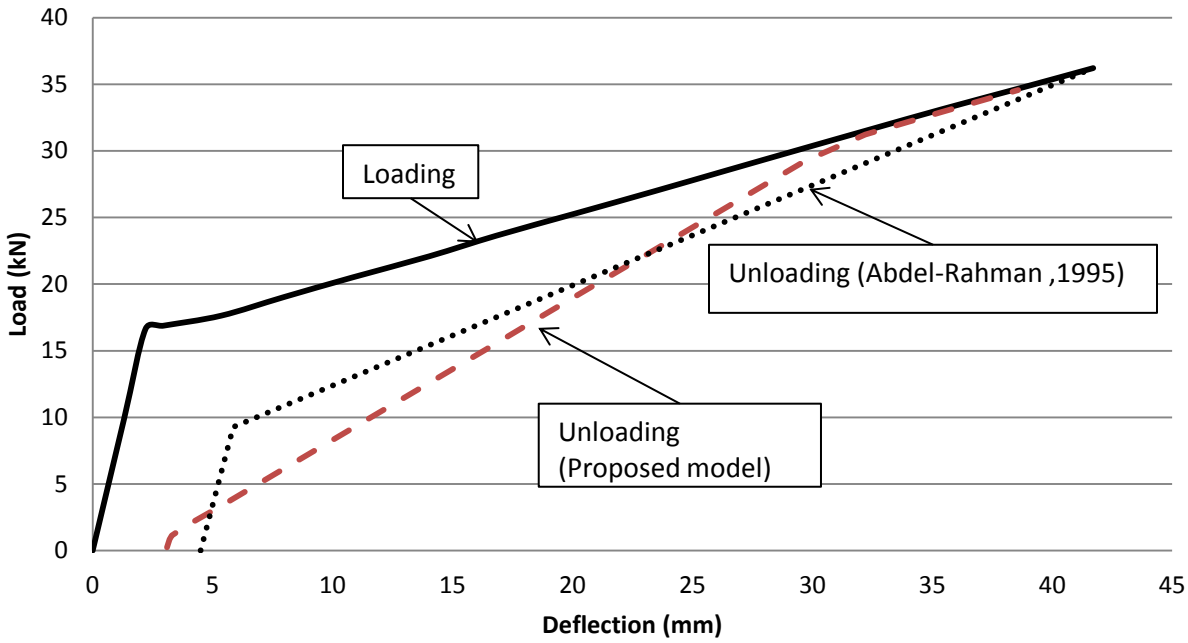

Figure 5.26: Analytical short-term loading/unloading behaviour for N25-16-60

From the figures, the following remarks can be made:

- While the unloading behaviour predicted by Abdel-Rahman (1995) empirical model was bi-linear, the predicted unloading behaviour by the proposed model in this study was tri-linear. From the unloading point, the beam started unloading with a stiffness similar to the loading stiffness (cracked section stiffness) until the strains in the bottom layers reach the plastic strains indicating that the cracks started closing. This resulted in creating compression stresses at the bottom layers while the strains were still in tension. These compression stresses increased the beam effective stiffness giving it a value between the gross section stiffness and the cracked section stiffness. The beam continued unloading with this stiffness until the strains (and stresses) in the bottom layers reached the crack-closing strains indicating the full closure of the cracks as described previously in Section 5.5.2. At this point, the whole section was under compression stresses, which led to increasing the stiffness of the beam to be equal to the gross section stiffness. The beam continued unloading with the gross section stiffness until the load reached zero.

- The load at which the beam stiffness becomes equal to the gross section stiffness (stiffness conversion load) is assumed by Abdel-Rahman (1995) to be equal to the decompression load, which is the load at which the stress at the bottom layer of the beam becomes zero. This stiffness conversion load is calculated by the proposed model to be the load at which the stress at the bottom layers reaches the crack closing stress, which is 1/10 of the concrete compressive strength. This is why the stiffness conversion load by Abdel-Rahman (1995) is higher than that calculated by the proposed model.
- The predicted permanent deflection value is almost the same in both models, with the one predicted by Abdel-Rahman (1995) being slightly higher due to its higher assumed flipping load.

5.5.4.2 Long-term unloading model

The long-term unloading model was used to obtain the strain and stress profiles of the beam sections after unloading. The results for the non-prestressed beam N0-16-60 and the prestressed beam N40-16-60 are shown in Figure 5.27 to Figure 5.30.

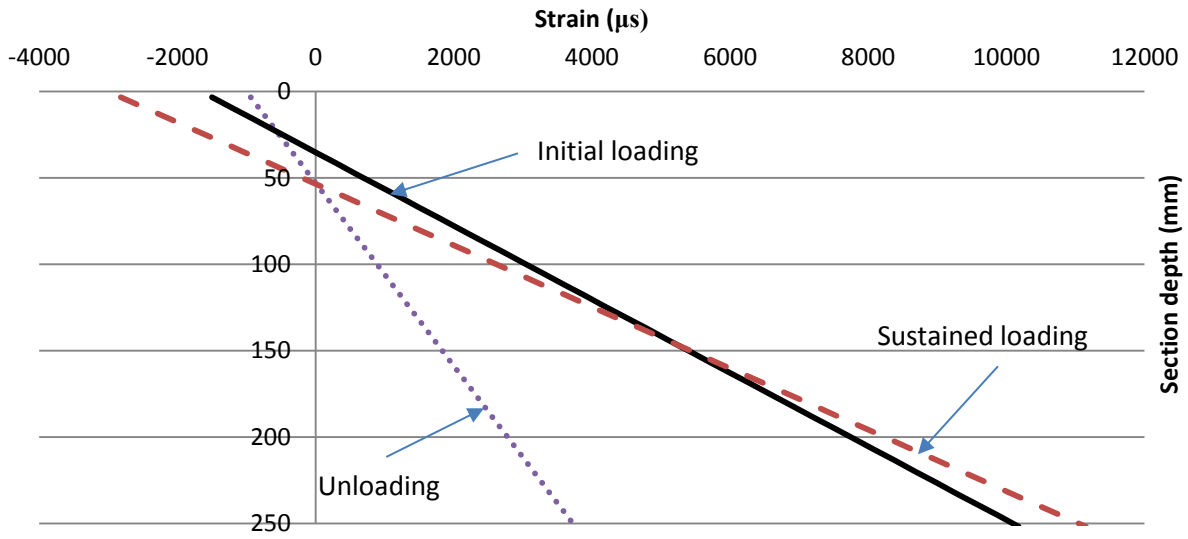

Figure 5.27: Strain profile after unloading for N0-16-60 beam

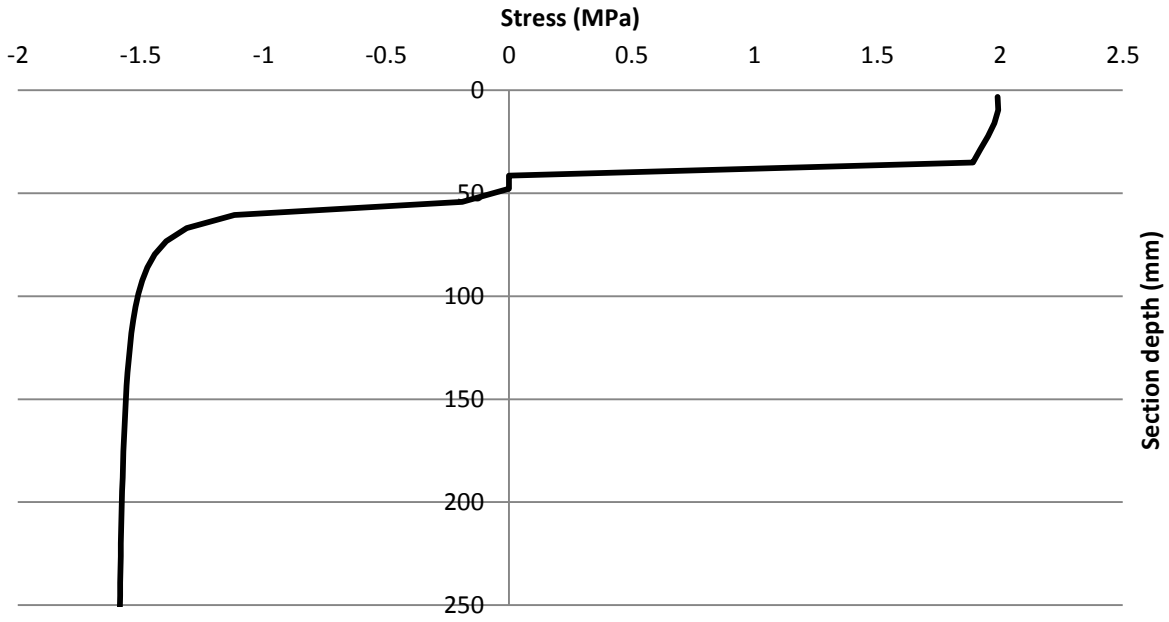

Figure 5.28: Stress profile after unloading for N0-16-60 beam

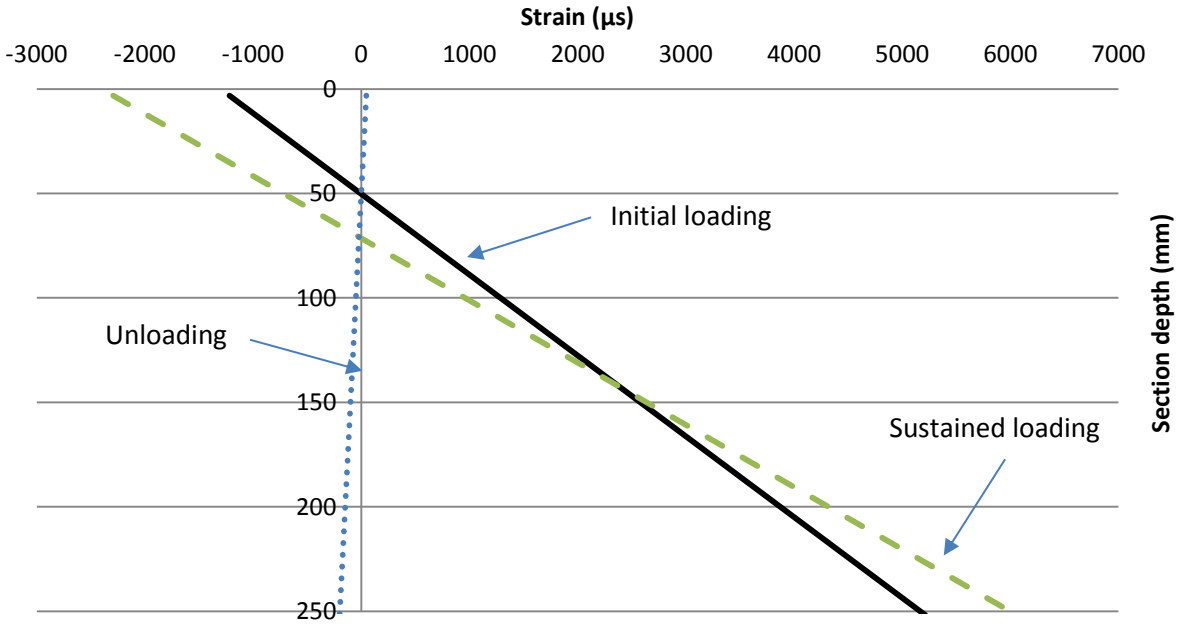

Figure 5.29: Strain profile after unloading for N40-16-60 beam

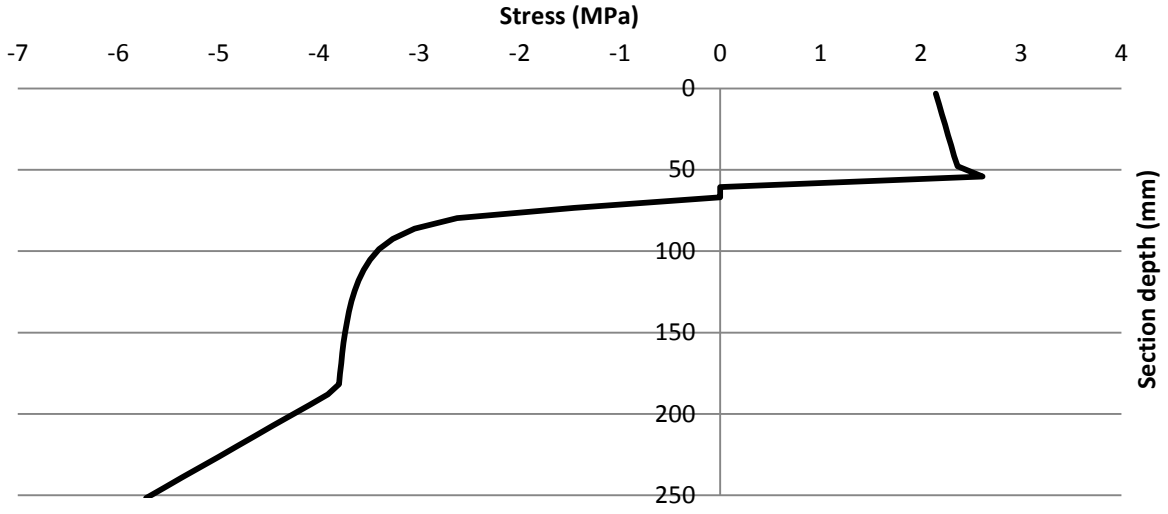

Figure 5.30: Stress profile after unloading for N40-16-60 beam

The stress and strain history of the top concrete layer, the layer at 54 mm depth, and the bottom layers for the N40-16-60 and the N0-16-60 beams were drawn using the short-term and the long-term loading models along with the long-term unloading model as shown in Figure 5.31 to Figure 5.36. The resulting load-deflection diagrams are shown for the same beams in Figure 5.37 and Figure 5.38, respectively.

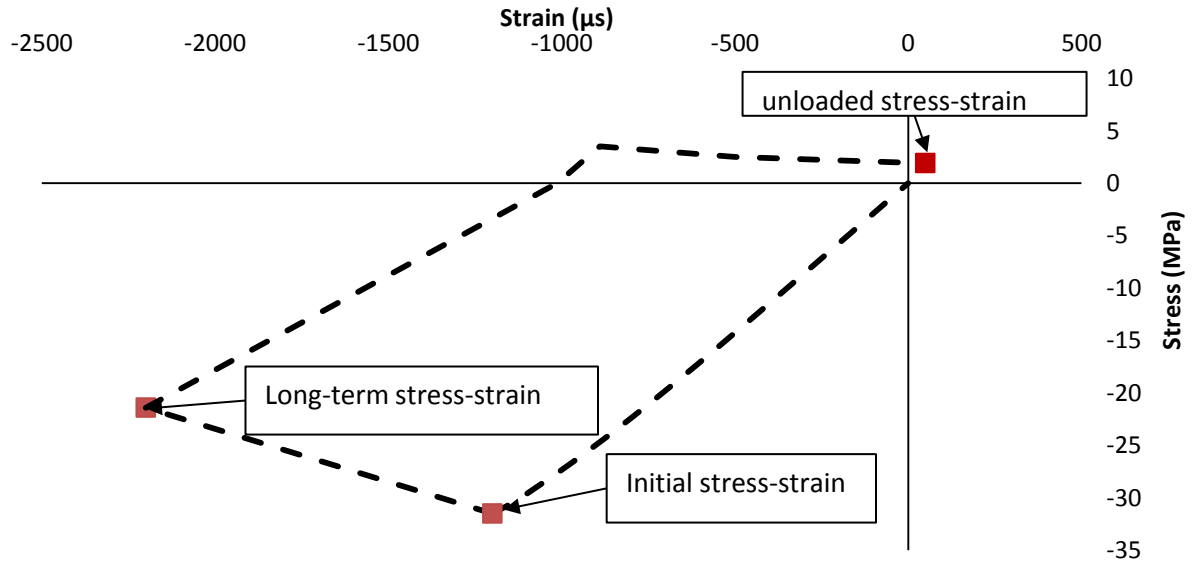

Figure 5.31: Stress-strain history of the top concrete layer for N40-16-60

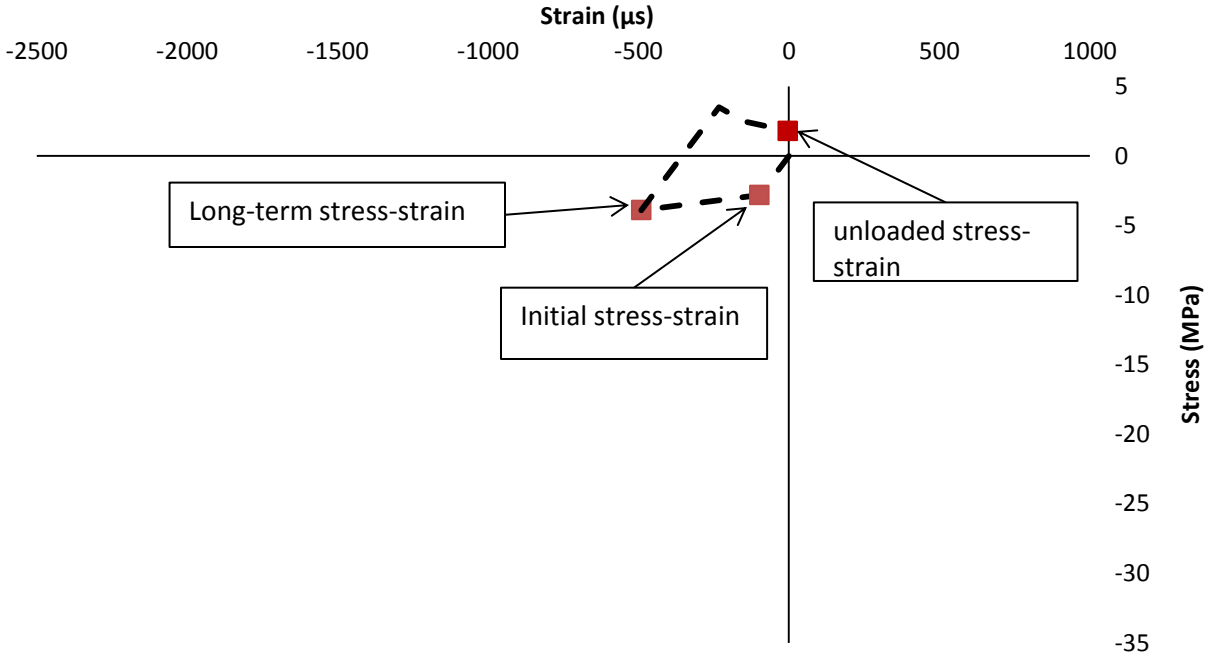

Figure 5.32: Stress-strain history of the layer at 54 mm depth for N40-16-60

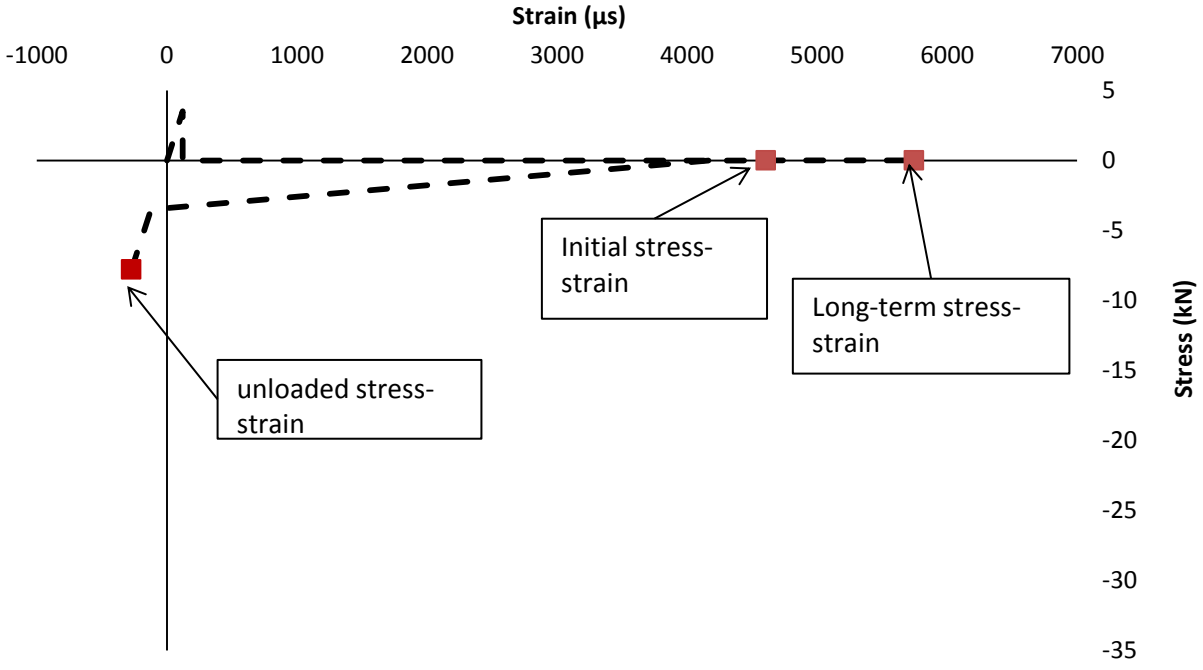

Figure 5.33: Stress-strain history of the bottom concrete layer for N40-16-60

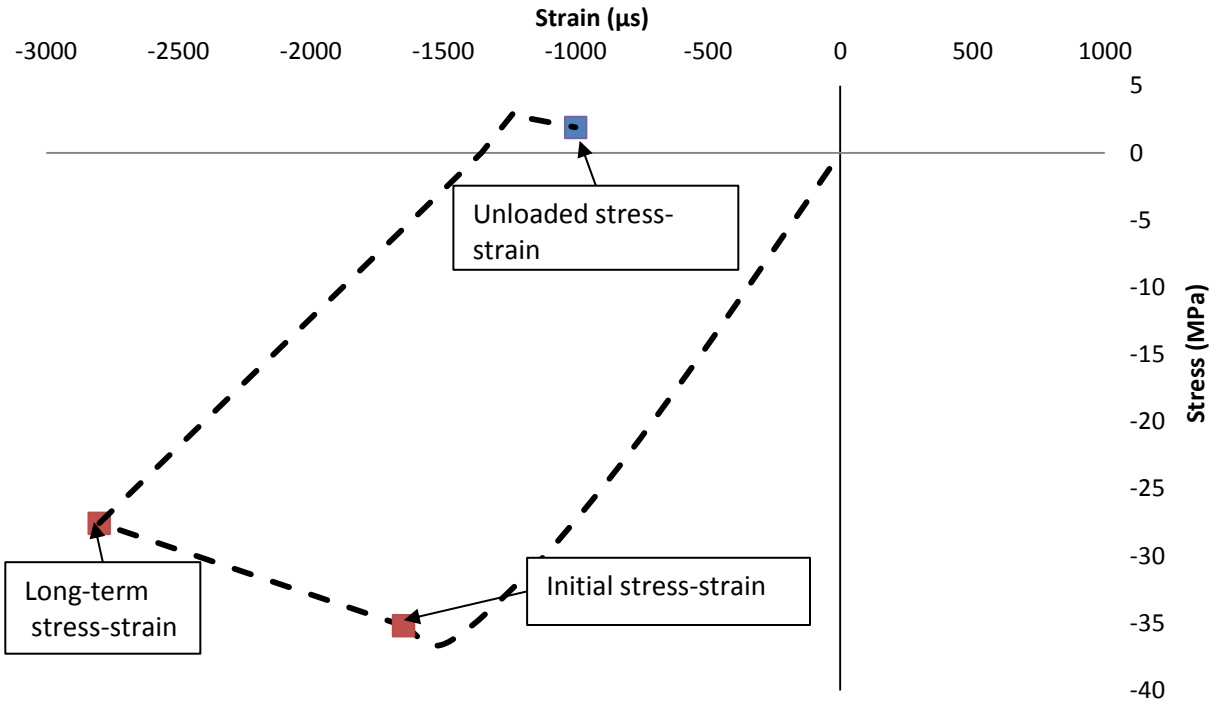

Figure 5.34: Stress-strain history of the top concrete layer for N0-16-60

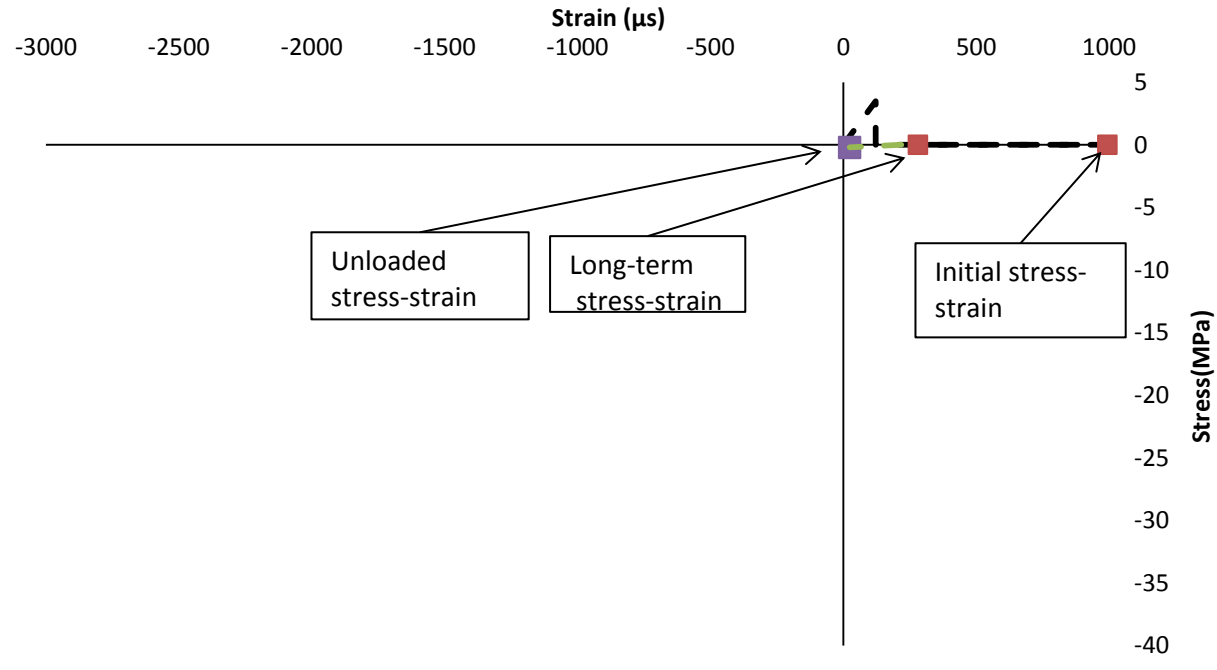

Figure 5.35: Stress-strain history of the layer at 54 mm depth for N0-16-60

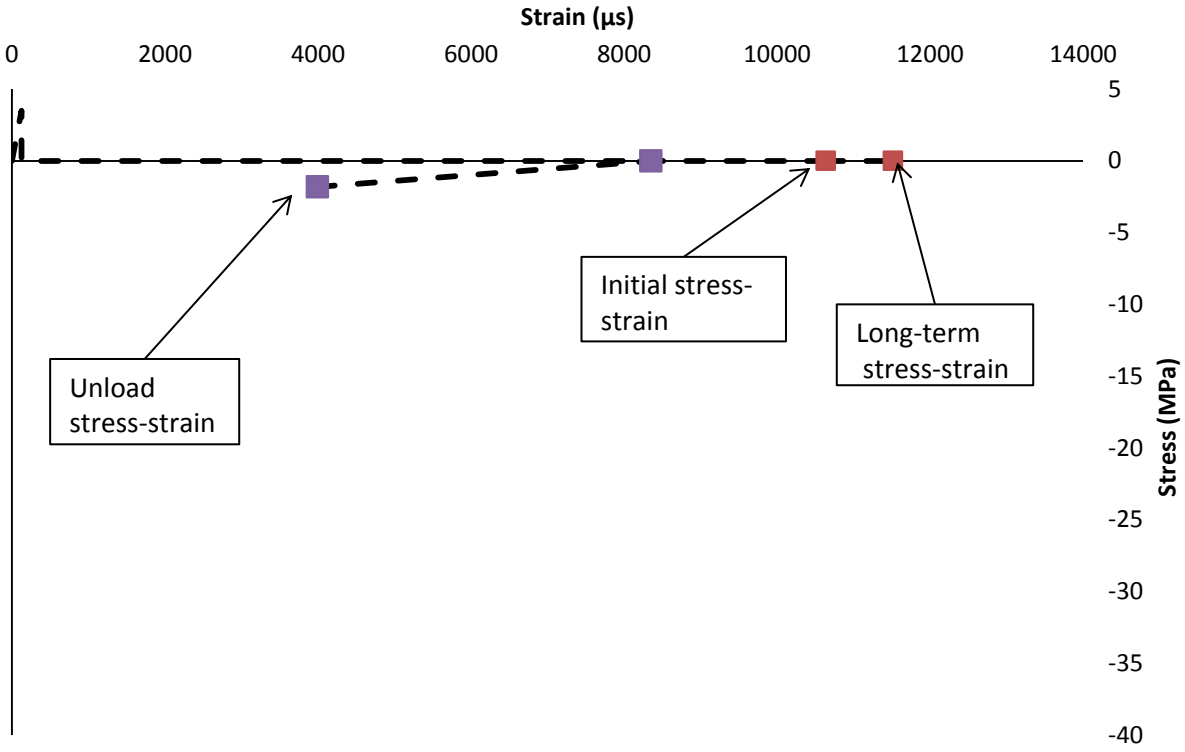

Figure 5.36: Stress-strain history of the bottom concrete layer for N0-16-60

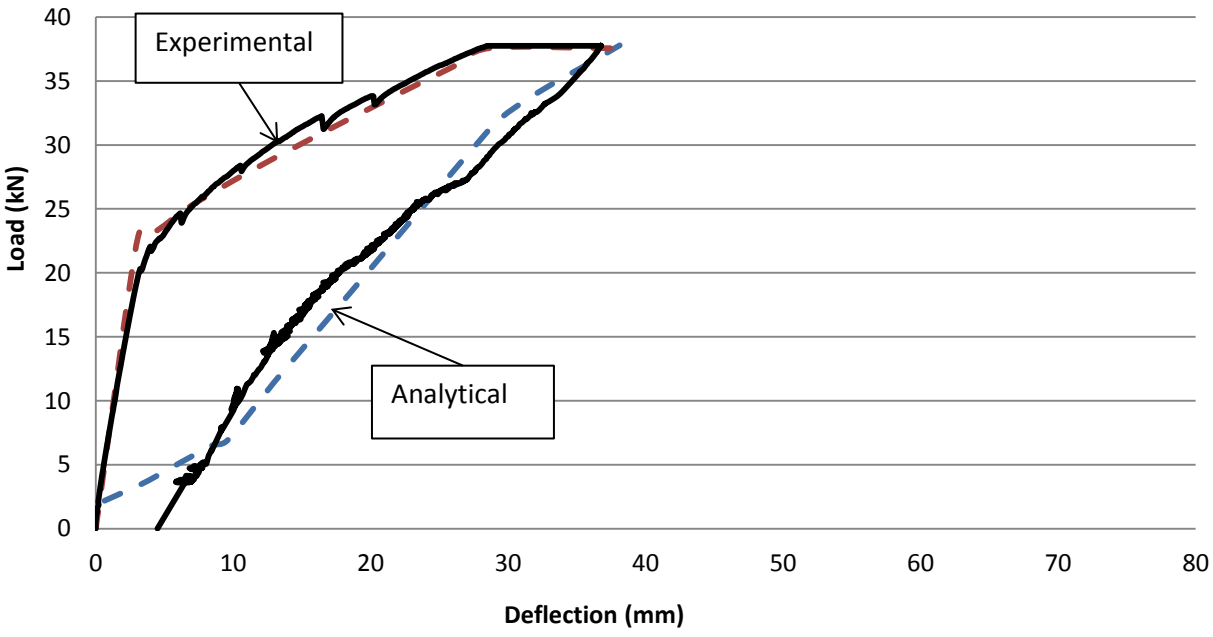

Figure 5.37: Loading/unloading-deflection behaviour for beam N40-16-60

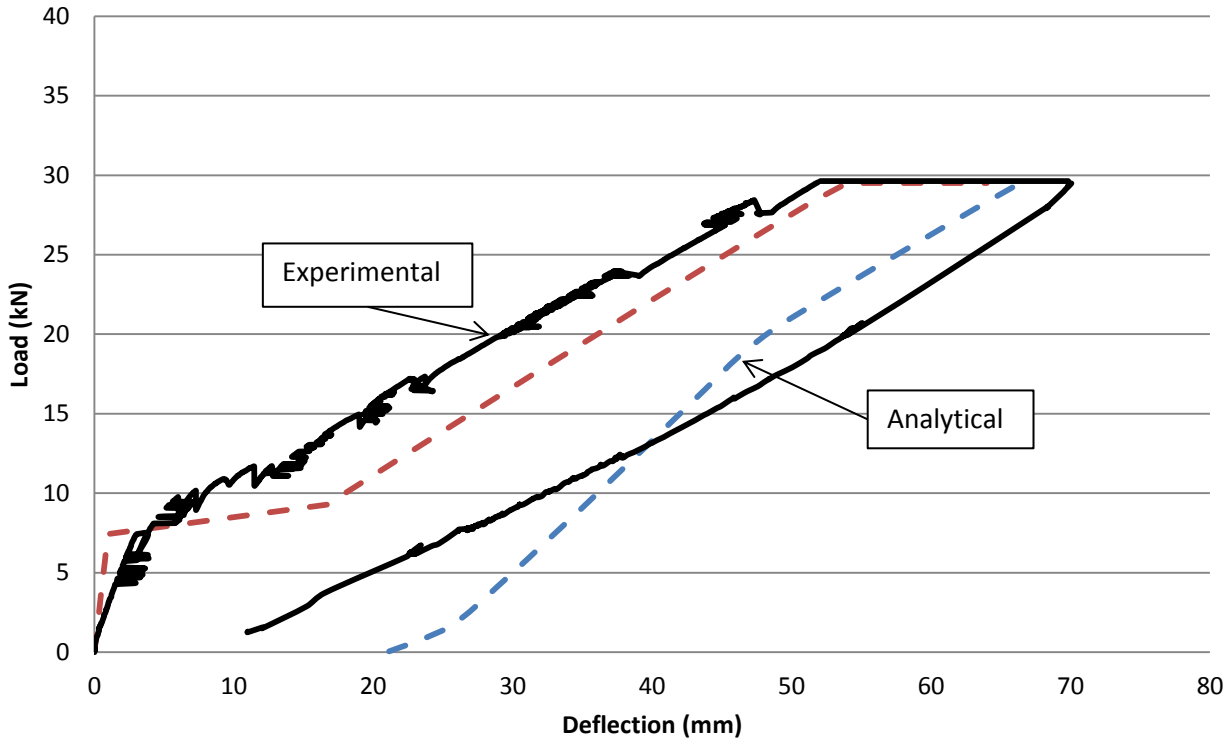

Figure 5.38: Loading/unloading-deflection behaviour for beam N0-16-60

The following notes and conclusions can be made regarding the long-term unloading model results:

- The stress-strain behaviour of concrete layers during unloading follows the assumptions made in sections 5.5.1 to 5.5.3.
- The overall stress and strain profiles obtained from the model agree with what was observed experimentally. For the non-prestressed beam N0-16-60, the final strains at the top of the section were compression strains, but the stresses were tension indicating a cracked surface due to exceeding the cracking strength of concrete. On the other hand, the strains in the prestressed beam N40-16-60 were tension strains due to the effect of the prestressing force, and the predicted stresses are also showing a cracked surface due to exceeding the cracking strength.
- In general, the predicted load-deflections curves are in good agreement with the experimental curves. The difference between the experimental and the predicted load-deflection curves during unloading for the non-prestressed beam presented in Figure 5.38 is due to

the difference between the measured and the predicted long-term deflection from the long-term model.

- A discrepancy appears between the experimental and the predicted curves, where the predicted load-deflection curve tends to flatten at the low load levels, which is more obvious in the prestressed beam. This discrepancy between the experimental results and the analytical results can be attributed to some of the assumptions made in the long-term unloading model. The main assumption causing the error is adding the creep strain to the short-term plastic strain. When the bottom layers reached the crack closing strains, the top layers had already reached the cracking tension strains, which led to decreasing the section stiffness of the beam instead of increasing it to be equal to the gross section stiffness like the case of the short-term unloading. This caused the flattening of the load-deflection curve at the low load levels. This puts a limit on the model that it cannot be used to directly predict the value of the permanent deflection after unloading for a beam that was subjected to sustained loads.
- Better assumptions that represent the actual effect of the sustained loading on the plastic strains of concrete are needed. These assumptions should be able to take into account the actual plastic strains of the concrete due to the short-term loading and the long-term loading so that the permanent deflection of the beams are properly predicted.
- There are no data in the literature that investigated the unloading behaviour of concrete subjected to sustained loading, and investigating that is beyond the scope of this study. Hence, better assumptions cannot be made at this time.

5.6 Reloading model

The load-deflection behaviour of beams prestressed by GFRP bars can be reasonably predicted before cracking using the gross moment of inertia, since the behaviour of the beams at this loading stage is elastic and linear.

When the beams are loaded beyond their cracking load, the deflection behaviour during unloading does not follow the same path as the initial cycle due to the cracking of the beams which causes permanent deformations (Abdel-Rahman, 1995). The effect of cracking becomes more

pronounced for beams subjected to sustained loading due to the effect of non-recoverable creep of the concrete.

Therefore, modeling the load-deflection behaviour of the cracked prestressed beams in the residual static loading (reloading) test is not simple and requires understanding of the beam loading and unloading history. In this study, the beams that were subjected to 60% or 80% sustained load levels were cracked during the initial loading.

The behaviour of these beams during reloading can be divided into two main stages: the first stage for loads lower than the decompression load, and the second stage for loads higher than the decompression load. The decompression load is defined as the load that causes the stress at the bottom fibre of the mid-span section to be zero.

The behaviour of the cracked prestressed beams during the first stage was linear. Since these beams were cracked under the sustained loads, the prestressing force caused the cracks in the tension zone to partially- but not fully- close after unloading, as described before in section 4.8.2. As a result, when the beams were reloaded in the static residual test, they had a stiffness that was less than the original gross section stiffness and more than the cracked section stiffness.

The experimental results showed that the degree of the crack closing, and hence the value of the effective stiffness of the beam during this first stage, is mainly dependent on the prestressing force. The effect of the prestressing force can be seen in Figure 5.39, where the beams H40-16-60, and N40-16-60 had a prestressing force of about 100 kN, and the beams N25-16-60 and N40-12-60 had a prestressing force of about 56 kN. The beams that had the same prestressing force had almost the same stiffness upon reloading. The figure also shows that at the same sustained load level, the beam stiffness increased as the prestressing force was increased. The experimental results also showed that the effect of the sustained loading level on the effective moment of inertia of cracked prestressed beams during reloading is negligible as shown in Figure 5.41 . The stiffness of the beams during the first stage was the same for the 60% and the 80% loading levels.

The deflections of the beams during the first stage were used with Equation 5.17 to calculate the effective moment of inertia for each of them. The relationship between the ratio of the effective moment of inertia to the cracked moment of inertia the non-prestressed section, and the pre-stressing force is almost linear as shown in Figure 5.40, and can be taken as follows:

$$I'_e/I_{cr} = 0.0483\ P_s + 1 \qquad \text{Equation 5.35}$$

where I'_e is the effective moment of inertia of the section due to the partial closing of the cracks, I_{cr} is the cracked moment of inertia of the non-prestressed section, and P_s is the prestressing force in kN.

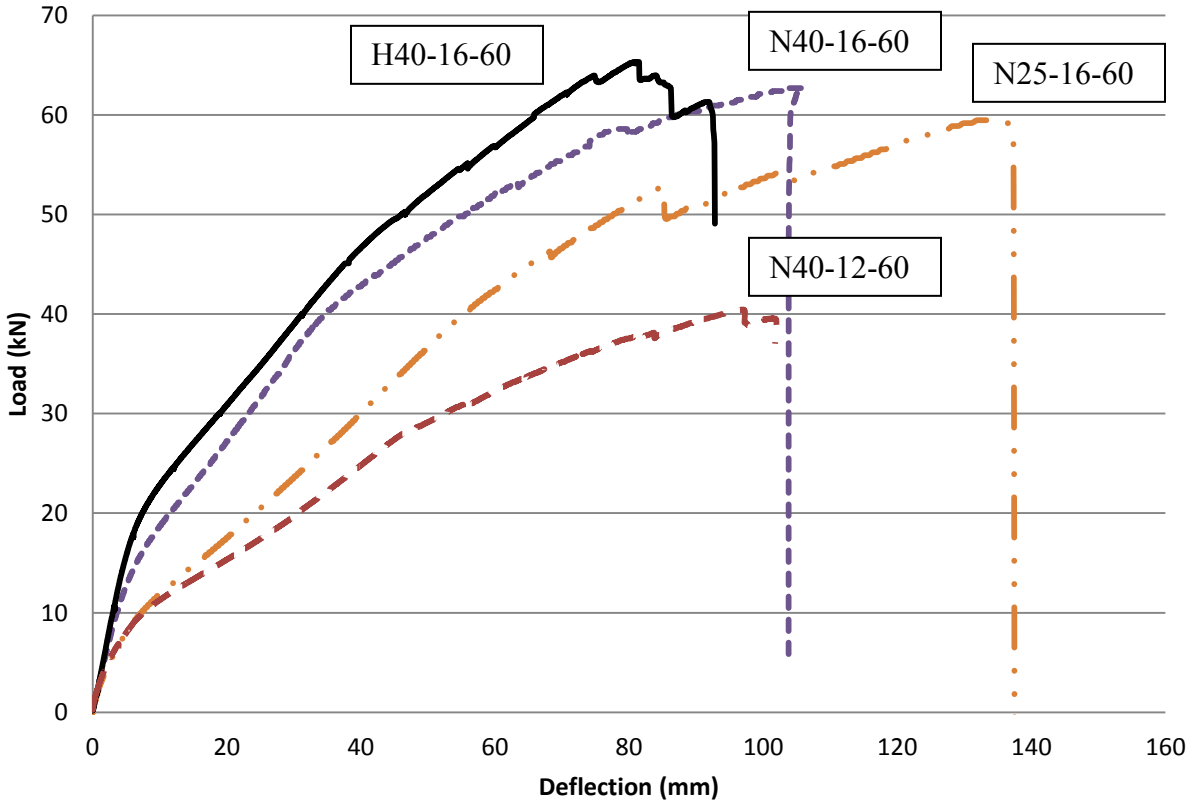

Figure 5.39: Load-deflection behaviour during reloading for 60% sustained loaded beams

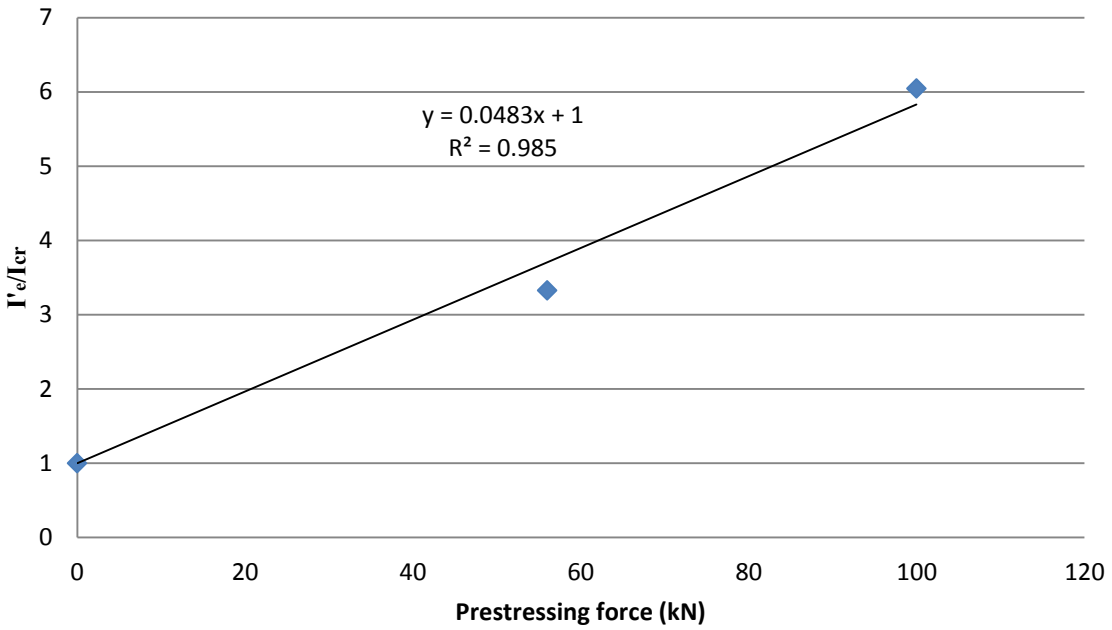

Figure 5.40:I'_e/I_{cr} vs. prestressing force

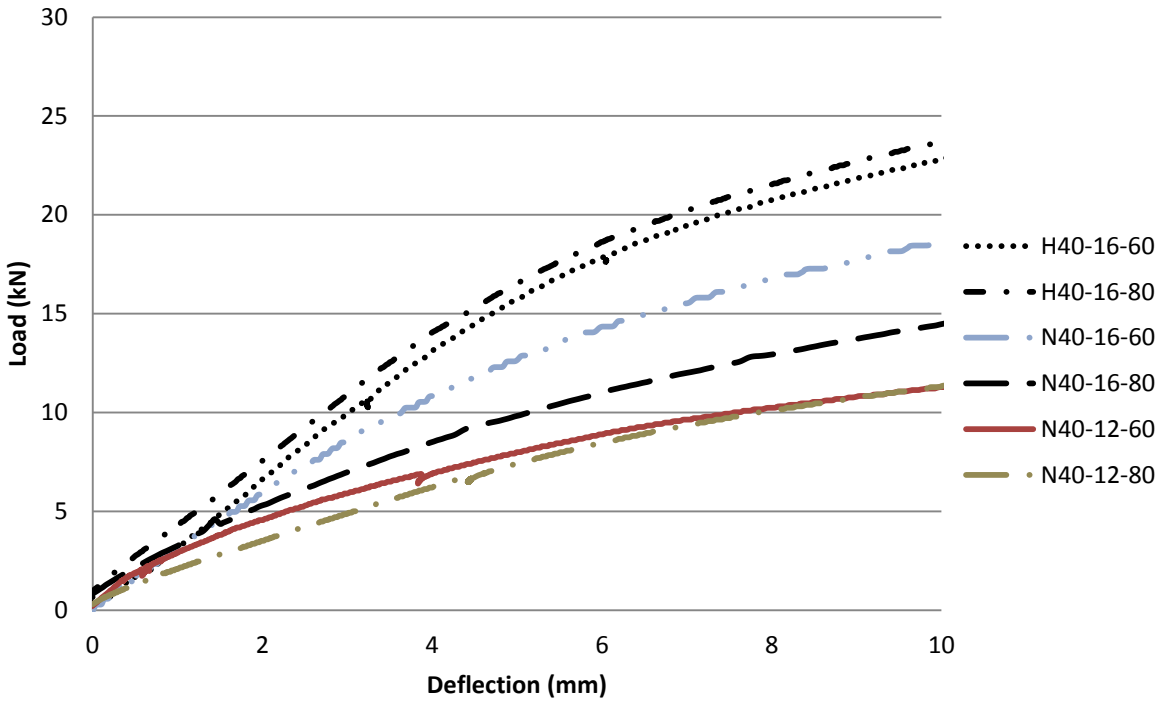

Figure 5.41: First stage of the load-deflection behaviour during reloading for beams with 40% prestressing level

The behaviour of the beams in the second stage was also linear. When the load exceeded the decompression load, its effect on the crack closure was eliminated. As mentioned before in section 4.9, the stiffness of the beams that were cracked under the sustained loads had a slightly higher stiffness than their control beams that were not subjected to any sustained loads. The effect of the increased stiffness is obvious in the beams that were subjected to 60% sustained load levels, while the ones that were subjected to 80% sustained load levels had less stiffness. As previously described in Section 4.9, the increase in the stiffness for the beams that were subjected to 60% sustained load levels is mainly due to "*a form of solid body compaction produced by the creep of the concrete and the autogenous healing of the internal cracks*" caused by the sustained loading (Cook and Chindaprasirt, 1980). The ratio of the stiffness increase was found by Cook and Chindaprasirt (1980) to be in the range between 3.8% and 10.5% for concrete cylinders subjected to sustained loading for 30 days loading (Cook and Chindaprasirt, 1980). The sustained loads ranged between 0.3 and 0.6 of the ultimate load capacity of the cylinders. Therefore, the stiffness of the beams that were subjected to 60% sustained load levels was multiplied by a modification factor of 1.1 during reloading. The stiffness increase was not noticed for the beams that were subjected to 80% sustained load levels. This is attributed to the excessive internal cracking that occurs at such high sustained load levels (Neville et al. 1983) which overcame the effect of the solid body compaction formed due to sustained loading (Cook and Chindaprasirt, 1980).

The typical behaviour of cracked concrete beams prestressed with GFRP bars in the static residual loading test is shown in Figure 5.42. The stiffness of the beam for loads up to the decompression load is taken as $(0.0483P_s + 1)^* E_cI_{cr}$. When the load exceeds the decompression load, the stiffness decreases to be equal to $\zeta^*E_cI_{cr}$, where ζ is a factor that accounts for the increase in the stiffness of concrete caused by the sustained loading and it is taken as 1.1 except for the beams that suffered from the excessive micro-cracking growth as mentioned before where it is taken to be equal to 1.0.

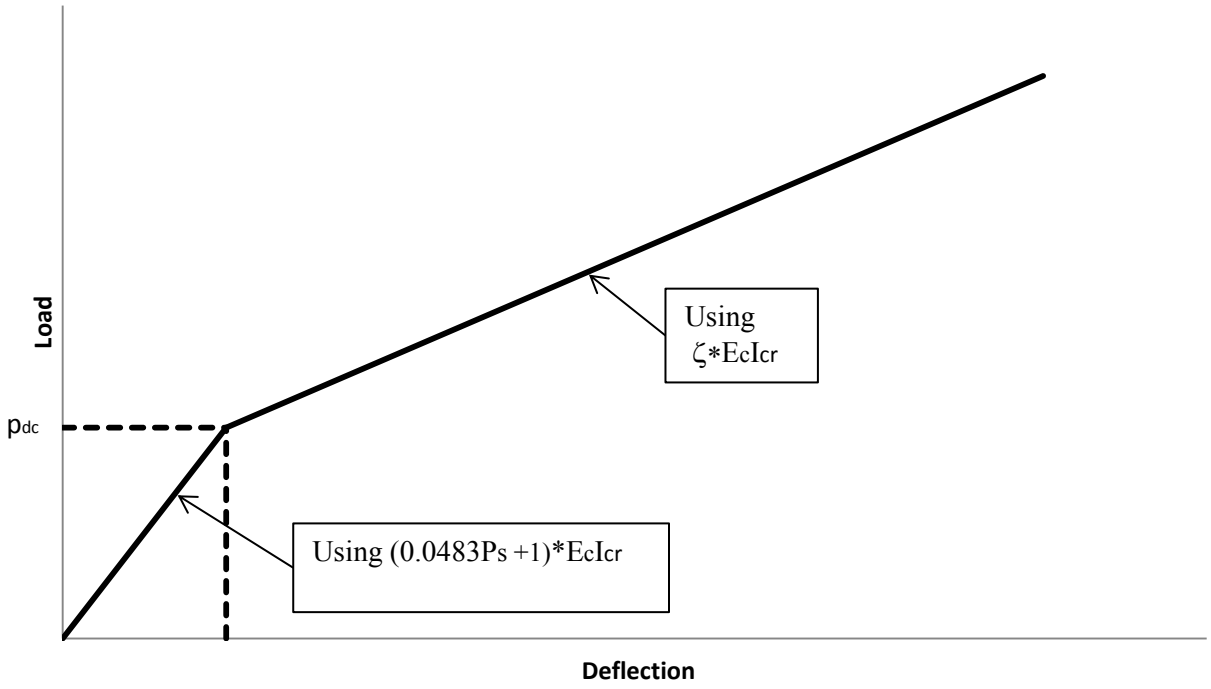

Figure 5.42: Typical behaviour of cracked concrete beams prestressed by GFRP bars during reloading

The predicted results by this model were plotted against the experimental results as shown in Figure 5.43 to Figure 5.46. It can be seen that the predicted results are in good agreement with the experimental results.

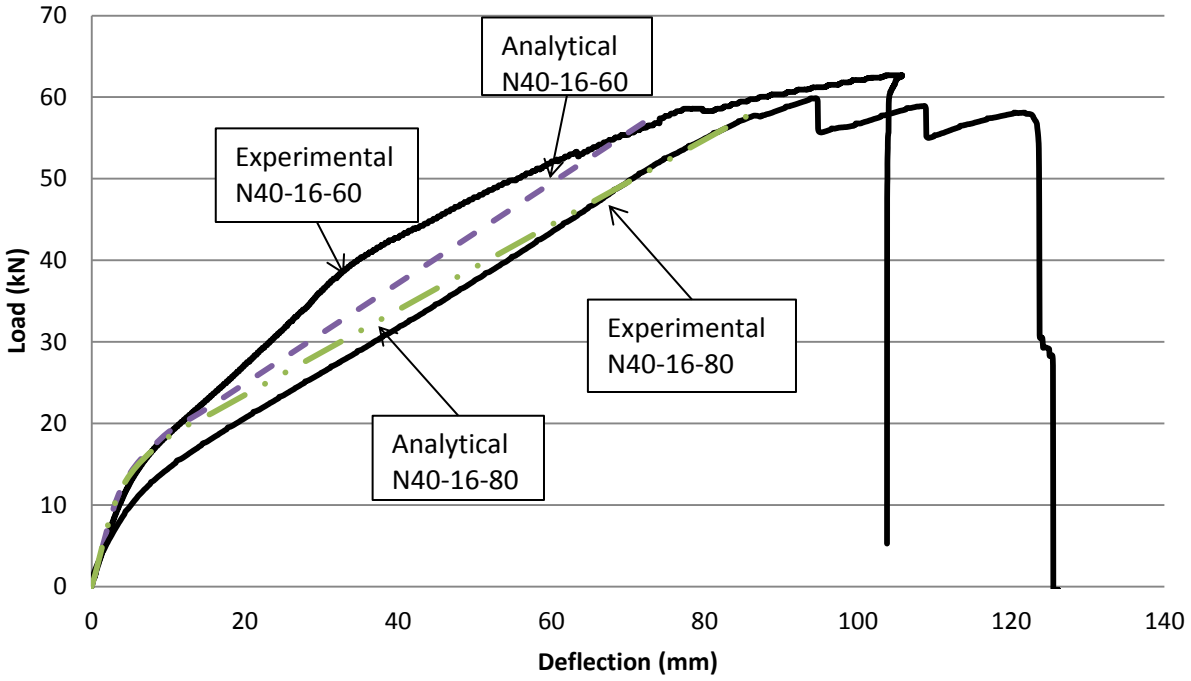

Figure 5.43: Analytical and reloading experimental "load-deflection" curves for H40-16-60 and H40-16-80

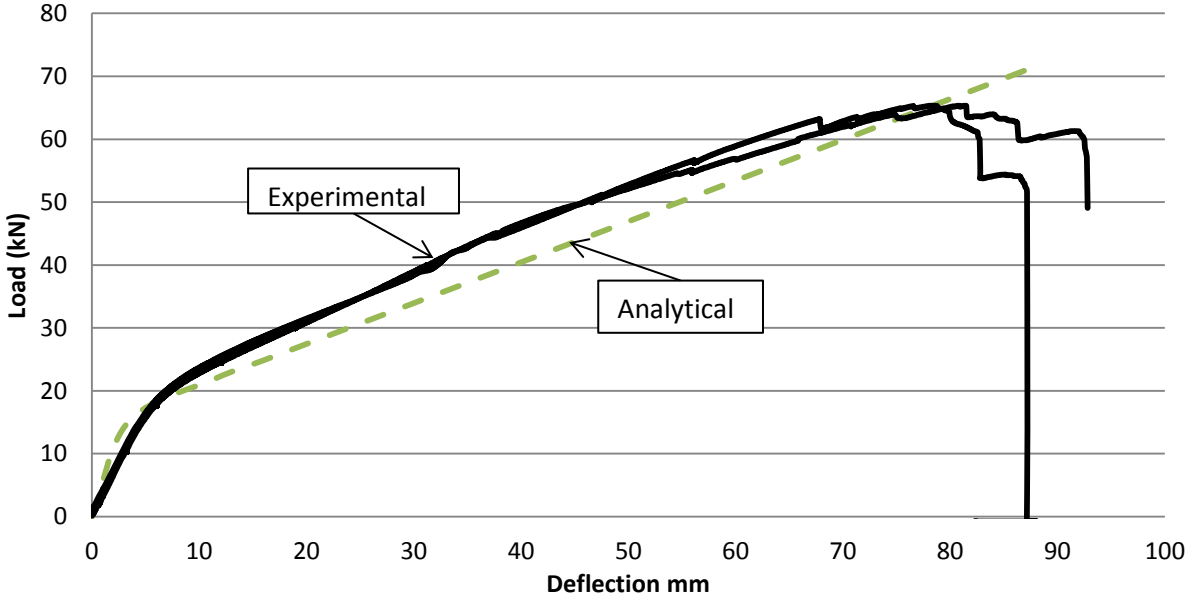

Figure 5.44: Analytical and reloading experimental "load-deflection" curves for H40-16-60 and H40-16-80

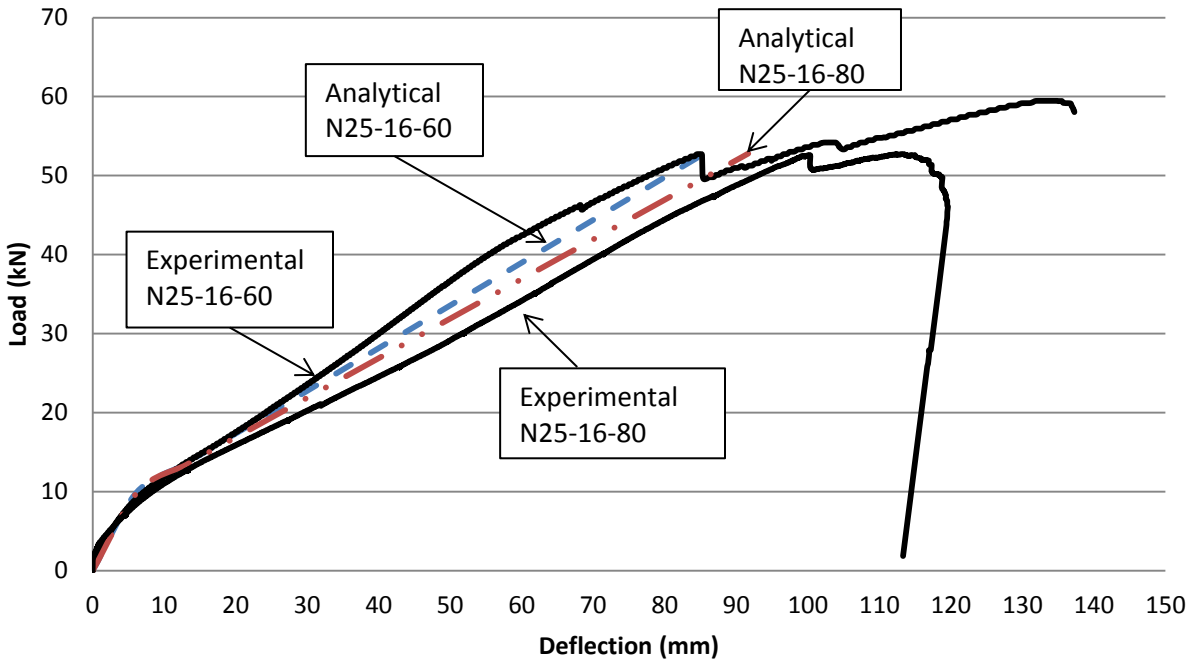

Figure 5.45: Analytical and reloading experimental "load-deflection" curves for N25-16-60 and N25-16-80

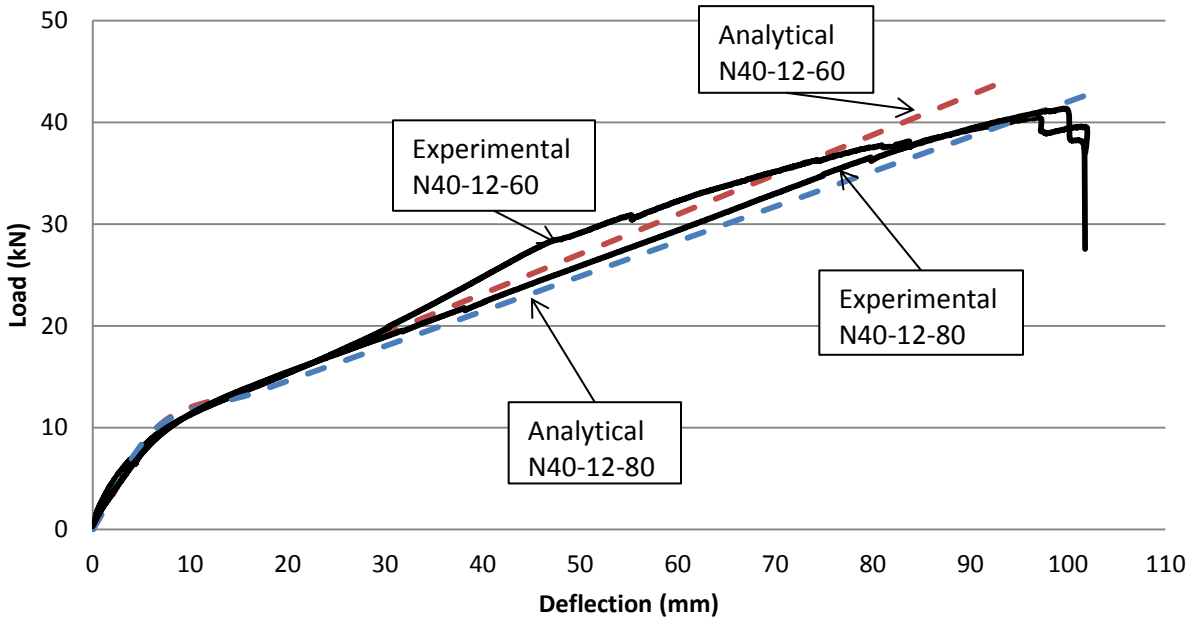

Figure 5.46: Analytical and reloading experimental "load-deflection" curves for N40-12-60 and N40-12-80

The behaviour of the cracked non-prestressed beams was linear up to failure since they had no prestressing force. The stiffness of the beams was taken as $\zeta * E_c I_g$. The predicted and the experimental results are shown in Figure 5.47 and Figure 5.48.

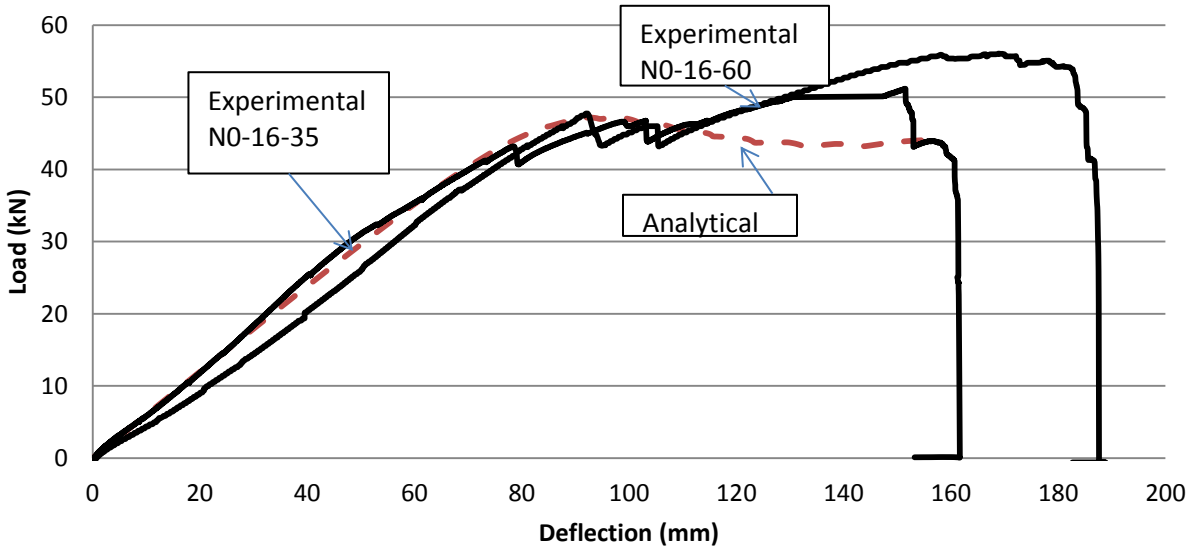

Figure 5.47: Analytical and reloading experimental "load-deflection" curves for N0-16-35 and N0-1-60

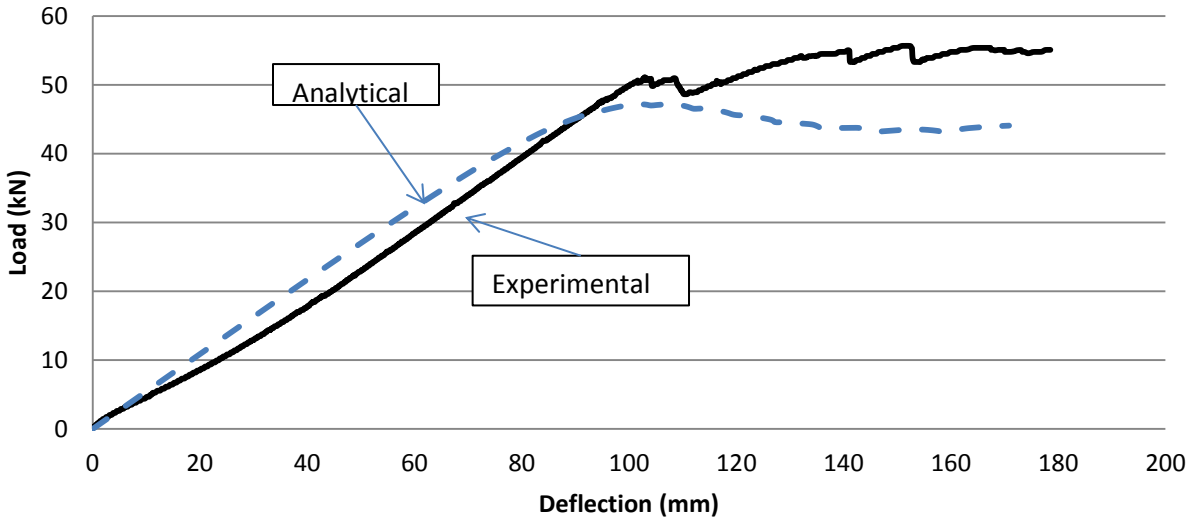

Figure 5.48: Analytical and reloading experimental "load-deflection" curves for N0-16-80

5.7 ACI equation calibration

Equation 5.36 is the equation provided by the ACI 440.4R-04 for predicting the transfer length of prestressed CFRP bars, and it was originally proposed by Mahmoud et al. (1999).

$$L_t = \frac{f_{pi} \times d_p}{\alpha_t f_{ci}^{o.67}} \qquad \text{Equation 5.36}$$

where L_t is the transfer length in mm, f_{pi} is the initial prestressing level in MPa, d_p is the bar diameter in mm, α_t is material dependent coefficient which equals 1.9 for Leadline CFRP bars and 4.8 for CFCC strands in N-mm units., f_{ci} is the concrete compressive strength at time of transfer.

The material dependent coefficient (α_t) was determined from the regression analysis of the test data. The measured transfer length data for GFRP bars used in this study were used to calibrate the equation to come up with a value of α_t for this type of GFRP bars. The curve in Figure 5.49 was drawn with the x-axis being $f_{pi} \times d_p / f_{ci}^{o.67}$ and the y-axis being the measured transfer length L_t. The slope of the straight line from regression analysis is 0.379 which is 1/ α_t. This gives a value of approximately 2.6 in N-mm units for α_t. Calculating the average value for α_t using all of the transfer length readings gives a value of 2.6 in N-mm units with a standard deviation of 0.2 as shown in Table 5.11.

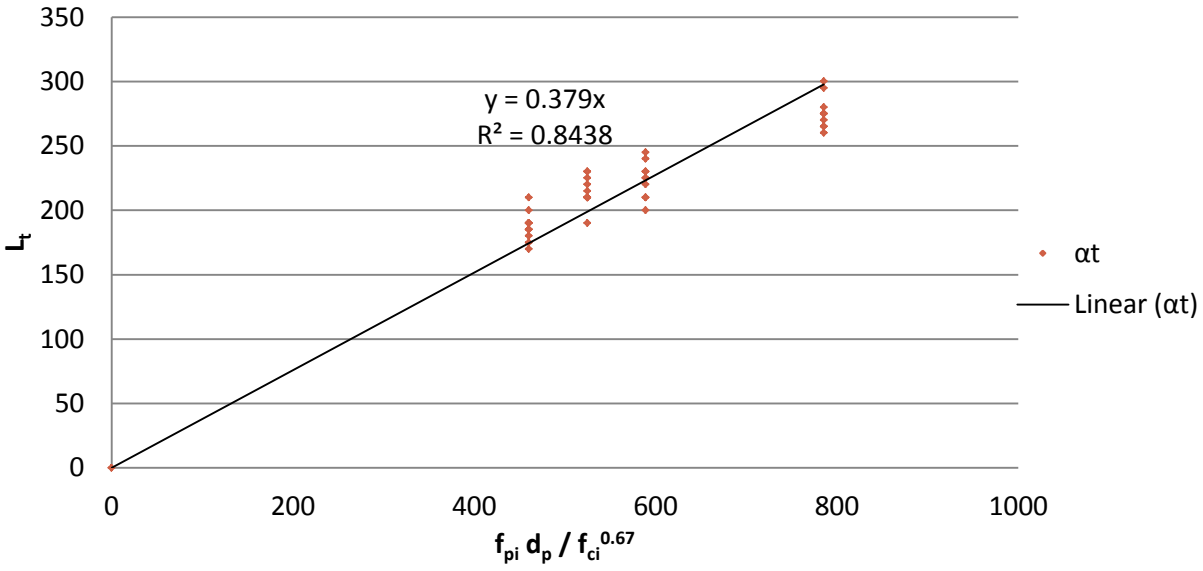

Figure 5.49: Transfer length correlation to establish α_t

Table 5.11: α_t values

Beam	Transfer length (mm)*			α_t			Average	Standard deviation
	Concrete surface strain		Strain gauges on bar					
	Live end	Dead end						
N 40-16-0	275	300	-	2.9	2.6	-	2.6	0.2
N 40-16-35	295	275	-	2.7	2.9	-		
N 40-16-60	275	265	265	2.8	3.0	2.9		
N 40-16-80	280	260	270	2.9	3.0	3.0		
N 40-12-0	230	220	-	2.6	2.7	-		
N 40-12-35	240	200	-	2.5	2.9	-		
N 40-12-60	210	210	245	2.8	2.8	2.4		
N 40-12-80	230	225	225	2.6	2.6	2.6		
H 40-16-0	170	185	185	2.7	2.5	2.5		
H 40-16-35	190	210	180	2.4	2.2	2.6		
H 40-16-60	190	185	190	2.4	2.5	2.4		
H 40-16-80	200	175	190	2.3	2.6	2.4		
N 25-12-0	220	210	230	2.4	2.5	2.3		
N 25-12-35	225	190	245	2.3	2.8	2.4		
N 25-12-60	215	210	210	2.5	2.5	2.3		
N 25-12-80	210	210	230	2.4	2.5	2.5		

Chapter 6
Conclusions and Recommendations

6.1 General

A total of 20 GFRP reinforced/ prestressed beams were constructed and tested up to failure either directly under four-point bending test, or after being subjected to sustained loading for 300 days. The GFRP bars were prestressed to 40% of their ultimate capacity, which is more than the 25% prestressing limit at transfer that is set by CAN/CSA-S6-06 to avoid creep rupture. The effect of the prestressing level, the GFRP bar diameter and the concrete strength on the long-term behaviour of GFRP prestressed concrete was investigated. Transfer length measurements were taken for the prestressed beams, and data on the early relaxation of the GFRP bars was recorded for 277 hours. The study has been completed with the comparison of experimental results using analytical methodologies that were proposed to predict the short-term behaviour, the long-term behaviour, the unloading behaviour, and the residual strength behaviour of GFRP prestressed beams. In addition, the measured transfer length data were used to calibrate a value for the coefficient α_t used in the ACI 440.4R-04 to predict the transfer length values for prestressed GFRP bars.

6.2 Main conclusions

- The new generation of GFRP bars had no measurable relaxation over time up to 277 hours.
- Prestressing decreased total and creep mid-span deflections for all prestressing levels investigated.
- Sustained loading did not affect beams ultimate capacity.
- Analytically, the GFRP creep effect on the beams total deflection was negligible at service load levels and less than 5% at higher load levels.
- Code limit of 25% prestressing level appears to be conservative for the bars used in this study.
- L_t for 16M GFRP bars was about $17d_b$ and $14d_b$ for 30MPa concrete strength and prestressing levels of 40% and 25%, respectively.

- A value of 2.6 in N-mm units is proposed for the coefficient αt used in the ACI 440.4R-04 to predict transfer length values for FRP bars.
- A layer-by-layer strain compatibility model predicted results were in good agreement with the short-term and long-term experimental results.
- A layer-by-layer strain compatibility model was proposed to predict the unloading behaviour of the GFRP reinforced/prestressed beams. The predicted load-deflections curves were in good agreement with the experimental curves except for a discrepancy that appears at the low load levels.

6.3 Detailed conclusions

6.3.1 Long-term behaviour

- The new generation of GFRP bars had no measurable relaxation over time up to 277 hours compared to those reported in the recent literature by Fornůsek et al (2009) where the relaxation of the GFRP bars was 3.3% after 24 hours, and 7.3% after 28 days.
- Prestressing of GFRP bars significantly decreased the beam deflections under service loading conditions in comparison to non-prestressed beams with the same section.
- At the 35% and the 60% load levels (service loading levels), the total and the long-term deflections decreased as the prestressing level increased. The decrease in the total deflection was mainly due to the increase in the cracking moment of the prestressed beams. The decrease in the long-term deflection was attributed to the decrease in the concrete compressive stresses due to the prestressing forces.
- At the 80% sustained loading level, the prestressing level had no significant effect on the long-term deflection of the beams due to the severe internal micro-cracking that takes place in the concrete at high sustained stress levels.
- Loading the beams under different levels of sustained loading for 300 days did not affect their ultimate capacity. This suggests that creep or relaxation of the GFRP bars was not significant and did not affect the strength of the beams. The insignificant effect of the GFRP creep on the long-term behaviour of the beams was also proven analytically by implementing the creep data for the GFRP bars tested in air within the analytical model to investigate its effect on the overall long-term behaviour of the beams. The results

showed that the effect of the GFRP creep on the beam total deflection was almost negligible for the 35% sustained load level beams, and it resulted in about 5% increase in the total deflection of the 60% and 80% sustained load level beams. This was in spite of having prestress levels of up to 40% of ultimate (which exceeds the typical Code prestress limit of 25%) and having sustained stress levels under load of up to 75% of ultimate.

- The Code limits on the prestressing levels of GFRP bars (only 25% of the bar ultimate capacity) appear to be conservative for the bars used in this study. The beams prestressed to 40% of the GFRP bars ultimate capacity did not show any signs of adverse effects due to the high prestressing levels. The Code limitations for prestress level should be revised to consider the performance of the bars in standard tests (performance based) rather than a single stress level.
- The concrete strength had no significant effect on the long-term performance of GFRP prestressed concrete beams at the 35% and the 60% sustained load levels.
- The higher concrete strength decreased the total deflection, the total concrete strain, the long-term deflection and the creep concrete strain for the beams at 80% sustained load levels. The reason was that the ratio between the applied stress and the concrete strength was about 80% for the normal concrete strength beams and was about 50% for the high strength concrete beams. The high stress to strength ratio for the normal concrete strength beams led to the initiation of severe internal micro-cracking in the concrete that resulted in increased creep (Neville et al. 1983), while the severe micro-cracking did not take place for the high strength concrete beams.
- Long-term deflections increased as the sustained load level increased. For the prestressed beams in the N40-16 group, the long-term deflections at 60% sustained load and 80% sustained load were 1.8 times and 4.4 times the long-term deflection for the beams subjected to sustained load at 35% of ultimate for 300 days. For the non- prestressed beams, the increase was not that significant, where the long-term deflections at 60% sustained load were almost the same as the beams at 35% of ultimate, and the long-term deflections at 80% sustained load were 1.1 times for the beams subjected to sustained load at 35% of ultimate. The greater increase for the prestressed beams was due to the fact that the beams subjected to 35% of ultimate were uncracked for the prestressed case and cracked for the non-prestressed case.

6.3.2 Unloading-reloading behaviour

- When concrete is loaded and then the load is removed, the elastic strain will be recovered but the plastic strain will act as a strain offset similar to the elastic offsets resulting from thermal expansion or other pre-strain effects (Vecchio, 1999). This causes a shift in the tensile base curve to the compressive plastic offset strain. Therefore, the concrete can change the sense of the stress from compression to tension only after recovering the elastic part of the strain and not the total strain. This is why the beams that were cracked under sustained loading experienced tension cracks on their top fibres when the load was removed.
- The behaviour of the cracked prestressed beams during reloading was linear up the decompression load, and then linear with a reduced stiffness.
- The initial stiffness of the cracked prestressed beams during reloading was only dependent on the prestressing level of the beam. It increased with the increase of the prestressing level.
- The reduced stiffness of the cracked prestressed beams during reloading after the load exceeded the decompression moment was higher than the cracked section stiffness of the control beam for the 35% and the 60% sustained load levels. This increase in the stiffness was mainly due to "*a form of solid body compaction produced by the creep of the concrete and the autogenous healing of the internal cracks* "caused by the sustained loading (Cook and Chindaprasirt, 1980).

6.3.3 Analytical models

- A model based on layer-by-layer strain compatibility analysis was used to predict the short-term load-deflection behaviour and the long-term deformations of GFRP prestressed concrete beams. The predicted values were in good agreement with the experimental results.
- The creep coefficient value calculated from the ACI 209-92 does not account for the increase in the concrete creep, for beams subjected to high sustained load levels (more than 0.6-0.8 of the concrete ultimate strength). Neville et al. (1983) provided scale factors for

the creep coefficients that could be used for concrete subjected to sustained load values that are 0.8 of the concrete ultimate strength.

- A simplified short-term unloading model was proposed assuming the unloading behaviour of concrete is linear between the unloading strain and the plastic strain. The results were comparable to those obtained from the empirical model proposed by Abdel-Rahman (1995).
- A model to predict the unloading behaviour of the GFRP reinforced/prestressed beams after being subjected to sustained loading was proposed. The model was based on layer-by-layer strain compatibility analysis. The predicted load-deflections curves from the model were in good agreement with the experimental curves except for a discrepancy that appears between the experimental and the predicted curves where the predicted load-deflection curve tends to flatten at the low load levels, which is more obvious in the pre-stressed beams. The error was mainly due to adding the creep strain to the plastic strain, especially for the concrete layers in compression, which widened the zone where concrete has compression strain values and tension stress values.

6.3.4 Transfer length

- The transfer length of 16 mm diameter GFRP bars in concrete with compressive strength of 30 MPa was about $17d_b$ (bar diameter), and $14d_b$ for prestressing levels of 40% and 25%.
- The transfer length of GFRP bars decreases with increasing concrete compressive strength at the time of release.
- The transfer length of GFRP bars decreases with decreasing the prestressing stress.
- Expressing the transfer length in terms of the bar diameter alone may result in inaccurate results since it depends also on the prestressing level and the concrete compressive strength.
- A value of 2.6 in N-mm units is proposed for the coefficient α_t used in the ACI 440.4R-04 to predict transfer length values for FRP bars.

6.4 Recommendations for future work

A number of parameters were outside the scope of the present work, although they would provide a deeper understanding of some of the observations made in this study. It is recommended that the following be considered for future work:

- An investigation of the effect of the high temperature on the long-term behaviour of GFRP prestressed concrete beams.
- An experimental and analytical program focusing on the unloading behaviour of concrete members after being subjected to sustained loading.
- An experimental and analytical program focusing on the fatigue behaviour of GFRP prestressed concrete beams

References

Abdelrahman, A. (1995). Serviceability of concrete beams prestressed by carbon reinforced plastics tendons. (PhD thesis, University of Manitoba,Winnipeg, Manitoba, Canada).

ACI Committee 209. (1992). *ACI 209R-92: Prediction of creep, shrinkage, and temperature effects in concrete structures (reapproved 2008)*. Farmington Hills, Michigan, USA: American Concrete Institute.

ACI Committee 440. (2004). *ACI 440.4R-04:Prestressing concrete structures with FRP tendons (reapproved 2011)*. Farmington Hills, Michigan, USA: American Concrete Institute.

ACI Committee 440. (2006). *ACI 440.1R-06 :Guide for the design and construction of structural concrete reinforced with FRP bars*. Farmington Hills, Michigan, USA: American Concrete Institute.

ACI Committee 440. (2007). *ACI 440R-07 : Report on fibre-reinforced polymer (FRP) reinforcement for concrete structures*. Farmington Hills, Michigan, USA: American Concrete Institute.

Aitcin, P. (1999). Demystifying autogenous shrinkage. *Concrete International, 21*(11).

Al-Mayah, A., Soudki, K., & Plumtree, A. (2006). Development and assessment of a new CFRP rod-anchor system for prestressed concrete. *Applied Composite Materials, 13*(5).

Almusallam, T. H., & Al-Salloum, Y. A. (2006). Durability of GFRP rebars in concrete beams under sustained loads at severe environments. *Journal of Composite Materials, 40*(7).

Al-Salloum, Y. A., & Almusallam, T. H. (2007). Creep effect on the behavior of concrete beams reinforced with GFRP bars subjected to different environments. *Construction and Building Materials, 21*(7).

Antoine, E. N. (2004). *Prestressed concrete analysis and design: Fundamentals-2nd Edition*. Ann Arbor, Michigan, USA: Techno Press 3000.

Aslani, F., & Jowkarmeimandi, R. (2012). Stress–strain model for concrete under cyclic loading. *Magazine of Concrete Research, 64*(8)

ASTM D7205 / D7205M-06. (2011). *Standard test method for tensile properties of fiber reinforced polymer matrix composite bars*. ASTM International, West Conshohocken, PA,USA.

Bacinskas, D., Kaklauskas, G., Gribniak, V., Sung, W. -., & Shih, M. -. (2012). Layer model for long-term deflection analysis of cracked reinforced concrete bending members. *Mechanics of Time-Dependent Materials, 16*(2).

Barnes, R. W., Grove, J. W., & Burns, N. H. (2003). Experimental assessment of factors affecting transfer length. *ACI Structural Journal, 100*(6).

Braimah, A., Green, M., Soudki, K., & Clapp, F. (1999). Long-term behavior of concrete beams prestressed with carbon fiber tendons. *ACI Special Publication, 188*.

Braimah, A. (2000). Long-term and fatigue behaviour of carbon fibre reinforced polymer prestressed concrete beams. (PhD, Queen's University, Kingston, ON, Canada).

Branson, D. E. (1977). *Deformation of concrete structures*. New York, NY, USA: McGraw-Hill Companies.

Bruegger, J. P. (1974). Methods of analysis of the effects of creep in concrete structures. (PhD, Universty of Toronto, Toronto, ON., Canada).

CAN/CSA A23.3-04. (2004). *Design of concrete structures*. Mississauga, Ontario, Canada: Canadian Standards Association.

CAN/CSA S6-06. (2006). *Canadian highway bridge design code*. Mississauga, Ontario, Canada: Canadian Standards Association.

CAN/CSA S806-12. (2012). *Design and construction of building structures with fibre-reinforced polymers*. Mississauga, Ontario, Canada: Canadian Standards Association.

Canadian Precast/Prestressed Concrete Institute. (2007). *CPCI design manual 4*. 100-196 Bronson Avenue, Ottawa,ON Canada.

Collins, M. P., & Mitchell, D. (1991). *Prestressed concrete structures*. Upper Saddle River, NJ, USA: Prentice Hall College Div.

Cook, D. J., & Chindaprasirt, P. (1980). Influence of loading history upon the compressive properties of concrete. *Magazine of Concrete Research, 32*(111).

Debaiky, A. S., Nkurunziza, G., Benmokrane, B., & Cousin, P. (2006). Residual tensile properties of GFRP reinforcing bars after loading in severe environments. *Journal of Composites for Construction.*

El Aziz, A., & Fathy, M. (2006). Non-linear analysis of concrete beams prestressed and post-tensioned with carbon fiber reinforced polymer (CFRP) bars. (PhD, University of Windsor, Windsor, ON, Canada.).

El Maaddawy, T., Soudki, K., & Topper, T. (2005). Long-term performance of corrosion-damaged reinforced concrete beams. *ACI Structural Journal, 102*(5).

El Maddaawy, T. (2004). Performance of corrosion-damaged reinforced concrete beams repaired with CFRP laminates. (PhD, University of Waterloo, Waterloo, ON, Canada).

fib Fédération internationale du béton. (2006). *Design and use of fibre reinforced polymer reinforcement (FRP) for reinforced concrete structures*. Stuttgart, Germany: Sprint-Digital-Druck.

Fornůsek, J., Konvalinka, P., Sovják, R., & & Vítek, J. L. (2009). Long-term behaviour of concrete structures reinforced with pre-stressed GFRP tendons. *WIT Transactions on Modelling and Simulation, 48.*

Ghali, A., Favre, R., & Elbadry, M. (2002). *Concrete structures: Stresses and deformations*. New York, NY: Spon press.

Gilbert, R. I., & Ranzi, G. (2011). *Time-dependent behaviour of concrete structures*. New York city , NewYork, USA: Spon Press.

Hall, T., & Ghali, A. (2000). Long-term deflection prediction of concrete members reinforced with glass fibre reinforced polymer bars. *Canadian Journal of Civil Engineering, 27*(5).

ISIS Canada Corporation. (2008). *Design manual no. 5: Prestressing concrete structures with fibre-reinforced polymers*. Winnipeg, Manitoba, Canada: ISIS Canada Corporation.

Issa, M., Sen, R., & Amer, A. (1993). Comparative study of transfer length in fiberglass and steel pretensioned concrete members. *Precast/prestressed Concrete Institute.Journal, 38*(6).

Iyer, S., L., Khubchandani, A., & Feng, J. (1991). Fiberglass and graphite cables for bridge decks. *Advanced Composite Materials in Civil Engineering Structures, ASCE* , New York, NY,USA.

Joh, O., Wang, Z., & Goto, Y. (1999). Long-term deflection of fiber reinforced polymer concrete beams. *ACI Special Publication, 188.*

Kaklauskas, G. (2004). Flexural layered deformational model of reinforced concrete members. *Magazine of Concrete Research, 56*(10).

Kose, M. M., & Burkett, W. R. (2005). Evaluation of code requirement for 0.6 in.(15 mm) pre-stressing strand. *ACI Structural Journal, 102*(3).

Krem, S., & Soudki, K. (2012). Transfer length of carbon fibre reinforced polymer bars in self consolidating concrete. *The 6th International Conference on Advanced Composite Materials in Bridges and Structures, ACMBS-VI,* Kingston, ON,Canada.

La Borderie, C., Mazars, J., & Pijaudier-Cabot, G. (1992). Response of plain and reinforced concrete structures under cyclic loadings. *ACI Special Publication, 134.*

Lu, Z., Boothby, T. E., Bakis, C. E., & Nanni, A. (2000). Transfer and development lengths of FRP prestressing tendons. *PCI Journal, 45*(2).

Mahmoud, Z. I., Rizkalla, S. H., & Zaghoul, E. R. (1999). Transfer and development lengths of carbon fiber reinforced polymers prestressing reinforcement. *ACI Structural Journal, 96*(4).

Minosaku, K. (1992). Using FRP materials in prestressed concrete structures. *Concrete International, 14*(8).

Nanni, A., Utsonomiya, T., Yonekura, H., & Tanigaki, M. (1992). Transmission of prestressing force to concrete by bonded fiber reinforced plastic tendons. *ACI Structural Journal, 89*(3)

Neville, A. M. (1995). *Properties of concrete; 4th and final ed.* Harlow, Essex, England: Longman.

Neville, A. M., Dilger, W. H., & Brooks, J. J. (1983). *Creep of plain and structural concrete*. New York, USA: Construction Press.

Nkurunziza, G., Benmokrane, B., Debaiky, A. S., & Masmoudi, R. (2005). Effect of sustained load and environment on long-term tensile properties of glass fiber-reinforced polymer reinforcing bars. *ACI Structural Journal, 102*(4).

Oskouei, A. V., & Taleie, S. M. (2010). Experimental investigation of relaxation of fiber-reinforced polymer composites. *Journal of Reinforced Plastics and Composites, 29*(17).

Palermo, D., & Vecchio, F. J. (2003). Compression field modeling of reinforced concrete subjected to reversed loading: Formulation. *ACI Structural Journal, 100*(5).

Rao, G. A. (2001). Long-term drying shrinkage of mortar—influence of silica fume and size of fine aggregate. *Cement and Concrete Research, 31*(2).

Rusch, H. (1960). Researches toward a general flexural theory for structural concrete. *ACI Journal Proceedings, 57* (7).

Russell, B. W., & Burns, N. H. (1993). *Design guidelines for transfer, development and debonding of large diameter seven wire strands in pretensioned concrete girders. final report*. Austin, Tex, USA: Centre for Transportation Research, University of Texas at Austin.

Schoeck Canada Inc. (2009). *Technical information*. Kitchener, Ontario, Canada: Schöck Bauteile GmbH.

Sheard, P. A., Clarke, J. L., Dill, M. J. U., & Hammersley, G. P. (1997). Eurocrete—Taking account of durability for design of FRP reinforced concrete structures. *Proceedings of the Third International Symposium on Non-Metallic (FRP) Reinforcement for Concrete Structures,* Japan Concrete Institute. *, 2.*

Sima, J. F., Roca, P., & Molins, C. (2008). Cyclic constitutive model for concrete. *Engineering Structures, 30*(3).

Singh, M., & Svecova, D. (2014). Long term deflection of GFRP prestressed concrete slabs. *Proceedings of the 7th International Conference on FRP Composites in Civil Engineering, CICE 2014.*

Sinha, B., Gerstle, K. H., & Tulin, L. G. (1964). Stress-strain relations for concrete under cyclic loading. *ACI Journal Proceedings, 61* (2).

Sovják, R., Máca, P., Konvalinka, P., & Vítek, J. L. (2009). Experimental and numerical analysis of concrete slabs prestressed with composite reinforcement. *WIT Transactions on Modelling and Simulation, 48.*

Sritharan, S., & Fenwick, R. (1995). Creep and shrinkage effects in prestressed beams. *Magazine of Concrete Research, 47*(170).

Staton, B. W., Do, N. H., Ruiz, E. D., & Micah Hale, W. (2009). Transfer lengths of prestressed beams cast with self-consolidating concrete. *PCI Journal, 54*(2).

Thorenfeldt, E., Tomaszewicz, A., & Jensen, J. J. (1987). Mechanical properties of high-strength concrete and application in design. *Proceedings of the Symposium "Utilization of High Strength Concrete.*

Vecchio, F. (1999). Towards cyclic load modeling of reinforced concrete. *ACI Structural Journal, 96*(2).

Weber, A., & Baquero, C. W. (2010). New durability concept for FRP reinforcing bars. *Concrete International, 32*(7).

Yamaguchi, T., Kato, Y., Nishimura, T., & Uomoto, T. (1997). Creep rupture of FRP rods made of aramid, carbon and glass fibers. *The 3rd Int. Symposium on Non-Metallic Reinforcement for Concrete Structures (FRPRCS-3), 2.*

Youssef, T. (2010). Time dependent behaviour of fibre reinforced polymer (FRP) bars and FRP reinforced concrete beams under sustained load. (Doctoral dissertation, L'Université de Sherbrooke, Québec, Canada).

Youssef, T., & Benmokrane, B. (2011). Creep behavior and tensile properties of GFRP bars under sustained service loads. *American Concrete Institute, ACI Special Publication, , 2*. (275 SP).

Youssef, T., El-Gamal, S., & Benmokrane, B. (2009). Long-term deflection of GFRP-reinforced concrete beams under uniform sustained load. *Proceedings, Annual Conference - Canadian Society for Civil Engineering, 3*.

Zamblauskaite, R., Kaklauskas, G., & Bacinskas, D. (2005). Deformational analysis of prestressed high-strength concrete members using flexural constitutive model. *Journal of Civil Engineering and Management, 11*(2).

Zawam, M., & Soudki, K. (2012). GFRP prestressed concrete beams - A pilot study. *6th International Conference on Advanced Composite Materials in Bridges and Structures (ACMBS),* Kingston, Ontario, Canada.

Zawam, M., & Soudki, K. (2014). Transfer length of GFRP prestressed bars. *Proceedings of the 7th International Conference on FRP Composites in Civil Engineering, CICE 2014,* Vancouver, BC, Canada.

Zhang, M., Tam, C., & Leow, M. (2003). Effect of water-to-cementitious materials ratio and silica fume on the autogenous shrinkage of concrete. *Cement and Concrete Research, 33*(10).

Zou, P. X. (2003). Long-term properties and transfer length of fiber-reinforced polymers. *Journal of Composites for Construction, 7*(1).

Zou, P. X., & Shang, S. (2007). Time-dependent behaviour of concrete beams pretensioned by carbon fibre-reinforced polymers (CFRP) tendons. *Construction and Building Materials, 21*(4).

Appendix A

Transfer length measurements

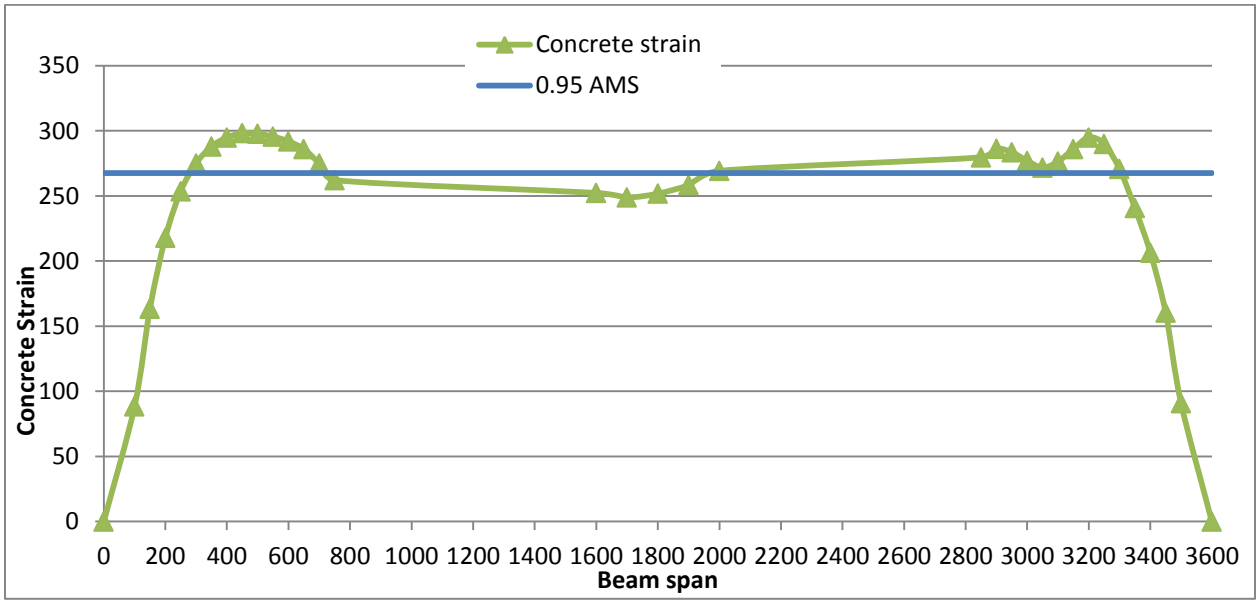

Figure A-1: Concrete surface strain profile for beam N40-16-0

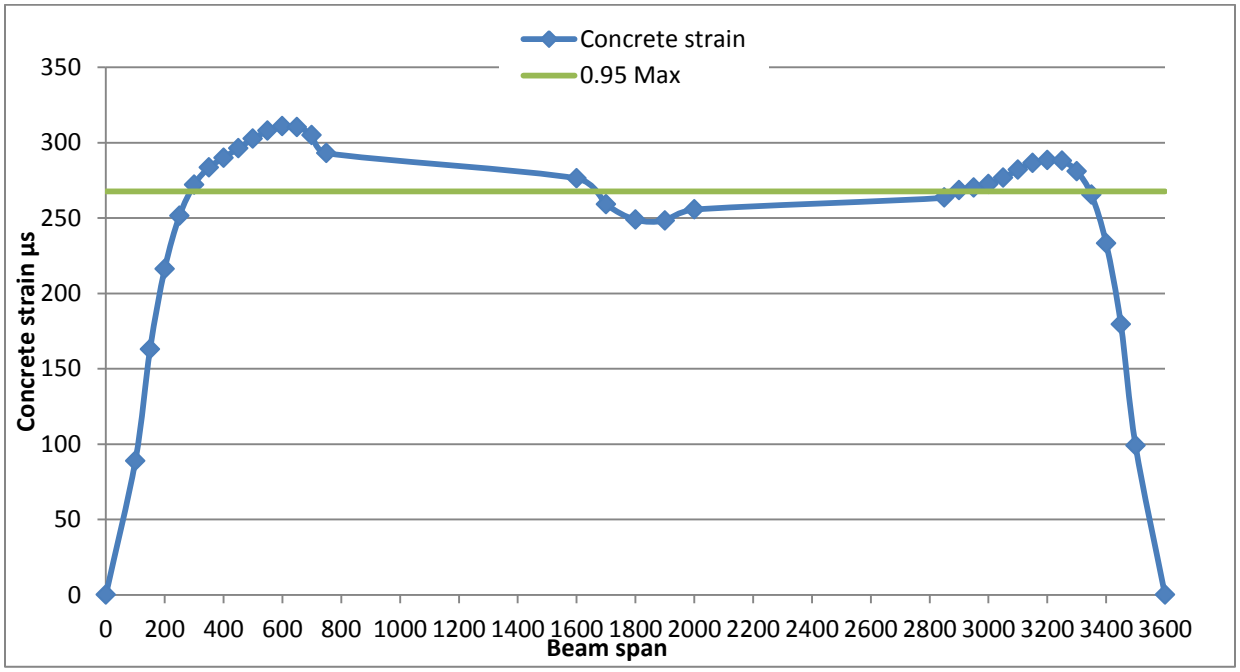

Figure A-2: Concrete surface strain profile for beam N40-16-35

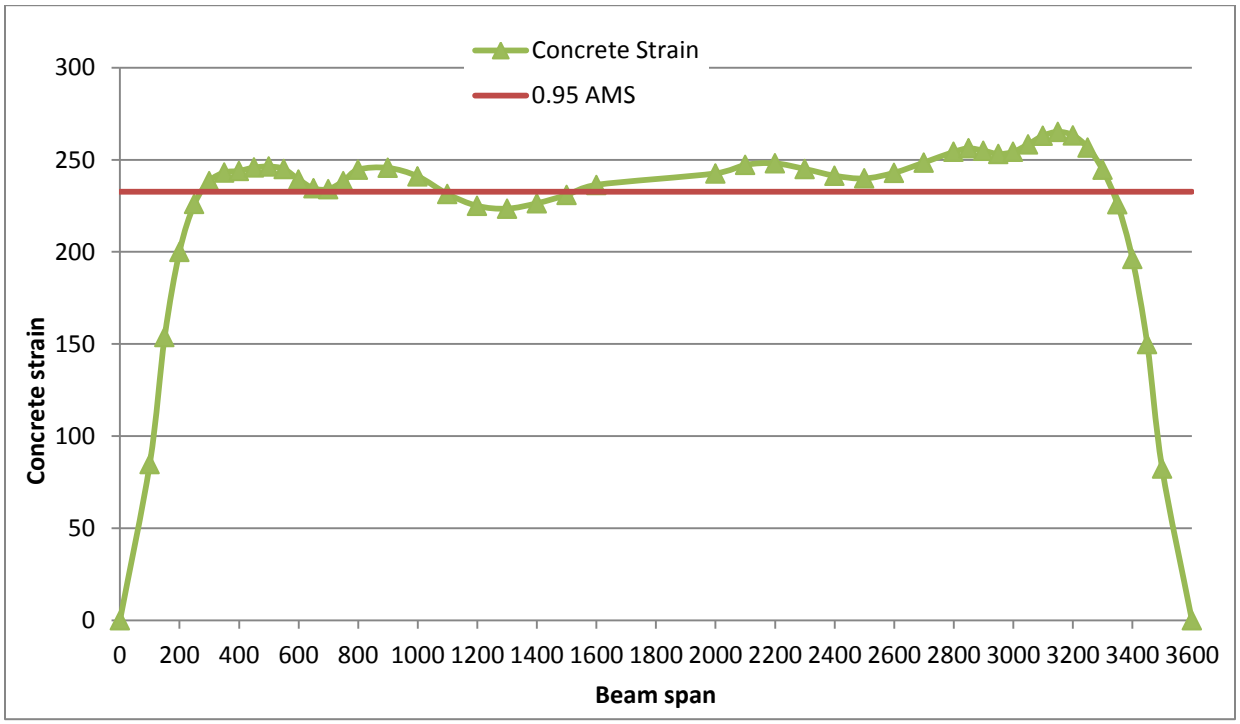

Figure A-3: Concrete surface strain profile for beam N40-16-80

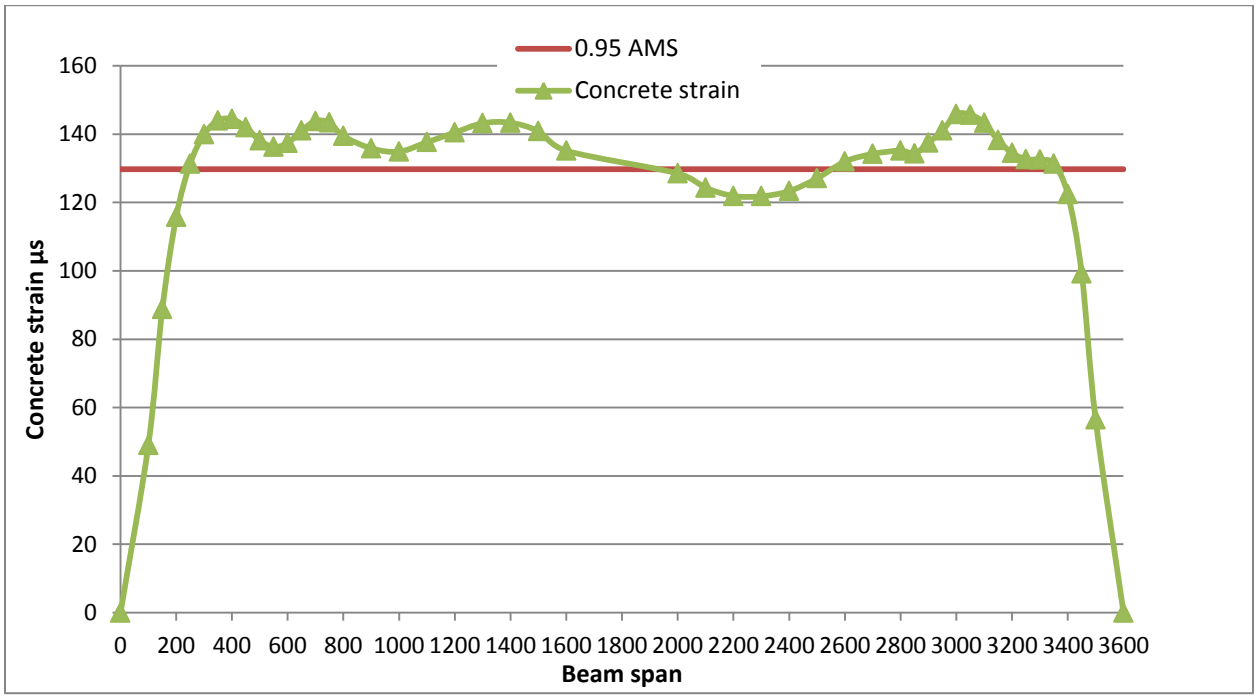

Figure A-4: Concrete surface strain profile for beam N40-12-80

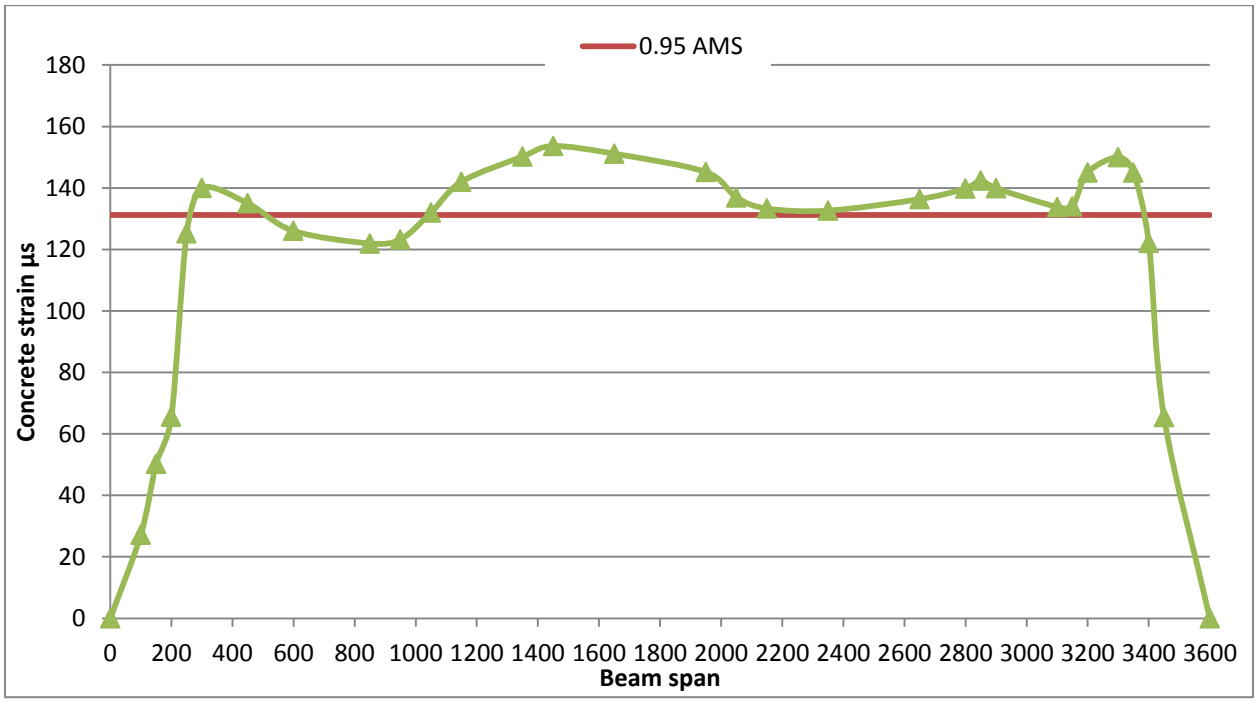

Figure A-5: Concrete surface strain profile for beam N40-12-35

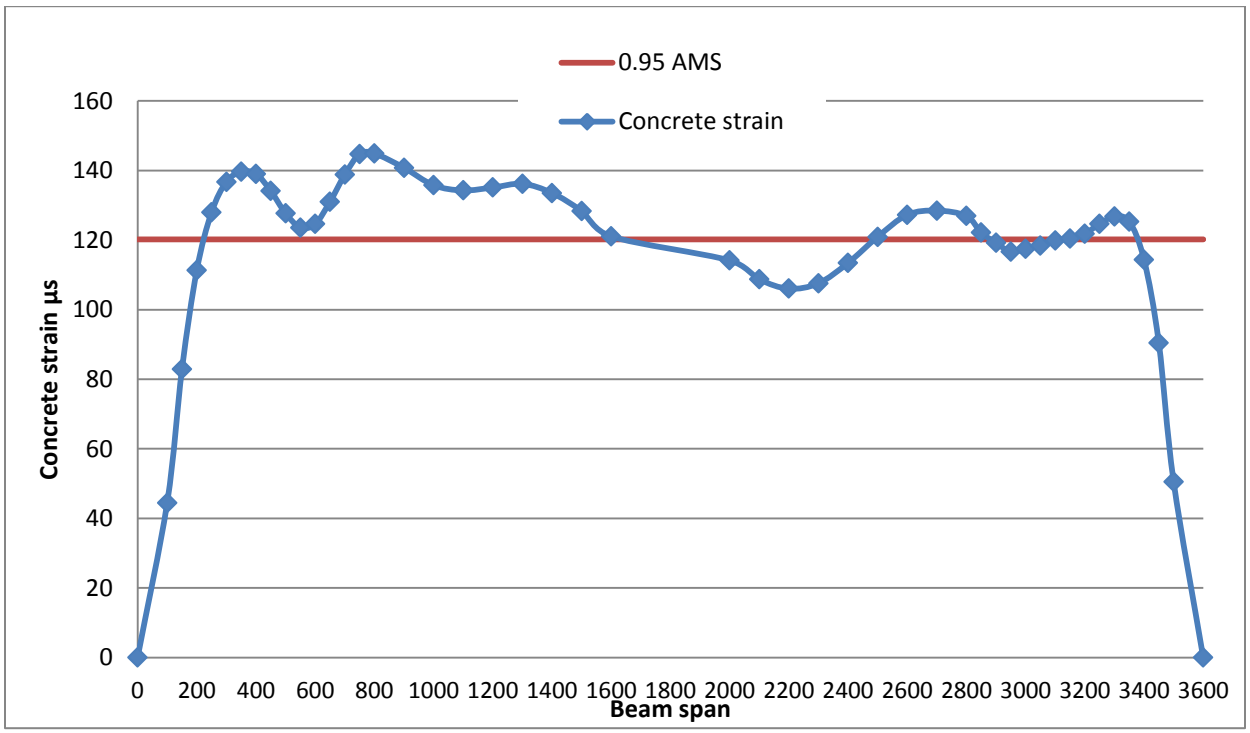

Figure A-6: Concrete surface strain profile for beam N40-12-80

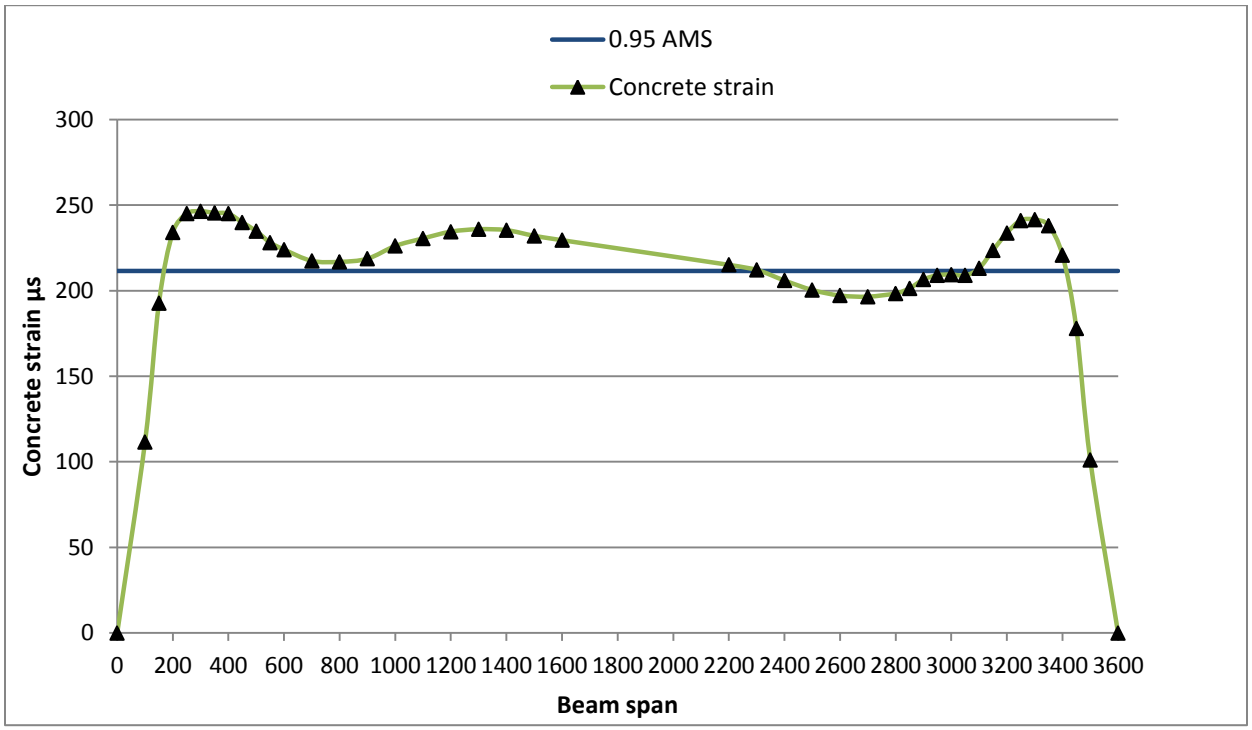

Figure A-7: Concrete surface strain profile for beam H40-16-0

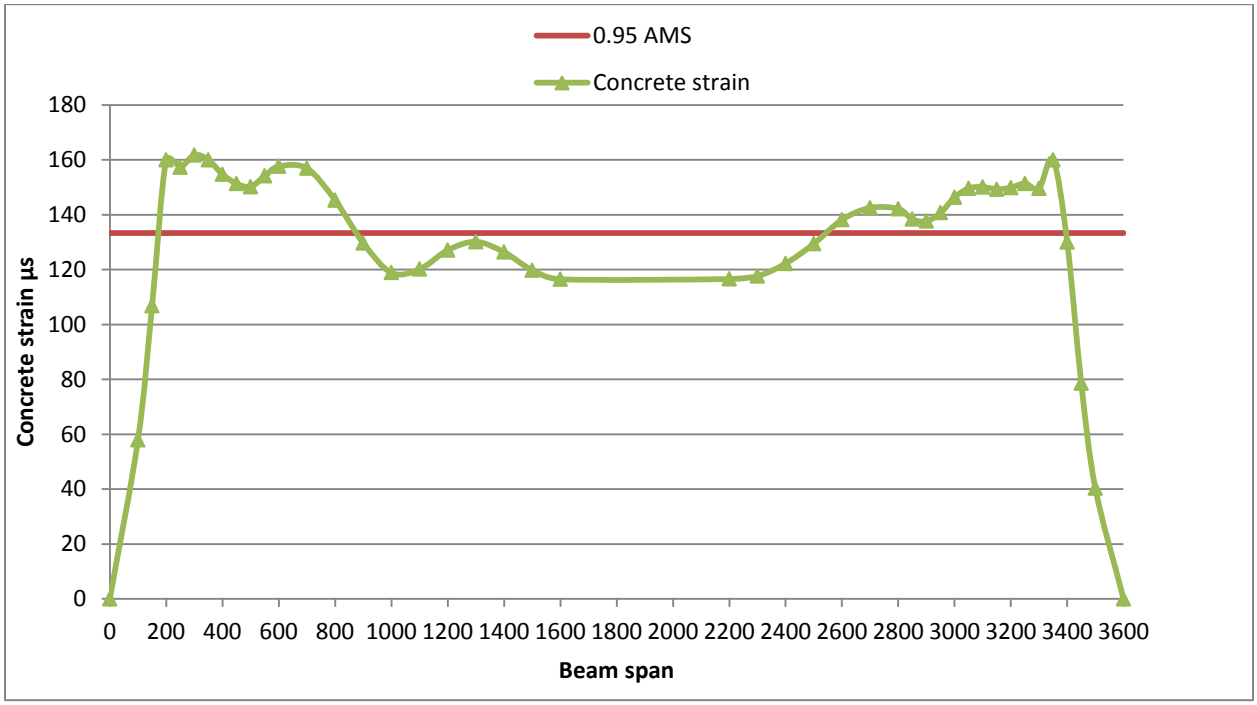

Figure A-8: Concrete surface strain profile for beam H40-16-35

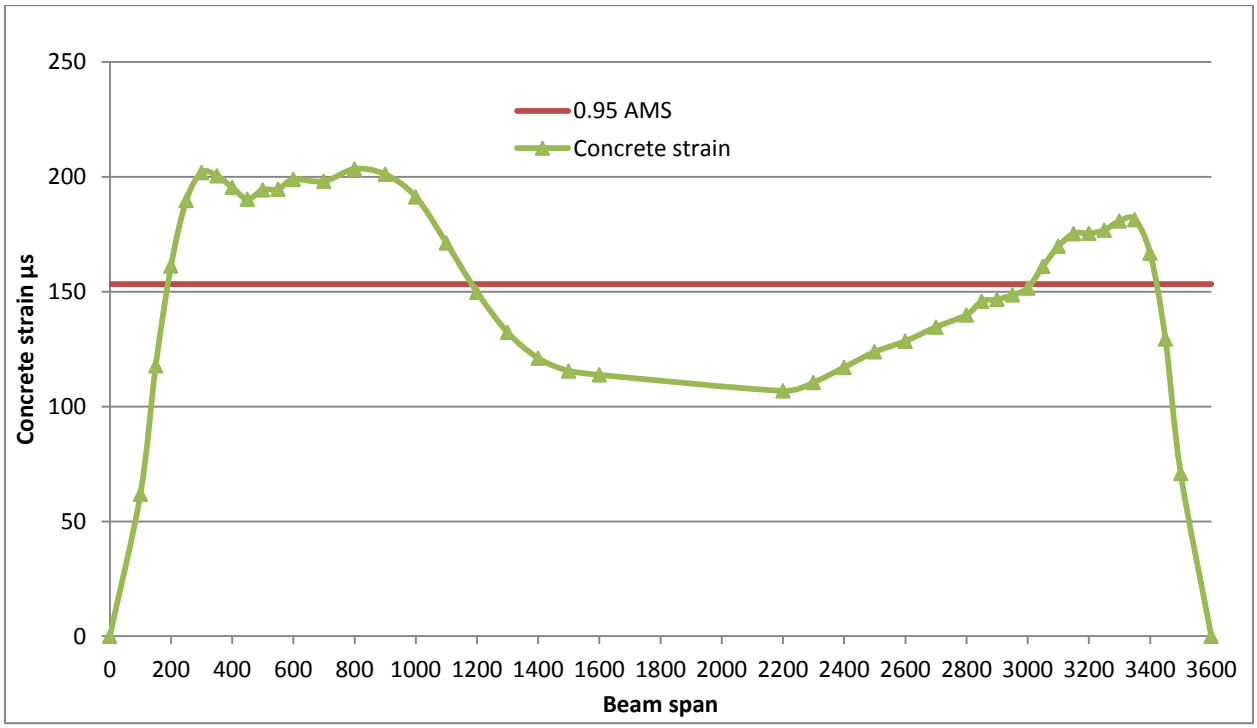

Figure A-9: Concrete surface strain profile for beam H40-16-60

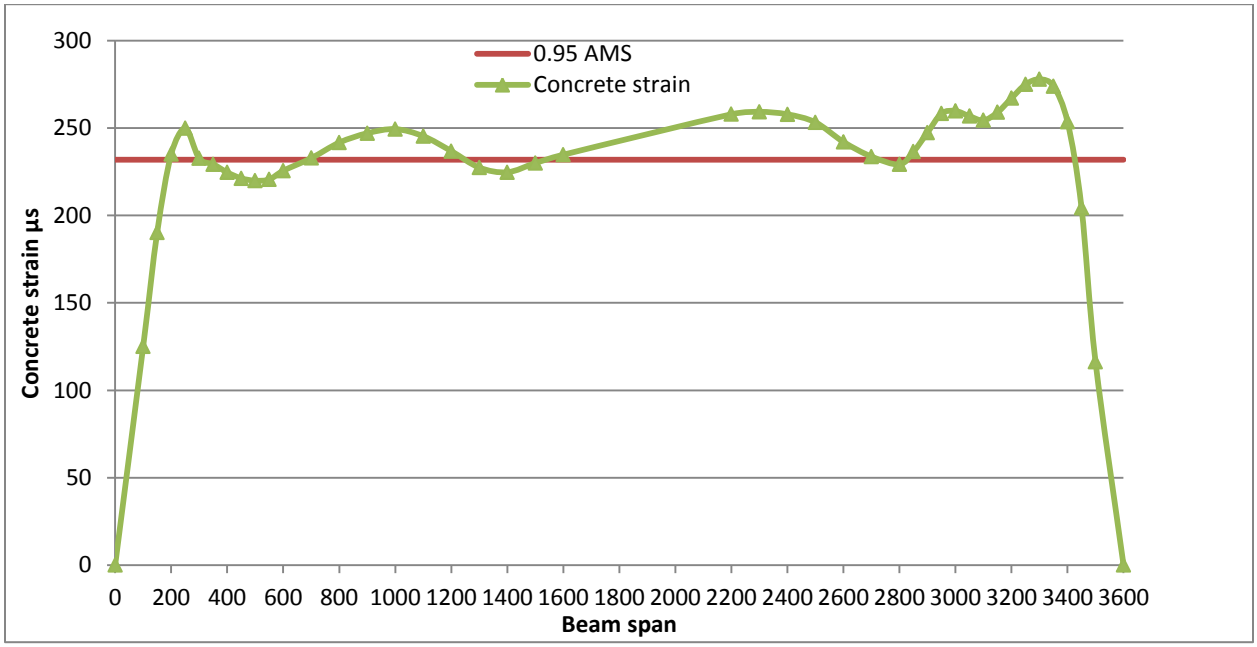

Figure A-10: Concrete surface strain profile for beam H40-16-80

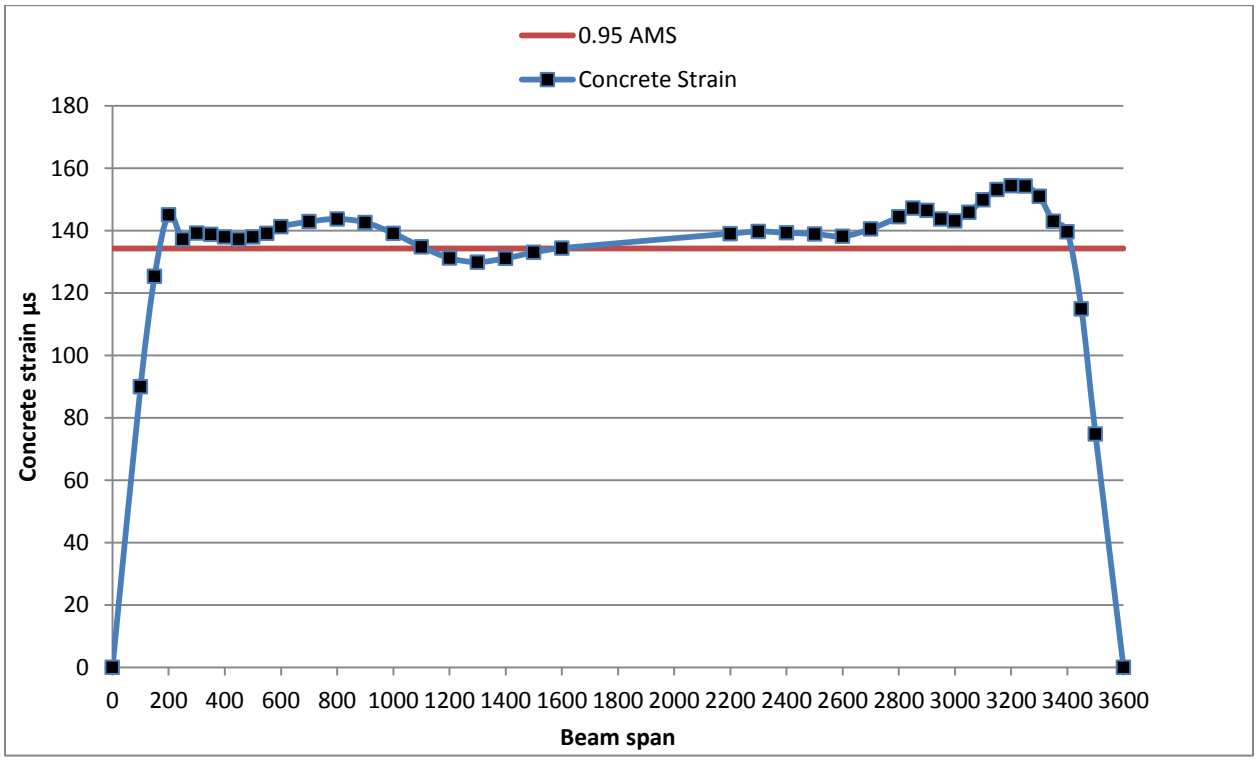

Figure A-11: Concrete surface strain profile for beam N25-16-0

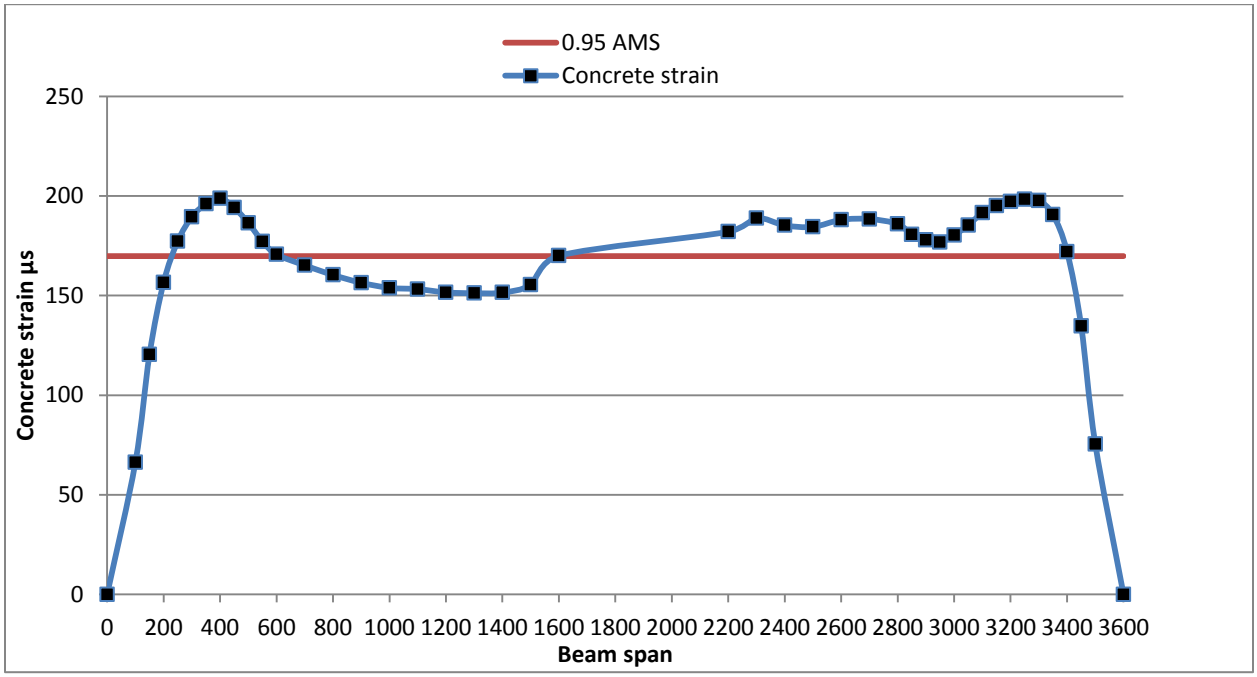

Figure A-12: Concrete surface strain profile for beam N25-16-35

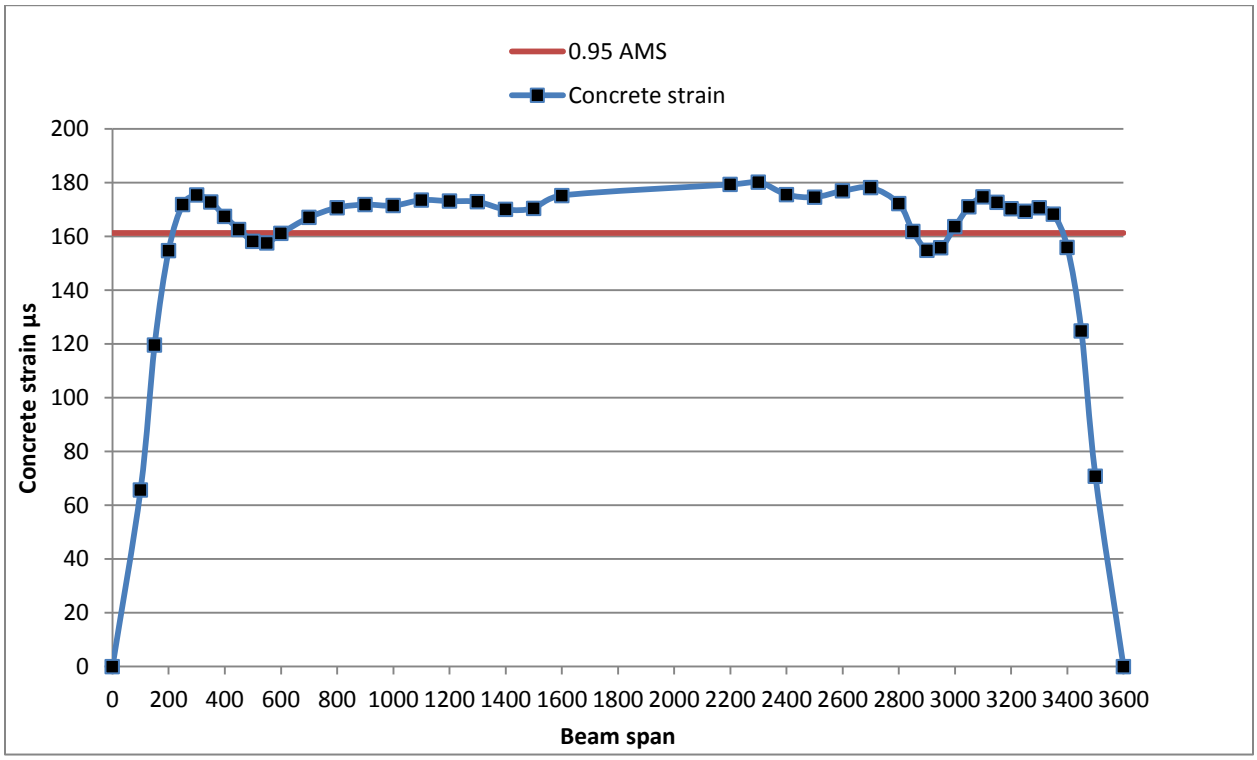

Figure A-13: Concrete surface strain profile for beam N25-16-60

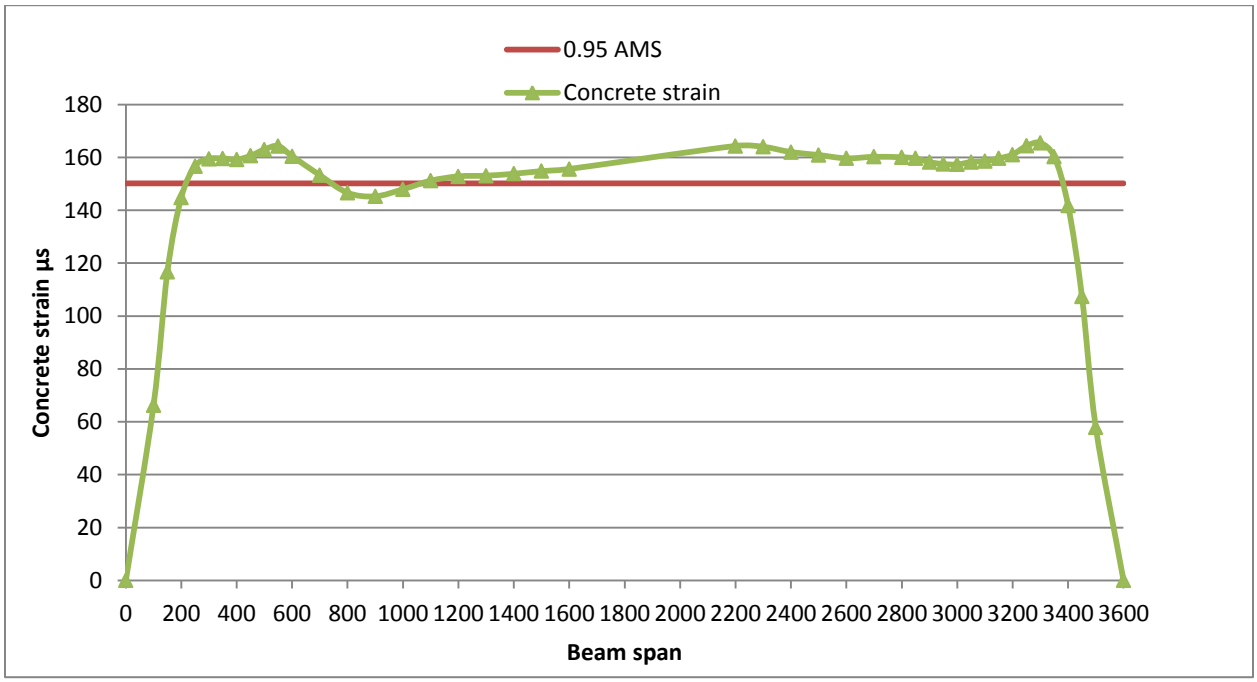

Figure A-14: Concrete surface strain profile for beam N25-16-60

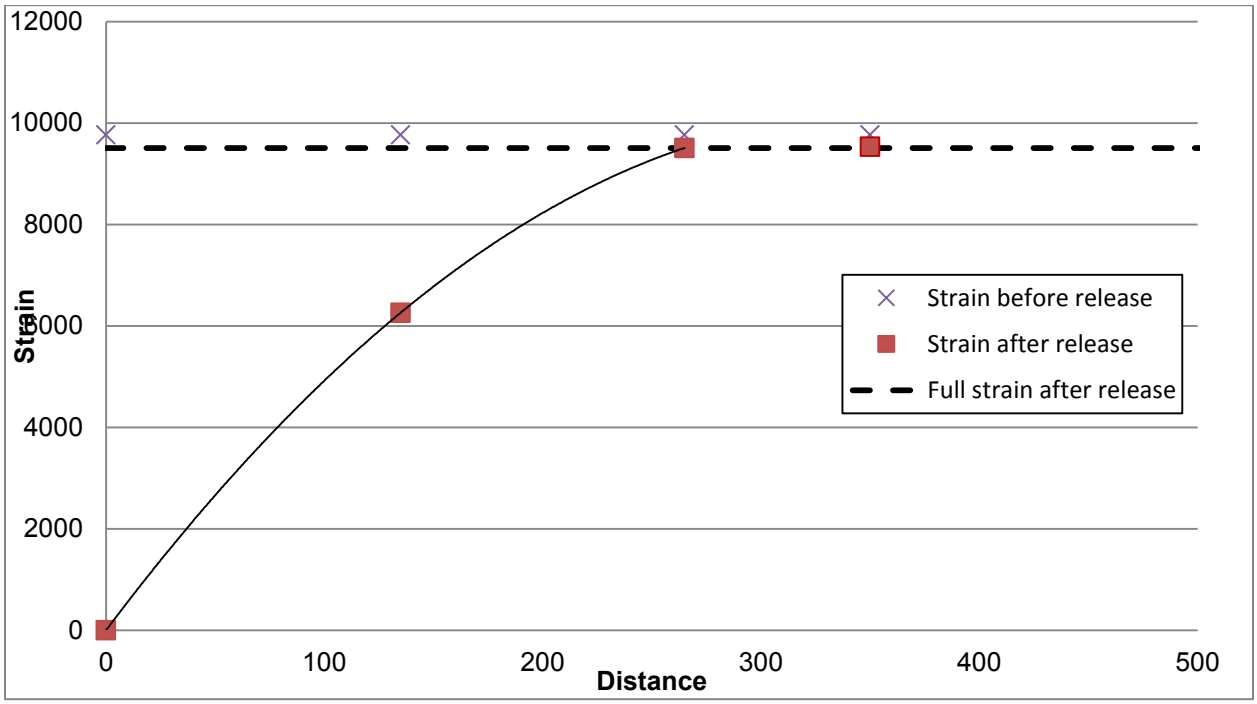

Figure A-15: GFRP bar strains after transfer for beam N40-16-80

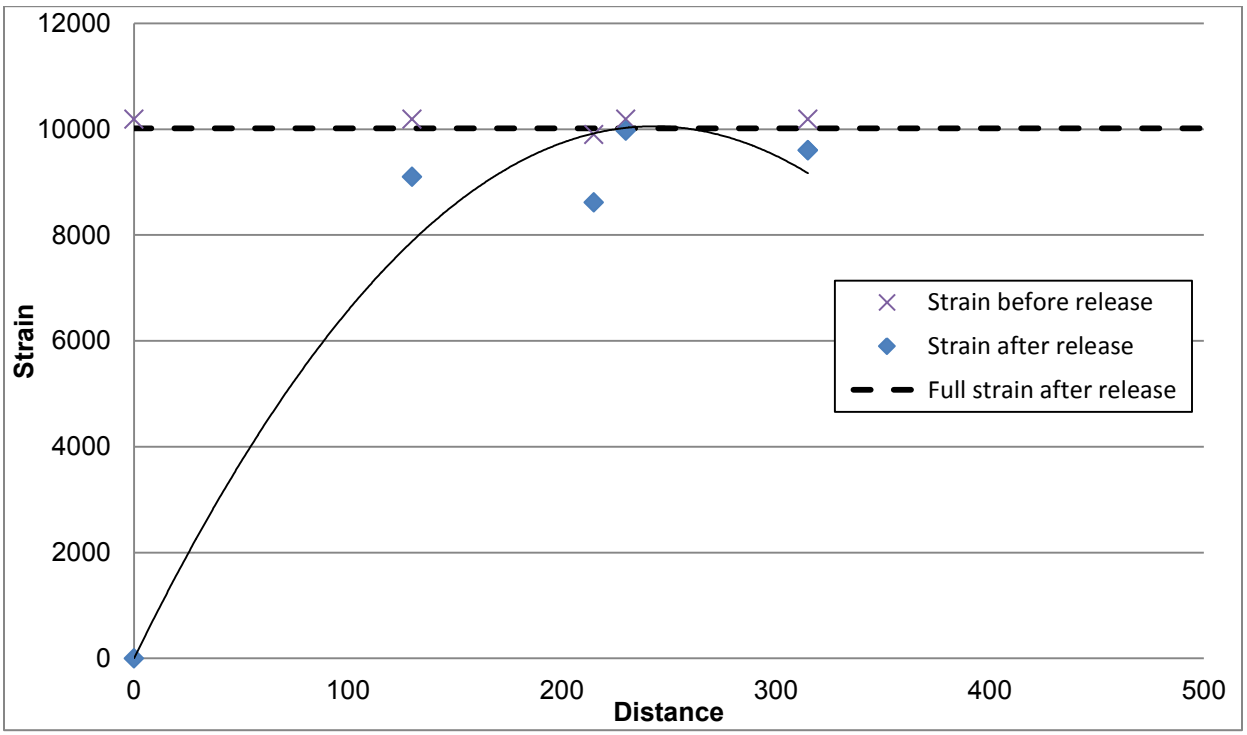

Figure A-16: GFRP bar strains after transfer for beam N40-12-80

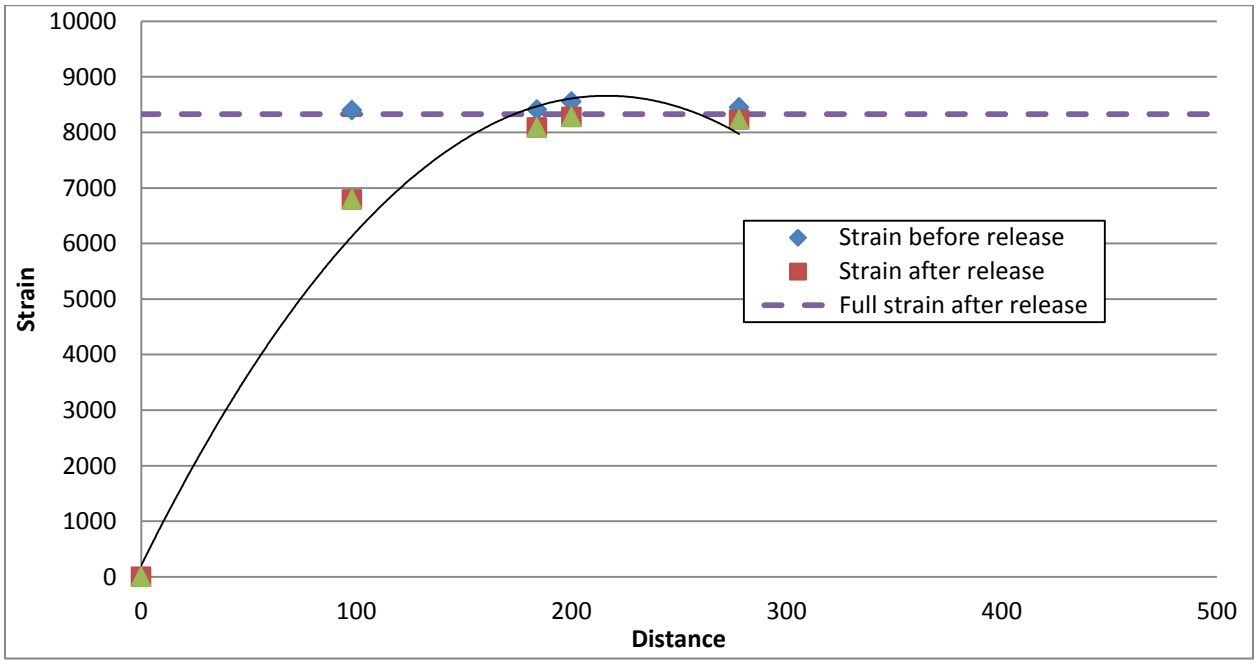

Figure A-17: GFRP bar strains after transfer for beam H40-16-0

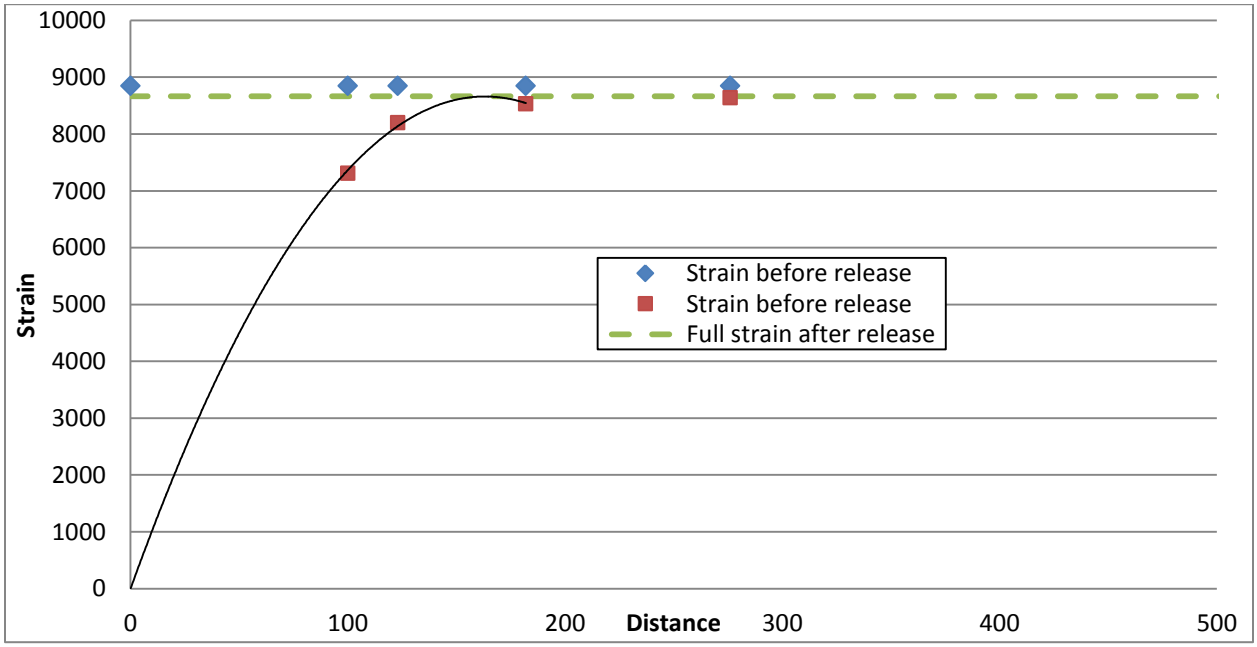

Figure A-18: GFRP bar strains after transfer for beam H40-16-35

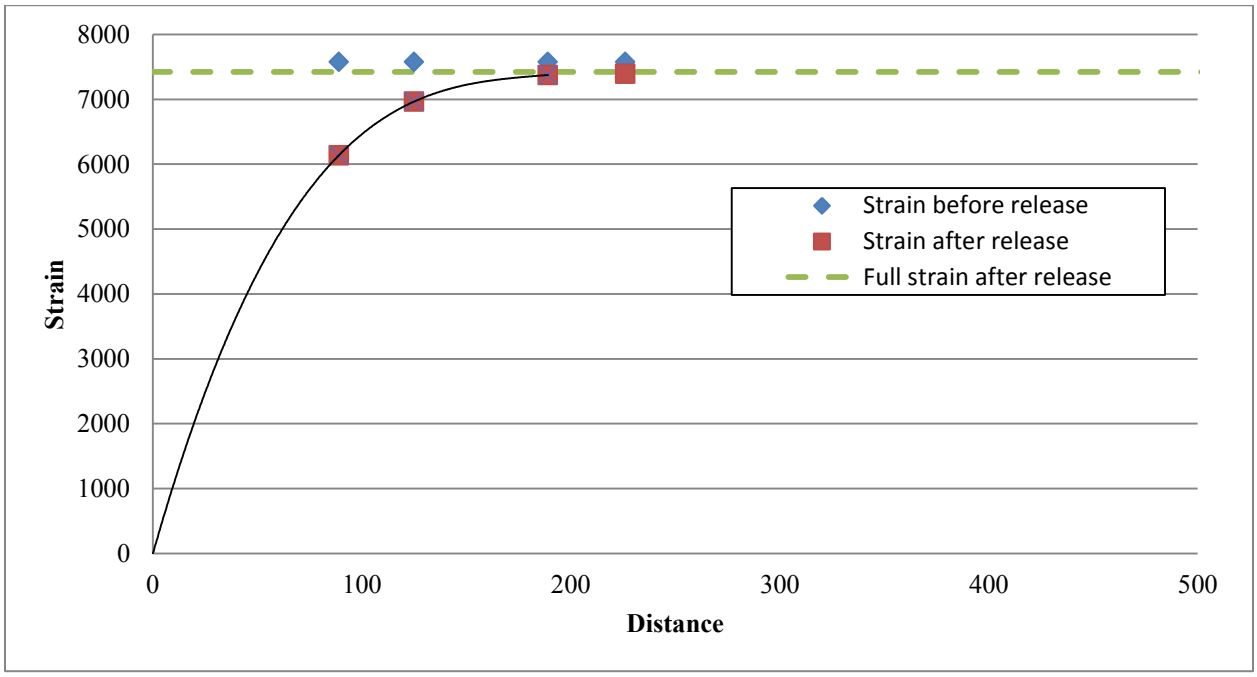

Figure A-19: GFRP bar strains after transfer for beam H40-16-60

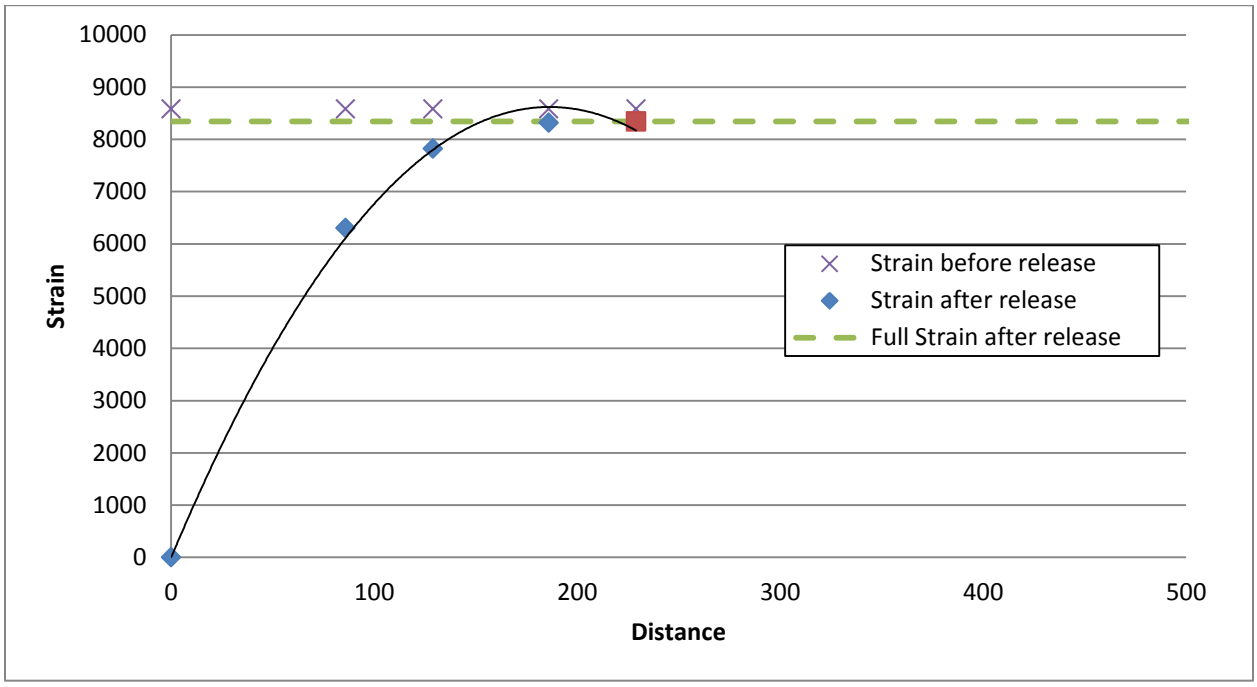

Figure A-20: GFRP bar strains after transfer for beam H40-16-80

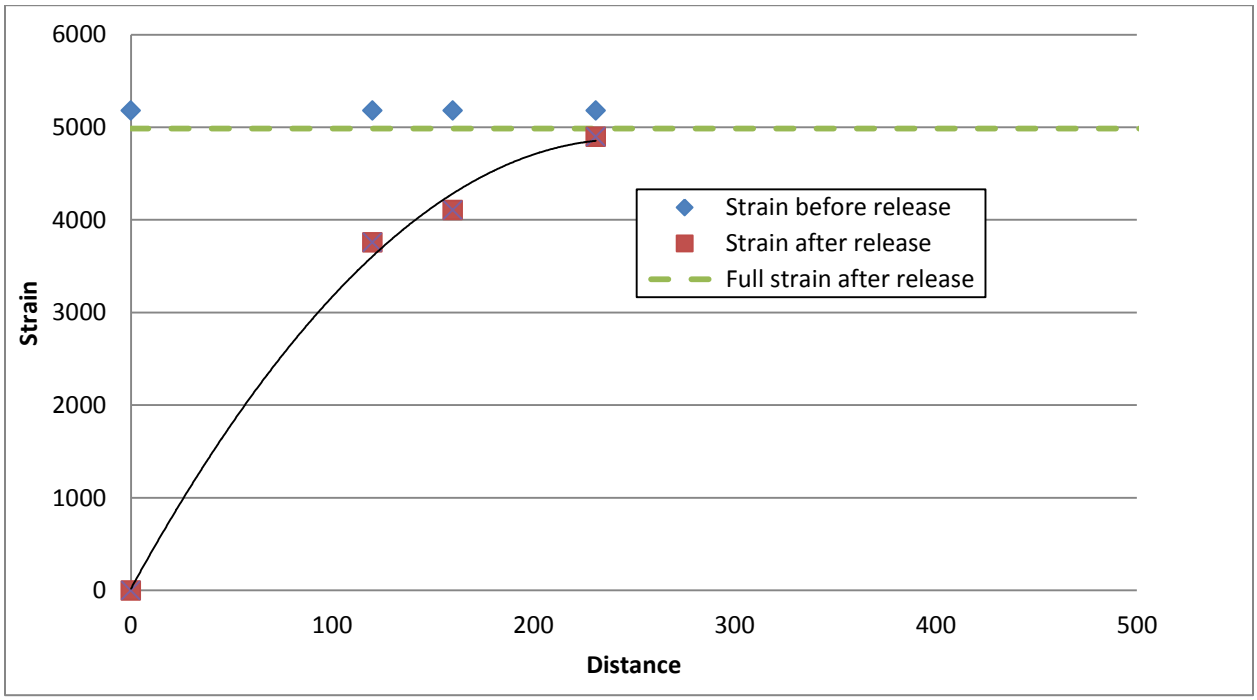

Figure A-21: GFRP bar strains after transfer for beam N25-16-0

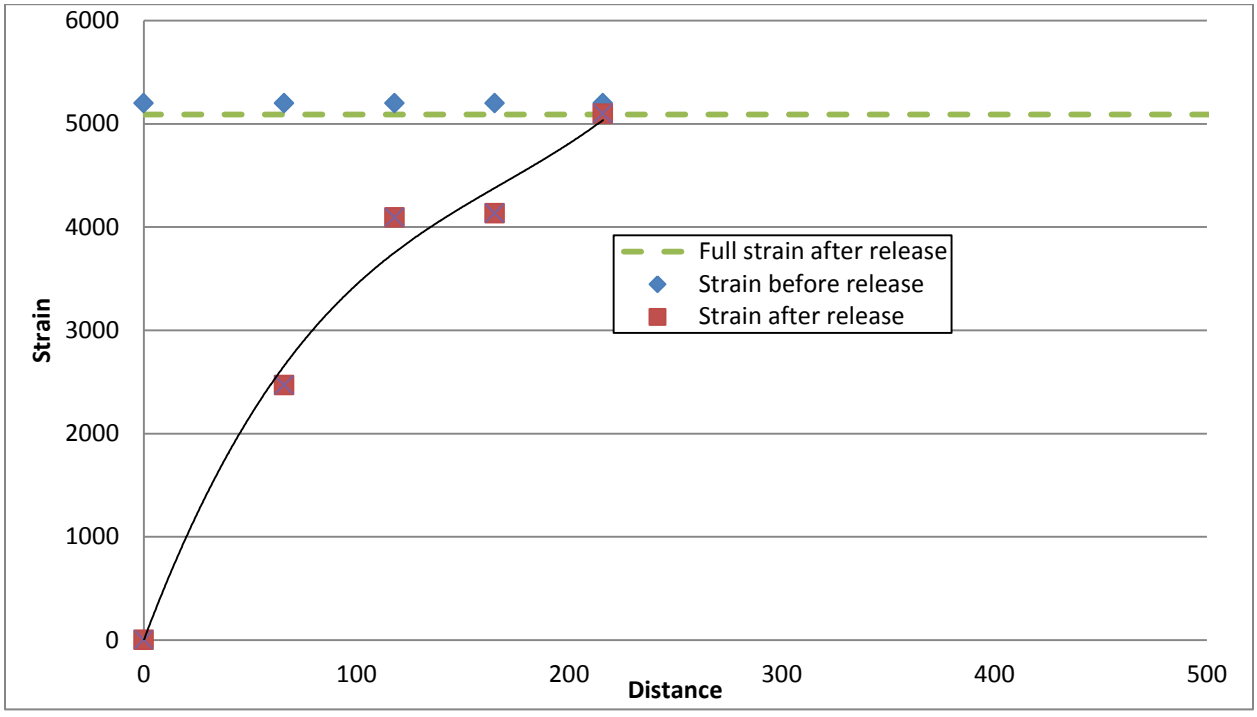

Figure A-22: GFRP bar strains after transfer for beam N25-16-35

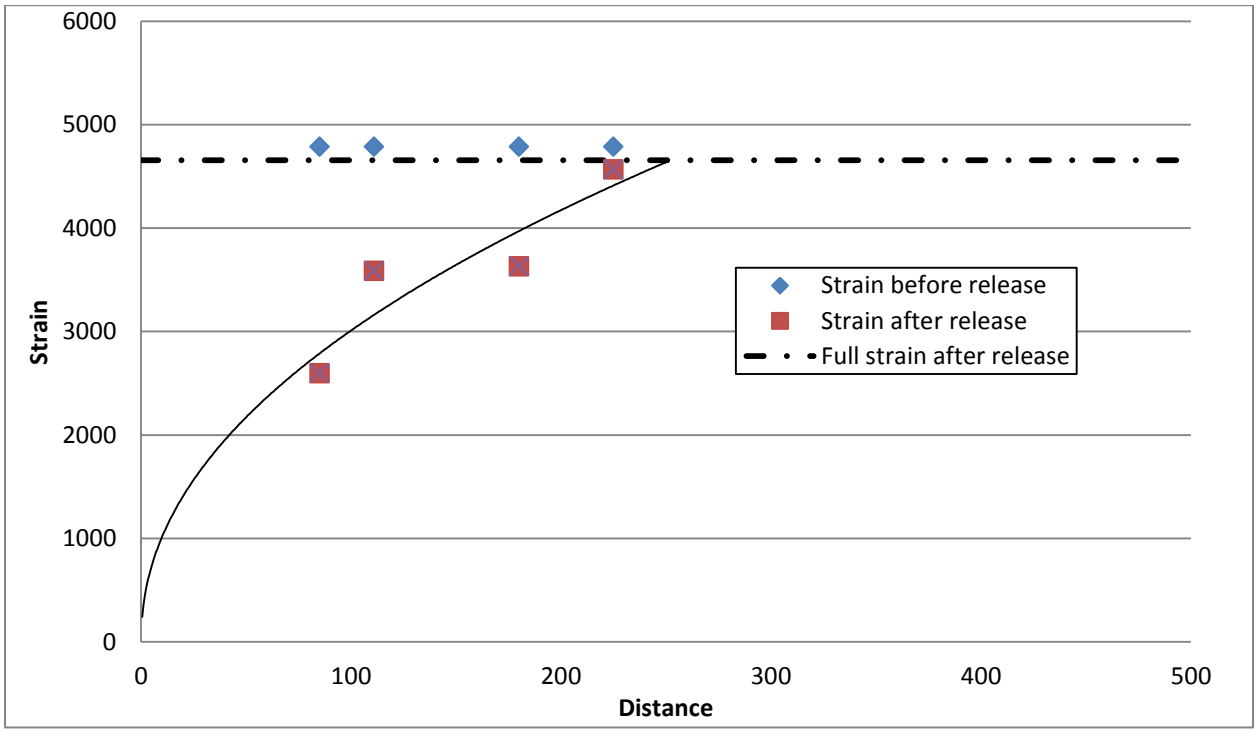

Figure A-23: GFRP bar strains after transfer for beam N25-16-60

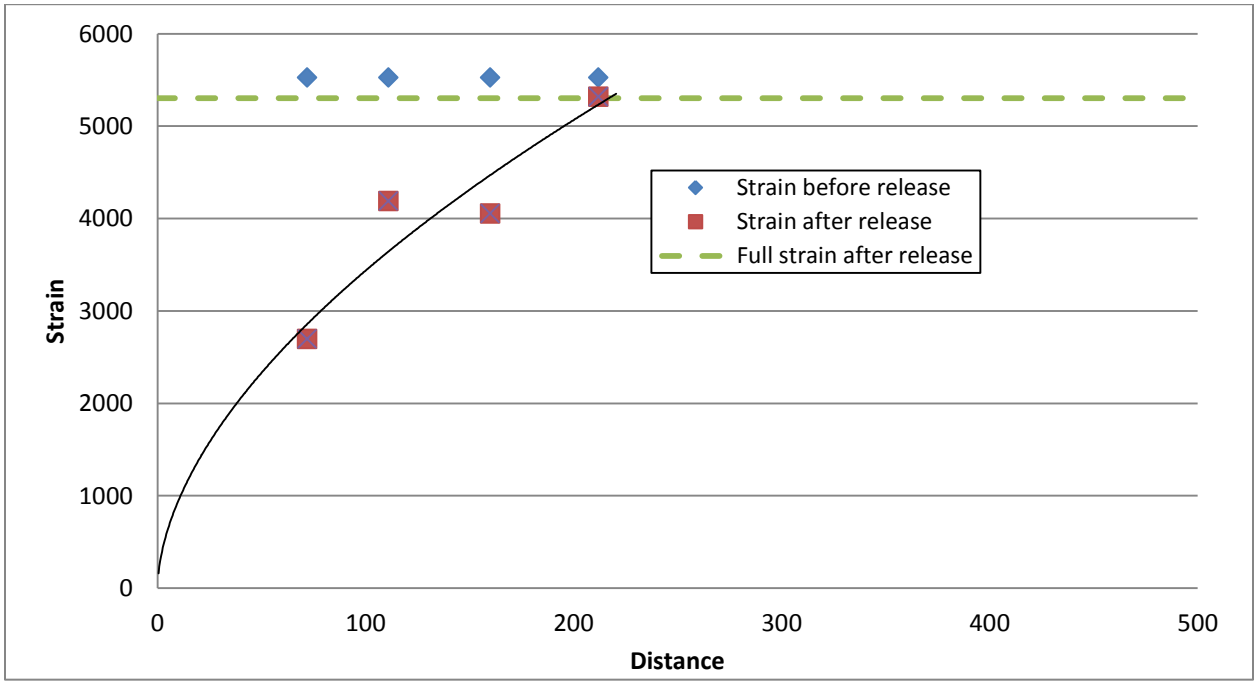

Figure A-24: GFRP bar strains after transfer for beam N25-16-80

Appendix B

Modification factors for calculating shrinkage and creep coefficient

Modification factors for calculating the shrinkage strain (ACI 209-92):

$k_1 = 1.25\ t_0^{-0.118}$ for moist curing.

$k_1 = 1.13\ t_0^{-0.095}$ for steam curing.

$k_2 = 1.27\text{-}0.006h$.

$k_3 = 1.14 - 0.00364\ V/S$. (For $37.5 < V/S < 95$ mm, and $t\text{-}t_0 \leq 1$ year)

Table B.1: Values for coefficient k_3 for $V/S < 37.5$ and $(t\text{-}t_0) \leq 1$ year

V/S	k_3
12.5	1.30
19.0	1.17
25.0	1.11
31.0	1.04
37.5	1.00

where V is the volume of the concrete member, and S is the member surface area, t is the age at predicting the creep coefficient, and t_0 is the time that loading started.

$k_3 = 1.10 - 0.00268\ V/S$. (For $V/S < 95$ mm, and $t\text{-}t_0 > 1$ year)

$k_3 = \frac{2}{3}\left[1 + 1.13\ e^{-0.0212(\frac{V}{S})}\right]$ (For $V/S \geq 95$ mm)

$k_4 = 0.82 + 0.00264\ s.$ (s is the slump in mm)

$k_5 = 0.88 + 0.0024\ A_f/A.$ (A_f/A is the fine aggregate / total aggregate ratio)

$k_6 = 0.46 + 0.09\ a \geq 1$ (a is the air content)

Modification factors for calculating the shrinkage strain (ACI 209-92):

$k'_1 = 1$ for steam curing for a period of 1 to 3 days.

Table B.2: Values for coefficient k'_1 for moist curing

Period of moist curing	**k'_1**
1	1.20
3	1.10
7	1.00
14	0.93
28	0.86
90	0.75

$k'_2 = 1.40 - 0.01h$ $(40 \leq h \leq 80)$

$k'_2 = 3.00 - 0.03h$ $(80 \leq h \leq 100)$

$k_3 = 1.23 - 0.006\ V/S.$ (For $37.5 < V/S < 95$ mm, and $t\text{-}t_0 \leq 1$ year)

Table B.3: Values for coefficient k_3 for V/S < 37.5 and $(t-t_0) \leq 1$ year

V/S	k'_3
12.5	1.35
19.0	1.25
25.0	1.17
31.0	1.08
37.5	1.00

where V is the volume of the concrete member, and S is the member surface area, t is the age at predicting the creep coefficient, and t_0 is the time that loading started.

$k'_3 = 1.17 - 0.006$ V/S. (For V/S < 95 mm, and $t-t_0 > 1$ year)

$k'_3 = 1.2\, e^{-0.00473(\frac{V}{S})}$ (For V/S ≥ 95 mm)

$k'_4 = 0.89 + 0.00264$ s. (s is the slump in mm)

$k'_5 = 0.30 + 0.014\ A_f/A$. (For $A_f/A \leq 50$)

$k'_5 = 0.90 + 0.002\ A_f/A$. (For $A_f/A > 50$)

where ; A_f/A is the fine aggregate / total aggregate ratio

$k'_6 = 0.75 + 0.00061\ ɤ$ (ɤ is the cement content)

$k'_7 = 0.95 + 0.008\ a \geq 1$ (a is the air content)

Appendix C
Prestressing losses calculations

- Losses at transfer (Elastic shortening, ES):

$$\Delta f_{pES} = \frac{E_{frp}}{E_c} \times f_{cgp}$$

$E_{frp} = 60000$ MPa

$E_c = 4500\sqrt{f'_{ci}}$MPa = 24647 MPa for normal strength concrete, and 67650 MPa for high strength concrete

$$f_{cgp} = \frac{P}{A} + \frac{P \times e^2}{I} - \frac{M_d \times e}{I}$$

For beams with 16M GFRP bar prestressed at 40%.

$$f_{cgp} = \frac{100000}{38760} + \frac{100000 \times 80^2}{210 \times 10^6} - \frac{1.4 \times 10^6 \times 80}{210 \times 10^6} = 5.25 \text{ MPa}$$

f_{cgp} = 2.58 MPa for the N40-12 group and 3.13 for N25-16 group.

Δf_{pES} = 11.1 MPa for the N40-16, 5.8 MPa for the N40-12, 6.6 for the N25-16 groups, and 4.8 for the H40-16 group.

- Long-term losses due to creep and shrinkage of concrete:

The long-term losses due to shrinkage and creep of concrete only are calculated as follows (CPCI 2007):

$$\Delta f_p = \frac{n_0 f_c C_t + \varepsilon_{sh} E_{frp}}{1 + n(\rho_{frp})(1 + {e^2}/{r^2})(1 + 0.8C_t)}$$

Following the ACI 209-92, the creep coefficient C_t for the period of 3 month was 2.0 for the normal concrete, and 2.12 for the high strength concrete, while the shrinkage strain ε_{sh} was 225 x 10^{-6} for the normal strength concrete, and was 330 x 10^{-6} for the high strength concrete.

ρ_{frp} = 0.0052 for the 16M beams, and 0.0029 for the 12M beams.

$r^2 = \frac{I_c}{A_c}$ =5471 mm^2

For the N40-16 group:

$$\Delta f_p = \frac{2.1 \times 5.35 \times 2.0 + 225 \times 10^{-6} \times 60000}{1 + 2.1(0.0052)\left(1 + {80^2}/{5471}\right)(1 + 0.8 \times 2.0)} = 33.9 \text{ MPa}$$

For the N40-12 group:

$$\Delta f_p = 24.3 \text{ MPa}$$

For the N25-16 group:

$$\Delta f_p = 25.1 \text{ MPa}$$

For the H40-16 group:

$$\Delta f_p = 29.2 \text{ MPa}$$

Appendix D

Stresses at transfer

Applied stresses at transfer:

For beams with 16M GFRP bar prestressed at 40% with normal strength concrete.

$$f_{top} = -\frac{P}{A} + \frac{P \times e^2}{I} - \frac{M_d \times e}{I}$$

$$f_{top} = -\frac{100000}{38760} + \frac{100000 \times 80 \times 127.5}{210 \times 10^6} - \frac{1.4 \times 10^6 \times 127.5}{210 \times 10^6} = 1.18 \text{ MPa} \quad (tension)$$

$$f_{bottom} = -\frac{P}{A} + \frac{P \times e^2}{I} - \frac{M_d \times e}{I}$$

$$f_{bottom} = -6.59 \text{ MPa} \quad (Compression)$$

Permissible concrete stresses at transfer (A23.3-04):

For Normal concrete

$$\text{Compression} = 0.6 f'_{ci} = 0.6 \times 30 = 18 \text{ MPa} > f_{bottom}$$

$$\text{Tension} = 0.25 \sqrt{f'_{ci}} = 0.25 \sqrt{30} = 1.37 \text{ MPa} > f_{top}$$

These calculations show that the stresses at transfer were less than the limits set by the A23.3-04. Other sets of beams have either less prestressing force or higher concrete strength; therefore they also have stresses at transfer that are less than the limits.

Applied stresses due 35% sustained loading:

Beam	Applied service moment	Top stress (MPa) (compression)	Bottom stress (MPa) (Tension)
N40-16-35	15.8	-8.1	3.1
N40-12-35	9.8	-5.5	2.7
H40-16-35	17.2	-8.9	3.9
N25-16-35	19.0	-8.4	5.3

Permissible concrete stresses at service loads (A23.3-04)

For Normal concrete:

Extreme fiber stress in compression due to sustained loads = $0.45f'_{ci} = 18$ MPa

Extreme fiber stress in tension due to sustained loads = $0.5\sqrt{f'_{ci}} == 3.2$ MPa

For High strength concrete:

Extreme fiber stress in compression due to sustained loads = $0.45f'_{ci} = 36$ MPa

Extreme fiber stress in tension due to sustained loads =$0.5\sqrt{f'_{ci}} = 4.5$ MPa